UNIVERSITY OF MESSINA

Department of Chemical, Biological, Pharmaceutical and Environmental Sciences
Doctoral Course in
Advanced Catalytic Processes for using Renewable Energy Sources (ACCESS)

Electrocatalytic and Cold Plasma Technologies for Advancing Sustainable Chemistry

PhD thesis of:

Francesco Pio Abramo

Supervisor:

Prof. Gabriele Centi

Prof. Salvatore Abate

The coordinator of the Doctoral Course:

Prof. Gabriele Centi

Academic Year 2022-2023- XXXVI cycle

S.S.D. CHIM/04

PREFACE

This thesis exemplifies how chemical research, particularly in the industry, is shifting towards new technologies to counteract and reduce the devastating effects of global warming. The efforts are not limited to one technology, but rather a range of possibilities as mentioned in the first chapter. It is essential to avoid repeating past mistakes. If 19th-century research had embraced new challenges instead of solely focusing on the use of fossil fuels, we may have been better equipped to face the current global problem. This issue is particularly shocking and oppressive for current and future generations.

However, it is unlikely that any of the new technologies based on renewable sources will be as revolutionary as the advent of oil. Nonetheless, each sector should use the most suitable technology depending on the case to avoid relying solely on one type of technology. This will allow for replacements of technologies that could lead to unforeseen critical issues in the future, as has happened with oil and the rise in global temperatures.

Finally, a warning to governments. Despite numerous climate conferences, none have resulted in significant reductions in emissions. The lack of commitment and economic interests are likely contributing factors. However, if there was a genuine desire to address the issue, it is possible to mitigate and solve the problem of global warming. For instance, international collaboration has successfully led to the closing of the ozone hole.

Therefore, I invite governments to follow the example of the scientific community, which has always collaborated and exchanged information to combat common problems, regardless of political, ethnic, and religious divisions. We all share one home, Earth.

ABSTRACT

The continuous rise in atmospheric CO_2 concentration has resulted in global warming, which is perhaps the most pressing issue of the 21st century. All environmental spheres are impacted, and significant changes in industrial production are necessary. The electrification of the chemical industry is crucial in this regard. This thesis focuses on two technologies for sustainable development: electrochemical reduction of oxalic acid catalyzed by titanium nanotubes and plasma-assisted CO_2 splitting. The first part of the thesis will study the morphology and activity of titanium nanotubes by changing anodization time and potential, aging of the electrolyte solution, and type of pretreatment (thermal, electrochemical, or no pretreatment). The text discusses the effect of rapid breakdown anodization on nanostructure and its relation to data obtained from FESEM, AFM, and ECSA. Higher performances were measured by longer and rougher nanotubes suggesting a synergic effect. A Faradaic efficiency to glycolic acid (86 %) and oxalic conversion (48 %) at −0.8 V vs. RHE was obtained, superior to the existing literature on TiO_2-only electrodes at room temperature. Moreover, the chemical nature of the active sites and its relationship with nanostructure was investigated by CV and XPS, showing that oxygen vacancies are crucial to catalyze the reaction.

The second part of the thesis focuses on improving a DBD reactor for CO_2 splitting using cold plasma. It compares the performances (conversion, SEI, and energy efficiency) of a classic DBD reactor with a smooth electrode to an innovative reactor with an internal electrode of two different porosities (0.2 μm and 0.5μm). The data indicate that porosity has a beneficial effect, likely due to a higher plasma density within the pores and a tip effect that increases the local electric field. Additionally, this study will demonstrate the impact of a boehmite layer deposited on porous electrodes through dip coating. Compared to a packed configuration, the results demonstrate higher conversion and energy efficiency, while avoiding a reduction in residence time. This could also be a turning point to reduce the costs. The data were collected using both pure CO_2 and CO_2 diluted.

SUMMARY

ACRONYMUS

AFM atomic force microscopy
AO anodic oxidation
CRM critical raw materials
DBD dielectric barrier discharge
DMO dimethyl oxalate
EG ethylene glycol
GA gliding arc
GC glycolic acid
GHG green house gasses
GO glyoxylic acid
ECSA electrochemical active surface area
FAD field assisted dissolution theory
FE faradaic efficiency
HER hydrogen evolution reaction
MG methyl glycolate
MW microwave
NTs nanotubes
NZE net-zero emissions
OBT oxygen bubble theory
OX oxalic acid
O2v oxygen vacancies
PAA porous anodic alumina
PDF powder diffraction file
PTX power-to-X
RBA rapid breakdown anodization
RHE reverse hydrogen electrode
RMS root mean square roughness
SEI specific energy input
SMR steam methane reforming
VOC volatile organic compound
VT vibrational – translation

LIST OF TABLES

LIST OF SCHEMES

LIST OF IMAGES

1

GLOBAL WARMING

The challenge of current century

1.1 Climate and humanity

Over millions of years, the average global temperature has varied enormously because of external and internal phenomena, profoundly marking life on Earth from time to time (figure 1.1). These changes, however, occurred over centuries or millennia, allowing the earth and life to adapt [1]. Nevertheless, the average global temperature has almost stabilized over the past 10000 years or so. This has allowed life to explode and evolve into all the wonderful creatures that populate our planet today.

However, minor changes in global climate temperature have had large impacts on humans not only physically but also socially and intellectually. As German historian Wolfgang Behringer points out in *Cultural History of Climate from the Ice Age to Global Warming* [2], historically relevant events are often the consequences of major climatic events that have disrupted entire populations. For example, in 2400 B.C., due to a great drought and the following ecological crisis, populations living in what is now Pakistan and northwestern India migrated to Mesopotamia and Central Europe. Think again of the Black Death that struck Europe in the 14th century, decimating its population, caused by a great famine immediately preceding, a consequence of the hardening of climatic conditions. The French Revolution also had among its triggers a severe winter drought accompanied by a particularly rainy summer that led to poor harvests, famine, and the rising cost of bread.

Since the first industrial revolution, that is, since the massive use of fossil fuels (coal), global temperature began to rise at a frighteningly high rate. We are currently living in a time when anthropogenic activity and population growth is causing

profound, and now irreversible climate changes, due to the uncontrolled emission of greenhouse gases (firstly CO_2) and the increase of global temperature. As stated by Burke et al.[3] the Earth system is well on its way to a climate condition unlike any that we have known since the advent of agricultural civilizations (7 kyear) and the history of the human species (360–240 kyear), while Pliocene and Eocene seems to be the best analogs for near future climates (figure 1.1) [3].

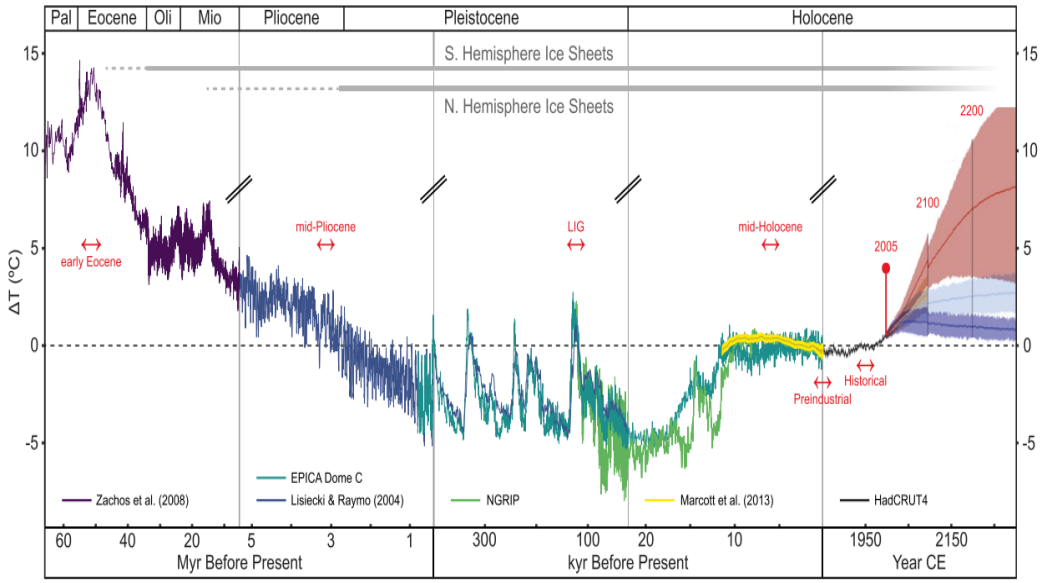

Figure 1.1 *Temperature trends for the past 65 Ma and potential geohistorical analogs for future climates. From ref. [3]*

This quickly change has devastating consequences, which are already beginning to be evident such as the wildfires that in last years affected the Amazon rainforest, Siberia, Canada, and Australia, or the increased frequency of powerful hurricanes, such as Hurricane Dorian, which devastated the Caribbean islands and the eastern coasts of the U.S, and terrible floods such as the one that occurred in Libya in September 2023, with over 11,000 deaths. These extreme events are also afflicting Italy, causing extreme and anomalous drought during winter months and floods not only in autumn, but also during warmer periods as happen in Emilia-Romagna in May 2023.

1.2 The greenhouse effect and global warming

Greenhouse effect is the atmospheric phenomenon that contributes most to climate change, but at the same time it is a natural effect that allowed life on Earth. Solar radiation passing through the earth's atmosphere is partly absorbed or scattered:

• 30% is reflected and scattered by atmospheric molecules, clouds, and aerosol particles.

• 20% of solar energy is absorbed by the atmosphere, which then heats up.

• the remaining 50% is absorbed by the earth's surface.

The Earth's surface, heated to a temperature of about 255 K, radiates the absorbed heat as long-wavelength infrared radiation in the range of 4-100 μm. Certain gases in the atmosphere, called greenhouse gases (GHG), which were largely transparent to incoming solar radiation, are able to absorb the IR radiation emitted by the Earth and re-emit it back into the atmosphere due to the vibrational motions of the atoms that make up these molecules. The gases, responsible for the greenhouse effect, are varied in nature and consequently manage to retain heat with varying efficiency (figure 1.2). The most important GHG are the following ones [4]:

• Carbon dioxide (CO_2): It is part of a biogeochemical cycle in which carbon is exchanged among the Earth's oceans, soil, rocks, and biosphere. CO_2 absorbs IR radiation at wavelengths of 4.26 μm (asymmetric stretching) and 14.99 μm (bending). Although it does not have a high absorption capacity it is present in high concentrations compared to other GHG and consequently plays a significant role in influencing the greenhouse effect. It is emitted in the atmosphere by human activities as a byproduct of the burning of fossil fuels (such as coal, natural gas, and oil), solid waste, the decomposition of trees and other biological materials, as well as some chemical reactions (such as the manufacturing of cement).

• Water vapor: it handles about two-thirds of the natural greenhouse effect because it absorbs IR radiation over a wide range. However, there is a constant balance between temperature and water vapor concentration because of the short life cycle

of water vapor.

• Methane (CH_4): it has a high capacity in retaining heat; in fact, over a 20-year period, it traps 84 times more heat per unit mass than carbon dioxide but has a concentration about 200 times lower than CO_2. It is naturally released by volcano eruption principally, but the anthropic activities have a higher impact. In fact, it derives especially by the production and transport of fossil fuels, the anaerobic decay of organic waste in municipal solid waste landfills and by intensive livestock farming.

• Nitrous oxide (N_2O): it has 206 times the heat-absorbing capacity of CO_2 but is present in significantly smaller quantities. It is emitted during agricultural, land use, and industrial activities but also it derives from the combustion of fossil fuels and solid waste as well as during treatment of wastewater.

• Tropospheric ozone (O3): it handles about 3-7% of the natural greenhouse effect. Although it is crucial for Earth life because it block most of the UV radiation (especially UVA and UVC) in the ozonosphere (from 15 to 30 Km) it is a pollutant in the troposphere. It is formed by the so-called photochemical smog, as consequence of oxidation of Volatile Organic Compounds (VOC) and CO in presence of light and nitrogen oxides (NO_x).

• Chlorofluorocarbons (CFCs): they are the only GHG that do not exist in nature but have been developed by humans for industrial purposes. They are extremely potent GHG, in fact they can trap up to 22,000 times more heat than CO_2 and remain in the atmosphere for thousands of years, but they too are found in small quantities.

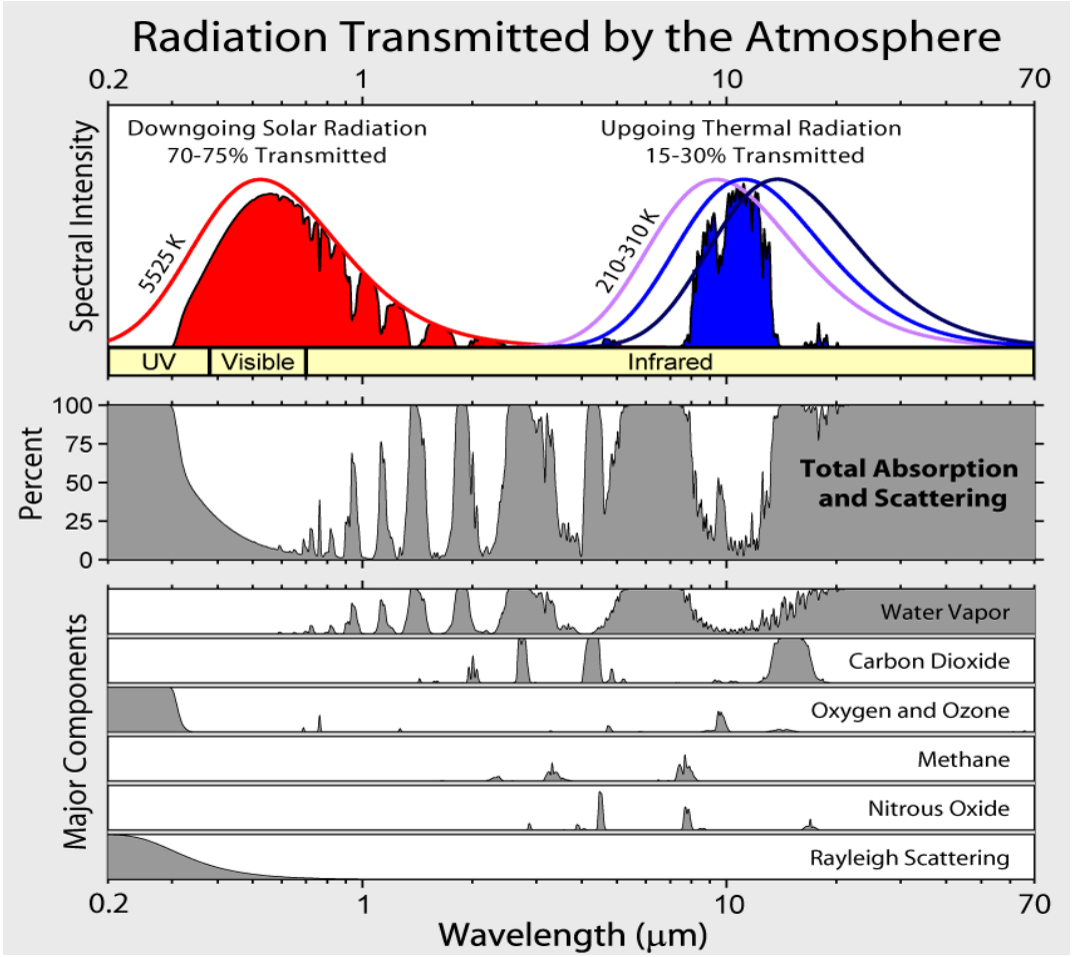

Figure 1.2 *IR radiation absorption of the most important greenhouse gases. Global IR absorption of all greenhouse gases is shown above. Source: image prepared by Robert A. Rohde for the Global Warming Art. https://creativecommons.org/licenses/by-sa/3.0/d*

Thus, the greenhouse effect is a natural phenomenon and in itself does not cause any climate problems; on the contrary, it allows the atmosphere and the earth's surface to warm up, maintaining ideal conditions for the development of terrestrial life. In fact, without the greenhouse effect, the average temperature of the globe would be -15°C. However, anthropogenic activity since the first industrial revolution, due to the use of fossil fuels, constant population growth and intensive livestock farming, has and does input massive amounts of GHG, resulting in an intensification of the natural greenhouse effect. Indeed, the IPCC Fifth Assessment Report stated that: "It is

extremely likely that human influence has been the dominant cause of observed warming since the mid-20th century"[5]. Global warming is thus defined as the rise in the average temperature of the globe caused by human activity.

1.3 Consequences of global warming

Global warming is having repercussions in every environmental sphere, and as time goes on, they will become more ominous if immediate actions are not taken. The most important consequences are described below.

Rising temperatures

As early as 1895, Swedish chemist Svante Arrhenius calculated that doubling CO_2 concentrations in the atmosphere would result in an increase of about 5-6°C in the average temperature of the globe[6]. Multiple independently produced instrumental datasets confirm that the decade 2011-2020 was 1.1 ± 0.07°C warmer (figure 1.3), than the pre-industrial period (1850-1900).

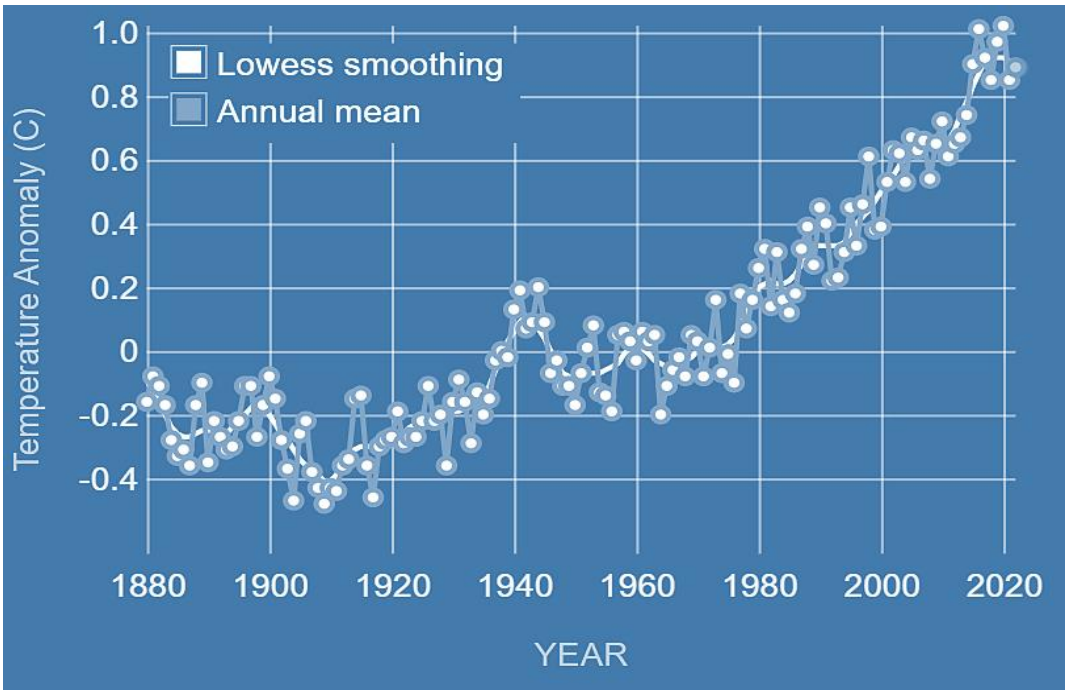

Figure 1.3 *Change in global surface temperature compared to the long-term average from 1951 to 1980. Source: NASA.*

An average temperature increase of between 0.1°C and 0.3°C per decade is estimated (figure 1.3) [7,8]. Global warming is also likely to exceed 1.5°C before 2030 if it continues to increase at the current rate[9]. In addition, heat transmitted to the atmosphere will lead to the intensification and spread of extreme weather events such as droughts, hurricanes, and floods.

Ocean acidification

About 50% of atmospheric CO_2 dissolves in the oceans where it forms carbonic acid according to this ration:

CO_2 (g) + $H_2O \leftrightarrow H_2CO_3$ (aq.)

In turn, carbonic acid dissolves, releasing H_3O^+:

H_2CO_3 (aq.) + $H_2O \leftrightarrow H_3O^+ + HCO_3^-$

This mechanism leads to a decrease in the pH of the oceans, in fact it is estimated that in the last two centuries the pH of seawater has dropped from 8.2 to 8.1. Acidification will affect most marine species, for example, coral reefs are expected to decrease by 70-90% for a warming of 1.5°C[10].

Melting of glaciers

Rising global temperatures also cause glaciers to melt, including Arctic glaciers where warming is two to three times higher [8]. In turn, this results in sea level rise. Projections suggest an average sea level rise in an indicative range of 0.26 to 0.77 meters by 2100 for a global warming of 1.5°C and small islands, low-lying coastal areas and river deltas will be submerged.

Loss of biodiversity

If global warming reaches 1.5°C about 4% of ecosystems will undergo serious transformations, leading to loss of biodiversity. It is predicted that 6% of insects, 8% of plants and 4% of vertebrates will be lost.

Diseases

There are between 3.3 and 3.6 billion people who reside in extremely sensitive areas to climate change[8]. An increase in heat-related mortality and tropical diseases, especially vector-borne diseases such as malaria, is expected, even in countries

where it has been eradicated.

Economy

Rising global temperatures will pose risks to economic growth. For example, it is estimated that at 1.5°C there will be a reduction in the catch of 1.5 million tons. There will also be a reduction in yields of corn, rice, wheat, and other grain crops especially in the Americas, Africa and Asia [5]. In addition, the economic damage (meaning material damage) caused by extreme weather events will increase exponentially.

Migrations

Global warming is a greater risk to less developed and developing countries as poverty and economic disadvantage will increase. As a result, millions of people are expected to migrate to more industrialized countries [5].

1.4 Policy measures to reduce global warming

To address the problem of global emissions, several international conferences have been convened over the years with the goal of creating agreements that would codify a coordinated and collective commitment to reduce emissions to threshold levels within a certain time frame (see figure 1.4).

One of the first environmental policy measures was the Kyoto Protocol, drafted in 1997 by more than 180 countries at the United Nations Conference of the Parties on Climate Change (UNFCCC). However, the protocol did not enter into force until 2005, when Russia joined, thus reaching the minimum quota of 55 states adhering to the protocol and responsible for 55 percent of pollution. In 2012, a renewal of the Kyoto Protocol until 2020 was arranged in Doha. The main goal of the Kyoto Protocol was to cut emissions of key anthropogenic GHG by at least 5.2% from 1990 levels.

The Paris Agreement, on the other hand, is an agreement among 184 states that make up the UNFCCC held in December 2015, and provides for the reduction of GHG emissions starting in the year 2020. The long-term goal of the Paris Agreement is to contain the global average temperature increase well below the threshold of 2 °C

above pre-industrial levels, and to limit this increase to 1.5 °C, as this would substantially reduce the risks and effects of climate change. The European Union formally ratified the Paris Agreement, thus enabling its entry into force on November 4, 2016. The UN has also established 17 Sustainable Development Goals, popularly known as the 2030 Agenda, as of 2015. The 17 points cover a wide variety of social and economic concerns. Combating climate change and responsible consum ption and production are two of them.

In November 2022, there was a new Conference of the Parties of the UNFCCC (COP27) that incorporates the 17th Conference of the Parties to the Kyoto Protocol (CMP17) and the 4th Conference of the Parties to the Paris Agreement (CMA4). The conference decided to establish a monetary fund, called 'Loss and Damage', for the poorest countries that have suffered the devastating effects of climate change. In addition, the final document approved at the COP stressed that to achieve the goal of limiting global warming to 1.5°C from pre-industrial levels, emissions must be reduced by 43% by 2030 compared to 2019. However, there is a lack of agreement that mandates the phase-out of fossil fuel use. In fact, the document only highlights the need for transition to a renewable-based system and the importance of reducing fossil fuel use through mitigation and adaptation policies. Furthermore, the latest IPCC report suggests that global warming can realistically be limited to only 2°C [9]. In December 2023 there was the last Conference of the Parties (COP28) in Dubai. The results of COP 28 are called "historic" or "disappointing" depending on point of view. Assessing its impact is by no means simple. Only time will provide these answers. However, the final agreement includes (i) a reference to moving beyond fossil fuels to achieve climate neutrality by 2050; (ii) a new target to triple renewable energy and double energy efficiency by 2030; (iii)The acceleration of

zero- and low-emission technologies, including nuclear power and carbon capture and storage.

Figure 1.4 *Timeline of most important climate conferences.*

In 2019, the European Union decided to adopt the so-called green deal, through which reducing emissions by at least 55% by 2030 becomes a legal obligation. The ultimate goal is to make the EU climate neutral by 2050 by funding research and new technologies (net-zero emissions - NZE) [11].

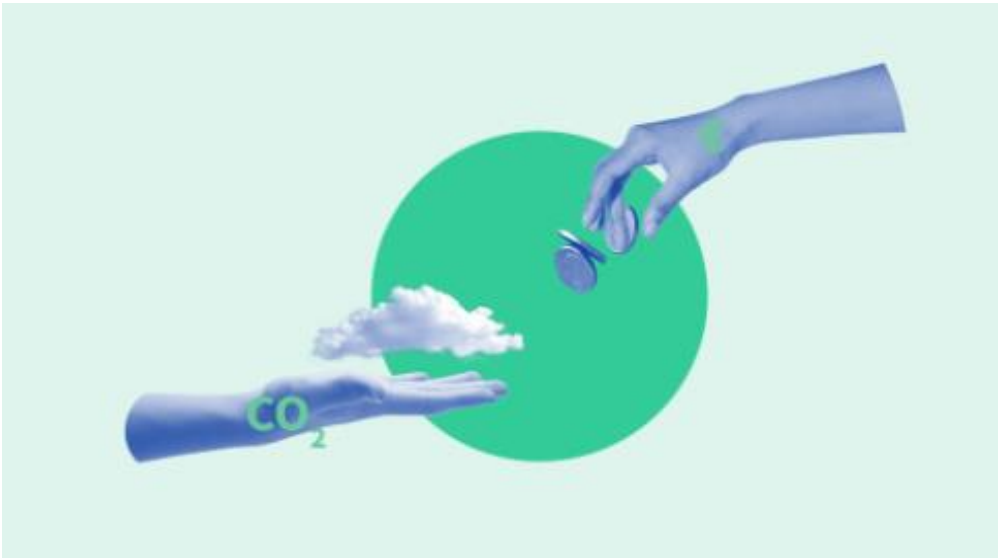

Figure 1.5 *EU ETS Iconography. Source: Council of the European Union*

Among the instruments adopted by the EU is The EU Emissions Trading Scheme (EU ETS), in place since 2005. Each industrial/aircraft operator must offset its

emissions on an annual basis with a corresponding number of quotes (1 quote =1 ton of CO_2) which are generally sold in a dedicated market. The number of quotes, however, decreases each year, precisely because of the reduction in emissions. This has already resulted in the reduction of about 41% of emissions compared to 2005.

1.5 Mitigation and adaptation: two strategies for coping with global warming

Global warming and related climate changes are already underway, and the effects will be increasingly severe and catastrophic if concrete actions are not implemented soon. There are two possible strategies to address these changes and limit global warming to within 1.5°C: mitigation and adaptation.

The IPCC defines climate change adaptation as "the adaptation of nature or human systems in response to actual or projected climatic stimuli or their effects, with moderate damage or exploitation of beneficial opportunities" [7]. Adaptation is thus a strategy that aims to adapt humanity to climate change through changing government policies and developing new technologies and ways to reduce the effects of global warming [12,13].

Mitigation is defined by the IPCC as "an anthropogenic intervention to reduce the source or enhance the storage of greenhouse gases." Unlike adaptation, which focuses on the effects of global warming, mitigation addresses the cause and aims to reduce anthropogenic GHG emissions. Mitigation can be accomplished in two ways [13–15]:

The first method is to develop innovative technologies aimed at both increasing efficiency in energy use, thereby reducing emissions, and absorbing those emissions.

the second way is decarbonization, that is, reducing economic dependence on coal or fossil fuels more generally.

Considering the potential future strategies from a purely economic point of view, assuming only one of them entails extremely prohibitive costs as shown in figure 1.6.

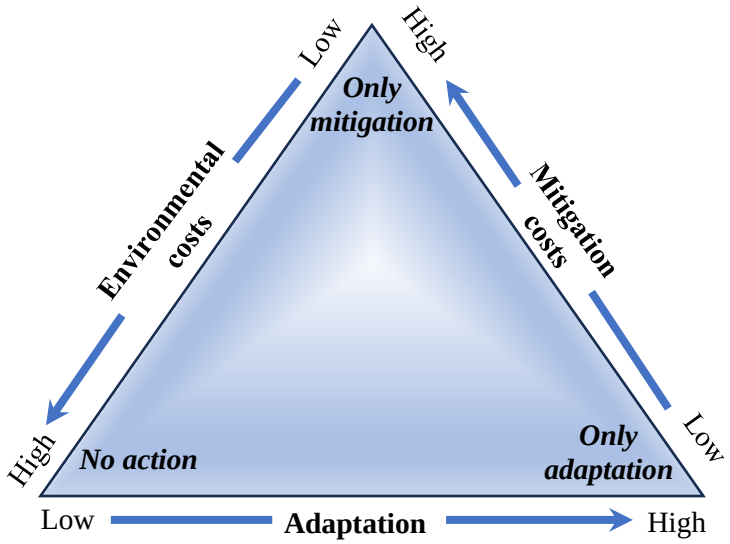

Figure 1.6 *Interrelationship diagram between the cost of adaptation, mitigation, and non-intervention. Adaptation from reference [15]*

Failure to take measures leads to technological unpreparedness and thus, eventually to increased costs associated with the consequences of climate change. At the same time, however, adopting a mitigation-only policy is not economically possible because one would have to completely eliminate all anthropogenic GHG. Adaptation is also an extremely expensive strategy because it involves the continuous development of technologies to cope with the growing consequences of global warming[15]. Therefore, the most economically feasible option is the combination of adaptation and mitigation: reducing GHG emissions within a certain limit will decrease the costs of adaptation because the future effects of climate change will be less intense [12–16].

1.6 The CO_2 issue and the CCS and CCUS technologies

Currently, mitigation and adaptation are focused on reducing CO_2 emissions. In fact, the anthropogenic intensification of the greenhouse effect is mainly due to the increase of CO_2 emissions into the atmosphere. Its predominant role over other GHG is justified by the greater amount poured into the atmosphere by humans. As the Keeling curve shows (figure 1.7) there has been a steady increase of CO_2 in the atmosphere during last decades.

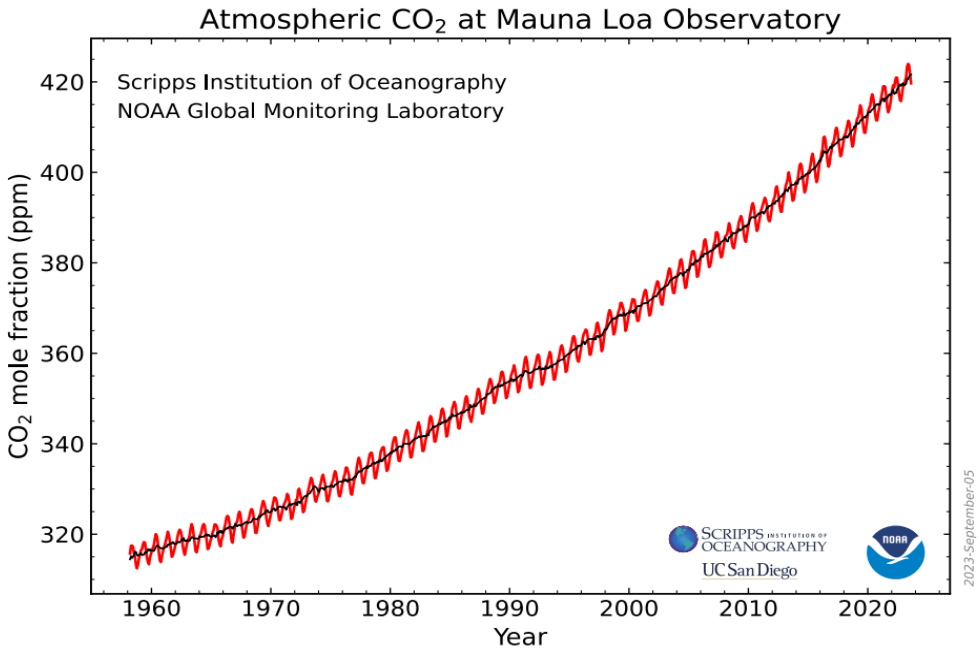

Figure 1.7 *Keeling curve, the red curve shows average monthly CO_2 concentrations, and the dark curve is a smoothed trend. Data from Dr. Pieter Tans, NOAA / ESRL and Dr. Ralph Keeling, Scripps Institution of Oceanography.*

The global annual average concentration of CO_2 has increased by more than 45% since the beginning of the Industrial Revolution, from 280 ppm in the first half of the 18th century to 422 ppm in January 2024, an average increase of about 2 ppm each year, and it is accelerating [17]. The increase in the concentration of CO_2 in the atmosphere is due firstly to the use of fossil fuels, especially coal, to obtain energy and secondly to deforestation, which produces 30% of the GHG emitted annually

[13,17,18]. In fact, deforestation on the one hand prevents trees from storing CO_2 as they grow, and on the other hand releases huge amounts of CO_2 into the atmosphere due to fires[19].

However, there are specific sectors in which innovative technologies and energy efficiency allow for a drastic reduction in emissions. Power and energy production is among the most promising sectors in which to apply mitigation policies (see figure 1.8). Firstly, because this sector alone is responsible for 37% of global carbon dioxide emissions, increasing by 0.9 percent or 321 Mt in 2022, setting a new record [20]. Secondly, technologies already exist to implement them, reducing waste and emissions [7,21].

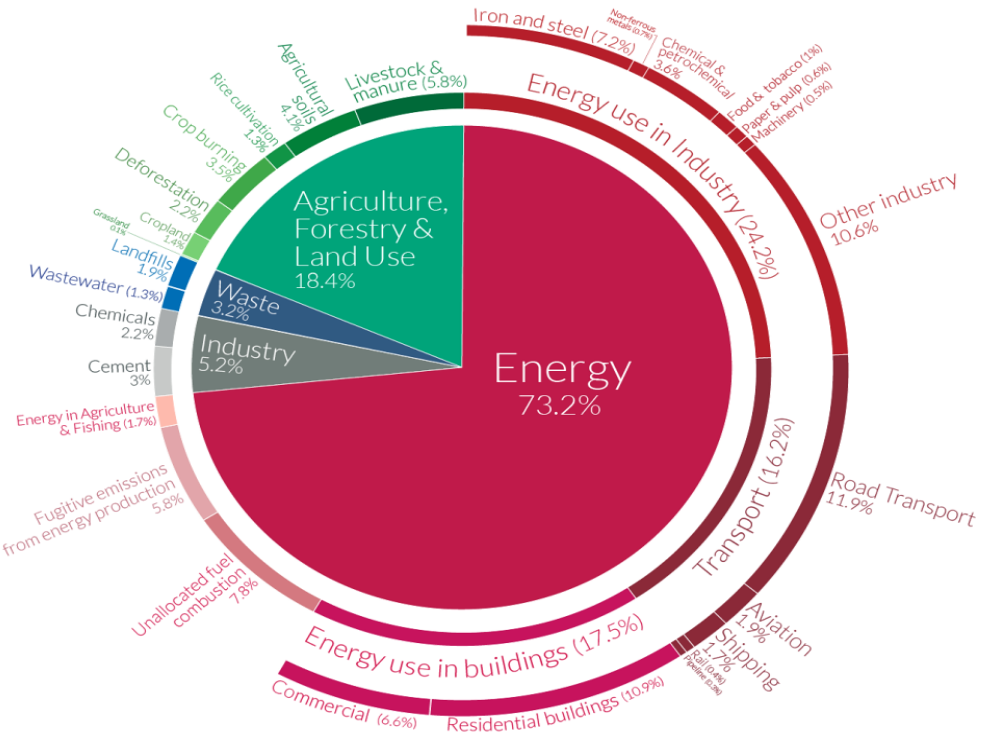

Figure 1.8 *Global greenhouse gas emissions by sector. Source: Climate Watch, the World resources institute (2020)*

An indispensable role toward decarbonization is played by renewables, which could help halve CO_2 emissions by 2050 if their use is increased to produce about 40% of

global electricity [22]. For example, it was estimated that by 2022 renewable energy technologies, especially solar and wind power, helped to avoid the emission of about 550 Mt CO_2 in power generation [20]. However, the biggest problem with this technology is that renewable energy sources (such as the sun or wind) produce energy intermittently, with energy peaks that cannot be stored in batteries. A viable alternative could be nuclear power because of the possibility of being able to produce it continuously and with low GHG emissions. However, the nuclear industry since 1993 has experienced a continuous decline due to low consumer confidence, fueled by major nuclear accidents such as Chernobyl and Fukushima. A further decrease in carbon dioxide emissions could come from the industrial sector. Energy intensity in industry could be reduced by about 45% through deployment of the best available technologies and continued technological innovation [13].

To ensure an efficient energy transition to a low-emission economy, several strategies can be adopted in addition to decarbonization. Optimization and intensification of existing processes aim to reduce energy demand by taking advantage of technologies that allow reuse of emissions to obtain useful products. In fact, the interest of the scientific community in carbon capture and storage (CCS) and carbon capture, utilization and storage (CCUS) technologies has increased in recent years [23–28].

The CCS process involves three main stages: (i) capture and CO_2 purification, (ii) compressing it and transportation and (iii) finally storage in underground.

Transport of CO_2 can be carried out either through a pipeline (liquid phase) or by trucks, rail, and ships (dense phase). Importantly, when continuous flow from the CO_2 capture facility is necessary, transporting CO_2 through pipelines supplies a number of advantages over alternative methods. In addition, compared to alternative CO_2 transport methods, pipelines enable the more economical transportation of a higher volume of CO_2 over long distances, which might have been taken from several point sources [29]. For the effective implementation of CCS systems, a few issues

with CO_2 transit via pipelines must be handled. For instance, compression and transport are especially susceptible to the presence of steep slopes and contaminants when CO_2 is carried in a pipeline during the supercritical phase [29,30]. This influences the fluid dynamics and thermodynamic behavior of the CO_2 stream as well as the pipeline system's re-pressurization distance, leading to distinct flow regimes that change the operating conditions for the pipeline.

Storage involves the injection of CO_2 at depths of 1 km or more within preexisting geological formations characterized by an impermeable layer, called caprock [31]. Suitable candidate areas include deep coal seams, depleted oil fields, and deep saline aquifers, the latter having greater storage potential than the others [32]. Storage in geological formations allows for a sufficiently stable long-term carbon dioxide sink that is not linked to carbon fixation in the form of plants through reforestation. Under these conditions, CO_2 has a density close to that of a liquid; therefore, storage is more efficient than at the surface, and it is also possible as well for carbon dioxide to undergo mineralization, thus permanently fixing the gas in the form of mineral carbonates, at present, however, the amounts of gas sequestered with this technology are in the range of $MtCO_2/yr$ compared to the $GtCO_2/yr$ needed for important mitigation effects[32,33].

Carbon dioxide capture is the most complicated and consequently expensive step, which accounts for more than 75% of the cost of the entire process [33]. CO_2 can be captured in several ways and from various sources. This depends also on concentration, partial pressure and operating conditions [21] which can vary considerably depending on whether it is industrial production or power generation facilities as shown in table 1.1 [18].

Table 1.1 *CO_2 concentration and partial pressure in the flue gas streams for different power generation plant or industry. From ref.* [18,33]

Plant or Industry Type	Average CO_2 conc. (v%)	P_{CO2} (MPa)
Coal-fired power generation	12 – 14	0.012 – 0.014
Natural gas turbine power generation	3 – 4	0.003 – 0.004
Oil-fired power generation	11 – 13	0.011 – 0.013
Integrated gasification combined cycle	12 – 14	0.012 – 0.014
Cement production	14 – 33	0.014 – 0.033
Steel production (*by blast furnace*)	20	0.04 – 0.06
Ammonia production	18	0.5
Ethylene oxide production	8	0.2
H_2 production (by *steam reforming*)	15 – 20	0.3 – 0.5
Methanol production	10	0.27

There are three main ways for CO_2 capture, summarized in figure 1.9 [28,34]:

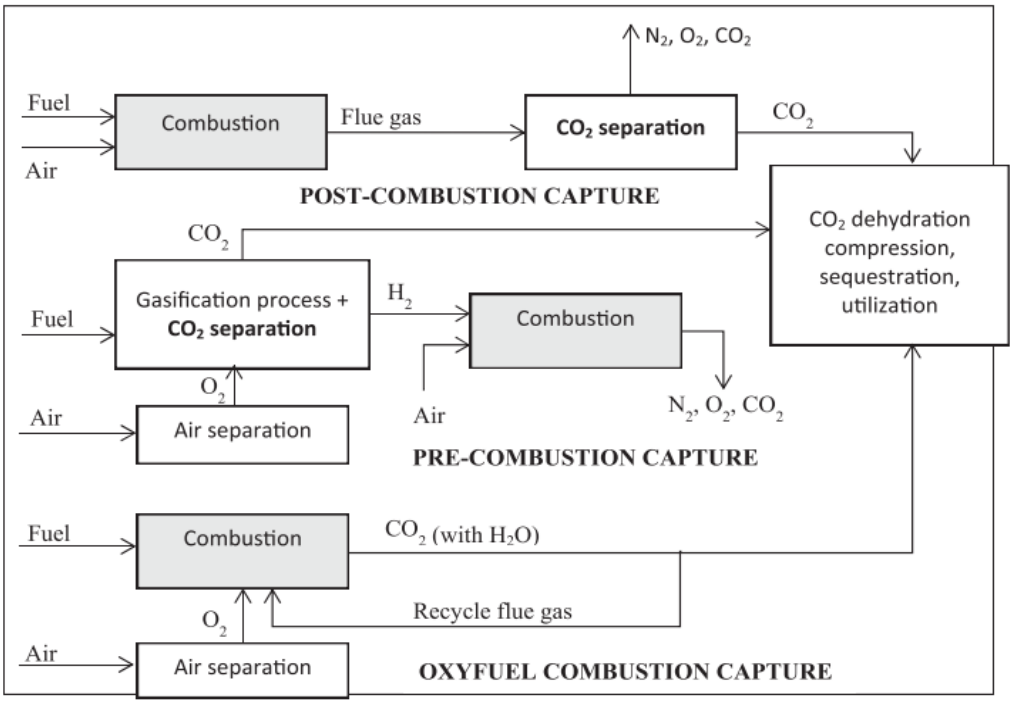

Figure 1.9 *CO_2 capturing processes. From ref. [28]*

In the energy sector the post-combustion technique is generally adopted to remove CO_2 from waste gas streams after the conversion of the carbon source. It is adopted in this sector for the lower CO_2 concentration and because many of the technologies in this category can be added to existing power plants without causing significant interruptions or modifications to the process flow, it is particularly effective at reducing carbon emissions from point sources. Downstream of the combustion process, a wide range of CO_2 collection systems are used. These typically include adsorption, absorption, and membrane separation and, as well as electrochemical separation using fuel cells. In addition, they include cryogenic separation and mineralization. Anyway, regardless of the type, CO_2 separation and capture significantly increase the energy and financial costs of the process. [33,35]. Only the most commonly used processes are briefly described below.

Absorption involves first the chemical and selective absorption of CO_2 by interfacial equilibrium with a proper solvent in an absorption tower, then the gas in desorbed in a regeneration tower, recovering the solvent for the next stage of CO_2 capture. Although aqueous solutions of alkali metal hydroxides can be used, they are not suitable for large CO_2 sources.

The alternative still most widely used consists of amines solution, such as primary amines (monoethanolamine), secondary amines (diethanolamine) and tertiary amines (triethanolamine or methyldiethanolamine), which flows countercurrent to the gas. Afterwards, the rich-CO_2 solution is pumped to the head of a stripping column where it flows countercurrent to a heated vapor stream. The heat allows desorption of the gas which is condensed, compressed, and sent toward storage sites.[24,25,33]

Even if the CO_2 recovery efficiencies are more than 80%, fundamental problems with this method are the cost of the solvents and the energy required for the entire process, which is currently about 2.6 GJ per ton of CO_2, corrosion of equipment and materials and not last the carbon footprint as amines derives from ammonia, whose synthesis involves important CO_2 emissions [23,33].

Membrane separation is a fairly mature technology, but one that is only recently entering the world of CCS technologies. With its comparatively low environmental effect and ease of scaling up, membrane-based separation is preferable to alternative techniques. In addition, it may be used continuously without the requirement for a solvent or sorbent, and industry prefers its regeneration over traditional processes. This technology can separate the gas (permeate) from all other contaminants (retentate) by the membrane module. In this process, pre-treated exhaust gas containing CO_2 is sent to the high-pressure side of the membrane and it is recovered from the low-pressure side [36].

Several materials can be used for membranes. Organic membranes, usually polymers (such as polyacetylene, polycarbonates, polyaniline, polyvinylamine etc.), cannot be used at elevated temperatures and in presence of water but they are no expensive and easy to control. Inorganic membranes include ceramics, metals, or zeolite, so materials with high chemical and thermal stability but the costs are greater than organic membranes. A viable alternative, combining the advantages of both types at moderate cost, are mixed membranes consisting of a polymer matrix filled with inorganic filler [37].

Adsorption involves a physical interaction between the gas and the adsorbent material. Liquid solvents are not used for the low liquid/gas interfacial contact area while solid sorbents are preferred because it is possible to fabricate solids with extremely high surface area, maximizing the contact area with the gas. In addiction the mass transport in gas phase is several orders of magnitude higher ($\sim 10^{-5}$ m^2/s) than liquid phase ($\sim 10^{-9}$ m^2/s), facilitating the separation [33].

However, a major problem is the adsorption of water and other flue gas impurities in the micropores of solid sorbents. In any case, the intensity of the van der Walls interaction between the polar surface sites and the huge quadrupole moment of the dipolar CO_2 molecule controls the selective adsorption of this gas onto the sorbent material. Therefore, careful selection of the chemical nature of the sorbent is necessary to optimize the selective separation of CO_2. Again, the process is an

adsorption-regeneration cycle in which two towers working in tandem are involved. Usually, the gas is desorbed by varying pressure, as in pressure swing adsorption (PSA) and vacuum swing adsorption (VSA), or by temperature differences, as in temperature swing adsorption (TSA).

In industry, the capture of CO_2 occurs through pre-combustion, which is a method of separating the carbon dioxide obtained as a co-product of a given process, such as in coal gasification and syngas production, using pure or highly enriched (>90%) oxygen for the fuel combustion or gasification process.

The overall process can be schematized into several stages. A priori steps consists in oxygen separation from air, as it is a cheap and abundant source for oxygen [33]. The collected oxygen is used for partial oxidation of the fuel, obtaining syngas that is further converted by water-shift reaction, into carbon dioxide and hydrogen, via water vapor, and thus increase the amount of hydrogen that can be obtained and used for power generation [22,38–40].

This process produces a gaseous mixture from which CO_2 is separated by adsorption, absorption, membranes or cryogenic processes. Even though Pre-combustion is extremely successful in reducing emissions, but the overall cost and performance of the plant are often lower [41,42].

Oxyfuel process is similar to post-combustion but pure oxygen at high temperature is used to increase the total amount of attenable CO_2 [43]. In addiction almost pure and ready for storage CO_2 is obtained avoiding another extensive post separation step. In fact, the product flue released by oxy-combustion usually contains about 70% CO_2 plus water vapor, while nitrogen, one of the most difficult impurities in CO_2 stream, is not included in the process, allowing an easier CO_2 capture [33]. Anyway, several issues connected to excessive cost, limits the interest and investment on this technology. In fact, expensive materials tolerant at elevated temperature are needed. In addition, oxy-combustion usually produces more pollutants in the flue gas than do air-based combustion processes, including inert gasses, HCl, SO_2, ash, and Hg, and their removal is difficult [44].

Although CCS has a larger CO_2 mitigation potential [45] the high costs of various processes and the uncertainties associated with long-term geologic storage have led the scientific community's interest in CCUS technologies. Indeed, it is economically more feasible as it allows sequestered CO_2 to be used for the production of high value-added products. For the last, these technologies appear to have greater potential than CCS technologies to reduce carbon dioxide emissions. In fact, the IPCC has stated that without the development of such technologies, the cost of mitigation could increase by 138% [46]. Moreover, CCUS allows a cyclic process of CO_2 use and if renewable technologies are employed, the quantity of renewable energy injected into energy systems to replace fossil fuels rises [47]. There are numerous ways to reuse CO_2, but the following applications are the most promising in the industrial and energy sectors to implement the mitigation strategy.

➢ *Enhanced oil recovery (EOR)*: also known as tertiary recovery, is a method of increasing the amount of oil that can be extracted from a reservoir by 30-60%. In fact, by injecting various agents such as CO_2, natural gas or polymers directly into the reservoirs, it is possible to extract the oil trapped in the rocks. Most commonly, supercritical CO_2 is used because it is naturally available, inexpensive, and by reducing the viscosity of the oil, it facilitates its transport to the well. In addition, the CO_2 used can be stored directly in the same reservoir after extraction is complete. Alternatively, it is also possible to inject a mixture of water and CO_2 (Water Alternating Gas, WAG) for better recovery because water reduces the mobility of carbon dioxide, making the gas more effective for the purpose [35,48].

➢ *Enhanced coal-bed methane (ECBM)*: is a method to increase the amount of methane that can be extracted from coal deposits. Again, CO_2 is injected, which, when absorbed by the coal, pushes methane trapped in the coal to the surface for capture and consumption as fuel. Anyway, this method is not commercial available because not economically feasible [43].

➢ *Carbonation:* is a process by which carbon dioxide is converted into inorganic carbonates that can be used in the construction industry. During this process, alkali metal oxides, usually MgO and CaO, which occur naturally in rocks, react with CO_2 to obtain magnesium carbonate and calcium carbonate, respectively, in the form of limestone.

$$CaO + CO_2 \leftrightarrow CaCO3 \qquad \Delta H = -179 \text{ kJ/mol}$$

$$MgO + CO_2 \leftrightarrow MgCO3 \qquad \Delta H = -118 \text{ kJ/mol}$$

Although both reactions are exothermic and thermally favored, they have slow kinetics. Therefore, research is focused on finding ways that are able to speed up the process [43,48,49]. One advantage of carbonation is that the CO_2 is not stored in geological cavities but is stored in carbonates that are stable for an extended period and thus without concern of possible CO_2 leakage that could pose health, safety, and environmental risks. From an economic point of view, carbonates can used in the construction industry but revenues are highly dependent on demand and the cost of carbonates [50].

➢ *Biofuel production:* algae are photo-cellular organisms that require light, inorganic salts, and CO_2 as a source of carbon that they can absorb from the atmosphere, soluble carbonates, and industrial waste gases. A range of hydrocarbons can be extracted from algae, from which biofuel can be obtained at a rate that varies with the type of algae and growth rate. For this reason, algae cultivation is a renewable method of producing energy and is a viable alternative to CO_2 capture and storage alone [43,48,51]. In addition, unlike biofuel derived from agriculture, that derived from algae has no impacts on the environment or food supply [52].

➢ *Power to fuels:* refers to a series of processes to convert CO_2 into fuel using renewable energy. Excess electricity obtained from renewable sources (such as wind power generated at night when demand is lower) can be used to do electrolysis of water and obtain H_2 ($2H_2O \leftrightarrow 2H_2 + O_2$) which is considered a green energy carrier to store electricity (power to hydrogen). Hydrogen can be used to reduce CO_2 into

methane by the Sabatier reaction and thus be fed into pipelines. This technology, renamed power to gas, has a significant advantage compared to other technologies in terms of storage capacity and discharge time [23,25,53]. However, these technologies have a number of issues related to lack of infrastructure and process costs that currently make the products obtained too expensive compared to those obtained from fossil fuels [54].

➢ *Production of chemicals and fuels:* as a carbon source, carbon dioxide can be converted into chemicals of organic nature with technologies that can improve or replace current synthesis methods in the chemical, pharmaceutical and plastic industries.[43,48,55] It has been estimated that conversion into has a large CO_2 sequestration potential of about 500 Mt/year [56].

There are several patents such as US2006023509136 in which CO_2 is converted to formic acid by electrochemical reduction. The formic acid in turn can serve as a source of carbon or hydrogen to obtain methanol, dimethyl ether, and other compounds. In patent US2015034503437 a method is described for converting CO_2 into hydrocarbons, such as methanol, formic acid, formaldehyde, ethanol, or butanol, by electrochemical or photoelectrochemical route. In addition, CO_2 can be synthesized into various products by hydrogenation with various catalysts. For example, solid ZnO-ZrO catalysts allow both the production of methanol with a selectivity of about 90% [57] and short olefins such as ethylene and propylene [58] However, all these processes are highly endothermic, and therefore expensive, so they cannot yet be used on a large scale.

The conversion of carbon dioxide into fuels and chemicals has a wide range of intra-sectoral benefits in the energy sector, including carbon removal from the energy and industrial sectors, production of fuels and chemicals through sustainable processes, and reduction of fossil emissions and fuel consumption in the production of fuels and chemicals.

1.7 Not only CCS and CCUS: the role of e-chemistry

The goals proposed by the European green deal by 2030 and the net-zero emissions (NZE) by 2050 can not be achieved by CCS and CCUS alone but it is essential to develop new synthesis strategies to reduce *a priori* the emission of CO_2. In fact, only around 50% of the target reduction needed to reach NZE by 2050 will be realize if actual trend in the reduction is kept until that year[11]. In chemical industry sector, the major emissions are connected to energy use primary and then for chemical processes themselves. Moreover, only 30–40% of the inlet carbon (as fossil fuels) is preserved in the end chemicals, with the remaining carbon being utilized for transformation and then released as CO_2.

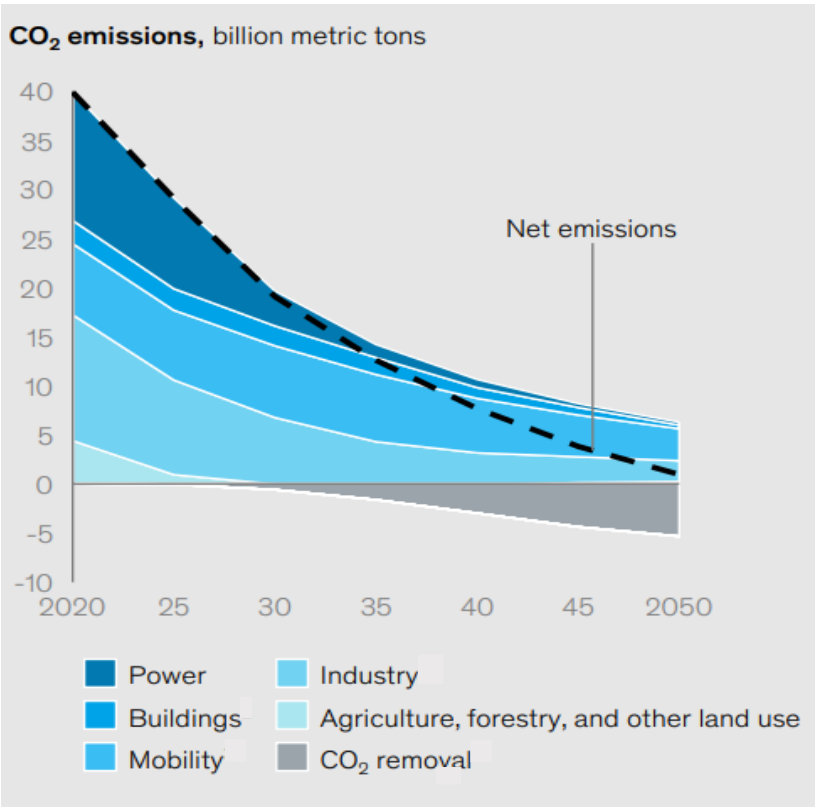

Figure 1.10 *Net Zero 2050 scenario pathway – CO_2 emisions. From ref. [11]*

Therefore for reaching a neutral carbon footprint, chemical production must undergo a profound shift toward a fossil-free model, necessitating the simultaneous and synergistic convergence of all required actions to achieve so-called e-chemistry [59].

The realization of e-chemistry relies on crucial points for the future:

- A circular CO_2 economy in chemical production, that aims to re-use waste and end-life chemicals in order to minimize, or ideally avoid, emissions and the supply of virgin raw materials.
- Direct use of renewables as energy input by electrification of chemical industries.
- Developing of synthetic route that use renewable energy as direct energy input (power-to-lumps and e-fuels)

1.7.1 CO_2 circular economy

A circular economy of carbon can be realized by the connection and cooperation of different technologies. CCS and CCUS are among them, but they will not make the industry truly circular because chemical industry always require fresh carbon input. One example is plastic recycling. Even if reuse of plastic involves several step in order to minimize waste (reuse, then mechanical recycling, then depolymerization and conversion in hydrocarbon feedstock and, as a last resort, energy recovery) only about 50% of the overall plastic is recycled[60]. Consequently, fresh carbon input is needed to compensate for losses and, together with demand rising, it is expected to exceed 400 Mt by 2050. To reduce net CO_2 emissions in the short to medium term, the fresh carbon input may also include fossil carbon and CCS. Conversely in the long-term scenario CCUS and the so-called power-to-chemical lumps will be central to develop a cyclic CO_2 economy.

1.7.2 Electrification for heating

In order to meet the requirements for NZE, it is also necessary not only to replace fossil fuel as the carbon source for the chemical industry, but also to electrify unit operations (especially chemical reactors) in industrial plants with the purpose of increase the use of renewables as an energy source for the operation of these units [59,61]. The energy demand in the chemical industry nowadays is mostly for heating and cooling, and in minor part for mass transfer and mixing. Electrification of

chemical industry aim to substitute completely the use of fossil fuel with electricity in this sector, reaching a neutral carbon footprint if electricity derives only from renewable energy [62]. To achieve these purposes, the electrification can be made on different stages, with a gradually but constant change in the production systems.

Surely, in a short-term scenario the reduction of the energy losses, which count for almost one-third of the energy input, are essential to increase the efficiency of the processes. This is possible by advanced control or better insulation, which is already a daily business in chemical industry. In the near future new technologies for heating, called power-to-heat, will be essential to break free from fossil fuels [61]. The typologies of electric heating technologies for chemical reactors can be divided into three types, based on the physical phenomenon beyond heating:

1. Resistive heating. In this case an electric resistor is used to generate heat. The main advantage of this heating method is the minimization of the heat losses if it is compared to traditional fired reactors. Resistors can be placed outside the reactor, using a heat-transferring fluid if the temperature is lower than 550°C as in the case of electric boilers, therefore a change of the rector design or catalysts is not required, making this electrification method more adaptable to current production processes. Otherwise, the resistor can be integrated inside the reactor by exploiting the joule heating. In the latter case, the heat could derive either from (i) directly incorporation of an electrical resistances into the body of the catalyst's support, or (ii) using a resistive conductor (a metallic support, for instance) where the catalyst is supported [63]. The heating is more efficient, and a better control of the temperature can be done than heat-transferring fluid. In addition, as the reactant in contact with the catalyst may have a lower temperature than that of the catalyst layer, new strategies to improve stability or selectivity could be explorer.
Nevertheless, this electrification way requires a redesign of the catalyst to minimize the temperature fluctuations that can afflict performances and stability. This was

made by Wismann and colleagues, which presented a novel reactor idea for electrifying the steam methane reforming (SMR) reactor by joule heating. They used a tube made of Fe-Cr-Al alloy with a thin ZrO_2 washcoat layer and a Ni-film as catalyst. The current was applied into reactor by copper connector and transformed into heating. The conversion of methane at output temperatures of up to 900°C was found to be around 87%, and a CO_2 emission reduction of 20–50%, compared to traditional industrial reformer was attained [64,65]. Instead, Zhou et al. [66] developed a plate-type alumina supports impregnated with nickel for SMR. A high methane conversion of 97% at 700°C was achieved, but the used plate support showed a very low hydrothermal stability after 50 h. In fact, its surface area was reduced to only 36% of the starting value, hindering industrialization. Zhen et al. [67] studied same reaction adopting a Rh/Al_2O_3 catalyst on a commercial SiC foam that deserves as support and resistive heating element. Full methane conversion was achieved at 650°C with a specific energy demand as low as 1.24 kWh/Nm^3_{H2} and a catalyst density of 86.3 g/L. Sekine et al. [68] used a $Ce_xZr_{1-x}O_2$ catalysts at low temperature (190°C) and a stainless electrode rode as heating element. Even if the methane conversion was low (12%) the energy consumption was around 4 kWh Nm^{-3}_{H2}.

2. Magnetic or inductive heating. Heating is created by an oscillating magnetic field that generates eddy currents and heat by joule heating in a conductor or magnetic losses hysteresis in a ferromagnetic material [69]. Compared to resistive hating, in this case there is no direct contact between the electric heat source and the catalyst. It is a simple technology to scale up and the heat is transferred very quickly [70], allowing a fast temperature fluctuation. However, as conducting or ferromagnetic materials are involved, a thorough redesign of the catalysts is needed, such as using nanoparticles with magnetic cores on which the non-magnetic catalyst is deposited [61]. This was made by Mortensen at al. [71] employing a magnesium aluminate ($MgAl_2O_4$) spinel coated with an inductively heated Ni-Co NP alloy for methane

steam reforming. Complete conversions with little carbon production were measured at low flow rates because the inclusion of nickel further catalyzes this process. Later, it was discovered that by adding tiny quantities of copper to the alloy, it was possible to obtain practically full conversion (95%) at lower electromagnetic fields and greater flow rates (Q = 152 NL/h), as well as reduced carbon production and no loss of catalytic activity [72].

An advantage of inductive heating is the possibility to fast control the temperature. This could be an advantage because it can induce the creation of metastable state for the catalyst, able to enhance performances or, by fasting adsorption-desorption cycles, it is possible to remove poisoning species [63]. An interesting application of this propriety was reported by Giambastiani's team [73] about CO_2 methanation (Sabatier reaction), developing nickel nanoparticles deposited on a oxidized carbon-felt disks. In fact, as the reaction is exothermic a big drawback is the over-heating of the catalyst. By inductive heating they were able to real-time control of the target temperature at the catalyst active sites, balancing the undesired and sudden temperature changes at the catalyst bed. A CO_2 conversion up to 74% and CH_4 selectivity close to 97% was measured at 320 °C with pure gas stream.

3. Microwave (MW)/RF (radio frequency) heating. A microwave or radiofrequency create an alternating electric field that induces moving of dipolar moment of receiving molecules or ions in a liquid and current is generated. Therefore, it is simple to control because of immediate response to applied electric field but it is a heating method mainly for liquid homogeneous catalyzed reactions or no-catalytic reaction. Moreover, only small dipole molecules materials are suitable for this method limiting applications but water is included as receiving material [70]. Nevertheless, some possible advantages should be explorer [63,74]. They include:

- selective heating of catalyst zones: the surface rather than the bulk of the catalyst or a particular area of the catalyst having a different composition from other parts even at a nanoscale level can be heated differently.

- creation of hotspot zones by non-uniform distribution of electromagnetic field on the catalyst surface.
- selective heating of some of the adsorbed species: the molecules adsorbed usually have a dipole moment and thus they can be selectively heated under microwave irradiation, with possible poisoning reduction.

A summary of recent developed catalysts for MW assisted dry reforming of methane is reported in table 1.2.

Table 1.2 *Catalysts for MW assisted dry reforming of methane. Revisited from ref.* [75]

Catalysis	Operating condition	χ_{CH4}; χ_{CO2}	Reference
Ni/SiC	MW Power= 45–60 W WHSV= 11L h^{-1} g^{-1} Temperature= 800°C	80%; 90%	[76]
Ni/Al_2O_3-SiC	MW Power= 45–60 W WHSV= 11L h^{-1} g^{-1} Temperature= 800°C	90%; 90%	[76]
Fe/HZSM-5	MW Power= 700 W WHSV= 24L h^{-1} g^{-1}	63%; 91%	[77]
$LaxSr_2{-}xCoO_4$-Mn	MW Power= 140 W WHSV= 10L h^{-1} g^{-1}	80%; 80%	[78]

Co-Mo/TiO_2	MW Power= 100 W WHSV= 10L h^{-1} g^{-1}	81%; 86%	[79]
Cu-Mo/TiO_2	MW Power= 140 W WHSV= 10L h^{-1} g^{-1}	76%; 62%	[79]

1.7.3 Technology for future full electrification: Power to chemical lumps

In a long-term scenario, electricity can be ideally used not only for heating or cooling the reactors, but it should actively take part in the reaction. In fact, reaching this goal means integrating renewable energies in the chemical industry production chain. Many efforts are currently focused on the so called power-to-X technologies (PtX), where X indicate gas, liquid, heat, or chemicals, depending on what is being produced [34,47,80,81]. Anyway, PtX could have a potential only in the mid-scenario. In fact, these are multistep processes, including (i) CO_2 capture and purification; (ii)green H_2 production by electrolysis and (iii) thermal production of chemical by thermo-catalytic steps. Therefore, the use renewable energy source is included only for H_2 production. In addition, in a long-term scenario, the cost and energy required by PtX technologies do not make them suitable with NZE targets [82].

Therefore, a 2nd generation technologies is highly necessary to include renewables in all the steps and to achieve a complete sustainable chemical industry. This is the aim of power-to-chemical lumps technologies [61,63] where electricity is directly integrated in the reactions in the form of either activated species (plasma-catalyzed processes) or of charged species generated on the surface of the catalyst (electrocatalysis) or as light absorption in a semiconductor (photocatalysis). These e-technologies have also the greatest potential for process intensification through the elimination of intermediate stages (purifications, storage, transportation etc.) letting

a possible reduction of fixed and operating costs. Moreover, the introduction of new production modalities and reactors design will make easier and greater use of local resources by distributed production.

Electrochemistry

The most often used and advanced electrified chemical process is electrochemistry which is why in a few decades (2040) it may be usable instead of traditional processes [63]. Inorganic compounds, metal refining, and electrolysis are the principal applications for the few large-scale manufacturing facilities that exist on a global scale. For example, one of the most important industries is the combined chlorine and caustic soda (NaOH) production (chlor-alkali) and aluminum electrowinning.

Anyhow, electrochemical technology offers an innovative solution to reduce GHG emissions while still being competitive and attractive through high potential cost reduction and increased efficiency. In fact, among the major advantage of electrochemistry, creating redox agent in-situ (H^+/e^-, *OOH, *OH, *O, H_2O_2) is one of the most important, ending the need to separate and store them. One example is the ammonia production, one of the largest chemicals that each year produces more that 1% of total CO_2 emissions over word. Electrification of the reactor is useful to reduce the carbon footprint, but emission is still notably because the main source of emissions is the methane involved for thermal production of H_2 need in N_2 conversion to ammonia by Haber-Bosh process. The electrocatalytic reaction is able to produce the H_2 equivalent in the form of H^+/e^- reactive species at room temperature, avoiding also expensive and pollutant processes of the conventional route (especially H_2 production and compression over 100 bar and temperature over 400 °C for the ammonia synthesis conditions), reducing the emission of the overall process over 70% [83].

Concerning electro-organic syntheses, few of them have reached scaled production even though have been explored for a long time. This is not just because of the price

of electricity, but more frequently because of technical difficulties [70,84]. Anyway, organic electrochemical reaction, especially for CO_2 reduction, are extremely attractive because can provide the non-avoidable fresh carbon input inside circular economy processes [60,84], as discussed above. From this point of view, the direct production of C2+ chemicals by electrocatalytic coupling of CO_2 has attracted a lot of interests but it is challenging because of the difficulty in C−C coupling[85,86]. Remarkable examples can be found in literature. For instance, Marepally et al. [87] enhanced the selectivity to C>1 products (Methanol, ethanol, acetone and isopropanol) incorporating commercial imidazolate-based metal–organic framework (SIM-1) in a Zn-GDL gas-phase electrode. Arrigo et al. studied a novel mechanism of formation for methanol, acetaldehyde, and C3 (acetone and isopropanol) on the Fe-phase [88]. Nanostructured copper is the most studied electrocatalyst for CO_2 to ethylene, but together with other metals can also catalyze selectively the formation of C2 products under proper reaction conditions. Some illustrative examples are reported in table 1.3.

However, electrochemistry must be competitive respect the traditional synthesis route for an industrial commercialization. In fact, the electrocatalytic process cost is highly influenced by the electricity cost. It was estimated that to become economically viable, even if the procedure and cost of CO_2 are both zero, the price of renewable electrical energy must drop by a factor of at least 5 and efficiency in manufacturing the protons required for the CO_2 reduction must rise for electrocatalytic reduction [89].

Table 1.3 *Examples of Cu catalyst doped with different element and their performance* [85]

Cu structure	Dopant element	Potential (V vs *RHE*)	Efficiency to ethylene (%)	Reference
Nanoporous	Al	-1.5	80	[90]

Powder agglomeration	Ag	-0.7	48	[91]
CuO nanosheets	Sn	-1.1	48	[92]
Powder	SiO2	-4.1	65	[93]

The production of raw aromatics (benzene, toluene, xylenes etc.) is essential for a complete transformation to a fossil fuel-free chemical industry because of the wide variety of chemicals that can be produced, especially polymers and plastic. For example, styrene derives from benzene, and it is the major compound for the polystyrene production, instead cumene and phenol are involved in healthcare products and in the synthesis of epoxy-resins and polycarbonates. Cyclo-hexane is an intermediate in nylon production, p-Xylene is used to create polyesters and polyethene terephthalate (PET) while o-Xylene is utilized for flexible PVC (polyvinyl chloride) [60,61].

The primary low-carbon methods for producing monocyclic aromatic hydrocarbons that can replace fossil fuels in chemical production mainly involve the use of biomass to produce the basic component involved in the reactions. For example, Meng et al. [94] developed a benzene synthesis route by RuW catalyst supported on high silica zeolite, achieving a direct production of around 20% by *in situ* lignin hydrolyzation. Methanol-to-aromatics (MTA) process is another encouraging way to produce aromatics because it can also be realized in one direct step from CO_2. For instance, Liu et al. [95] using a composite catalyst of ZnAlOx with a nano-scaled spinel structure and H-ZSM-5 zeolite achieved an aromatics selectivity of around 74% and around 9% for CO_2 conversion at 320°C, with a stability proven until 100h.

Photochemistry

Among the new power to chemical lumps technologies, photocatalysis has the advantage to directly use the renewable source i.e., sunlight, without a step for the conversion and store of electricity. Photons are the reactive species, and they can induce the catalytic transformation by solid vibrational modes (phonon), energy transfers and excitement phenomena. Multi-electron and multi-proton processes are typically involved in these solar-to-chemical conversions, and remarkable progress in photocatalytic H_2 evolution, water oxidation, CO_2 reduction, and organic transformations has been documented in the last decade, with ever-improving efficiency, selectivity, and durability. Is estimated that in a long-term scenario the carbon footprint should be reduced of >70% [80] .

At the same time photochemical reactions have some intrinsic limitations:

Process intensification, for instance by staked reactor, is more difficult because photocatalytic devices need direct sunlight irradiation.

Irradiation intensity must be as high as possible, so there are limitations in time (during night) ant place (meteorological aspects, localization, etc.)

Low productivity due to low efficiency as current density generated by sunlight irradiation are in the order of 10 A/cm^2 while in electrochemical process it can be twice as high.

On other hand, direct sun irradiation gives another advantage: adaptability. In fact, this technology allows a change from a centralized model to a distributed production type by efficient small-medium scale plants. It can reduce also geopolitical dependence from fossil fuel rich countries, pushing investments and technological competition and creating new opportunities. In addition, in a long-term scenario, shift to a distributed production could be realized by developing of compact photovoltaic module, called artificial leaf, able to produce e-chemicals directly in a process, avoiding expensive and environmental impacting steps.

The most studied reactions in photochemistry are N_2 fixation and CO_2 reduction, therefore reactions with a great commercial value and high carbon footprint reduction potential.

Currently ammonia is produced by Haber-Bosh process, developed in the early 1900s. It has significant drawbacks: extreme synthetic conditions are needed, such as 300–500 °C and 150–300 atm, with efficiency around 20%, therefore a significant amount of energy (more than 1% of the world's energy production) is required, which creates environmental issues with an annual CO_2 generation of more than 400 Mt [96–98].

The artificial photosynthetic nitrogen reduction reaction (photo-NRR) is a more flexible and environmentally friendly alternative to the Haber-Bosch process because it can work at room temperature and atmospheric pressure, with consequently important operation cost reductions [98]. Very interesting are the ongoing development about artificial leaf devices [63,99], so compact photochemical cell able to directly reduce N_2 into NH_3 and then into fertilizers (in the form of NH_4NO_3 aqueous solution) [100]. A scheme of a possible cell is reported in figure 1.11.

Figure 1.11 *Concept of a compact photochemical for a distributed production of fertilizers. From ref [63]*

The module is characterized by one section for N_2 capture from air and a photovoltaic module to drive the reaction. The anode holds an electrocatalyst for N_2 oxidation (NOR) and the cathodic part has an electrocatalyst for N_2 reduction to ammonia. A wide variety of catalyst has been developed but the most promising candidate are defects rich TiO_2, g-C_3N_4, and Bi-based catalysts. In fact, defective sites (as oxygen vacancies, heteroatoms, etc.) can increase the light absorption, the change separation or weak the triple bond by retro-donation in anti-bonding orbitals of N_2. Some examples are reported in table 1.4.

Nevertheless, the present rate of NH_3 synthesis is still considerably below the desired level (a solar-to-chemical conversion efficiency of 10%), but usually production is in the range from $\mu mol \cdot L^{-1}$ to $mmol \cdot L^{-1}$ [98].

Table 1.4 *List of common catalysts for N_2 fixation by photocatalysis*

Catalyst	Conditions	Productivity	Reference
WS_2@TiO_2 nanoporous film	Area: $4cm^2$ Electrolyte: H_2O + Na_2SO_3 light source: simulated sunlight	1390 $\mu mol \cdot gcat^{-1}h^{-1}$	[101]
Cu doped TiO_2	Catalyst weight: 20 mg Electrolyte: water Light source: 300 W Xe lamp	78.9 $\mu mol \cdot gcat^{-1}h^{-1}$	[102]
Defective TiO_2 nanobamboo arrays	Area: $4cm^2$ Electrolyte: water Light source: 300 W Xe lamp	178 $\mu mol \cdot gcat^{-1}h^{-1}$	[103]

Oxygen vacancy rich Bi_5O_7Br nanotubes	Catalyst weight: 25 mg Electrolyte: water Light source: 300 W Xe lamp	1380 $\mu mol \cdot gcat^{-1}h^{-1}$	[104]
Oxygen vacancy rich Bi_3O_4Br Nanosheets	Catalyst weight: 50 mg Electrolyte: water Light source: 300 W Xe lamp	50.8 $\mu mol \cdot gcat^{-1}h^{-1}$	[105]
Bi_5O_7I Nanosheets	Catalyst weight: 5 mg Electrolyte: water Light source: 300 W Xe lamp	2230 $\mu mol \cdot gcat^{-1}h^{-1}$	[106]
Nitrogen vacancy g-C_3N_4 induced	Catalyst weight: 50 mg Electrolyte: water and methanol Light source: 300 W Xe lamp	1240 $\mu mol \cdot gcat^{-1}h^{-1}$	[107]
S-doped g-C_3N_4 nanosheets with carbon vacancies	Catalyst weight: 20 mg Electrolyte: water and methanol Light source: 500 W Xe lamp	5990 $\mu mol \cdot L^{-1} \cdot gcat^{-1} \cdot h^{-1}$	[108]
g-C_3N_4/40 wt% Fe_2O_3	Catalyst weight: 50 mg Electrolyte: water and methanol Light source: 300 W Xe lamp	4380 $\mu mol \cdot L^{-1} \cdot gcat^{-1} \cdot h^{-1}$	[109]

Photochemical and photoelectrochemical conversion of CO_2 is another fascinating synthetic route because it allows to close the carbon cycle by production of carbon fuels (called e-fuels) ready to be introduced into the current energy infrastructure. They include carbon monoxide (CO) and formate ($HCOO^-$) that are produced with high faradic efficiencies, but additional chemicals are methanol (CH_3OH), ethylene (C_2H_4), and other C2+ products, especially alcohols, hydrocarbons, and acids [81]. Among them formate has a big potential because is a base chemical for several applications and industrial products [110] but also it is a low cost H_2 carrier, with a volumetric H_2 storage capacity of 53 $g_{H2}\,L^{-1}$ [111].

Many works were published about this topic with energy efficiency around 10%, but mostly involved critical raw materials. For example, a high 10% energy-conversion was measured by Zhou et al.[112] using a costly InGaP/GaAs. Iridium often is used as electrode, as in the work of Piao teams, reporting an overall solar conversion efficiency of about 8.5% but using IrO_2 and Cl-based promoter that increase safety issue about Cl_2 formation[113]. A scale up beyond lab-scale was reported by Kato teams, which using a Si-based photovoltaic cell with $1m^2$ of active electrodes area reach a conversion of 10.5% but again costly materials (IrO_2 and molecular Ru-complex) were involved[114]. Conversely, a 10.1% formate efficiency (when combined with H_2) was obtained by Ampelli et al. [115] using only earth-abundant and non-critical raw materials, consisting in Cu–S and Ni–Fe–Zn oxide supported on gas-diffusion layer for electrochemical cell (EC), integrated with a low-cost Si-based photovoltaic module (PV). In addition, even if the H_2 productivity is quite low (2 g h^{-1} m^{-2}) is one of first work demonstrating the feasibility of a continuous production of H_2 (24 h) by a PV-EC device .

Plasma

Plasma is usually described as the ‘fourth state of matter’ or the state of an ionized gas. Man-made plasma can be classified into (i) fusion plasma, when the gas is almost completely ionized and it is in thermonuclear plasma systems or into (ii)

warm plasma, when the gas is not completely ionized, and it is the focus of currently research in chemistry. In fact, the main advantage is the fact that the gas is close to room temperature while the gas electrons are extremely energetic (~ 1 eV or 10000 K) [116].

Plasma is a technology extremely suitable for carbon-free future [34,117]:

Since the non-thermal plasma is a reactive chemical mixture, it can activate gas at room temperature, even thermal stable gases such as CO_2.

There is no need to heat the gas or reactor because the plasma is initiated and sustained by the high-energy electrons, applying the electromagnetic field. This makes plasma a very flexible technology because it can be easily and instantaneously switched on and off, as the plasma stabilization time is less than 30 minutes.

Power consumption can easily be modulated. This results in suitable technology for the irregular supply of renewable electricity (e.g., from wind turbines or solar panels), because by storing electricity in a desirable chemical form, it can make up for the fluctuating imbalance between energy supply and market demand.

Plasma reactor can be easily scaled up due to their low cost because they do not use rare earth elements or critical raw materials.

Plasma technology can use electricity from different energy sources. On one hand, this could be a limitation for the energy efficiency, but on other hand it makes plasma technology more flexible, as it can be operated 24/7, even when other renewable sources are not available (e.g., when the sun is not shining, or it is not a windy day).

At present, plasma processes have only had a little impact on chemistry. The majority of uses are in the fields of lighting (discharge lamps) or ozone creation, as well as material modification (cutting, welding, and surface modification) [70,118,119]. Processes using plasma as a catalyst are another promising technology. To bring plasma-catalysis technology for chemical synthesis to a commercial level, it is still important to address issues with energy efficiency, selectivity control, productivity, and reactor scale-up [63]. However, there are some specialized areas where plasma-

catalysis looks to be one of the potential routes for commercial implementation, for example the direct synthesis of fertilizers from the air [120,121]. An exhaustive description about plasma technology will be provided in chapter 3.

In conclusion, the NZE objectives in a high-tech future scenario show a number of problems for catalysis in the short-, medium-, and long-term timescales.
In the next years the most feasible solution is the re-design classical thermal reactor for a complete electric heating. This includes more efforts to exploit the effect of defined temperature gradients inside the reactor and immediate dynamic temperature control.
In the middle-term electrochemistry should be developed enough for a competitive value chain for chemical production and energy vectors. More efforts must be done in order to achieve high performances, not only in terms of conversion but also selectivity in order to abate cost and make these technologies cost competitive with fossil fuel-based processes.
In long-term, the focus should be addresses to photochemistry and plasma technologies. In artificial-like leaf solutions, the ability to operate without a separate unit to capture or purify reagents (such as N_2 or CO_2) is one of the many integrated functions of these devices to make the most of the potential of solar irradiation. Additional renewable sources, on the other hand, could provide electricity for plasma technologies, as it can make up for the fluctuating imbalance between energy supply and market demand. These tools are essential for realizing distributed manufacturing and overcoming the many drawbacks of the present centralized production paradigm.

Bibliography

1. Timmermann, A.; Yun, K.S.; Raia, P.; Ruan, J.; Mondanaro, A.; Zeller, E.; Zollikofer, C.; Ponce de León, M.; Lemmon, D.; Willeit, M.; et al. Climate Effects on Archaic Human Habitats and Species Successions. *Nature* **2022**, *604*, 495–501, doi:10.1038/s41586-022-04600-9.

2. Behringer, W. *A Cultural History of Climate*; Wiley, 2010; ISBN 9780745645292.

3. Burke, K.D.; Williams, J.W.; Chandler, M.A.; Haywood, A.M.; Lunt, D.J.; Otto-Bliesner, B.L. Pliocene and Eocene Provide Best Analogs for Near-Future Climates. *Proc. Natl. Acad. Sci. U. S. A.* **2018**, *115*, 13288–13293, doi:10.1073/pnas.1809600115.

4. Venkataramanan, M.; Smitha Causes and Effects of Global Warming. *Indian J. Sci. Technol.* **2011**, *4*, 226–229, doi:10.17485/ijst/2011/v4i3/29971.

5. Kaito, C.; Ito, A.; Kimura, S.; Kimura, Y.; Saito, Y.; Nakada, T. *Climate Change 2014 Synthesis Report AR5*; 2000; Vol. 218; ISBN 9789291691432.

6. Il, A.P.R. London , E D I N B U R G H , ~ . ~ D D U B L I N P H I L O S O P H I C a L Maga _ Zine of Science . **1896**, *41*.

7. Masson-Delmotte, V.; Zhai, P.; Pörtner, H.-O.; Roberts, D.; Skea, J.; Shukla, P.R.; Pirani, A.; Moufouma-Okia, W.; Péan, C.; Pidcock, R.; et al. *Intergovernmental Panel on Climate Change-Global Warming of 1.5 Degrees Celcius*; 2018; ISBN 9789291691432.

8. Climate change 2007 Synthesis Report - Summary for Policymakers. *An Assess. Intergov. Panel Clim. Chang.* **2007**, *335*, 1318.

9. Garza-Reyes, J.A. SYNTHESIS REPORT OF THE IPCC SIXTH ASSESSMENT REPORT (AR6) 2022. *Eur. Univ. Inst.* **2012**, 2–5.

10. Logan, C.A. A Review of Ocean Acidification and America's Response. *Bioscience* **2010**, *60*, 819–828, doi:10.1525/bio.2010.60.10.8.

11. McKinsey The Net-Zero Transition. *McKinsey Co.* **2022**, 1–64.

12. Pisier, G. *Real Interpolation and Transposition of Certain Function Spaces*; 2013; Vol. 26; ISBN 9780521880107.

13. Al-Ghussain, L. Global Warming: Review on Driving Forces and Mitigation. *Environ. Prog. Sustain. Energy* **2019**, *38*, 13–21, doi:10.1002/ep.13041.

14. Adger, N.; Coauthors including Fischlin, A. Summary for Policymakers. *Clim. Chang. 2007 Impacts, Adapt. vulnerability. Contrib. Work. Gr. II to Fourth Assess. Rep. Intergov. Panel Clim. Chang.* **2007**, 7–22, doi:http://www.ipcc.ch/publications_and_data/ar4/wg2/en/spm.html.

15. Zhao, C.; Yan, Y.; Wang, C.; Tang, M.; Wu, G.; Ding, D.; Song, Y. Adaptation and Mitigation for Combating Climate Change–from Single to Joint. *Ecosyst. Heal. Sustain.* **2018**, *4*, 85–94, doi:10.1080/20964129.2018.1466632.

16. Fankhauser, S. The Costs of Adaptation. *Wiley Interdiscip. Rev. Clim. Chang.* **2010**, *1*, 23–30, doi:10.1002/wcc.14.

17. NOAA ESRL Global Monitoring Division - Global Greenhouse Gas Reference Network. *J. Geophys. Res.* 2014, *101*, 4115.

18. Rossing, T.D.; Chiaverina, C.J. IPCC Special Report on Carbon Dioxide Capture and Storage, Chapter 2. Sources of CO2. *Light Sci.* **2019**, 203–228, doi:10.1007/978-3-030-27103-9_8.

19. Martin, A.R.; Thomas, S.C. A Reassessment of Carbon Content in Tropical Trees. *PLoS One* **2011**, *6*, doi:10.1371/journal.pone.0023533.

20. CO2 Emissions in 2022. *CO2 Emiss. 2022* **2023**, doi:10.1787/12ad1e1a-en.

21. Yamasaki, A. An Overview of CO2 Mitigation Options for Global Warming - Emphasizing CO2 Sequestration Options. *J. Chem. Eng. Japan* **2003**, *36*, 361–375, doi:10.1252/jcej.36.361.

22. Farhani, S.; Rejeb, J. Ben Energy Consumption, Economic Growth and CO2 Emissions: Evidence from Panel Data for MENA Region. *Int. J. Energy Econ. Policy* **2012**, *2*, 71–81.

23. Koytsoumpa, E.I.; Bergins, C.; Kakaras, E. The CO2 Economy: Review of CO2 Capture and Reuse Technologies. *J. Supercrit. Fluids* **2018**, *132*, 3–16, doi:10.1016/j.supflu.2017.07.029.

24. Sood, A.; Vyas, S. Carbon Capture and Sequestration- A Review. *IOP Conf. Ser. Earth Environ. Sci.* **2017**, *83*, doi:10.1088/1755-1315/83/1/012024.

25. Mebrahtu, C.; Krebs, F.; Abate, S.; Perathoner, S.; Centi, G.; Palkovits, R. *CO 2 Methanation: Principles and Challenges*; 1st ed.; Elsevier B.V., 2019; Vol. 178; ISBN 9780444641274.

26. Wang, Y.; Zhao, L.; Otto, A.; Robinius, M.; Stolten, D. A Review of Post-

Combustion CO2 Capture Technologies from Coal-Fired Power Plants. *Energy Procedia* **2017**, *114*, 650–665, doi:10.1016/j.egypro.2017.03.1209.

27. Viebahn, P.; Vallentin, D.; Höller, S. Prospects of Carbon Capture and Storage (CCS) in India's Power Sector - An Integrated Assessment. *Appl. Energy* **2014**, *117*, 62–75, doi:10.1016/j.apenergy.2013.11.054.

28. Rahman, F.A.; Aziz, M.M.A.; Saidur, R.; Bakar, W.A.W.A.; Hainin, M.R.; Putrajaya, R.; Hassan, N.A. Pollution to Solution: Capture and Sequestration of Carbon Dioxide (CO2) and Its Utilization as a Renewable Energy Source for a Sustainable Future. *Renew. Sustain. Energy Rev.* **2017**, *71*, 112–126, doi:10.1016/j.rser.2017.01.011.

29. Onyebuchi, V.E.; Kolios, A.; Hanak, D.P.; Biliyok, C.; Manovic, V. A Systematic Review of Key Challenges of CO2 Transport via Pipelines. *Renew. Sustain. Energy Rev.* **2018**, *81*, 2563–2583, doi:10.1016/j.rser.2017.06.064.

30. Wetenhall, B.; Aghajani, H.; Chalmers, H.; Benson, S.D.; Ferrari, M.C.; Li, J.; Race, J.M.; Singh, P.; Davison, J. Impact of CO2 Impurity on CO2 Compression, Liquefaction and Transportation. *Energy Procedia* **2014**, *63*, 2764–2778, doi:10.1016/j.egypro.2014.11.299.

31. Raza, A.; Gholami, R.; Rezaee, R.; Rasouli, V.; Rabiei, M. Significant Aspects of Carbon Capture and Storage – A Review. *Petroleum* **2019**, doi:10.1016/j.petlm.2018.12.007.

32. Kelemen, P.; Benson, S.M.; Pilorgé, H.; Psarras, P.; Wilcox, J. An Overview of the Status and Challenges of CO2 Storage in Minerals and Geological Formations. *Front. Clim.* **2019**, *1*, 1–20, doi:10.3389/fclim.2019.00009.

33. Gür, T.M. Carbon Dioxide Emissions, Capture, Storage and Utilization: Review of Materials, Processes and Technologies. *Prog. Energy Combust. Sci.* **2022**, *89*, 100965, doi:10.1016/j.pecs.2021.100965.

34. Mustafa, A.; Lougou, B.G.; Shuai, Y.; Wang, Z.; Tan, H. Current Technology Development for CO2 Utilization into Solar Fuels and Chemicals: A Review. *J. Energy Chem.* **2020**, *49*, 96–123, doi:10.1016/j.jechem.2020.01.023.

35. Cuéllar-Franca, R.M.; Azapagic, A. Carbon Capture, Storage and Utilisation Technologies: A Critical Analysis and Comparison of Their Life Cycle Environmental Impacts. *J. CO2 Util.* **2015**, *9*, 82–102, doi:10.1016/j.jcou.2014.12.001.

36. Kamolov, A.; Turakulov, Z.; Rejabov, S.; Díaz-Sainz, G.; Gómez-Coma, L.;

Norkobilov, A.; Fallanza, M.; Irabien, A. Decarbonization of Power and Industrial Sectors: The Role of Membrane Processes. *Membranes (Basel).* **2023**, *13*, doi:10.3390/membranes13020130.

37. Kamble, A.R.; Patel, C.M.; Murthy, Z.V.P. A Review on the Recent Advances in Mixed Matrix Membranes for Gas Separation Processes. *Renew. Sustain. Energy Rev.* **2021**, *145*, 111062, doi:10.1016/j.rser.2021.111062.

38. Koytsoumpa, E.I.; Atsonios, K.; Panopoulos, K.D.; Karellas, S.; Kakaras, E.; Karl, J. Modelling and Assessment of Acid Gas Removal Processes in Coal-Derived SNG Production. *Appl. Therm. Eng.* **2015**, *74*, 128–135, doi:10.1016/j.applthermaleng.2014.02.026.

39. Jansen, D.; Gazzani, M.; Manzolini, G.; Dijk, E. Van; Carbo, M. Pre-Combustion CO2 Capture. *Int. J. Greenh. Gas Control* **2015**, *40*, 167–187, doi:10.1016/j.ijggc.2015.05.028.

40. Theo, W.L.; Lim, J.S.; Hashim, H.; Mustaffa, A.A.; Ho, W.S. Review of Pre-Combustion Capture and Ionic Liquid in Carbon Capture and Storage. *Appl. Energy* **2016**, *183*, 1633–1663, doi:10.1016/j.apenergy.2016.09.103.

41. Elgarahy, A.M.; Hammad, A.; El-Sherif, D.M.; Abouzid, M.; Gaballah, M.S.; Elwakeel, K.Z.; Cau, G.; Tola, V.; Ferrara, F.; Porcu, A.; et al. Comparative Techno-Economic Analysis of Carbon Capture Combustion Operations. *Fuel* **2021**, *214*, 423–435.

42. Olabi, A.G.; Obaideen, K.; Elsaid, K.; Wilberforce, T.; Sayed, E.T.; Maghrabie, H.M.; Abdelkareem, M.A. Assessment of the Pre-Combustion Carbon Capture Contribution into Sustainable Development Goals SDGs Using Novel Indicators. *Renew. Sustain. Energy Rev.* **2022**, *153*, 111710, doi:10.1016/j.rser.2021.111710.

43. Ghiat, I.; Al-Ansari, T. A Review of Carbon Capture and Utilisation as a CO2abatement Opportunity within the EWF Nexus. *J. CO2 Util.* **2021**, *45*, 101432, doi:10.1016/j.jcou.2020.101432.

44. Zeng, Z.; Natesan, K.; Cai, Z.; Gosztola, D.J. Effects of Chlorine in Ash on the Corrosion Performance of Ni-Based Alloys in a Simulated Oxy-Fuel Environment. *Energy and Fuels* **2018**, *32*, 10502–10512, doi:10.1021/acs.energyfuels.8b02233.

45. Aldaco, R.; Butnar, I.; Margallo, M.; Laso, J.; Rumayor, M.; Dominguez-Ramos, A.; Irabien, A.; Dodds, P.E. Bringing Value to the Chemical Industry from Capture, Storage and Use of CO 2 : A Dynamic LCA of Formic Acid Production.

Sci. Total Environ. **2019**, *663*, 738–753, doi:10.1016/j.scitotenv.2019.01.395.

46. Jarraud, M.; Steiner, A. *Summary for Policymakers*; 2012; Vol. 9781107025; ISBN 9781139177245.

47. Centi, G.; Perathoner, S. The Chemical Engineering Aspects of CO2 Capture, Combined with Its Utilisation. *Curr. Opin. Chem. Eng.* **2023**, *39*, doi:10.1016/j.coche.2022.100879.

48. Norhasyima, R.S.; Mahlia, T.M.I. Advances in CO2 Utilization Technology: A Patent Landscape Review. *J. CO2 Util.* 2018, *26*, 323–335.

49. Olajire, A.A. A Review of Mineral Carbonation Technology in Sequestration of CO2. *J. Pet. Sci. Eng.* **2013**, *109*, 364–392, doi:10.1016/j.petrol.2013.03.013.

50. Pasquier, L.C.; Mercier, G.; Blais, J.F.; Cecchi, E.; Kentish, S. Technical & Economic Evaluation of a Mineral Carbonation Process Using Southern Québec Mining Wastes for CO2 Sequestration of Raw Flue Gas with By-Product Recovery. *Int. J. Greenh. Gas Control* **2016**, *50*, 147–157, doi:10.1016/j.ijggc.2016.04.030.

51. Bundschuh, J.; Yusaf, T.; Maity, J.P.; Nelson, E.; Mamat, R.; Indra Mahlia, T.M. Algae-Biomass for Fuel, Electricity and Agriculture. *Energy* **2014**, *78*, 1–3, doi:10.1016/j.energy.2014.11.005.

52. Adeniyi, O.M.; Azimov, U.; Burluka, A. Algae Biofuel: Current Status and Future Applications. *Renew. Sustain. Energy Rev.* **2018**, *90*, 316–335, doi:10.1016/j.rser.2018.03.067.

53. Schaaf, T.; Grünig, J.; Schuster, M.R.; Rothenfluh, T.; Orth, A. Methanation of CO2 - Storage of Renewable Energy in a Gas Distribution System. *Energy. Sustain. Soc.* **2014**, *4*, 1–14, doi:10.1186/s13705-014-0029-1.

54. Koytsoumpa, E.-I.; Bergins, C.; Buddenberg, T.; Wu, S.; Sigurbjörnsson, Ó.; Tran, K.C.; Kakaras, E. The Challenge of Energy Storage in Europe: Focus on Power to Fuel. *J. Energy Resour. Technol.* **2016**, *138*, 1–10, doi:10.1115/1.4032544.

55. Dibenedetto, A.; Angelini, A.; Stufano, P. Use of Carbon Dioxide as Feedstock for Chemicals and Fuels: Homogeneous and Heterogeneous Catalysis. *J. Chem. Technol. Biotechnol.* **2014**, *89*, 334–353, doi:10.1002/jctb.4229.

56. Chauvy, R.; Meunier, N.; Thomas, D.; De Weireld, G. Selecting Emerging CO2 Utilization Products for Short- to Mid-Term Deployment. *Appl. Energy* **2019**, *236*, 662–680, doi:10.1016/j.apenergy.2018.11.096.

57. Wang, J.; Li, G.; Li, Z.; Tang, C.; Feng, Z.; An, H.; Liu, H.; Liu, T.; Li, C. A Highly Selective and Stable ZnO-ZrO2 Solid Solution Catalyst for CO2 Hydrogenation to Methanol. *Sci. Adv.* **2017**, *3*, 1–11, doi:10.1126/sciadv.1701290.

58. Li, Z.; Wang, J.; Qu, Y.; Liu, H.; Tang, C.; Miao, S.; Feng, Z.; An, H.; Li, C. Highly Selective Conversion of Carbon Dioxide to Lower Olefins. *ACS Catal.* **2017**, *7*, 8544–8548, doi:10.1021/acscatal.7b03251.

59. Papanikolaou, G.; Centi, G.; Perathoner, S.; Lanzafame, P. Catalysis for E-Chemistry: Need and Gaps for a Future De-Fossilized Chemical Production, with Focus on the Role of Complex (Direct) Syntheses by Electrocatalysis. *ACS Catal.* **2022**, *12*, 2861–2876, doi:10.1021/acscatal.2c00099.

60. Lange, J.P. Towards Circular Carbo-Chemicals – the Metamorphosis of Petrochemicals. *Energy Environ. Sci.* **2021**, *14*, 4358–4376, doi:10.1039/d1ee00532d.

61. Centi, G.; Perathoner, S. Status and Gaps toward Fossil-Free Sustainable Chemical Production. *Green Chem.* **2022**, *24*, 7305–7331, doi:10.1039/d2gc01572b.

62. Schüwer, D.; Schneider, C. Electrification of Industrial Process Heat: Long-Term Applications, Potentials and Impacts. *Eceee Ind. Summer Study Proc.* **2018**, *2018-June*, 411–422.

63. Centi, G.; Perathoner, S. Catalysis for an Electrified Chemical Production. *Catal. Today* **2022**, doi:10.1016/j.cattod.2022.10.017.

64. Wismann, S.T.; Engbæk, J.S.; Vendelbo, S.B.; Eriksen, W.L.; Frandsen, C.; Mortensen, P.M.; Chorkendorff, I. Electrified Methane Reforming: Understanding the Dynamic Interplay. *Ind. Eng. Chem. Res.* **2019**, *58*, 23380–23388, doi:10.1021/acs.iecr.9b04182.

65. Wismann, S.T.; Engbæk, J.S.; Vendelbo, S.B.; Eriksen, W.L.; Frandsen, C.; Mortensen, P.M.; Chorkendorff, I. Electrified Methane Reforming: Elucidating Transient Phenomena. *Chem. Eng. J.* **2021**, *425*, doi:10.1016/j.cej.2021.131509.

66. Zhou, L.; Guo, Y.; Yagi, M.; Sakurai, M.; Kameyama, H. Investigation of a Novel Porous Anodic Alumina Plate for Methane Steam Reforming: Hydrothermal Stability, Electrical Heating Possibility and Reforming Reactivity. *Int. J. Hydrogen Energy* **2009**, *34*, 844–858, doi:10.1016/j.ijhydene.2008.10.057.

67. Zheng, L.; Ambrosetti, M.; Zaio, F.; Beretta, A.; Groppi, G.; Tronconi, E. Direct Electrification of Rh/Al2O3 Washcoated SiSiC Foams for Methane Steam Reforming: An Experimental and Modelling Study. *Int. J. Hydrogen Energy* **2023**,

48, 14681–14696, doi:10.1016/j.ijhydene.2022.12.346.

68. Sekine, Y.; Haraguchi, M.; Matsukata, M.; Kikuchi, E. Low Temperature Steam Reforming of Methane over Metal Catalyst Supported on CexZr1-XO2 in an Electric Field. *Catal. Today* **2011**, *171*, 116–125, doi:10.1016/j.cattod.2011.03.076.

69. Kuhwald, C.; Türkhan, S.; Kirschning, A. Inductive Heating and Flow Chemistry – a Perfect Synergy of Emerging Enabling Technologies. *Beilstein J. Org. Chem.* **2022**, *18*, 688–706, doi:10.3762/bjoc.18.70.

70. Schultz, T.; Nagel, M.; Engenhorst, T.; Nymand-Andersen, A.; Kunze, E.; Stenner, P.; Lang, J.E. Electrifying Chemistry: A Company Strategy Perspective. *Curr. Opin. Chem. Eng.* **2023**, *40*, doi:10.1016/j.coche.2023.100916.

71. Mortensen, P.M.; Engbæk, J.S.; Vendelbo, S.B.; Hansen, M.F.; Østberg, M. Direct Hysteresis Heating of Catalytically Active Ni-Co Nanoparticles as Steam Reforming Catalyst. *Ind. Eng. Chem. Res.* **2017**, *56*, 14006–14013, doi:10.1021/acs.iecr.7b02331.

72. Vinum, M.G.; Almind, M.R.; Engbæk, J.S.; Vendelbo, S.B.; Hansen, M.F.; Frandsen, C.; Bendix, J.; Mortensen, P.M. Dual-Function Cobalt–Nickel Nanoparticles Tailored for High-Temperature Induction-Heated Steam Methane Reforming. *Angew. Chemie - Int. Ed.* **2018**, *57*, 10569–10573, doi:10.1002/anie.201804832.

73. Wang, W.; Duong-Viet, C.; Xu, Z.; Ba, H.; Tuci, G.; Giambastiani, G.; Liu, Y.; Truong-Huu, T.; Nhut, J.M.; Pham-Huu, C. CO2 Methanation under Dynamic Operational Mode Using Nickel Nanoparticles Decorated Carbon Felt (Ni/OCF) Combined with Inductive Heating. *Catal. Today* **2020**, *357*, 214–220, doi:10.1016/j.cattod.2019.02.050.

74. Muley, P.D.; Wang, Y.; Hu, J.; Shekhawat, D. *Microwave-Assisted Heterogeneous Catalysis*; 2021; Vol. 33; ISBN 9781839162046.

75. Meloni, E.; Iervolino, G.; Ruocco, C.; Renda, S.; Festa, G.; Martino, M.; Palma, V. Electrified Hydrogen Production from Methane for PEM Fuel Cells Feeding: A Review. *Energies* **2022**, *15*, doi:10.3390/en15103588.

76. de Dios García, I.; Stankiewicz, A.; Nigar, H. Syngas Production via Microwave-Assisted Dry Reforming of Methane. *Catal. Today* **2021**, *362*, 72–80, doi:10.1016/j.cattod.2020.04.045.

77. Zhang, F.; Zhang, X.; Song, Z.; Chen, H.; Zhao, X.; Sun, J.; Mao, Y.; Wang, X.; Wang, W. Fe/HZSM-5 Synergizes with Biomass Pyrolysis Carbon to Reform

CH4–CO2 to Syngas in Microwave Field. *Int. J. Hydrogen Energy* **2022**, *47*, 11153–11163, doi:10.1016/j.ijhydene.2022.01.158.

78. Marin, C.M.; Popczun, E.J.; Nguyen-Phan, T.D.; Tafen, D.N.; Alfonso, D.; Waluyo, I.; Hunt, A.; Kauffman, D.R. Designing Perovskite Catalysts for Controlled Active-Site Exsolution in the Microwave Dry Reforming of Methane. *Appl. Catal. B Environ.* **2021**, *284*, 119711, doi:10.1016/j.apcatb.2020.119711.

79. Nguyen, H.M.; Pham, G.H.; Tade, M.; Phan, C.; Vagnoni, R.; Liu, S. Microwave-Assisted Dry and Bi-Reforming of Methane over M-Mo/TiO2(M = Co, Cu) Bimetallic Catalysts. *Energy and Fuels* **2020**, *34*, 7284–7294, doi:10.1021/acs.energyfuels.0c00757.

80. Appolloni, A.; Centi, G.; Yang, N. Promoting Carbon Circularity for a Sustainable and Resilience Fashion Industry. *Curr. Opin. Green Sustain. Chem.* **2023**, *39*, 100719, doi:10.1016/j.cogsc.2022.100719.

81. Perathoner, S.; Centi, G. Catalysis for Solar-Driven Chemistry: The Role of Electrocatalysis. *Catal. Today* **2019**, 157–170, doi:10.1016/j.cattod.2018.03.005.

82. Centi, G.; Perathoner, S.; Salladini, A.; Iaquaniello, G. Economics of CO2 Utilization: A Critical Analysis. *Front. Energy Res.* **2020**, *8*, 1–16, doi:10.3389/fenrg.2020.567986.

83. Smith, C.; Hill, A.K.; Torrente-Murciano, L. Current and Future Role of Haber-Bosch Ammonia in a Carbon-Free Energy Landscape. *Energy Environ. Sci.* **2020**, *13*, 331–344, doi:10.1039/c9ee02873k.

84. Scott, K. Process Intensification : An Electrochemical Perspective . Renewable and Sustainable Energy Reviews (2017) DOI : Https://Doi.Org/10.1016/j.Rser.2017.05.189 Date Deposited : **2018**.

85. Kuo, L.; Dinh, C.T. Toward Efficient Catalysts for Electrochemical CO2 Conversion to C2 Products. *Curr. Opin. Electrochem.* **2021**, *30*, 100807, doi:10.1016/j.coelec.2021.100807.

86. Zhao, K.; Quan, X. Carbon-Based Materials for Electrochemical Reduction of CO2to C2+oxygenates: Recent Progress and Remaining Challenges. *ACS Catal.* **2021**, *11*, 2076–2097, doi:10.1021/acscatal.0c04714.

87. Marepally, B.C.; Ampelli, C.; Genovese, C.; Saboo, T. Enhanced Formation of > C1 Products in Electroreduction of CO 2 by Adding a CO 2 Adsorption Component to a Gas-Diffusion Layer-Type Catalytic Electrode. **2017**, 4442–4446, doi:10.1002/cssc.201701506.

88. Arrigo, R.; Blume, R.; Streibel, V.; Genovese, C.; Roldan, A.; Schuster, M.E.; Ampelli, C.; Perathoner, S.; Velasco Vélez, J.J.; Hävecker, M.; et al. Dynamics at Polarized Carbon Dioxide–Iron Oxyhydroxide Interfaces Unveil the Origin of Multicarbon Product Formation. *ACS Catal.* **2022**, *12*, 411–430, doi:10.1021/acscatal.1c04296.

89. De Luna, P.; Hahn, C.; Higgins, D.; Jaffer, S.A.; Jaramillo, T.F.; Sargent, E.H. What Would It Take for Renewably Powered Electrosynthesis to Displace Petrochemical Processes? *Science (80-.).* **2019**, *364*, doi:10.1126/science.aav3506.

90. Zhong, M.; Tran, K.; Min, Y.; Wang, C.; Wang, Z.; Dinh, C.T.; De Luna, P.; Yu, Z.; Rasouli, A.S.; Brodersen, P.; et al. Accelerated Discovery of CO2 Electrocatalysts Using Active Machine Learning. *Nature* **2020**, *581*, 178–183, doi:10.1038/s41586-020-2242-8.

91. Chen, C.; Li, Y.; Yu, S.; Louisia, S.; Jin, J.; Li, M.; Ross, M.B.; Yang, P. Cu-Ag Tandem Catalysts for High-Rate CO2 Electrolysis toward Multicarbons. *Joule* **2020**, *4*, 1688–1699, doi:10.1016/j.joule.2020.07.009.

92. Jiang, Y.; Choi, C.; Hong, S.; Chu, S.; Wu, T.S.; Soo, Y.L.; Hao, L.; Jung, Y.; Sun, Z. Enhanced Electrochemical CO2 Reduction to Ethylene over CuO by Synergistically Tuning Oxygen Vacancies and Metal Doping. *Cell Reports Phys. Sci.* **2021**, *2*, 100356, doi:10.1016/j.xcrp.2021.100356.

93. Li, J.; Ozden, A.; Wan, M.; Hu, Y.; Li, F.; Wang, Y.; Zamani, R.R.; Ren, D.; Wang, Z.; Xu, Y.; et al. Silica-Copper Catalyst Interfaces Enable Carbon-Carbon Coupling towards Ethylene Electrosynthesis. *Nat. Commun.* **2021**, *12*, 1–10, doi:10.1038/s41467-021-23023-0.

94. Meng, Q.; Yan, J.; Wu, R.; Liu, H.; Sun, Y.; Wu, N.N.; Xiang, J.; Zheng, L.; Zhang, J.; Han, B. Sustainable Production of Benzene from Lignin. *Nat. Commun.* **2021**, *12*, 1–12, doi:10.1038/s41467-021-24780-8.

95. Ni, Y.; Chen, Z.; Fu, Y.; Liu, Y.; Zhu, W.; Liu, Z. Selective Conversion of CO2 and H2 into Aromatics. *Nat. Commun.* **2018**, *9*, 1–7, doi:10.1038/s41467-018-05880-4.

96. Pfromm, P.H. Towards Sustainable Agriculture: Fossil-Free Ammonia. *J. Renew. Sustain. Energy* **2017**, *9*, doi:10.1063/1.4985090.

97. U.S.G.S *Mineral Commodity Summaries 2022*; 2022; ISBN 9780333227794.

98. Nguyen, D.L.T.; Tekalgne, M.A.; Nguyen, T.H.C.; Dinh, M.T.N.; Sana, S.S.; Grace, A.N.; Shokouhimehr, M.; Vo, D.V.N.; Cheng, C.K.; Nguyen, C.C.; et al.

Recent Development of High-Performance Photocatalysts for N2fixation: A Review. *J. Environ. Chem. Eng.* **2021**, *9*, 104997, doi:10.1016/j.jece.2020.104997.

99. Meng, S.L.; Li, X.B.; Tung, C.H.; Wu, L.Z. Nitrogenase Inspired Artificial Photosynthetic Nitrogen Fixation. *Chem* **2021**, *7*, 1431–1450, doi:10.1016/j.chempr.2020.11.002.

100. Centi, G.; Perathoner, S.; Genovese, C.; Arrigo, R. Advanced (Photo)Electrocatalytic Approaches to Substitute the Use of Fossil Fuels in Chemical Production. *Chem. Commun.* **2023**, *59*, 3005–3023, doi:10.1039/d2cc05132j.

101. Shi, L.; Li, Z.; Ju, L.; Carrasco-Pena, A.; Orlovskaya, N.; Zhou, H.; Yang, Y. Promoting Nitrogen Photofixation over a Periodic WS2@TiO2 Nanoporous Film. *J. Mater. Chem. A* **2020**, *8*, 1059–1065, doi:10.1039/c9ta12743g.

102. Lu, M.; Li, Q.; Liu, J.; Zhang, F.M.; Zhang, L.; Wang, J.L.; Kang, Z.H.; Lan, Y.Q. Installing Earth-Abundant Metal Active Centers to Covalent Organic Frameworks for Efficient Heterogeneous Photocatalytic CO2 Reduction. *Appl. Catal. B Environ.* **2019**, *254*, 624–633, doi:10.1016/j.apcatb.2019.05.033.

103. Zhang, Y.; Chen, X.; Zhang, S.; Yin, L.; Yang, Y. Defective Titanium Dioxide Nanobamboo Arrays Architecture for Photocatalytic Nitrogen Fixation up to 780 Nm. *Chem. Eng. J.* **2020**, *401*, 126033, doi:10.1016/j.cej.2020.126033.

104. Wang, S.; Hai, X.; Ding, X.; Chang, K.; Xiang, Y.; Meng, X.; Yang, Z.; Chen, H.; Ye, J. Light-Switchable Oxygen Vacancies in Ultrafine Bi5O7Br Nanotubes for Boosting Solar-Driven Nitrogen Fixation in Pure Water. *Adv. Mater.* **2017**, *29*, 1–7, doi:10.1002/adma.201701774.

105. Di, J.; Xia, J.; Chisholm, M.F.; Zhong, J.; Chen, C.; Cao, X.; Dong, F.; Chi, Z.; Chen, H.; Weng, Y.X.; et al. Defect-Tailoring Mediated Electron–Hole Separation in Single-Unit-Cell Bi3O4Br Nanosheets for Boosting Photocatalytic Hydrogen Evolution and Nitrogen Fixation. *Adv. Mater.* **2019**, *31*, 1–8, doi:10.1002/adma.201807576.

106. Bai, Y.; Ye, L.; Chen, T.; Wang, L.; Shi, X.; Zhang, X.; Chen, D. Facet-Dependent Photocatalytic N2 Fixation of Bismuth-Rich Bi5O7I Nanosheets. *ACS Appl. Mater. Interfaces* **2016**, *8*, 27661–27668, doi:10.1021/acsami.6b08129.

107. Dong, G.; Ho, W.; Wang, C. Selective Photocatalytic N2 Fixation Dependent on G-C3N4 Induced by Nitrogen Vacancies. *J. Mater. Chem. A* **2015**, *3*, 23435–23441, doi:10.1039/c5ta06540b.

108. Cao, S.; Fan, B.; Feng, Y.; Chen, H.; Jiang, F.; Wang, X. Sulfur-Doped g-

C3N4 Nanosheets with Carbon Vacancies: General Synthesis and Improved Activity for Simulated Solar-Light Photocatalytic Nitrogen Fixation. *Chem. Eng. J.* **2018**, *353*, 147–156, doi:10.1016/j.cej.2018.07.116.

109. Mou, H.; Wang, J.; Zhang, D.; Yu, D.; Chen, W.; Wang, D.; Mu, T. A One-Step Deep Eutectic Solvent Assisted Synthesis of Carbon Nitride/Metal Oxide Composites for Photocatalytic Nitrogen Fixation. *J. Mater. Chem. A* **2019**, *7*, 5719–5725, doi:10.1039/c8ta11681d.

110. Al-Tamreh, S.A.; Ibrahim, M.H.; El-Naas, M.H.; Vaes, J.; Pant, D.; Benamor, A.; Amhamed, A. Electroreduction of Carbon Dioxide into Formate: A Comprehensive Review. *ChemElectroChem* **2021**, *8*, 3207–3220, doi:10.1002/celc.202100438.

111. Eppinger, J.; Huang, K.W. Formic Acid as a Hydrogen Energy Carrier. *ACS Energy Lett.* **2017**, *2*, 188–195, doi:10.1021/acsenergylett.6b00574.

112. Zhou, X.; Liu, R.; Sun, K.; Chen, Y.; Verlage, E.; Francis, S.A.; Lewis, N.S.; Xiang, C. Solar-Driven Reduction of 1 Atm of CO2 to Formate at 10% Energy-Conversion Efficiency by Use of a TiO2-Protected III-V Tandem Photoanode in Conjunction with a Bipolar Membrane and a Pd/C Cathode. *ACS Energy Lett.* **2016**, *1*, 764–770, doi:10.1021/acsenergylett.6b00317.

113. Piao, G.; Yoon, S.H.; Han, D.S.; Park, H. Ion-Enhanced Conversion of CO2 into Formate on Porous Dendritic Bismuth Electrodes with High Efficiency and Durability. *ChemSusChem* **2020**, *13*, 698–706, doi:10.1002/cssc.201902581.

114. Kato, N.; Takeda, Y.; Kawai, Y.; Nojiri, N.; Shiozawa, M.; Mizuno, S.; Yamanaka, K.I.; Morikawa, T.; Hamaguchi, T. Solar Fuel Production from CO2Using a 1 M-Square-Sized Reactor with a Solar-to-Formate Conversion Efficiency of 10.5%. *ACS Sustain. Chem. Eng.* **2021**, *9*, 16031–16037, doi:10.1021/acssuschemeng.1c06390.

115. Ampelli, C.; Giusi, D.; Miceli, M.; Merdzhanova, T.; Smirnov, V.; Chime, U.; Astakhov, O.; Martín, A.J.; Veenstra, F.L.P.; Pineda, F.A.G.; et al. An Artificial Leaf Device Built with Earth-Abundant Materials for Combined H2 Production and Storage as Formate with Efficiency > 10%. *Energy Environ. Sci.* **2023**, *16*, 1644–1661, doi:10.1039/d2ee03215e.

116. Fridman, A. *Plasma Chemistry*; 2008; ISBN 9780521847353.

117. Snoeckx, R.; Bogaerts, A. Plasma Technology – a Novel Solution for CO2. *Chem. Soc. Rev.* **2017**, *46*, doi:10.1039/c6cs00066e.

118. Mehta, P.; Barboun, P.; Go, D.B.; Hicks, J.C.; Schneider, W.F. Catalysis Enabled by Plasma Activation of Strong Chemical Bonds: A Review. *ACS Energy Lett.* **2019**, *4*, 1115–1133, doi:10.1021/acsenergylett.9b00263.

119. Huang, M.; Hasan, M.K.; Rathore, K.; Baky, M.A.H.; Lassalle, J.; Kraus, J.; Burnette, M.; Campbell, C.; Wang, K.; Jemison, H.; et al. *Plasma Generated Ozone and Reactive Oxygen Species for Point of Use PPE Decontamination System*; 2022; Vol. 17; ISBN 1111111111.

120. Kelly, S.; Bogaerts, A. Nitrogen Fixation in an Electrode-Free Microwave Plasma. *Joule* **2021**, *5*, 3006–3030, doi:10.1016/j.joule.2021.09.009.

121. Vervloessem, E.; Aghaei, M.; Jardali, F.; Hafezkhiabani, N.; Bogaerts, A. Plasma-Based N2Fixation into NOx: Insights from Modeling toward Optimum Yields and Energy Costs in a Gliding Arc Plasmatron. *ACS Sustain. Chem. Eng.* **2020**, *8*, 9711–9720, doi:10.1021/acssuschemeng.0c01815.

2

ELECTROCATALYTIC HYDROGENATION OF OXALIC ACID

State of art and TiO_2 nanotubes as electrocatalysts

2.1 Introduction

As described in chapter 1, electrochemical technologies are a promising solution to replace, in a mid-term scenario, the traditional synthetic routes based on fossil fuel use [1]. It is crucial to note that electrochemical processes are among the most suitable alternatives for reducing reliance on fossil fuels.

Along with the indirect use of renewable energies, electrochemical processes offer an innovative way to decrease greenhouse gas emissions while maintaining competitiveness and appeal through significant cost savings and improved efficiency. Electrochemistry offers also a considerable advantage in producing redox agents in situ (H^+/e^-, *OOH, *OH, *O, H_2O_2), which eliminates the need for costly and challenging separation and storage processes. Furthermore, electrochemical reactions allow for control over several reaction parameters, such as applied potential, current, or temperature. Additionally, the viability of this technology is due to its compact electrolysis cells and modular design, which allows for on-demand use, making it suitable for small and large-scale applications. Its compact size and modularity also facilitate ease of use and configuration [2–4].

However, achieving high performance with regard to electrocatalyst stability and deactivation remains a challenge. Furthermore, the utilization of rare-earth elements and critical raw materials (CRM) and their associated costs pose additional barriers to developing a process that is fully competitive with nonrenewable sources [5,6]. In any case, these limitations could be overcome in the coming decades through the use of improved electrocatalysts. Within the context of a circular economy, electrocatalytic CO_2 reduction plays a key role as it combines process intensification,

recycling of waste CO_2, and the incorporation of renewable sources into the production chain, primary goals to establish a fossil-free chemical industry [6–8].
C1 products, derived through CO_2 reduction (CO, CH_3OH, formic acid) have limited economic value, but they facilitate the manufacturing of C2 and C3 fuels and chemicals. This generates new and attractive industrial prospects. Therefore, C1 products can be considered the starting point for implementing electrocatalytic CO_2 utilization techniques [5-10]. Nonetheless, the range of commodities obtainable through direct electrocatalytic CO_2 reduction is significantly limited (mainly ethanol, ethylene, and acetic acid/acetate) [9–13].
A process using oxalic acid (OX) as the initial reactant, generates a new value chain as an option to direct reduction. As shown in figure 2.1 OX can be produced through direct reductive dimerization of CO_2 or through of formic acid (or K-formate) by electrocatalytic synthesis or thermal conversion, followed by the electrocatalytic reduction of OX. In this way, the European project OCEAN (Oxalic acid from CO_2 using electrochemistry at demonstration scale, grant agreement ID: 767798) aims to establish a new value chain for producing C2 chemicals from CO_2 at a demo scale (figure 2.1).

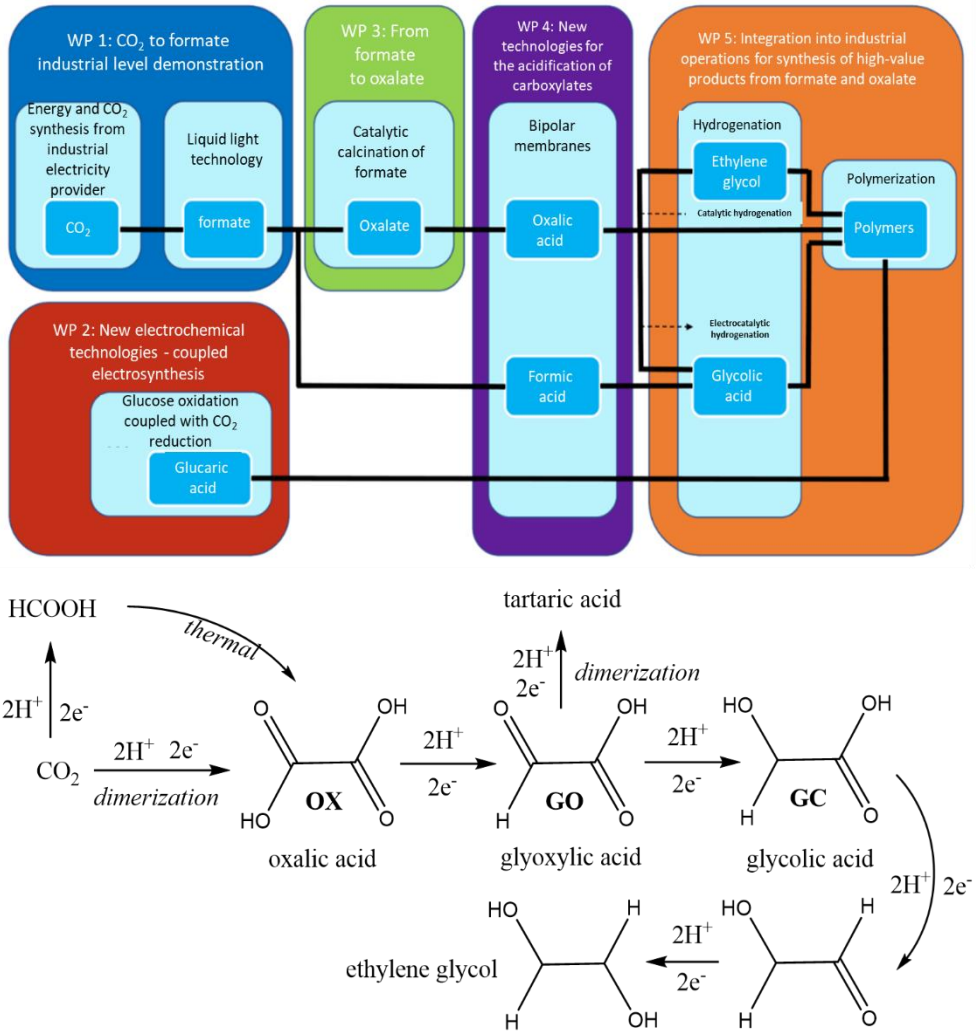

Figure 2.1 *Schematic and simplified representation of the OCEAN project and reactions involved.*

2.2 Hydrogenation of oxalates

Nowadays, oxalic acid serves mainly as a bleaching agent due to its ability to sequester metal ions, and as a preservative for agricultural products[14]. It is also being considered as a solid CO_2 storage solution to prevent the transport of carbon dioxide via conduits in a liquid or supercritical state[15]. Furthermore, its structural integrity has led to extensive use as a chemical reagent. The presence of two carboxyl groups confers chelating properties, enabling key reactive sites for interactions in

both heterogeneous and homogeneous catalysis, making it an essential means of strategic interaction with various substances.

2.2.1 Catalytic hydrogenation

In conventional hydrogenation methods, the hydrogen source can be molecular hydrogen or derived from reducing agents, such as sodium boron hydride ($NaBH_4$) or lithium aluminum hydride ($LiAlH_4$). While most hydrogenation reactions are thermodynamically favored, their kinetics are slow, and a homogeneous or heterogeneous catalyst is necessary. However, direct hydrogenation of oxalic acid is not a widely studied reaction. Takeda et al. [16] developed Re-Pd/SiO_2 catalysts to transform succinic acid and other dicarboxylic acids into their respective diols in a heterogeneous phase. Meanwhile, J Santos et al. [17] synthesized a Ru/activated carbon catalyst that selectively converts oxalic acid to ethylene glycol and glycolic acid, achieving a 87.33% selectivity for glycolic acid and over 90% conversion. B. Grømer and colleagues [18] investigated homogeneous-phase catalysts that employ Iridium PNNP complexes that are sterically bulky, along with Lewis acids, to aid in reducing dicarboxylic acids, like oxalate.

As a greener alternative to ethylene oxide hydration, there is a growing interest in using oxalic acid ester reduction, specifically Dimethyl Oxalate (DMO), for producing Ethylene Glycol (EG). DMO has the advantage of being producible from syngas, which can be obtained through a range of environmentally friendly or low-emission techniques that utilize non-fossil carbon sources such as biomass followed by coupling carbon monoxide with methanol, to obtain DMO. The catalytic hydrogenation of DMO in the vapor phase results in the production of methyl glycolate (MG), ethylene glycol (EG) or ethanol (scheme 2.1).

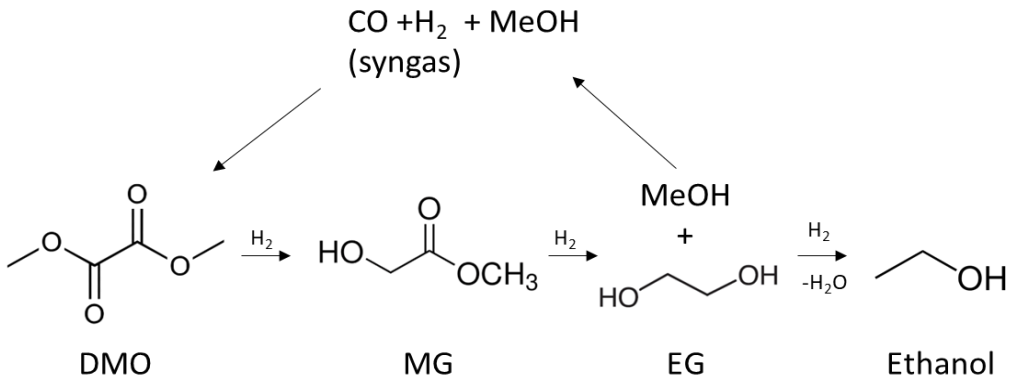

Scheme 2.1 *Catalytic process for the reduction of DMO*

The EG process involves two steps: an initial reduction of DMO to MG followed by hydrogenation to EG. An interesting aspect of this process is that the methanol produced during hydrogenation can be reused in the DMO synthesis process[19,20]. In homogeneous catalytic systems, Ag[21] and Ru[22–24] based complexes have been utilized, but the most favorable outcomes have arisen from employing a homogeneous catalyst synthesized with $Ru(acac)_3$ and $MeC(CH_2PPh_2)_3$ as the tridentate ligand. This particular catalyst operates under less severe conditions, and the coordination of Ru with the tridentate ligand is crucial in maintaining high catalytic activity, resulting in a yield of 95%. However, homogeneous catalysis still faces several challenges, including a high cost of the noble metal catalyst, difficulty separating the catalyst in the homogeneous phase, challenges in synthesizing the catalytic system on an industrial scale, and the requirement of high H_2 pressures. Conversely, these issues do not affect heterogeneous-phase catalysts, which are typically composed of metal distributed on a porous substrate, such as activated carbon, alumina, or silica-alumina. This configuration increases the metal's surface area and enhances the catalyst's efficacy. As a result, there are various publications in the literature on reducing oxalates through heterogeneous catalysis.

One of the most commonly employed industrially heterogeneous catalysts for reducing DMO to EG in the vapor phase is a Cu/SiO_2 catalyst [25,26]. In fact, Cu selectively hydrogenates the C-O bond without affecting the C-C bond, producing

higher yields, and operating under milder conditions. Furthermore, copper's wide availability and low cost facilitate its utilization on an industrial scale[26]. Several studies have demonstrated that copper on the catalyst surface exists in the forms of Cu^0 and Cu^+. Cu atoms adsorb hydrogen molecules in a dissociative way, while Cu atoms stabilize methoxyl and acyl groups from activated DMO molecules[26–28]. The two species tend to have an optimal ratio of unity, while the ideal loading of Cu on the SiO support is 20%[29].

However, the catalyst's industrial application is restricted by its instability under reaction conditions. Deactivation of the catalyst occurs due to two main factors: sintering of copper particles, which reduces the active surface area, and a valence change in Cu^+ atoms caused by the redox reaction with the reactants, impacting the synergistic effect between Cu^0 and Cu^+[30]. To solve this issue, one can modify the catalyst's properties by incorporating trace amounts of metals that act as promoters. For instance, Zhu et al. [31] synthesized Cu-Ni/SiO_2 catalysts, demonstrating that the addition of Ni to the catalyst stabilized it against copper deactivation caused by Ni-O species formation. The reaction was conducted at a pressure of 3.0 MPa and a temperature ranging between 210-230°C. Instead, He et al.[27] achieved better dispersion of active phase particles and reduced sintering tendency by optimizing the ratio of copper to boron, used as a dopant. Wang et al. [32] developed a Cu/ZrO_2-SiO_2 catalyst to enhance support proprieties, combining the high thermal stability and catalytic properties of ZrO_2 with the high surface area of SiO_2. The catalyst's characterization revealed that ZrO_2 improves copper dispersion and optimizes the Cu^+/Cu^0 ratio. Additionally, electron transfer between Zr and Cu improves copper anchorage on the support and increases the stability and lifetime of the catalyst.

Nevertheless, ethylene glycol (EG) is not the sole product of the catalytic hydrogenation of DMO. The selectivity of the process can be adjusted towards other products, including methyl glycolate or ethanol, by modifying the catalyst and reaction conditions [26].

MG is a valuable organic solvent, playing a crucial role as an intermediate in the synthesis of various fine chemicals due to the presence of both carboxylic and alcoholic groups. Currently, MG is synthesized by catalyzing a coupling reaction between formaldehyde and methyl formate using different acid catalysts. However, this process is challenging to replicate on an industrial scale due to low yields and significant environmental pollution [33,34]. Catalytic hydrogenation of DMO in the gas phase is a synthesis method with the advantage of being cheaper and more eco-friendly. However, the catalyst that facilitates the catalytic hydrogenation of DMO to EG (Cu/SiO_2) is not applicable in this case. This is because the thermodynamic equilibrium constant of MG to EG hydrogenation is two orders of magnitude stronger than that of hydrogenation of DMO to MG, leading poor MG selectivity at high temperatures or low DMO conversion at low temperatures [26]. Nevertheless, the utilization of a catalyst featuring less prominent hydrogenation properties along with milder reaction circumstances enables the incomplete hydrogenation of DMO while concurrently increasing selectivity toward MG. Huang et al. [34] enhanced MG yields in partial hydrogenation of DMO by modifying the Cu/SiO2 catalyst with Na_2SiO_3. The experiments revealed that hydrolysis of Na_2SiO_3 releases SiO_4^- ions capable of integrating into copper phyllosilicates. These silicates not only minimize the quantity of Cu^0 on the catalytic surface, thus reducing the amount of adsorbed H_2, but also increase the percentage of mesopores, promoting quick MG diffusion. The catalyst Cu/SiO_2 containing 0.5 wt of Na_2SiO_3 demonstrated an 83% yield of MG and a 99.8% selectivity towards MG. Additionally, altering the substrate's nature has enhanced the efficiency of multiple copper-based catalysts, including activated carbon[35], reduced graphene oxide[36], hydroxyapatite [37], ZrO_2-SiO_2[32] and MgO[38].

Another compound that can be obtained through catalytic hydrogenation of DMO is ethanol. Varying the catalyst and adjusting the reaction conditions can increase selectivity towards ethanol. This compound is typically produced via the alcoholic

fermentation of agricultural raw materials using microorganisms of the genus Saccharomyces or through the hydration of ethylene on solid acid catalysts. Both methods of synthesis have disadvantages. The former involves a costly and time-consuming biological process, whereas the latter is reliant on oil [39,40]. On the other side for two primary reasons, the DMO hydrogenation pathway presents significant challenges. Firstly, a considerable amount of alcoholic byproducts may be produced simultaneously. Secondly, the catalysts exhibit poor stability at significantly higher temperatures (270-300 °C). In fact, the catalysts utilized for this reaction closely resemble those employed in EG synthesis but typically possess greater surface acidity (e.g., via Al or B doping) and require stricter reduction conditions.

Gong and colleagues [41] demonstrated that manipulating the reaction temperature can augment the selectivity and yield of ethanol using an identical catalyst used for the reduction of DMO to EG (Cu/SiO_2 with 20% wt Cu). EG can be obtained at 473 K and ethanol can be obtained at a temperature above 553 K to achieve superior hydrogenation. The findings indicate that the catalyst remains stable after 200 hours of operation at 553 K with 100% DMO conversion and 80% selectivity towards ethanol production. However, an issue that arises with this catalyst is the loss of silica due to methanol, which diminishes the support's surface area, leading to copper particle agglomeration and lower-quality ethanol production [42]. Ai et al. [43]therefore studied the Cu/B-CNTs catalyst, in which copper is supported on carbon nanotubes doped with boron atoms. The incorporation of boron into the carbon nanotube structure results in defects that enhance the anchoring of copper particles, ultimately leading to better dispersion[44]. Additionally, the boron atoms serve as acidic sites that catalyze dehydration of hydroxyl groups, which increases copper's ability to hydrogenate unsaturated intermediates during the ethanol process[45].

2.2.2 Electrocatalytic hydrogenation

Electrocatalytic hydrogenation is conducted under less drastic temperature and pressure conditions than catalytic hydrogenation, and thus has the advantage of being both cheaper and less polluting due to its limited energy consumption[9]. This process combines a low carbon footprint from renewable energy and recovered CO_2 with strong industrial potential for high-value products and low-cost feed, making it economically viable and environmentally sustainable. Compared to conventional hydrogenation utilizing heterogeneous catalysts, electrocatalytic reduction of OX has the advantages of bypassing a separate H_2 generation step, directly utilizing renewable energy sources, and evading energy losses resulting from pressure operation at high temperatures [46–49].

Among the possible products, glyoxylic acid (GO) and glycolic acid (GC) are of particular interest as high-value compounds with promising market potential. The process is carried out by gaining two electrons from water oxidation at each step (scheme 2.2) while applying a potential equal to or greater than -0.8 V vs. RHE [49–51].

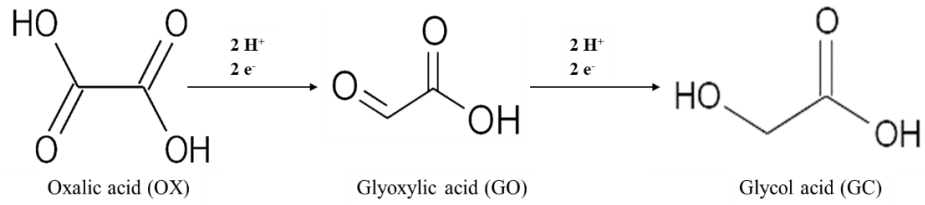

Scheme 2.2 *Simplified reduction scheme of oxalic acid into glyoxylic acid (GO)and glycolic acid (GC)*

The half-reactions occurring at the electrodes, with corresponding potentials, are as follows:

cathode: +0.13 V vs RHE

$(COOH)_2 + 4H^+ + 4\,e^- \rightarrow HOOC\text{-}CH_2OH + H_2O$ (1)

anode: +1.23 V

$2H_2O \rightarrow 4H^+ + 4\,e^- + O_2$ vs RHE (2)

Therefore, the overall reaction is:

$(COOH)_2 + H_2O \rightarrow HOOC\text{-}CH_2OH + O_2$ + 1.1 V vs RHE (3)

The interest in this reaction lies not only in its innovative low-emission process but also in the economic market of products.

GC, the smallest of the α-hydroxy acids, thanks to its carboxylic group and an alcohol function finds extensive use in various industries. Specifically, it is utilized as a whitening and tanning agent in the textile industry, as a flavoring in the food industry, in pharmacology as principal component of skin-care products and as a monomer for the synthesis of polyglycolic acid (PGA), a biodegradable and thermoplastic polymer used as a suture material because it can be obtained in the form of a strong, biocompatible fiber, or poly(lactic-co-glycolic) acid (PLGA), a biodegradable and biocompatible copolymer used within the polymers industry for creating therapeutic devices [46,49,52–54]. Pharmaceuticals, agrochemicals, and other components used in food, personal care, and cosmetics are all produced with glyoxylic acid (GO). The markets for these OX derivates are envisioned to surpass one billion US dollars by 2025. Additionally, the existing market value for GO and GC is approximately 4.000 \$ ton^{-1} and 2.000 \$ ton^{-1}, respectively. This is up to 2-3 times higher than the standard for petrochemical intermediates. They are industrially produced through sophisticated multistep processes. In 1939, DuPont developed a process that uses sulfuric acid as a catalyst to react formaldehyde, water, and an excess of carbon monoxide at 5 atm at temperatures ranging from 140°C to 225°C. Glycolic acid is currently produced either by hydrative carbonylation of formaldehyde under extremely harsh conditions or by chlorination of acetic acid followed by hydrolysis of the resulting chloroacetic acid in the presence of sodium hydroxide. An alternative is to use bio-based feedstocks and catalytic or enzymatic processes. Examples include ethylene glycol-oxidizing microorganisms or enzymatic synthesis by

reacting glyconitrile with a biocatalyst with nitrilase activity, but these methods are still under development at the laboratory scale[55–58]. Because GO is created via selective catalytic oxidation of GC, its commercial value is approximately double that of GC.

The electrocatalytic pathway of OX combines several benefits, including potential cost savings, reduced carbon footprint, process simplification (via step reduction and integration), use of environmentally friendly industrial operations, substitution of fossil fuels as raw materials, and use of renewable energy sources for the process. Previous research on the electrocatalytic reduction of OX utilized a lead cathode, which has serious issues with deactivation and toxic effects on the environment and humans [59–61]. Conversely, alternative TiO_2 cathode materials, which are more sustainable and exhibit greater selectivity to GC or GO, present a viable solution for these challenges[49,50].

Electrocatalytic hydrogenation of organic substrates is typically realized using metal electrodes or metal nanoparticles supported on a conductive substrate. However, there are extremely few examples of effective electrodes based solely on a metal oxide layer. Furthermore, their development is critical both from a physicochemical point of view to elucidate the nature of effective metal-oxide electrocatalysts for selective hydrogenation, and from an application point of view to avoid the inherent risk of metal leaching during the production of monomers for polymerization or other selective hydrogenations (e.g. for food components), which is crucial for industrial progress. Therefore, pure metal oxide electrodes for selective electrocatalytic hydrogenation are an important industrial goal[62,63]. Thus, nanostructured TiO_2 shows potential as a cathode material for OX electrocatalytic reduction. However, the available literature provides limited data and contrasting indications regarding the specific role of titania and the optimal method to improve electrocatalytic performances.

Zhao et al.[50] proposed for the first time the use of TiO_2 as cathodic material for selective OX hydrogenation, using a roughened TiO_2 film electrode generated by

anodic oxidation. They tested the performance of the electrodes in a batch-type undivided electrochemical cell at high voltages (2.9-3.4 V). Despite changes in conditions and electrocatalytic reactor type, they found GO formation rather than GC formation, with a maximum yield of about 57% after 8 h at 3.3 V. When a polished Ti electrode was used instead of a roughened TiO_2 film electrode, the yield decreased significantly. The latter suggests that titania-specific properties most likely govern the electrocatalytic behavior in OX reduction. These results are in contrast with Masaaki et al., who used a porous anatase TiO_2 formed directly on a Ti mesh as the cathode but combined it with an expensive IrO_2-based anode. GC was synthesized with 50% selectivity, while GO was produced in trace amounts. At the optimal applied voltage of 2.4 V, the OX conversion was also low (15%). Furthermore, the catalyst was deactivated within one hour. Conversely De Luca et al. [64] demonstrated that a composite electrode based on graphite-C_3N_4 decorated TiO_2 nanotubes can achieve GC selectivities of up to 76%, while virgin TiO_2 nanotubes are only about 34% selective. The result seems to be related to the change in the electronic structure of TiO_2 caused by the heterojunction with g-C_3N_4[65].

Therefore, while various nanostructures can produce a TiO_2 cathode, a preferred option is a TiO_2 film composed of well-ordered and vertically aligned TiO_2 nanotubes (NTs) is preferred [66–68]. This is due to the numerous advantages NTs offer [69]. In fact, due to its vertical orientation and internal size in the range of 50-100 nm, this nanostructure allows a good access to the inner region of the nanotube. In addition, NTs induce a higher electrical conductivity compared to a thin titania layer of the same thickness. Thus, as a result of the compact TiO_2 and their elevated surface-to-volume ratios, a highly active (accessible) surface (a three-dimensional (3D)-like electrode) can be created. This was confirmed by Farkhondehfal et al. work[69], highlighting better performances of NTs than titania nanoflame structures and nanopowders. Xu et al.[70] remarked the role of high surface area mesoporous TiO_2 to maximize selectivity to GC, while GO is largely produced on low surface area TiO_2. According to Eguchi et al. [71], the most exposed facets of TiO_2

nanoparticles determine the selectivity, while Im et al. [72] showed that the length of the NTs influences the GC selectivity.

Furthermore , TiO_2 NTs have a range of applications in electrochemistry, as well as in various energy-related fields like batteries, dye-sensitized solar cells (DSSCs) [73–76], sustainable hydrogen[77,78] and biodiesel production[79] and waste pollution treatments[80]. As a result, the study presented in chapter 3 may have relevance for all the field of innovative energy materials using titania electrodes.

2.3 TiO_2 synthesis

TiO_2 NTs are intriguing due to their size-dependent characteristics and high surface-to-volume ratios. TiO_2 nanotubes have undergone extensive research with multiple synthesis methods (figure 2.2) including deposition into a nanoporous alumina template, sol–gel, hydrothermal processes and anodic oxidation.

By using tubular-like structures as templates for the construction of tube pillars,

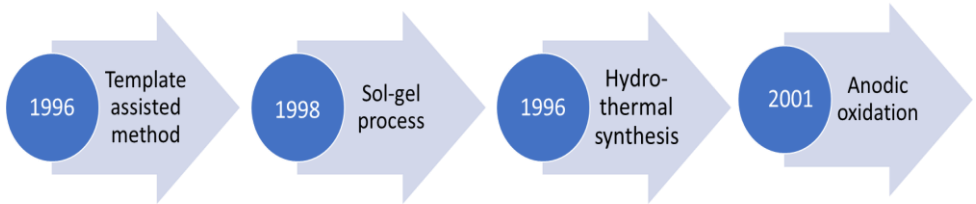

Figure 2.2 *Chronology of the various methods of nanotube synthesis*

titanium dioxide nanotubes are generated in vertically aligned structures on a thin film material using the template-assisted approach, usually anodic aluminum oxide (AAO)[81,82]. However, the process in quite complicated and the tubular structure could be damaged during the synthesis.

Until completion of the TiO_2 nanotube fabrication process, the sol-gel technique is typically utilized together with another procedure, such as the hydrothermal or template-assisted method [83,84].

Conversely, thanks to their simplicity, affordability, and versatility, hydrothermal treatment and electrochemical anodic oxidation are two of the most popular manufacturing techniques.

Hydrothermal synthesis involves combining titanium dioxide powder with a highly concentrated sodium hydroxide solution (10-11 M) and heating the resulting mixture at elevated temperatures (e.g., 100-130°C) for 24 hours in a Teflon-coated stainless-steel autoclave. This widely-used method is valued for its simple setup, excellent reactivity, and utilization of non-toxic reagents[85]. Nonetheless, the thermal synthesis in autoclave necessitates high temperature and pressure, and the prolonged synthesis time is an additional limitation. Furthermore, the nanotubes are randomly arranged and may combine with other nanostructures, such as nanofibers and nanopowders [86].

Of all the methods for producing nanotubes, the anodization process is the most effective technique for developing well-organized TiO_2 nanotube arrays. Although the process requires a solution containing fluoride ions and a more sophisticated setup, it is a simple, effective and very fast synthesis method. The direct contact between the titanium foil and the oxide layer further boosts mechanical stability, and the structural features of the tubes can be readily controlled.

2.3.1 TiO_2 NTs growth mechanism: field assisted dissolution theory (FAD)

The growth of nanotubes takes place through the simultaneous action of (i) Electrochemical oxidation of Ti to TiO_2 (eq. 3) and chemical dissolution of TiO_2 by F ions (eq 4), facilitated by the applied electric field [87] .

$$Ti + 2H_2O \rightarrow TiO_2 + 4H^+ \quad (4)$$

$$TiO_2 + 6F^- + 4H^+ \rightarrow [TiF_6]^{2-} + 2H_2O \quad (5)$$

However, the mechanism by which TiNT synthesis occurs is divided into several steps and can be monitored by recording the anodization curve, which shows how the current (at constant potential) varies over time[88–90] (figure 2.3 a-b).

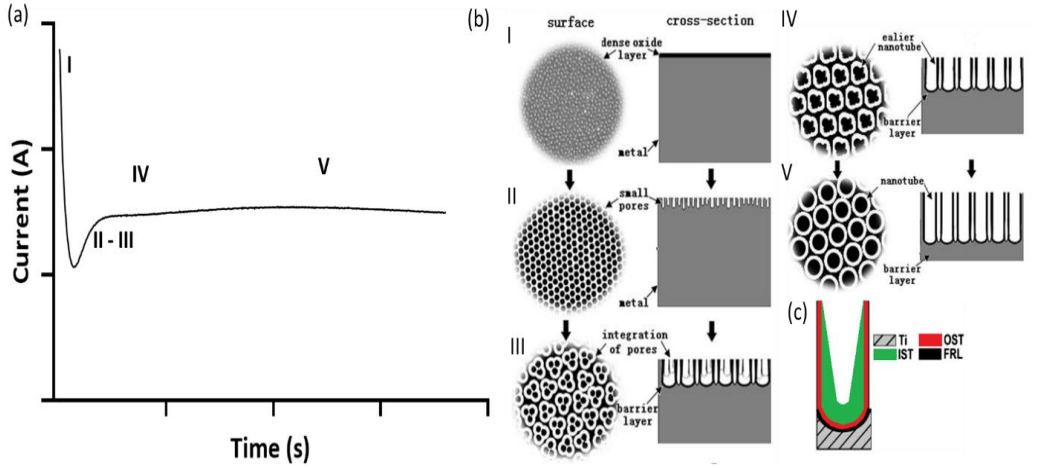

Figure 2.3 *TiNT growth mechanism. Traditional anodization curve (a) and illustration of different steps (b) involved in the mechanism steps and Internal geometry of TiO_2 NTs. Revisited from ref. [91] and [94]*

I. Formation of a dense oxide layer on titanium foils and its effect on pore nucleation: When voltage is applied, the current reading drops abruptly, indicating the development of a non-conductive oxidic layer. The current subsequently declines at a slower pace. Pore nucleation begins as the current rate shifts and continues until the minimum current level (I_{min}) is reached.

II. Pores generation: The newly formed oxide layer undergoes chemical attack by the F^- anion, resulting in the formation of small, closely spaced, and irregularly arranged pores. The dissolution of the oxide is accompanied by an increase in current during this phase. As the oxide layer thins, the electric field strength, TiO_2 dissolution rate, and H^+ ion concentration at the bottom of the pores all increase.

III. Pore evolution: Gradually, the fluorine ions dissolve the walls of the small pores under the influence of the electric field. This process leads to the creation of larger diameter pores and a peak current is recorded (I_{max}).

IV. Nanotubes growth: Because of the imbalance between the oxidation (eq. 4) and dissolution (eq. 5) phases, the measured current gradually drops.

V. Debris formation: nanotubes growth is finished when the rate of two reaction reach equilibrium and current remain constant. However, Due to the irregular accumulation of oxide particles (debris) on the top surface of the organized array of nanotubes, the current may either remain constant or gradually decrease.

The resulting titanium nanotubes exhibit high perpendicular alignment to the surface of the Ti foil, but internal uniformity is lacking. The thickness decreases asymmetrically downwards, forming a V-shape configuration. Figure 2.3 c illustrates the compact outer oxide shell (OST) and inner oxide shell (IST) of each nanotube that contains elements of the electrolyte solution, along with a fluoride ion-enriched layer (FRL) situated at the bottom. The lower layer, which is responsible for the special internal geometry, is caused by the F^- ions diffusing towards the bottom where the electric field strength is highest [91].

Anodic oxidation offers the advantage of regulating the NTs nanostructure through various physical parameters, such as potential, current, electrode distance, electrode shape, time, and chemical parameters, such as electrolyte composition, electrode material, and pH. These variables can modify the nanotubes' length, thickness, and diameter, along with their shape and porosity. To provide a comprehensive description of these parameters is beyond the scope of this paper and various literature reviews on the subject are referenced [90,92–94]. However, some of these parameters are briefly explained below:

- The applied voltage results in an increase in both the diameter and length of the nanotubes. As the potential increases, both oxidation (eq. 4) and dissolution (eq. 5) are enhanced. This results in a thicker oxide layer and an increased rate of TiO_2 dissolution by F^- ions. This leads to an expansion of the pores that were originally formed for the creation of the nanotubes and a deeper excavation of the Ti foil [95–97].

- The diameter of the nanotubes is not significantly impacted by the anodization time. However, as the anodization time increases, the length of the nanotubes increases until the rates of the dissolution reaction equal that of oxidation. Prolonged anodization time may result in debris formation on the surface of the nanotubes [49,98].
- The electrolyte solution has a notable impact on the anodic oxidation process. The reaction can occur in aqueous or nonaqueous solutions, affecting the rate of diffusion of F^- ions by viscosity and consequently, the rate of dissolution (eq. 5). Generally, the length of nanotubes increases as the dissolution rate decreases when using organic electrolytes like glycerol or ethylene glycol [98–100].
- Additionally, the rate of reactions involved in the growth of nanotubes is influenced by the pH of the electrolyte solution. A higher pH promotes oxidation and retards oxide dissolution, consequently extending the time to achieve equilibrium of the two reactions. pH not only impacts the nanotubes' size, with their length enlarging in acidic pH , but also their morphology [92,98]. Ampelli et al. [101] treated two Ti foil with a 15 V charge in a 0.5 wt% HF electrolyte solution - one at pH 4 and one at pH 0. Through FESEM, they observed the formation of nanotubes under pH 0 conditions and ribbon structures under pH 4 conditions.
- The concentration of fluoride ions affects the dissolution process. When the F^- concentration is less than 0.05% wt, the oxidation rate exceeds the dissolution rate resulting in the formation of only a dense oxide layer rather than nanotubes. Conversely, F^- concentrations exceeding 1% wt encourage such a rapid dissolution rate that it impedes nanotube growth. Nanotube synthesis can occur only at intermediate concentrations when the rate of the two reactions is fast enough. However, within this range, longer nanotubes result from increasing the number of fluoride ions [102,103].

- Water is essential for nanotube growth in organic solutions as it promotes the formation of interconnections between nanotube walls. Water facilitates the predominance of chemical dissolution over oxide growth between nanotubes, causing the formation of a fluoride ion-rich layer that creates irregularities on the nanotube walls. However, the appropriate quantity of water for this process depends on the concentration of fluoride ions. For instance, NTs lengthens with increasing water amounts up to 2 v/v% for F^- concentrations of up to 0.03 wt% [104,105].

2.3.2 Rapid breakdown anodization (RBA) TiO_2 NTs growth mechanism

The rapid breakdown anodization (RBA) is typically used to produce nanotubes with a porous structure [93,106]. However, the resulting nanotubes are often damaged, with holes in the walls and partially broken, reducing the applications which are limited to the use of TiNT powders [107–110].

As previously described, modifying the morphology of TiO_2 NTs can be achieved by changing the applied potential. The growth rate of NTs increases with the applied potential [111] due to the higher rate of oxidation and dissolution reactions [101], resulting in longer NTs and greater tube diameters [95,96,101,111]. However, a deviation occurs at high voltages due to the breakdown effect. Rapid breakdown anodization (RBA) occurs due to the incorporation of anion impurities, typically OH^- [112], at the interface of the metal-oxide layer [113–115]. These impurity centers become preferential electron injection sites because they can be ionized, releasing electrons into the oxide conduction band [116]. The electric field induces electron acceleration, producing electron avalanches through an impact ionization mechanism, leading to the formation of holes on the tube walls [112,117]. Additionally, a faster growth rate of NTs is observed during RBA [93,106].

The I vs t curves show that the anodizing total current is the result of two contributions [118,119]: i) ionic current due to the migration of Ti^{4+} and O^{2-}, which

is correlated to the oxide growth in the first stage of anodization. The current decreases until the oxide reaches the critical thickness; ii) The electronic current is correlated to the oxygen release and increases exponentially due to the impurity center's electron multiplication process [116] [134]. This leads to a continuous rise [113,120,121] and fluctuation [116,118,122] of the current in the I vs t curve.

However, the potential for critical breakdown depends on various parameters, including the electrolyte solution's composition, the electrolyte temperature, and the electrode surface condition. Alijani et al. [123] produced NTs through anodization in 22-hour aged electrolytes, which contained ethylene glycol as a solvent, 0.176 M NH_4F, and 1.5 vol% H_2O.The anodization times and applied potential were changed with the aim to investigate the initial breakdown occurrence, observing it at 80 V in 1h or at higher potential in shorter times.
In a study by Yang et al. [120], using ethylene glycol as an electrolyte containing 2% water, it was observed that the critical breakdown voltage decreases as the NH4F concentration increases. Specifically, the breakdown condition was observed at 60 V or 90 V with 0.5% or 0.2% NH_4F, respectively. Albu et al. [105] used ethylene glycol with the addition of 0.1 M NH_4F and 1 M H_2O to obtain NTs. They observed a linear increase in growth rate with the applied potential up to 50 V, but a deviation occurred at higher potentials (>60 V) due to RBA.

The porous morphology of the NTs can be attributed to the release of oxygen during anodization. In their study of the growth of pores in porous anodic alumina (PAA), Garcia-Vergara et al. [124] used a tungsten tracer layer incorporated into the anodic film and proposed a new mechanism based on the viscous flow of oxide film from the oxide barrier layer beneath the porous layer to the wall regions due to the plasticity of the alumina. Zhu et al. [125] discussed the formation processes of PAA, suggesting that the nanopores are formed due to the evolution of oxygen inside the oxide.

The evolution of oxygen at the anode is a side reaction:

$$2H_2O \rightarrow O_2 + 4H^+ + 4e^- \quad (6)$$

Oxygen evolution is generally more significant in aqueous media, nevertheless it has also been observed in organic media containing relatively small amounts of water. The process during RBA that leads to porous TiO_2 NTs is called oxygen bubble theory and it can be summarized into following steps (figure 2.4):

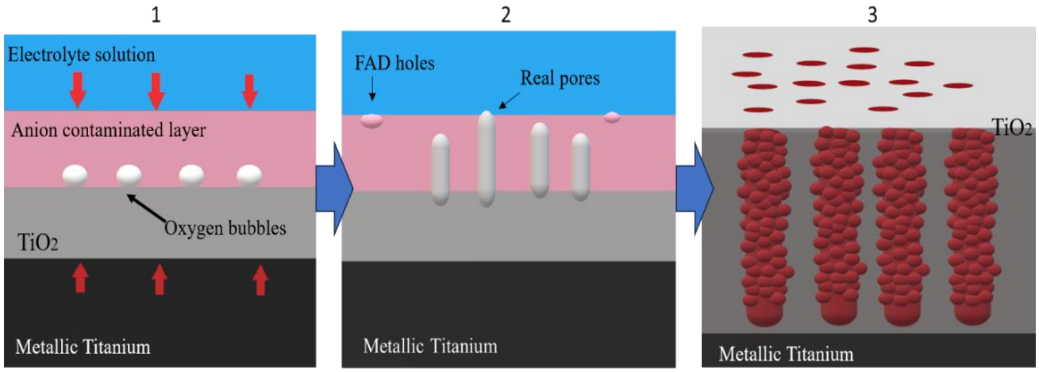

Figure 2.4 *Mechanism of Rapid breakdown anodization and oxygen bubble mold effect*

1. Formation of a dense oxide layer: when a potential is applied to Ti foils, a dense layer of non-conducting oxide and anion-contaminated layer is formed, resulting in a sudden decrease of the measured current due to the growth of a compact non-conductive oxide layer. During this phase, the main contribution to the current is the ionic current, which decreases as the oxide layer grows to a minimum value corresponding to a critical oxide thickness. The maximum oxide thickness generally increases with the applied potential. The TiO_2 layer forms rapidly at both the Electrolyte-Oxide (E-O) and Oxide-Metal (O-M) interfaces. This is in contrast to the FAD theory, which states that the oxide only grows at the oxide-metal interface. The oxide layer at the E-O interface is inevitably contaminated by anion impurities from the electrolyte, resulting in an anion-contaminated layer. When the oxide reaches its critical thickness, the electronic current begins to rise due to the discharge

of anionic electrons, and oxygen bubbles start to rise to the contaminated oxide-anion layer.

2. Rupture of the oxide layer and pore formation: the formation of pores is caused by the rupture of the oxide layer due to the accumulation of oxygen bubbles below the anion-contaminated layer. This results in hemispherical bottoms and protrusions on the top compact layer due to the plasticity of the oxide. Once the oxygen pressure reaches a certain value, the oxide layer breaks down and pores are formed, allowing the electrolyte to enter.
3. Nanotube growth: during the process of nanotube growth, a new oxide is formed at the base of the pores. However, the critical oxide thickness at the pore bottom remains unchanged. As a result, the newly formed oxide moves upward but flows around the bubbles due to the plasticity of the TiO_2, which acts as a mold. This phenomenon is known as the oxygen bubble mold effect [126,127]. TiO_2 NTs are formed with ribbed walls and cavities (as observed in a PAA-like morphology) instead of smooth walls, as indicated by references [94] and [127]. Due to the continuous increase in current for RBA [121], it is not possible to determine a maximum current value.

2.3.2 TiO_2 NTs crystalline phases

The efficiency and selectivity of the electrocatalytic process depend on the crystalline phase of TiO_2, which is altered by the temperature at which calcination takes place.

Up to around 500°C, the main crystalline phase is anatase, which has a tetragonal crystalline system. In this system, the titanium atom is located at the vertices and center of the tetragonal cell and is coordinated in an octahedral manner by oxygen atoms (figure 2.5). There are four oxygen atoms on the diagonals of the bases and two at the vertices, although the bond angles are considerably greater than 90°.

Between 550°C and 800°C, the most stable crystalline phase is rutile. Rutile is characterized by a tetragonal crystalline system, in which the titanium atom is coordinated in an octahedral way by oxygen atoms. The bond angles are less

distorted, but the impact of the oxygen atoms is still of a compact hexagonal type, even if distorted[128].

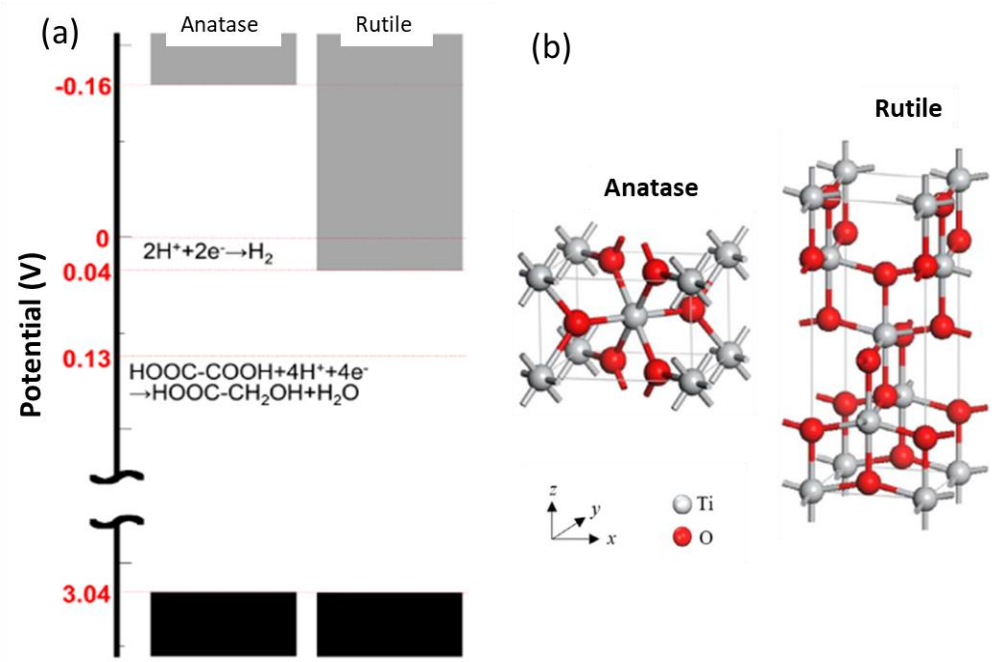

Figure 2. 5 *(a) Energy diagrams of the conduction band (grey) and valence band (black) for TiO_2-anatase and TiO_2-rutile. (b) Crystal structure of anatase and rutile. Based on ref. [110] and [111]*

The anatase phase exhibits better catalytic performance than rutile, including higher OX conversion, better selectivity, yield, and Faradic efficiency at GC. The difference in energy gap between the conduction band and the valence band of the two crystalline phases is the reason for this. Specifically, the conduction band of anatase is located approximately 0.2 V higher than that of rutile. The anatase conduction band allows for electrons to be placed at a higher potential than the reduction of H_2, unlike rutile. This is because the conduction band in rutile is placed at a potential only slightly lower than that for H_2 reduction, making the reaction difficult [129,130].

Bibliography

1. Centi, G.; Perathoner, S. Catalysis for an Electrified Chemical Production. *Catal. Today* **2022**, doi:10.1016/j.cattod.2022.10.017.

2. Qiao, J.; Liu, Y.; Hong, F.; Zhang, J. *A Review of Catalysts for the Electroreduction of Carbon Dioxide to Produce Low-Carbon Fuels*; 2014; Vol. 43; ISBN 8190600893.

3. Ye, W.; Guo, X.; Ma, T. A Review on Electrochemical Synthesized Copper-Based Catalysts for Electrochemical Reduction of CO2 to C2+ Products. *Chem. Eng. J.* **2021**, *414*, 128825, doi:10.1016/j.cej.2021.128825.

4. Noël, T.; Cao, Y.; Laudadio, G. The Fundamentals behind the Use of Flow Reactors in Electrochemistry. *Acc. Chem. Res.* **2019**, *52*, 2858–2869, doi:10.1021/acs.accounts.9b00412.

5. Wang, X.; Tang, Y.; Lee, J.M.; Fu, G. Recent Advances in Rare-Earth-Based Materials for Electrocatalysis. *Chem Catal.* **2022**, *2*, 967–1008, doi:10.1016/j.checat.2022.02.007.

6. Li, C.; Wang, P.; He, M.; Yuan, X.; Fang, Z.; Li, Z. Rare Earth-Based Nanomaterials in Electrocatalysis. *Coord. Chem. Rev.* **2023**, *489*, 215204, doi:10.1016/j.ccr.2023.215204.

7. Mustafa, A.; Lougou, B.G.; Shuai, Y.; Wang, Z.; Tan, H. Current Technology Development for CO2 Utilization into Solar Fuels and Chemicals: A Review. *J. Energy Chem.* **2020**, *49*, 96–123, doi:10.1016/j.jechem.2020.01.023.

8. Lanzafame, P.; Abate, S.; Ampelli, C.; Genovese, C.; Passalacqua, R.; Centi, G.; Perathoner, S. Beyond Solar Fuels: Renewable Energy-Driven Chemistry. *ChemSusChem* **2017**, *10*, 4409–4419, doi:10.1002/cssc.201701507.

9. Perathoner, S.; Centi, G. Catalysis for Solar-Driven Chemistry: The Role of Electrocatalysis. *Catal. Today* **2019**, 157–170, doi:10.1016/j.cattod.2018.03.005.

10. Papanikolaou, G.; Chillè, D.; Abate, S.; Perathoner, S.; Centi, G.; Giorgianni, G.; Cozza, D.; Dalena, F.; Migliori, M.; Giordano, G.; et al. Zeolite Templated Carbon from Beta Replica as Metal-Free Electrocatalyst for CO2 Reduction. *Appl. Mater. Today* **2022**, *26*, 101383, doi:10.1016/j.apmt.2022.101383.

11. Boutin, E.; Robert, M. Molecular Electrochemical Reduction of CO2 beyond Two Electrons. *Trends Chem.* **2021**, *3*, 359–372, doi:10.1016/j.trechm.2021.02.003.

12. Chen, Y.; Kang, Y.; Zhao, Y.; Wang, L.; Liu, J.; Li, Y.; Liang, Z.; He, X.; Li, X.; Tavajohi, N.; et al. A Review of Lithium-Ion Battery Safety Concerns: The Issues, Strategies, and Testing Standards. *J. Energy Chem.* **2021**, *59*, 83–99, doi:10.1016/j.jechem.2020.10.017.

13. Fan, L.; Xia, C.; Yang, F.; Wang, J.; Wang, H.; Lu, Y. Strategies in Catalysts and Electrolyzer Design for Electrochemical CO2 Reduction toward C2+ Products. *Sci. Adv.* **2020**, *6*, 1–18, doi:10.1126/sciadv.aay3111.

14. Yang, Y.; Wang, X.; Wang, M.; Wang, H.; Xian, P. Recovery of Iron from Red Mud by Selective Leach with Oxalic Acid. *Hydrometallurgy* **2015**, *157*, 239–245, doi:10.1016/j.hydromet.2015.08.021.

15. Breunig, H.M.; Rosner, F.; Lim, T.H.; Peng, P. Emerging Concepts in Intermediate Carbon Dioxide Emplacement to Support Carbon Dioxide Removal. *Energy Environ. Sci.* **2023**, 1821–1837, doi:10.1039/d2ee03623a.

16. Takeda, Y.; Tamura, M.; Nakagawa, Y.; Okumura, K.; Tomishige, K. Hydrogenation of Dicarboxylic Acids to Diols over Re-Pd Catalysts. *Catal. Sci. Technol.* **2016**, *6*, 5668–5683, doi:10.1039/c6cy00335d.

17. Santos, J.H.S.; Gomes, J.T.S.; Benachour, M.; Medeiros, E.B.M.; Abreu, C.A.M.; Lima-Filho, N.M. Selective Hydrogenation of Oxalic Acid to Glycolic Acid and Ethylene Glycol with a Ruthenium Catalyst. *React. Kinet. Mech. Catal.* **2020**, *131*, 139–151, doi:10.1007/s11144-020-01843-3.

18. Grømer, B.; Yoshioka, S.; Saito, S. Selective Reduction of Carboxylic Acids to Alcohols in the Presence of Alcohols by a Dual Bulky Transition-Metal Complex/Lewis Acid Catalyst. *ACS Catal.* **2022**, *12*, 1957–1964, doi:10.1021/acscatal.1c04392.

19. Yue, H.; Zhao, Y.; Ma, X.; Gong, J. Ethylene Glycol: Properties, Synthesis, and Applications. *Chem. Soc. Rev.* **2012**, *41*, 4218–4244, doi:10.1039/c2cs15359a.

20. Cui, G.; Meng, X.; Zhang, X.; Wang, W.; Xu, S.; Ye, Y.; Tang, K.; Wang, W.; Zhu, J.; Wei, M.; et al. Low-Temperature Hydrogenation of Dimethyl Oxalate to Ethylene Glycol via Ternary Synergistic Catalysis of Cu and Acid−base Sites. *Appl. Catal. B Environ.* **2019**, *248*, 394–404, doi:10.1016/j.apcatb.2019.02.042.

21. Huang, Y.; Ariga, H.; Zheng, X.; Duan, X.; Takakusagi, S.; Asakura, K.; Yuan, Y. Silver-Modulated SiO2-Supported Copper Catalysts for Selective Hydrogenation of Dimethyl Oxalate to Ethylene Glycol. *J. Catal.* **2013**, *307*, 74–83, doi:10.1016/j.jcat.2013.07.006.

22. Matteoli, U.; Menchi, G.; Bianchi, M.; Piacenti, F. Selective Reduction of Dimethyl Oxalate by Ruthenium Carbonyl Carboxylates in Homogeneous Phase Part IV1 1 For Part III See [11]. *J. Mol. Catal.* **1991**, *64*, 257–267, doi:10.1016/0304-5102(91)85135-O.

23. Teunissen, H.T.; Elsevier, C.J. Ruthenium Catalysed Hydrogenation of Dimethyl Oxalate to Ethylene Glycol. *Chem. Commun.* **1997**, 667–668, doi:10.1039/a700862g.

24. Boardman, B.; Hanton, M.J.; Van Rensburg, H.; Tooze, R.P. A Tripodal Sulfur Ligand for the Selective Ruthenium-Catalysed Hydrogenation of Dimethyl Oxalate. *Chem. Commun.* **2006**, *44*, 2289–2291, doi:10.1039/b601216g.

25. Giorgianni, G.; Mebrahtu, C.; Perathoner, S.; Centi, G.; Abate, S. Hydrogenation of Dimethyl Oxalate to Ethylene Glycol on Cu/SiO2 Catalysts Prepared by a Deposition-Decomposition Method: Optimization of the Operating Conditions and Pre-Reduction Procedure. *Catal. Today* **2022**, *390–391*, 343–353, doi:10.1016/j.cattod.2021.08.032.

26. Ye, R.P.; Lin, L.; Wang, L.C.; Ding, D.; Zhou, Z.; Pan, P.; Xu, Z.; Liu, J.; Adidharma, H.; Radosz, M.; et al. Perspectives on the Active Sites and Catalyst Design for the Hydrogenation of Dimethyl Oxalate. *ACS Catal.* **2020**, *10*, 4465–4490, doi:10.1021/acscatal.9b05477.

27. He, Z.; Lin, H.; He, P.; Yuan, Y. Effect of Boric Oxide Doping on the Stability and Activity of a Cu-SiO 2 Catalyst for Vapor-Phase Hydrogenation of Dimethyl Oxalate to Ethylene Glycol. *J. Catal.* **2011**, *277*, 54–63, doi:10.1016/j.jcat.2010.10.010.

28. Yu, X.; Vest, T.A.; Gleason-Boure, N.; Karakalos, S.G.; Tate, G.L.; Burkholder, M.; Monnier, J.R.; Williams, C.T. Enhanced Hydrogenation of Dimethyl Oxalate to Ethylene Glycol over Indium Promoted Cu/SiO2. *J. Catal.* **2019**, 1–8, doi:10.1016/j.jcat.2019.10.001.

29. Li, F.; Lu, C.S.; Li, X.N. The Effect of the Amount of Ammonia on the Cu0/Cu+ Ratio of Cu/SiO2 Catalyst for the Hydrogenation of Dimethyl Oxalate to Ethylene Glycol. *Chinese Chem. Lett.* **2014**, *25*, 1461–1465, doi:10.1016/j.cclet.2014.05.050.

30. Ye, R.P.; Lin, L.; Li, Q.; Zhou, Z.; Wang, T.; Russell, C.K.; Adidharma, H.; Xu, Z.; Yao, Y.G.; Fan, M. Recent Progress in Improving the Stability of Copper-Based Catalysts for Hydrogenation of Carbon-Oxygen Bonds. *Catal. Sci. Technol.* **2018**, *8*, 3428–3449, doi:10.1039/c8cy00608c.

31. Zhu, J.; Ye, Y.; Tang, Y.; Chen, L.; Tang, K. Efficient Hydrogenation of Dimethyl Oxalate to Ethylene Glycol: Via Nickel Stabilized Copper Catalysts. *RSC Adv.* **2016**, *6*, 111415–111420, doi:10.1039/c6ra23474g.

32. Wang, D.; Zhang, C.C.; Zhu, M.; Yu, F.; Dai, B. Highly Active and Stable ZrO2-SiO2-Supported Cu–Catalysts for the Hydrogenation of Dimethyl Oxalate to Methyl Glycolate. *ChemistrySelect* **2017**, *2*, 4823–4829, doi:10.1002/slct.201700895.

33. Sun, Y.; Wang, H.; Shen, J.; Liu, H.; Liu, Z. Highly Effective Synthesis of Methyl Glycolate with Heteropolyacids as Catalysts. *Catal. Commun.* **2009**, *10*, 678–681, doi:10.1016/j.catcom.2008.11.015.

34. Huang, H.; Wang, B.; Wang, Y.; Zhao, Y.; Wang, S.; Ma, X. Partial Hydrogenation of Dimethyl Oxalate on Cu/SiO2 Catalyst Modified by Sodium Silicate. *Catal. Today* **2019**, 2–7, doi:10.1016/j.cattod.2019.08.048.

35. Niu, J.; Ai, P.; Guo, Q.; Jin, H.; Gao, Z.; Huang, W. The Effect of Nitrogen Doping on Hydrogenation Capability and Stability of Cu-Based Catalyst in Ester Hydrogenation to Methyl Glycolate. *Fuel* **2023**, *351*, 128866, doi:10.1016/j.fuel.2023.128866.

36. Abbas, M.; Chen, Z.; Chen, J. Shape- and Size-Controlled Synthesis of Cu Nanoparticles Wrapped on RGO Nanosheet Catalyst and Their Outstanding Stability and Catalytic Performance in the Hydrogenation Reaction of Dimethyl Oxalate. *J. Mater. Chem. A* **2018**, *6*, 19133–19142, doi:10.1039/c8ta07371f.

37. Wen, C.; Cui, Y.; Chen, X.; Zong, B.; Dai, W.L. Reaction Temperature Controlled Selective Hydrogenation of Dimethyl Oxalate to Methyl Glycolate and Ethylene Glycol over Copper-Hydroxyapatite Catalysts. *Appl. Catal. B Environ.* **2015**, *162*, 483–493, doi:10.1016/j.apcatb.2014.07.023.

38. Abbas, M.; Zhang, J.; Chen, Z.; Chen, J. Sonochemical Synthesis of Zn-Promoted Porous MgO-Supported Lamellar Cu Catalysts for Selective Hydrogenation of Dimethyl Oxalate to Ethanol and Their Long-Term Stability. *New J. Chem.* **2018**, *42*, 17553–17562, doi:10.1039/C8NJ03766C.

39. Maiti, U.N.; Lee, W.J.; Lee, J.M.; Oh, Y.; Kim, J.Y.; Kim, J.E.; Shim, J.; Han, T.H.; Kim, S.O. Chemically Modified/Doped Carbon Nanotubes & Graphene for Optimized Nanostructures & Nanodevices. *Adv. Mater.* **2014**, *26*, 40–67, doi:10.1002/adma.201303265.

40. Zhang, Y.; Zhang, J.; Su, D.S. Substitutional Doping of Carbon Nanotubes with Heteroatoms and Their Chemical Applications. *ChemSusChem* **2014**, *7*, 1240–

1250, doi:10.1002/cssc.201301166.

41. Gong, J.; Yue, H.; Zhao, Y.; Zhao, S.; Zhao, L.; Lv, J.; Wang, S.; Ma, X. Synthesis of Ethanol via Syngas on Cu/SiO 2 Catalysts with Balanced Cu 0-Cu + Sites. *J. Am. Chem. Soc.* **2012**, *134*, 13922–13925, doi:10.1021/ja3034153.

42. Wen, C.; Cui, Y.; Dai, W.L.; Xie, S.; Fan, K. Solvent Feedstock Effect: The Insights into the Deactivation Mechanism of Cu/SiO2catalysts for Hydrogenation of Dimethyl Oxalate to Ethylene Glycol. *Chem. Commun.* **2013**, *49*, 5195–5197, doi:10.1039/c3cc40570b.

43. Ai, P.; Tan, M.; Yamane, N.; Liu, G.; Fan, R.; Yang, G.; Yoneyama, Y.; Yang, R.; Tsubaki, N. Synergistic Effect of a Boron-Doped Carbon-Nanotube-Supported Cu Catalyst for Selective Hydrogenation of Dimethyl Oxalate to Ethanol. *Chem. - A Eur. J.* **2017**, *23*, 8252–8261, doi:10.1002/chem.201700821.

44. Yue, B.; Ma, Y.; Tao, H.; Yu, L.; Jian, G.; Wang, X.; Wang, X.; Lu, Y.; Hu, Z. CNx Nanotubes as Catalyst Support to Immobilize Platinum Nanoparticles for Methanol Oxidation. *J. Mater. Chem.* **2008**, *18*, 1747–1750, doi:10.1039/b718283j.

45. Zhu, Y.; Zhu, Y.; Kong, X.; Li, X.; Ding, G.; Li, Y.W. Cu Nanoparticles Inlaid Mesoporous Al2O3 as a High-Performance Bifunctional Catalyst for Ethanol Synthesis via Dimethyl Oxalate Hydrogenation. *ACS Catal.* **2014**, *4*, 3612–3620, doi:10.1021/cs5009283.

46. Murcia Valderrama, M.A.; van Putten, R.J.; Gruter, G.J.M. The Potential of Oxalic – and Glycolic Acid Based Polyesters (Review). Towards CO2 as a Feedstock (Carbon Capture and Utilization – CCU). *Eur. Polym. J.* **2019**, *119*, 445–468, doi:10.1016/j.eurpolymj.2019.07.036.

47. Centi, G.; Iaquaniello, G.; Perathoner, S. Role of Chemical Engineering in Renewable Energy. **2019**, 1–16.

48. Ganesh, I. Electrochemical Conversion of Carbon Dioxide into Renewable Fuel Chemicals - The Role of Nanomaterials and the Commercialization. *Renew. Sustain. Energy Rev.* **2016**, *59*, 1269–1297, doi:10.1016/j.rser.2016.01.026.

49. Abramo, F.P.; De Luca, F.; Passalacqua, R.; Centi, G.; Giorgianni, G.; Perathoner, S.; Abate, S. Electrocatalytic Production of Glycolic Acid via Oxalic Acid Reduction on Titania Debris Supported on a TiO2 Nanotube Array. *J. Energy Chem.* **2021**, *16*, doi:10.1016/j.jechem.2021.12.034.

50. Zhao, F.; Yan, F.; Qian, Y.; Xu, Y.; Ma, C. Roughened TiO2 Film Electrodes for Electrocatalytic Reduction of Oxalic Acid to Glyoxylic Acid. *J. Electroanal.*

Chem. **2013**, *698*, 31–38, doi:10.1016/j.jelechem.2013.03.014.

51. Fukushima, T.; Kitano, S.; Hata, S.; Yamauchi, M. Carbon-Neutral Energy Cycles Using Alcohols. *Sci. Technol. Adv. Mater.* **2018**, *19*, 142–152, doi:10.1080/14686996.2018.1426340.

52. Schmitt, E.E.; Rocco Albert Polistina SURGICAL DRESSINGS OF ABSORBABLE POLYMERS United States Patent PATENTED APR 29975 1973.

53. Lanao, R.P.F.; Jonker, A.M.; Wolke, J.G.C.; Jansen, J.A.; Van Hest, J.C.M.; Leeuwenburgh, S.C.G. Physicochemical Properties and Applications of Poly(Lactic-Co-Glycolic Acid) for Use in Bone Regeneration. *Tissue Eng. - Part B Rev.* **2013**, *19*, 380–390, doi:10.1089/ten.teb.2012.0443.

54. Yamamoto, Y.; Uede, K.; Yonei, N.; Kishioka, A.; Ohtani, T.; Furukawa, F. Effects of Alpha-Hydroxy Acids on the Human Skin of Japanese Subjects: The Rationale for Chemical Peeling. *J. Dermatol.* **2006**, *33*, 16–22, doi:10.1111/j.1346-8138.2006.00003.x.

55. Iglesias, J.; Martínez-Salazar, I.; Maireles-Torres, P.; Martin Alonso, D.; Mariscal, R.; López Granados, M. Advances in Catalytic Routes for the Production of Carboxylic Acids from Biomass: A Step Forward for Sustainable Polymers. *Chem. Soc. Rev.* **2020**, *49*, 5704–5771, doi:10.1039/d0cs00177e.

56. DiCosimo, R.; Payne, M.S.; Panova, A.; Thompson, J.; O'Keefe, D.P. *Enzymatic Production of Glycolic Acid*; 2007; Vol. Doctoral; ISBN 1539915409.

57. Kataoka, M.; Sasaki, M.; Hidalgo, A.R.G.D.; Nakano, M.; Shimizu, S. Glycolic Acid Production Using Ethylene Glycol-Oxidizing Microorganisms. *Biosci. Biotechnol. Biochem.* **2001**, *65*, 2265–2270, doi:10.1271/bbb.65.2265.

58. He, Y.C.; Xu, J.H.; Su, J.H.; Zhou, L. Bioproduction of Glycolic Acid from Glycolonitrile with a New Bacterial Isolate of Alcaligenes Sp. ECU0401. *Appl. Biochem. Biotechnol.* **2010**, *160*, 1428–1440, doi:10.1007/s12010-009-8607-y.

59. Ochoa, J.R.; De Diego, A.; Santa-Olalla, J. Electrosynthesis of Glyoxylic Acid Using a Continuously Electrogenerated Lead Cathode. *J. Appl. Electrochem.* **1993**, *23*, 905–909, doi:10.1007/BF00251025.

60. Zhou, Y.L.; Zhang, X.S.; Dai, Y.C.; Yuan, W.K. Studies on Chemical Activators for Electrode I: Electrochemical Activation of Deactivating Cathode for Oxalic Acid Reduction. *Chem. Eng. Sci.* **2003**, *58*, 1021–1027, doi:10.1016/S0009-2509(02)00643-7.

61. Li, J.; Hu, X.; Su, Y.; Li, Q. Modeling of a Packed-Bed Electrochemical Reactor for Producing Glyoxylic Acid from Oxalic Acid. *Chem. Eng. Sci.* **2007**, *62*, 6784–6793, doi:10.1016/j.ces.2007.02.021.

62. Centi, G.; Perathoner, S. Status and Gaps toward Fossil-Free Sustainable Chemical Production. *Green Chem.* **2022**, *24*, 7305–7331, doi:10.1039/d2gc01572b.

63. Papanikolaou, G.; Centi, G.; Perathoner, S.; Lanzafame, P. Catalysis for E-Chemistry: Need and Gaps for a Future De-Fossilized Chemical Production, with Focus on the Role of Complex (Direct) Syntheses by Electrocatalysis. *ACS Catal.* **2022**, *12*, 2861–2876, doi:10.1021/acscatal.2c00099.

64. de Luca, F.; Passalacqua, R.; Abramo, F.P.; Perathoner, S.; Centi, G.; Abate, S. G-C3N4 Decorated TiO2 Nanotube Ordered Thin Films as Cathodic Electrodes for the Selective Reduction of Oxalic Acid. *Chem. Eng. Trans.* **2021**, *84*, 37–42, doi:10.3303/CET2184007.

65. Passalacqua, R.; Abate, S.; De Luca, F.; Perathoner, S.; Centi, G. Graphitic Layered Structures Enhancing TiNT Catalyst Photo-Electrochemical Behaviour. *Coatings* **2023**, *13*, 1–18, doi:10.3390/coatings13020358.

66. Nie, X.; Yin, S.; Duan, W.; Zhao, Z.; Li, L.; Zhang, Z. Recent Progress in Anodic Oxidation of TiO2 Nanotubes and Enhanced 2 Photocatalytic Performance: A Short Review. *Nano* **2021**, 1–43.

67. Passalacqua, R.; Perathoner, S.; Centi, G. Use of Modified Anodization Procedures to Prepare Advanced TiO2 Nanostructured Catalytic Electrodes and Thin Film Materials. *Catal. Today* **2015**, *251*, 121–131, doi:10.1016/j.cattod.2014.11.003.

68. Centi, G.; Perathoner, S. The Role of Nanostructure in Improving the Performance of Electrodes for Energy Storage and Conversion. *Eur. J. Inorg. Chem.* **2009**, 3851–3878, doi:10.1002/ejic.200900275.

69. Farkhondehfal, M.A.; Savino, U.; Chiodoni, A.; Pirri, C.F.; Sacco, A. Electrocatalytic Reduction of Oxalic Acid Using Different Nanostructures of Titanium Oxide. *Electrocatalysis* **2023**, *14*, 195–201, doi:10.1007/s12678-022-00786-8.

70. Xu, W.; Cheng, Y.; Hou, J.; Kang, P. Selective Electroreduction of Oxalic Acid to Glycolic Acid by Mesoporous TiO2 Spheres. *ChemCatChem* **2023**, *15*, 1–7, doi:10.1002/cctc.202201687.

71. Eguchi, H.; Kato, K.; Juhasz, G.; Yamauchi, M. Selectivity Enhancement in the Electrochemical Reduction of Oxalic Acid over Titanium Dioxide Nanoparticles

Achieved by Shape and Energy-State Control. *Catal. Sci. Technol.* **2021**, *11*, 7592–7597, doi:10.1039/d1cy01239h.

72. Im, S.; Saad, S.; Park, Y. Facilitated Series Electrochemical Hydrogenation of Oxalic Acid to Glycolic Acid Using TiO2 Nanotubes. *Electrochem. commun.* **2022**, *135*, 107204, doi:10.1016/j.elecom.2022.107204.

73. Humayun, M.; Raziq, F.; Khan, A.; Luo, W. Modification Strategies of TiO2 for Potential Applications in Photocatalysis: A Critical Review. *Green Chem. Lett. Rev.* **2018**, *11*, 86–102, doi:10.1080/17518253.2018.1440324.

74. Sun, W. Review of the Application of TiO2 in the Field of Photoelectric Catalysis. *IOP Conf. Ser. Earth Environ. Sci.* **2020**, *440*, doi:10.1088/1755-1315/440/2/022032.

75. Yi, Z.; Zeng, Y.; Wu, H.; Chen, X.; Fan, Y.; Yang, H.; Tang, Y.; Yi, Y.; Wang, J.; Wu, P. Synthesis, Surface Properties, Crystal Structure and Dye-Sensitized Solar Cell Performance of TiO2 Nanotube Arrays Anodized under Different Parameters. *Results Phys.* **2019**, *15*, 102609, doi:10.1016/j.rinp.2019.102609.

76. Hou, X.; Aitola, K.; Lund, P. TiO2 Nanotubes for Dye-Sensitized Solar Cells—A Review. *Energy Sci. Enginering* **2020**.

77. Ge, M.; Cai, J.; Iocozzia, J.; Cao, C.; Huang, J.; Zhang, X.; Shen, J.; Wang, S.; Zhang, S.; Zhang, K.Q.; et al. A Review of TiO2 Nanostructured Catalysts for Sustainable H2 Generation. *Int. J. Hydrogen Energy* **2017**, *42*, 8418–8449, doi:10.1016/j.ijhydene.2016.12.052.

78. Abdullah, M.; Kamarudin, S.K. Titanium Dioxide Nanotubes (TNT) in Energy and Environmental Applications: An Overview. *Renew. Sustain. Energy Rev.* **2017**, *76*, 212–225, doi:10.1016/j.rser.2017.01.057.

79. Qamar, O.A.; Jamil, F.; Hussain, M.; Bae, S.; Inayat, A.; Shah, N.S.; Waris, A.; Akhter, P.; Kwon, E.E.; Park, Y.K. Advances in Synthesis of TiO2 Nanoparticles and Their Application to Biodiesel Production: A Review. *Chem. Eng. J.* **2023**, *460*, 141734, doi:10.1016/j.cej.2023.141734.

80. Li, R.; Li, T.; Zhou, Q. *Impact of Titanium Dioxide (TiO2) Modification on Its Application to Pollution Treatment—a Review*; 2020; Vol. 10; ISBN 2223501117.

81. Lee, J.; Kim, D.H.; Hong, S.H.; Jho, J.Y. A Hydrogen Gas Sensor Employing Vertically Aligned TiO2 Nanotube Arrays Prepared by Template-Assisted Method. *Sensors Actuators, B Chem.* **2011**, *160*, 1494–1498, doi:10.1016/j.snb.2011.08.001.

82. Chon Chen, C.; Cheng, C.H.; Lin, C.K. Template Assisted Fabrication of TiO2 and WO3 Nanotubes. *Ceram. Int.* **2013**, *39*, 6631–6636, doi:10.1016/j.ceramint.2013.01.100.

83. Liu, Z.; Liu, C.; Ya, J.; Lei, E. Controlled Synthesis of ZnO and TiO2 Nanotubes by Chemical Method and Their Application in Dye-Sensitized Solar Cells. *Renew. Energy* **2011**, *36*, 1177–1181, doi:10.1016/j.renene.2010.09.019.

84. Pang, Y.L.; Bhatia, S.; Abdullah, A.Z. Process Behavior of TiO2 Nanotube-Enhanced Sonocatalytic Degradation of Rhodamine B in Aqueous Solution. *Sep. Purif. Technol.* **2011**, *77*, 331–338, doi:10.1016/j.seppur.2010.12.023.

85. Ou, H.H.; Lo, S.L. Review of Titania Nanotubes Synthesized via the Hydrothermal Treatment: Fabrication, Modification, and Application. *Sep. Purif. Technol.* **2007**, *58*, 179–191, doi:10.1016/j.seppur.2007.07.017.

86. Moazeni, M.; Hajipour, H.; Askari, M.; Nusheh, M. Hydrothermal Synthesis and Characterization of Titanium Dioxide Nanotubes as Novel Lithium Adsorbents. *Mater. Res. Bull.* **2015**, *61*, 70–75, doi:10.1016/j.materresbull.2014.09.069.

87. Centi, G.; Passalacqua, R.; Perathoner, S.; Su, D.S.; Weinberg, G.; Schlögl, R. Oxide Thin Films Based on Ordered Arrays of 1D Nanostructure. A Possible Approach toward Bridging Material Gap in Catalysis. *Phys. Chem. Chem. Phys.* **2007**, *9*, 4930–4938, doi:10.1039/b703326p.

88. Bai, J.; Zhou, B.; Li, L.; Liu, Y.; Zheng, Q.; Shao, J.; Zhu, X.; Cai, W.; Liao, J.; Zou, L. The Formation Mechanism of Titania Nanotube Arrays in Hydrofluoric Acid Electrolyte. *J. Mater. Sci.* **2008**, *43*, 1880–1884, doi:10.1007/s10853-007-2418-8.

89. Apolinário, A.; Quitério, P.; Sousa, C.T.; Ventura, J.; Sousa, J.B.; Andrade, L.; Mendes, A.M.; Araújo, J.P. Modeling the Growth Kinetics of Anodic TiO2 Nanotubes. *J. Phys. Chem. Lett.* **2015**, *6*, 845–851, doi:10.1021/jz502380b.

90. Roy, P.; Berger, S.; Schmuki, P. TiO2 Nanotubes: Synthesis and Applications. *Angew. Chemie - Int. Ed.* **2011**, *50*, 2904–2939, doi:10.1002/anie.201001374.

91. Albu, S.P.; Ghicov, A.; Aldabergenova, S.; Drechsel, P.; LeClere, D.; Thompson, G.E.; Macak, J.M.; Schmuki, P. Formation of Double-Walled TiO2 Nanotubes and Robust Anatase Membranes. *Adv. Mater.* **2008**, *20*, 4135–4139, doi:10.1002/adma.200801189.

92. Macak, J.M.; Tsuchiya, H.; Ghicov, A.; Yasuda, K.; Hahn, R.; Bauer, S.;

Schmuki, P. TiO2 Nanotubes: Self-Organized Electrochemical Formation, Properties and Applications. *Curr. Opin. Solid State Mater. Sci.* **2007**, *11*, 3–18, doi:10.1016/j.cossms.2007.08.004.

93. Ghicov, A.; Schmuki, P. Self-Ordering Electrochemistry: A Review on Growth and Functionality of TiO2 Nanotubes and Other Self-Aligned MOx Structures. *Chem. Commun.* **2009**, 2791–2808, doi:10.1039/b822726h.

94. Regonini, D.; Bowen, C.R.; Jaroenworaluck, A.; Stevens, R. A Review of Growth Mechanism, Structure and Crystallinity of Anodized TiO2 Nanotubes. *Mater. Sci. Eng. R Reports* **2013**, *74*, 377–406, doi:10.1016/j.mser.2013.10.001.

95. Sopha, H.; Hromadko, L.; Nechvilova, K.; Macak, J.M. Effect of Electrolyte Age and Potential Changes on the Morphology of TiO2 Nanotubes. *J. Electroanal. Chem.* **2015**, *759*, 122–128, doi:10.1016/j.jelechem.2015.11.002.

96. Xie, Z.B.; Blackwood, D.J. Effects of Anodization Parameters on the Formation of Titania Nanotubes in Ethylene Glycol. *Electrochim. Acta* **2010**, *56*, 905–912, doi:10.1016/j.electacta.2010.10.004.

97. Durdu, S.; Cihan, G.; Yalcin, E.; Altinkok, A. Characterization and Mechanical Properties of TiO2 Nanotubes Formed on Titanium by Anodic Oxidation. *Ceram. Int.* **2021**, *47*, 10972–10979, doi:10.1016/j.ceramint.2020.12.218.

98. Cai, Q.; Paulose, M.; Varghese, O.K.; Grimes, C.A. The Effect of Electrolyte Composition on the Fabrication of Self-Organized Titanium Oxide Nanotube Arrays by Anodic Oxidation. *J. Mater. Res.* **2005**, *20*, 230–236, doi:10.1557/JMR.2005.0020.

99. Mohamed, A.E.R.; Kasemphaibulsuk, N.; Rohani, S.; Barghi, S. Fabrication of Titania Nanotube Arrays in Viscous Electrolytes. *J. Nanosci. Nanotechnol.* **2010**, *10*, 1998–2008, doi:10.1166/jnn.2010.2102.

100. Khudhair, D.; Bhatti, A.; Li, Y.; Hamedani, H.A.; Garmestani, H.; Hodgson, P.; Nahavandi, S. Anodization Parameters Influencing the Morphology and Electrical Properties of TiO2 Nanotubes for Living Cell Interfacing and Investigations. *Mater. Sci. Eng. C* **2016**, *59*, 1125–1142, doi:10.1016/j.msec.2015.10.042.

101. Ampelli, C.; Passalacqua, R.; Perathoner, S.; Centi, G.; Su, D.S.; Weinberg, G. Synthesis of TiO2 Thin Films: Relationship between Preparation Conditions and Nanostructure. *Top. Catal.* **2008**, *50*, 133–144, doi:10.1007/s11244-008-9113-0.

102. Macak, J.M.; Hildebrand, H.; Marten-Jahns, U.; Schmuki, P. Mechanistic Aspects and Growth of Large Diameter Self-Organized TiO2 Nanotubes. *J. Electroanal. Chem.* **2008**, *621*, 254–266, doi:10.1016/j.jelechem.2008.01.005.

103. Ku, Y.; Chen, Y.S.; Hou, W.M.; Chou, Y.C. Effect of NH 4F Concentration in Electrolyte on the Fabrication of TiO 2 Nanotube Arrays Prepared by Anodisation. *Micro Nano Lett.* **2012**, *7*, 939–942, doi:10.1049/mnl.2012.0488.

104. Wei, W.; Berger, S.; Hauser, C.; Meyer, K.; Yang, M.; Schmuki, P. Transition of TiO2 Nanotubes to Nanopores for Electrolytes with Very Low Water Contents. *Electrochem. commun.* **2010**, *12*, 1184–1186, doi:10.1016/j.elecom.2010.06.014.

105. Albu, S.P.; Roy, P.; Virtanen, S.; Schmuki, P. Self-Organized TiO2 Nanotube Arrays: Critical Effects on Morphology and Growth. *Isr. J. Chem.* **2010**, *50*, 453–467, doi:10.1002/ijch.201000059.

106. Kim, D.; Ghicov, A.; Schmuki, P. TiO2 Nanotube Arrays: Elimination of Disordered Top Layers ("nanograss") for Improved Photoconversion Efficiency in Dye-Sensitized Solar Cells. *Electrochem. commun.* **2008**, *10*, 1835–1838, doi:10.1016/j.elecom.2008.09.029.

107. Abbas, W.A.; Abdullah, I.H.; Ali, B.A.; Ahmed, N.; Mohamed, A.M.; Rezk, M.Y.; Ismail, N.; Mohamed, M.A.; Allam, N.K. Recent Advances in the Use of TiO2 Nanotube Powder in Biological, Environmental, and Energy Applications. *Nanoscale Adv.* **2019**, *1*, 2801–2816, doi:10.1039/c9na00339h.

108. Ali, S.; Granbohm, H.; Lahtinen, J.; Hannula, S.P. Titania Nanotubes Prepared by Rapid Breakdown Anodization for Photocatalytic Decolorization of Organic Dyes under UV and Natural Solar Light. *Nanoscale Res. Lett.* **2018**, *13*, doi:10.1186/s11671-018-2591-5.

109. David, T.M.; Wilson, P.; Mahesh, R.; Sagayaraj, P.; Murugesan, N.; Ramesh, C.; Seshadri, H. Photocatalytic Water Splitting of TiO2nanotubes Powders Prepared via Rapid Breakdown Anodization Sensitized with Pt, Pd and Ni Nanoparticles. *Mater. Technol.* **2018**, *33*, 288–300, doi:10.1080/10667857.2018.1433349.

110. Preethi, L.K.; Antony, R.P.; Mathews, T.; Walczak, L.; Gopinath, C.S. A Study on Doped Heterojunctions in TiO2 Nanotubes: An Efficient Photocatalyst for Solar Water Splitting. *Sci. Rep.* **2017**, *7*, 1–15, doi:10.1038/s41598-017-14463-0.

111. Sun, L.; Zhang, S.; Sun, X.W.; He, X. Effect of Electric Field Strength on the Length of Anodized Titania Nanotube Arrays. *J. Electroanal. Chem.* **2009**, *637*, 6–12, doi:10.1016/j.jelechem.2009.09.023.

112. Albella, J.M.; Montero, I.; Martínez-Duart, J.M.; Parkhutik, V. Dielectric Breakdown Processes in Anodic Ta2O5 and Related Oxides - A Review. *J. Mater. Sci.* **1991**, *26*, 3422–3432, doi:10.1007/BF00557127.

113. Huang, W.; Xu, H.; Ying, Z.; Dan, Y.; Zhou, Q.; Zhang, J.; Zhu, X. Split TiO2 Nanotubes − Evidence of Oxygen Evolution during Ti Anodization. *Electrochem. commun.* **2019**, *106*, 106532, doi:10.1016/j.elecom.2019.106532.

114. Jin, R.; Liao, M.; Lin, T.; Zhang, S.; Shen, X.; Song, Y.; Zhu, X. Formation and Evolution of Anodic TiO 2 Nanotube Embryos. *Mater. Res. Express* aa72b1, doi:10.1088/2053-1591/aa72b1.

115. Zhang, S.; Yu, D.; Li, D.; Song, Y.; Che, J.; You, S.; Zhu, X. Forming Process of Anodic TiO 2 Nanotubes under a Preformed Compact Surface Layer. *J. Electrochem. Soc.* **2014**, *161*, E135–E141, doi:10.1149/2.0661410jes.

116. Albella, J.M.; Montero, I.; Martinez-Duart, J.M. A Theory of Avalanche Breakdown during Anodic Oxidation. *Electrochim. Acta* **1987**, *32*, 255–258, doi:10.1016/0013-4686(87)85032-6.

117. So, S.; Lee, K.; Schmuki, P. Ultrafast Growth of Highly Ordered Anodic TiO 2 Nanotubes in Lactic Acid Electrolytes. *J. Am. Chem. Soc.* **2012**, *134*, 11316–11318, doi:10.1021/ja301892g.

118. Zhao, S.; Xing, J.; Fan, H.; Zhang, S.; Li, D.; Zhu, X. Derivation of a Mathematical Model for the Growth of Anodic TiO2 Nanotubes under Constant Current Conditions. *J. Electrochem. Soc.* **2017**, *164*, E187–E193, doi:10.1149/2.0421709jes.

119. Ruiquan, Y.; Longfei, J.; Xufei, Z.; Ye, S.; Dongliang, Y.; Aijun, H. Theoretical Derivation of Ionic Current and Electronic Current and Comparison between Fitting Curves and Measured Curves. *RSC Adv.* **2012**, *2*, 12474–12481, doi:10.1039/c2ra22124a.

120. Yang, F.; Feng, X.; Ge, F.; Zhang, T.; Qi, J.; Li, D.; Zhu, X. Rapid Growth of Titanium Oxide Nanotubes under the Critical Breakdown Voltage: Evidence against the Dissolution Reaction of Fluoride Ions. *Electrochem. commun.* **2019**, *103*, 17–21, doi:10.1016/j.elecom.2019.04.010.

121. Aladjem, A. Anodic Oxidation of Titanium and Its Alloys. *J. Mater. Sci.* **1973**, *8*, 688–704, doi:10.1007/BF00561225.

122. Tao, J.; Zhao, J.; Tang, C.; Kang, Y.; Li, Y. Mechanism Study of Self-Organized TiO2 Nanotube Arrays by Anodization. *New J. Chem.* **2008**, *32*, 2164–

2168, doi:10.1039/b808719a.

123. Alijani, M.; Sopha, H.; Ng, S.; Macak, J.M. High Aspect Ratio TiO2 Nanotube Layers Obtained in a Very Short Anodization Time. *Electrochim. Acta* **2021**, *376*, 138080, doi:10.1016/j.electacta.2021.138080.

124. Garcia-Vergara, S.J.; Skeldon, P.; Thompson, G.E.; Habazaki, H. A Flow Model of Porous Anodic Film Growth on Aluminium. *Electrochim. Acta* **2006**, *52*, 681–687, doi:10.1016/j.electacta.2006.05.054.

125. Zhu, X.F.; Song, Y.; Liu, L.; Wang, C.Y.; Zheng, J.; Jia, H.B.; Wang, X.L. Electronic Currents and the Formation of Nanopores in Porous Anodic Alumina. *Nanotechnology* **2009**, *20*, doi:10.1088/0957-4484/20/47/475303.

126. Yu, M.; Chen, Y.; Li, C.; Yan, S.; Cui, H.; Zhu, X.; Kong, J. Studies of Oxide Growth Location on Anodization of Al and Ti Provide Evidence against the Field-Assisted Dissolution and Field-Assisted Ejection Theories. *Electrochem. commun.* **2018**, *87*, 76–80, doi:10.1016/j.elecom.2018.01.003.

127. Yu, M.; Huang, W.; Li, P.; Huang, H.; Zhang, K.; Zhu, X. Morphology Evolution of TiO2 Nanotubes with Additional Reducing Agent: Evidence of Oxygen Release. *Electrochem. commun.* **2019**, *98*, 28–32, doi:10.1016/j.elecom.2018.11.010.

128. Diebold, U. The Structure of TiO2 Surfaces. In *Chemical Physics of Solid Surfaces*; 2001; Vol. 9, pp. 443–484.

129. Gomez, I.J.; Arnaiz, B.; Cacioppo, M.; Arcudi, F.; Prato, M. Nitrogen-Doped Carbon Nanodots for Bioimaging and Delivery of Paclitaxel. *J. Mater. Chem. B* **2018**, *6*, doi:10.1039/x0xx00000x.

130. Yang, J.; Cheng, J.; Tao, J.; Higashi, M.; Yamauchi, M.; Nakashima, N. Wrapping Multiwalled Carbon Nanotubes with Anatase Titanium Oxide for the Electrosynthesis of Glycolic Acid. *ACS Appl. Nano Mater.* **2019**, *2*, 6360–6367, doi:10.1021/acsanm.9b01357.

3

Optimization of titania nanotube electrocatalysts for the selective hydrogenation of oxalic acid

3.1 Aim of this chapter

This chapter discusses the effects of different anodization parameters on the nanostructure of TiO_2 nanotubes (NTs) and their impact on the electrocatalytic hydrogenation reaction of oxalic acid (OX). The chapter is divided into two sections.

1. The first part mainly focuses on the study of how the aging of the anodizing solution affects the growth of nanotubes. In addition, the section discusses the effect of thermal pretreatment prior to anodization which follows the field assisted dissolution (FAD) theory. Subsequently, the performance of the catalyst obtained by hydrothermal synthesis will be compared. The testing results will be linearly correlated with the results obtained by characterization and discussed below to understand the chemical nature of the active species of the reaction.
2. The second part focuses on the phenomenon of breakdown, which occurs at higher anodization potentials, and it leads to a different growth mechanism called rapid breakdown anodization (RBA). The chapter extensively discusses its role in NTs nanostructure and active area. The effect of two different anodization times and further electrochemical pretreatment will also be examined. Once again, a series of linear correlations between the characterization data and catalytic behavior provides additional information about selectivity in the process.

This chapter is based on:

Abramo, F. P. *et al.* Electrocatalytic production of glycolic acid via oxalic acid reduction on titania debris supported on a TiO2 nanotube array. *J. Energy Chem.* **16**, (2021).

Pio Abramo, F. *et al.* Nanostructure-performance relationships in titania-only electrodes for the selective electrocatalytic hydrogenation of oxalic acid. *J. Catal.* **429**, 115277 (2023).

Therefore, the goal of this chapter is to investigate the relationship between electrode nanostructure and performance in selective electrocatalytic hydrogenation. It is not intended to find the best electrocatalysts for this reaction, which usually involve critical raw material, or to maximize their utilization in connection to commercial applications.

To achieve this goal, the strategy employed can be summarized as follows:

- First, determine a set of NTs electrodes that have accurate control over macro-, micro-, and nanostructure features.
- Then, explain how adjusting the preparation technique may influence these features.
- Finally, examine the nanostructure of these Ti-only electrodes and their connections to electrocatalytic function, justifying their design in light of these connections and the variables affecting performance.

3.2 Experimental

With the exception of one sample prepared by hydrothermal synthesis using commercial TiO_2 P25 Degussa as precursor, all TiO_2 nanotubes were prepared by controlled anodic oxidation (AO) of titanium foils (Alpha Aesar).

3.2.1 Anodic oxidation

After a surface cleaning procedure, Ti foils (Alfa Aesar, diameter 35 mm, thickness 0.025 mm, purity 99.96%) were used as a substrate for the preparation of electrocatalysts. The Ti foils were repeatedly cleaned in an ultrasonic bath for 10 minutes using (i) distilled water, (ii) acetone, and (iii) isopropyl alcohol. Some Ti foils were subjected to thermal or electrochemical pretreatment.

The thermally treated Ti films (TiNT50-T; TiNT60-T) were calcined at 450°C for 30 minutes in air.

The electrochemically treated Ti foils (TiNT60-E) were obtained using a 1 M H_2SO_4 solution at 20 V for two hours at 45°C in a two-electrode configuration cell with a glassy carbon cathode.

The same procedure as described above was then used for anodizing. However, two reference electrocatalysts were also made using only the thermal pretreatment (Ti-T) and electrochemical treatment (Ti-E) of Ti foil, as previously described.

Anodization was carried out at room temperature using a fresh or aged electrolyte solution. The solution consisted of deionized water (2% wt), NH_4F (0.3% wt; Sigma-Aldrich, ≥ 98%), and ethylene glycol as solvent (Sigma-Aldrich, 99.8%) in a two-electrode configuration cell with a glassy carbon cathode. The AO potential and AO time were adjusted to produce NTs with different lengths (50 V, 60 V; 15 min, 60 min). The TiO_2NT/Ti electrodes underwent the following steps: (a) rinsing with deionized water to remove any remaining electrolyte; (b) drying overnight; and (c) calcining for three hours at 450 °C with a temperature ramp of 2 °C/min.

3.2.2 Hydrothermal synthesis

The Degussa P25 TiO_2 (purity 99.9%, 85% Rutile and 25% Anatase, surface area 50 $m^2\ g^{-1}$, pore volume 0.11 $cm^3\ g^{-1}$, density 4.26 g cm^{-3}) was dispersed in 65 mL of 10 M NaOH solution using an ultrasonic bath for 15 minutes. The resulting suspension was then subjected to hydrothermal treatment in a Teflon-lined, stirred autoclave for 24 hours at 130 °C and 600 rpm. After undergoing hydrothermal treatment, the sample underwent vacuum washing with ultrapure water until it reached a pH of 7. Subsequently, it was protonated for one hour at room temperature in 0.1 M HCl while being stirred at 600 rpm.

After drying overnight at 80°C, the protonated sample was ground and washed with distilled water until it reached a neutral pH. The powder was then spread in methanol

(10 mg/mL) using an airbrush (ABEST TJ-180K) and applied to a Ti foil, resulting in a theoretical TiO_2 loading of 1.5 mg/cm².

After an overnight drying process at 80 °C, the resulting sample was calcined at 450 °C for 3 hours (2 °C min^{-1}), yielding an experimental TiO_2 loading of 0.7 mg cm^{-2}. The catalyst produced is referred to as TiNT-HS. In total, thirteen samples were investigated in detail (see table 3.1 for a detailed description).

Table 3.1 *Summary of the preparation conditions and short name used for the tested cathodes. Ti-E and Ti-T were prepared as a reference without applying the AO procedure.*

#	*Ti foil Pretreatment*	*AO potential [V]*	*AO time [s]*	*Short Name*
1	None, as received	50	3600 *	TiNT
2			3600 ▫	TiNT-A
4	Thermal		3600 *	TiNT-T
5	None, as received		900	TiNT50-15
6			3600	TiNT50
7		60	900	TiNT60-15
8			3600	TiNT60
9	Thermal			TiNT60-T
10	Electrochemical			TiNT60-E
11		-	-	Ti-E
12	Thermal	-	-	Ti-T
13	-	-	-	TINT-HS •

* sample was anodized in a solution aged for 60 min
▫ sample was anodized in a solution aged for 240 min
• TiNT-HS was obtained by hydrothermal synthesis

3.2.3 Electrochemical tests

The electrocatalytic cell was controlled using an Amel (model 255) potentiostat/galvanostat. All measurements were conducted using a three-electrode

setup, with the electrocatalysts as working electrode (WE), a Pt counter electrode (CE), and Ag/AgCl reference electrode (RE). The electrochemical cell (Scheme 3.1) used for amperometric detection experiments (AD) and cyclovoltammetry analysis (CV) was developed and constructed in-house.

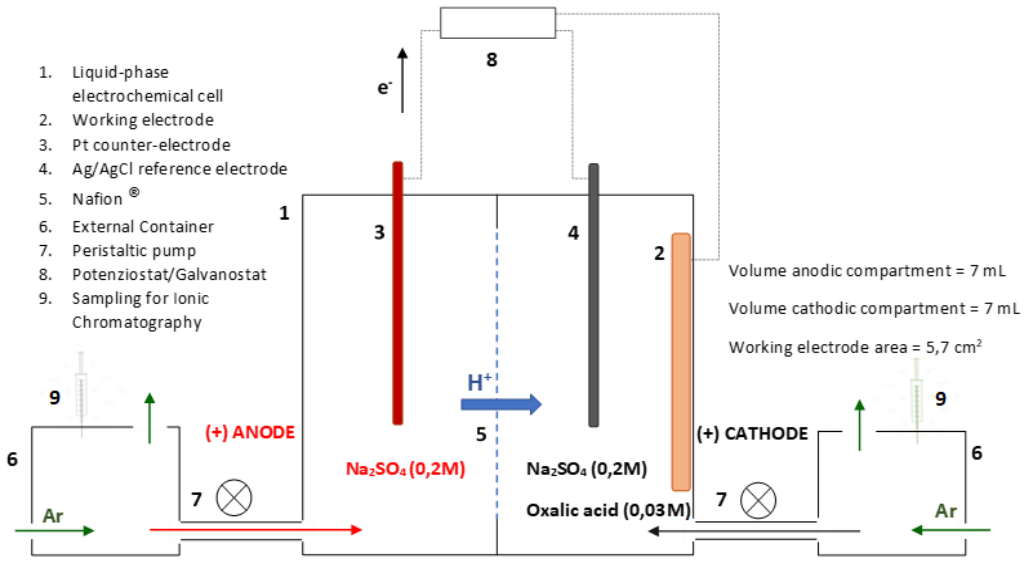

Scheme 3.1 *Home-made electrochemical cell used for testing.*

A proton exchange membrane (Nafion® 115) was used to divide the anodic (1) and cathodic compartments (2). A 0.2 M Na_2SO_4 solution (Carlo Erba, purity≥99.8%) containing 0.03 M OX acid solution [1] (OX, Sigma Aldrich $H_2C_2O_4 \cdot 2\ H_2O$, purity ≥ 99%) at pH 2 was used in the cathodic compartment for the reaction, while a 0.2 M Na_2SO_4 electrolyte solution was used in the anodic partition. The pH of the anodic compartment was adjusted by adding small amounts of a 1 M H_2SO_4 solution to match the pH of the cathodic compartment.

The electrolytic solutions in the external reservoirs (6) were purged with Argon (20 ml min^{-1}) for 30 minutes to remove O_2 before starting the reaction. A peristaltic pump (7) is used to flush the electrolytic solutions to both compartments. The solution volume, including the cathode, external tank and tubes is 35 ml. The net volume in

the cathodic compartment is 7 ml, which is the same as in the anode. Each investigated potential was tested for two hours. The resulting products were analyzed by Ionic Chromatography (Metrohm), equipped with a Metrosep Organic Acid Guard pre-column (L= 50 mm, 4 mm thick), an organic acids column (L= 25 cm, ID = 7.8 mm), and a UV/Vis detector (944 professional UV/vis Detector Vario), using a 0.5 mM H_2SO_4 as a mobile phase (0.5 ml min^{-1}), at 5 MPa, and products detected at 215 nm. A representative chromatogram is reported in the Appendix (figure A1).

3.2.3.1 Amperometric detection (AD) test

The amperometric detection experiments (AD) were performed for each electrocatalyst at constant applied potential (-0.8 V, -0.9V and -1 V vs RHE) at 25 °C. The surface electrode was 5.7 cm^2. Prior to each AD experiment, fresh oxalic acid solution ([OX] = 0.03 M, [Na_2SO_4] = 0.2 M) and cathodic solution ([Na_2SO_4]= 0.2 M, pH= 2) were added to the cathodic and anodic compartments. The electrolyte solutions were then degassed by an Ar flow (20 ml min^{-1}) for 20 minutes. Finally, the experiment's potential was set and maintained at a constant level for two hours while measuring the current in an Ar atmosphere at a rate of 20 ml min^{-1}.

Three representative catalysts, TiNT60-15, TiNT60-T and TiNT-T underwent an initial stability investigation for eight hours. In addition, to examine the effect of oxalic acid solution concentration, experiments were conducted with [OX]=0.1 M for TiNT60-E and TiNT50.

The catalytic performance, after AD tests, was measured in terms of Faradic Efficiencies of the formed products (FE_{Pi}) using eq. (1).

$$FE_{Pi}(\%) = \frac{n_i \, x \, n_e \, x \, F}{Q} \, x \, 100 \qquad (1)$$

n_i, n_e, F and Q represent the produced amount of product "i" (mol), the number of electrons required for the formation of glyoxylic acid (GO) and glycolic acid (GC) from OX (for the formation of GO and GC, n_e = 2 and 4, respectively), the Faradaic constant (96485 C mol^{-1} of electrons), and the total charge (Coulombs) passed through the electrodes during the AD experiments.

OX conversion in electro-reduction experiments was defined using the following equation:

$$\text{Oxalic acid conversion (\%)} = \frac{[OX]i-[OX]t}{[OX]i}\ x\ 100 \quad (2)$$

where [OX]i is the initial OX concentration and [OX]t is the OX concentration after 2 h of reaction time.

3.2.3.2 Cyclic voltammetry (CV)

Cyclic voltammetry (CV) curves were measured for the produced electrocatalysts using a potentiostat/galvanostat (Amel 2551) with and without oxalic acid (OX) as the substrate. Cyclic voltammograms were obtained at a scan rate of 50 mV sec^{-1} in the potential range of 0.31 to -1.68 V vs. RHE, using blank and OX solutions alternately. To conduct the blank CV tests, a solution of 0.1 M H_2SO_4 was utilized to lower the pH to 2. The cathodic and anodic compartments were then filled with a solution of Na_2SO_4 (0.2 M; Carlo Erba, Na_2SO_4 purity≥99.8%). For CV experiments performed in OX solution, the cathodic compartment was filled with a fresh 0.03 M oxalic acid solution (OX, Sigma Aldrich $H_2C_2O_4 \cdot 2\ H_2O$, purity ≥ 99%) containing Na_2SO_4 (0.2 M; Carlo Erba, Na_2SO_4 purity≥99.8%), while the anodic compartment was filled with the same solution used for the blank CV experiment (the pH was adjusted to 2 to get the same pH on both the anodic and cathodic compartments). In addition, the behavior in a higher OX concentration (0.1M) was investigated for some samples. The cathodic and anodic solutions were purged with argon (20 ml min^{-1}) and recirculated within the anodic and cathodic compartments for 20 minutes. Then, in the Ar environment, the voltammograms were measured. The onset potentials of OX reduction were also evaluated on each prepared electrocatalyst.

3.2.3.3 Electrochemical active surface area (ECSA)

Double Layer Capacitance (CDL) is determined by the interface phenomena between electrolyte and electrode. CDL is calculated based on the charge quantity supplied to the electrode surface area. The surface area is typically determined through electrochemical measurement, which provides a numerical representation of the possible surface area that the electrolyte ions can reach. To achieve CDL, cyclic

voltammetry (CV) requires several tests at varying scan speeds in a non-faradaic range [2]. Several CVs were recorded at 5, 10, 20, 40, 70, and 100 mV s^{-1} in a 0.2M N_2-saturated Na_2SO_4 solution with pH adjusted to 2 by adding H_2SO_4 using a TiO_2 NTs sample (geometric area of 5.7 cm^2) as a working electrode. As shown in figure 3.1, the investigated non-faradic range is from 0.31 to 0.28 V vs. RHE.

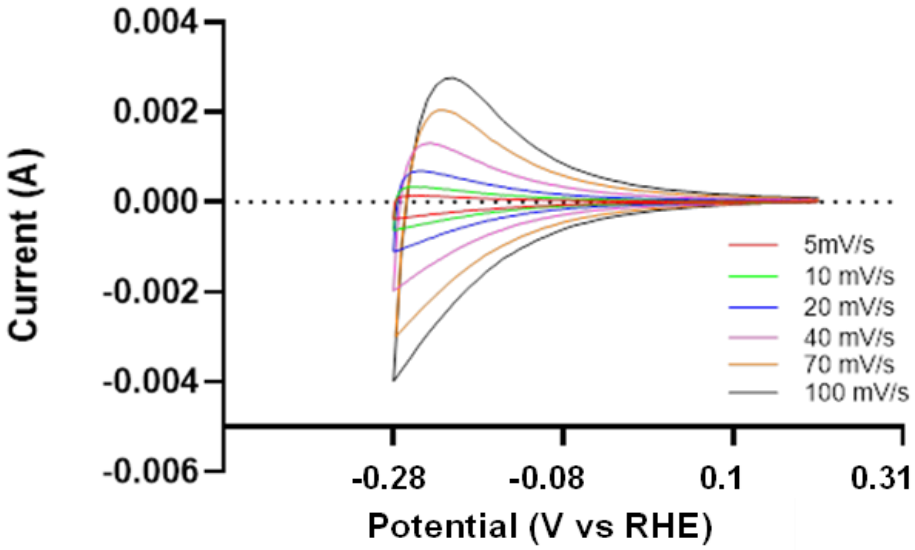

Figure 3.1 *Cyclic voltammetry ranged from 0.31 to 0.28 V vs RHE for TiNT60-15 at different scan rates (5, 10, 20, 40, 70, and 100 mV s^{-1})*

The current generated in this potential range is believed to be caused by double-layer charging. To calculate the CDL using CV measurement, the obtained average current values from the anodic and cathodic charging current at -0.035 V vs. RHE were plotted against the scan rate (V s^{-1}). An example of the TiNT60-15 findings is shown in figure 3.2.

According to eq. 3, it is possible to define the $C_{DL.}$

$$I = C_{DL} * v \qquad (3)$$

The results indicate a linear relationship between the two factors. To calculate the CDL value, the absolute value of the slope of the regression line was considered, as indicate in equation 3 [3].

Each prepared electrode exhibited double-layer capacitance values greater than the specific capacitance, C_s, of $2.3\ x\ 10^{-1}$ mF observed for smooth titanium at 100 mV s^{-1}.

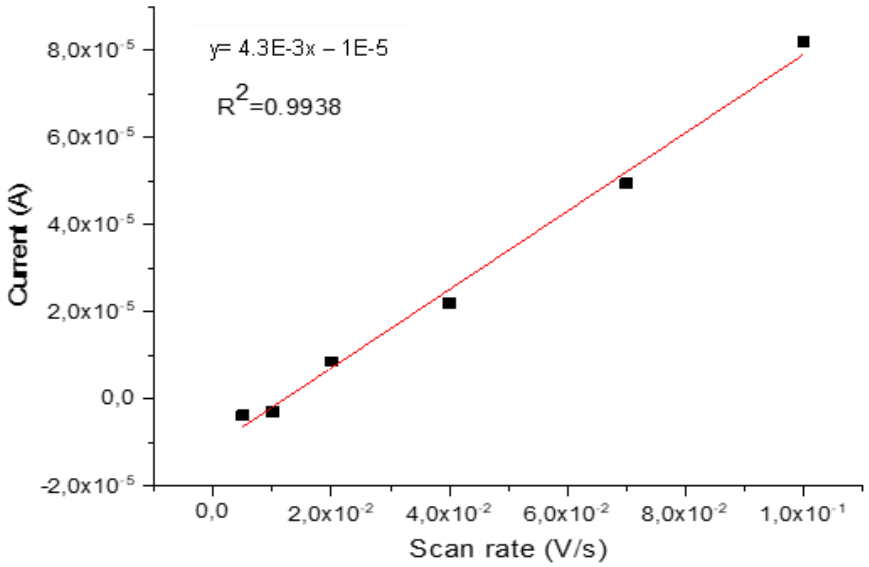

Figure 3.2 *Average current values from anodic and cathodic charging current at -0.035 V vs. RHE against different scan rates (5, 10, 20, 40, 70, and 100 mV s^{-1}). The slope of the regressed straight lines determines the value of the C_{DL}*

The specific capacitance was calculated using the eq. 4

$$C_s = \frac{1}{Av\ (V_2 - V_1)} \int_{V_2}^{V_1} I(V)dV \qquad (4)$$

Here, A represents the area of the working electrode in square centimeters, v represents the scan rate in volts per second, and (V_2-V_1) represents the potential range in volts.

Once the value of the CDL was determined, the electrochemical surface area (ECSA) was calculated according to eq. 5 [4].

$$ECSA = \frac{C_{DL}}{C_s} \qquad (5)$$

3.2.4 Characterization methods

3.2.4.1 FESEM

A field emission scanning electron microscope (FESEM, ZEISS Auriga) operating at an accelerating voltage of 5KV was used to examine the morphology of the samples. Images of the basic features of the samples, pore size and length of the titania nanotubes were collected in both cross-section and top view.

3.2.4.2 AFM

The AFM characterization was performed using a Perception SPM from Assing (Italy) in tapping mode. The etched silicon probe, model number RTESP-300 (Bruker), had a tip radius of 8 nm, a frequency of 300 KHz, and a spring constant of 40 N/m. After recording the 5x5 μm images, the Gwyddion program was used to assess the root mean square roughness (RMS).

3.2.4.3 GAXRD

Glading Angle X-ray diffraction (GAXRD) measurements were conducted using a Bruker D8-Advance diffractometer with a Cu-Kα (λ= 1.54186 Å) monochromatized radiation source. The scans were collected at a continuous rate of one degree per minute over an angular range of 20° to 80° at 25 °C. The step size was 0.02° with a dwell period of 1.2 s for each increment, by applying an accelerating voltage and current of 40 kV and 30 mA, respectively. A glancing angle of 0.5° was used for all measurements.

3.2.4.4 XPS

The XPS spectra were collected using a PHI Versa Probe II (Physical Electronics) equipped with an Al Kα (1486.6 eV) X-ray source. The C1s, O1s, and Ti2p core levels were measured at 23.5 eV passing energy. The survey spectra were recorded using an analyzer energy path of 117 eV. The X-ray beam size was 100 microns at 25 W. Prior to measuring the spectra, the samples underwent a charge neutralization process through simultaneous irradiation with a low-energy electron beam and an ion beam. The XPS peak positions were referenced to graphitic carbon (284.8 eV). The XPS peaks were deconvoluted using a Shirley backdrop curve and the Multipack Data Reduction Software (ULVAC-PHI, Inc.).

3.2.4.5 Raman

Micro-Raman measurements were carried out using a LabRam HR800 Horiba spectrometer equipped with a confocal microscope and a liquid nitrogen cooled charge coupled device (CCD) detector. The spectra were acquired in the range between 30-800 cm^{-1} at room temperature and using an 1800 gr mm^{-1} diffraction grating. The samples were excited using a laser beam with a wavelength of 532 nm that was focused by a 50 X microscope objective. The applied laser power density was of 10 mW in order to avoid laser-induced thermal degradation or phase transitions of the TiO_2 samples.

3.3 Results for TiO_2 NTs in aged solution and hydrothermal synthesis

3.3.1 Interpretation of anodization curves

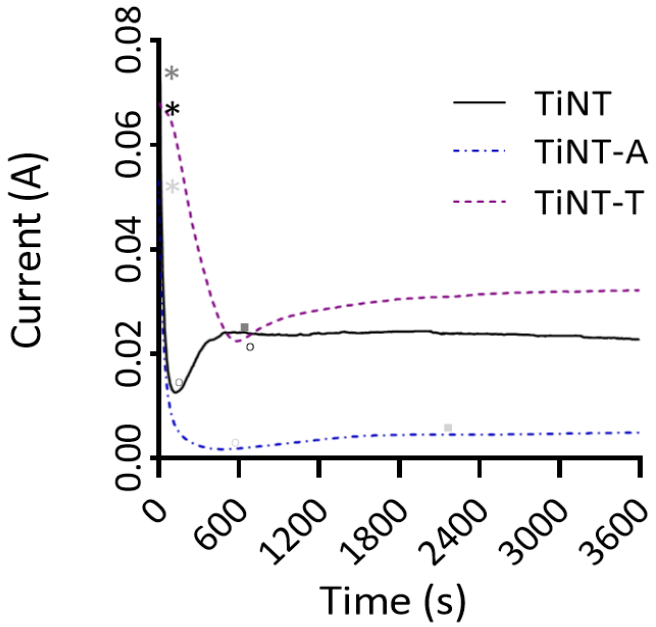

Figure 3.3 *Anodization curves during the anodic oxidation (50 V, 1 hour; *, o, ▪ indicate I_0, I_{min} and I_{max}, respectively)*

Figure 3.3 shows the anodization curves of current measured against anodization time for the three samples synthesized by anodic oxidation of Ti foils in aged solution (see Table 3.1 for a summary).

The anodization process used to create TiNT and TiNT-A was identical, except for the aging period. TiNT-T was made using a pre-calcinated Ti-foil before the anodization process. However, even small variations can significantly modify the anodization process, as shown in Figure 3.3.

The TiNT sample was prepared using cleaned Ti foil and aged for 60 minutes. It displayed an initial current (I_0) of 0.075 A, which rapidly decreased in the first 120 s. The current reached a minimum (I_{min}) of approximately 0.0124 A at 120 s (t_{min}) and a maximum (I_{max}) of 0.0241 A at 480 s (t_{max}). After 480 seconds, only a slight

decrease in current was observed until the anodization process was completed (final current = 0.0234 A).

Extending the electrode aging duration from 60 to 240 minutes (TiNT-A) resulted in a 30% reduction in I_0 compared to the TiNT sample. Both TiNT-A and TiNT samples showed a lower slope in the initial current reduction. However, in the TiNT-A sample, I_{min} and I_{max} were much lower at 0.046 A, and t_{min} and t_{max} increased to 470 and 1800 s, respectively.

The behavior of TiNT-T is unique. The current declines less abruptly upon applied potential and reaches after 570 seconds (t_{min}) a value of 0.022 A (I_{min}), which is 10% lower than TiNT. The current gradually rises until the conclusion of the anodization without reaching its maximum current (I_{max}).

The lower I_0 of TiNT-A compared to the TiNT sample was attributed to F^- ion depletion caused by the longer aging period. In fact, A lower concentration of F- ions can alter the electrical field and double layer at the solid-liquid interface, which modifies the rates of reactions involved in the mechanism of nanotube growth [5,7]. In agreement the reduction of I_{min} and I_{max}, and the increase of t_{min} and t_{max}, indicate the formation of a dense oxide layer with greater thickness (eq. 3), and a reduction of the nucleation rate and the growth rate of the nanotubes (eq. 4). Therefore, the TiNT-A sample exhibits less effective nanotube development as proven by SEM images (figure 3.4 b).

The thin TiO_2 layer that forms during the pre-oxidation process in the TiNT-T instance causes the first, less severe fall in current. This limits the exposition of metallic Ti and affects both reported reactions in (eq. 3 and 4) when the production of TiO_2 NTs is induced by a higher electrical field. The pre-calcination stage, which forms the oxide pre-layer, may partially slow the process of pore nucleation and nanotube development. This is suggested by the absence of a distinct I_{max}, as the current increase remains active even after 3500 seconds.

According to the literature, the anodization curves for TiNT, TiNT-A, and TiNT-T electrodes exhibit various tendencies [5–7]. However, this samples are excellent

representatives of the conditions encountered during the creation of the ordered array of TiO_2 nanotubes and titania debris on them.

3.3.2 Field emission scanning electron microscope (FESEM) images

Figure 3.4 (a-c) displays FESEM top-view micrographs of the anodic oxidation-prepared electrodes: TiNT, TiNT-A, and TiNT-T. For comparison, a FESEM image of the TiO_2 nanotube sample (TiNT-HS) synthesized by hydrothermal treatment and coated on Ti foil is provided (d). The surface of TiNT, where the ordered array of vertically aligned TiO_2 NTs is partially covered by TiO_2 debris, is shown in Figure 3.4 (a). The TiO_2 nanotubes are dense and compact, with an inner diameter ranging from 50 to 100 nm and a wall thickness of around 15-20 nm. Figure 3.4 (b) depicts the top view of the TiNT-A electrode, which shows the presence of a compact oxide layer on the surface, but no obvious underlying TiO_2 NTs array. The anodization curve is consistent with the depletion of F^- ions in the aged electrolyte solution [6,8]. Figure 3.4 (c) shows the top view of the TiNT-T electrode, where the TiO_2 NTs array is visible but partially hidden by large porous oxide patches on the surface, which are denser compared to the TiNT debris. In the TiNT-T case, the NTs have a more uniform inner diameter (between 40 and 60 nm) and a thinner wall thickness (about 10 nm) compared to TiNT, but a slightly lower packing density. Figure A2 in the Appendix shows a second view of the TiNT-T sample. The layer was cracked to better display the existence of a vertically aligned and highly ordered array of TiO_2 NTs with uniform diameters and a distinct structure. These findings support the suggestions made by Macak et al. [9] that pre-structured surfaces enhance tube ordering. Although there are large TiO_2 patches instead of debris as in TiNT, the thermal pretreatment creates initiation sites for TiO_2 NTs development during the anodization process, resulting in a more well-defined nanostructure compared to TiNT. The EDX analysis shown in figure A3 confirms the elemental composition based on a homogenous TiO_2 layer with hardly detectable F^- traces on both the TiNT and TiNT-T samples. All TiNT samples had a titania film thickness between 0.7 and 0.8 μm. Moazeni et al. [10] also reported similar indications.

The SEM micrographs of the TiNT-HS sample (Figure 3.4 d) reveal the existence of randomly oriented tubular nanostructures (see inset) and nanosheets (white circles). These TiO_2 nanosheets and nanotubes are packed less densely compared to TiNT samples.

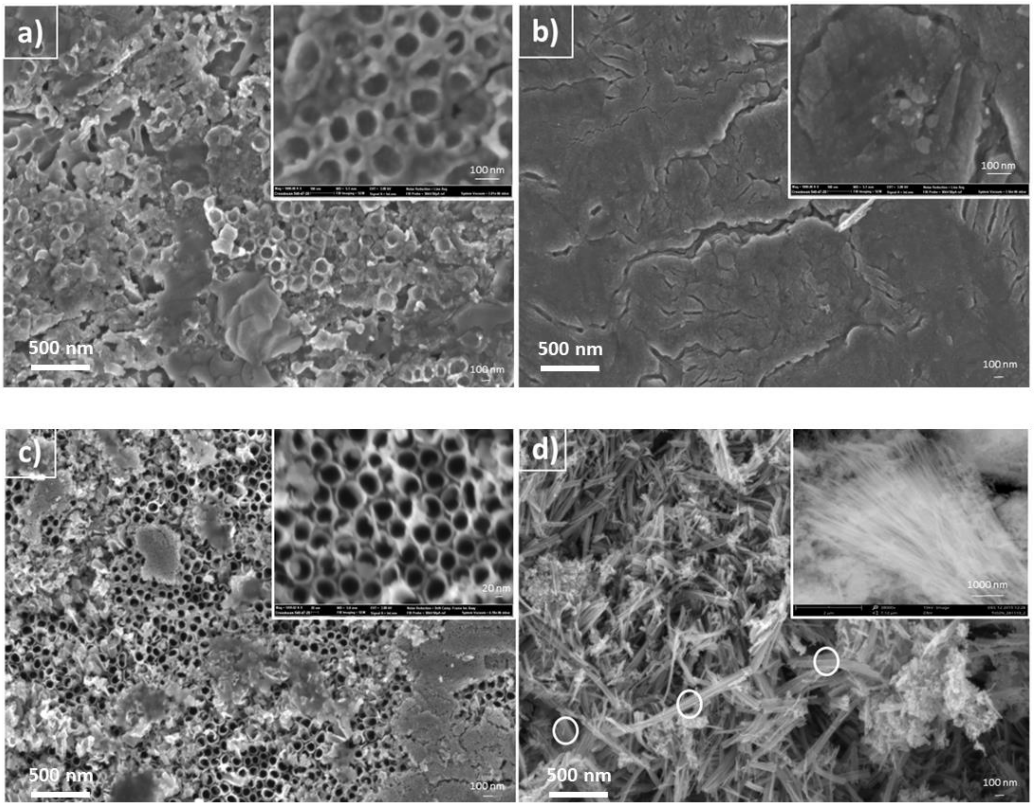

Figure 3.4 *SEM top-view images of the prepared electrodes:TiNT (a), TiNT-A (b), TiNT-T (c) and TiNT-HS (d). Insets show higher magnification micrographs.*

3.3.3 Cyclic voltammetry

The electrodes were investigated by CV to study their differences and their effect on the redox behavior [11–14]. Figure 3.5 (a) displays the voltammograms recorded for each sample in a 0.2 M Na_2SO_4 solution. A reversible reduction peak at -0.62 V vs. RHE was observed for all samples, indicating the reduction of Ti^{4+} to Ti^{3+} as indicated in eq. 6:

$$TiO_2 + H_2O + H^+ + e^- \leftrightarrow Ti(OH)_3 \quad (6)$$

At −0.96 V the formation of gaseous hydrogen occurs, according to eq. 7:

$$2H^+ + 2e^- \rightarrow H_2 \quad (7)$$

The electron transfer process related to proton insertion (eq. 8) occurs simultaneously with the negative current in this area [14].

$$TiO_2 + xe^- + xH^+ \leftrightarrow Ti^{IV}_{1-x}Ti^{III}_{x}(O)_{1-x}(OH)_x \quad (8)$$

This product's decomposition causes the anodic peak at about -0.86 V. All samples exhibit an anodic peak between -0.46V and -0.56 V, which is associated with the oxidation of Ti^{3+} to Ti^{4+}. The peak intensity sequence, TiNT-T > TiNT-HS > TiNT > TiNT-A, suggests that the TiNT-T sample may contain more Ti^{3+} species.

The presence of OX 0.03 M (fig. 3.5 b) leads to a decrease in the oxidation of Ti^{3+} species, resulting in weaker anodic peaks and a slight increase in cathode current. The anodic peaks in OX solution decrease in intensity, which is consistent with Zhao et al. [15] observations of similar behavior on a rough TiO_2 layer. This indicates that the electrogenerated Ti^{3+} species reduce OX. To validate this interpretation, a CV profile with a high concentration of OX (0.1 M) was conducted on the TiNT sample (see figure A4). In this instance, a higher cathode current was observed, and the oxidation peak disappeared completely, indicating that OX was electro-reduced by the electrons generated by the Ti^{3+}/Ti^{4+} redox pair. According to these findings, OX experiences quick chemical electroreduction and the nanoporous TiO_2 film electrode functions well as a heterogeneous redox catalytic electrode.

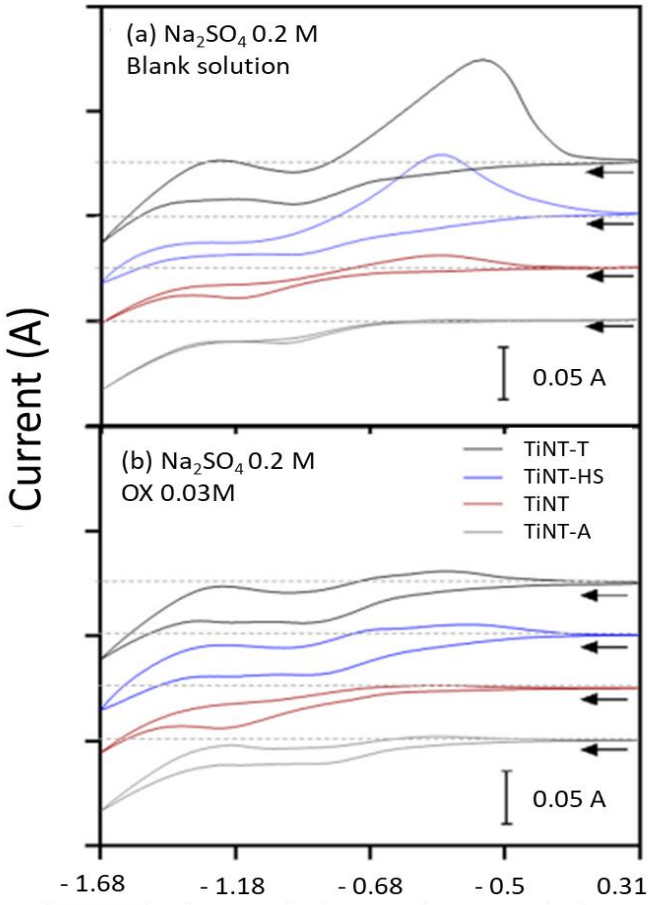

Figure 3.5 *Cyclovoltammetry curves measured with a scanning rate (v) of 50 mV s^{-1} in (a) Na_2SO_4 0.2 M (blank solution), and (b) adding an OX solution 0.03 M*

3.3.4 X-ray photoelectron spectroscopy

The surface properties of TiNT electrodes were examined using photoelectron spectroscopy. The survey spectra (Figure A5 in the appendix) indicate that the only impurities present in TiO_2 nanotubes are carbon (C*1s* peak) contamination and Ti and O elements. Similar features were observed in other survey spectra, which are not described here for clarity.

High-resolution XPS spectra of Ti*2p* and O*1s* were measured for each sample. The Ti *2p* core level spectra for every sample are shown in Figure A6. The doublet Ti$2p_{3/2}$ at 458.50±0.1 eV and Ti$2p_{1/2}$ at 464.04±0.1 eV in the fitted Ti*2p* spectra are compatible with Ti^{4+} in the TiO_2 lattice [16,17]. The shoulder peaks at 456.91±0.1

eV and 462.45±0.1 eV, respectively, are attributed to Ti^{3+} species Ti_2O_3 for Ti$2p_{3/2}$ and Ti$2p_{1/2}$ [18]. The splitting energy of Ti $2p_{1/2}$ and Ti $2p_{3/2}$ was 5.54 eV.

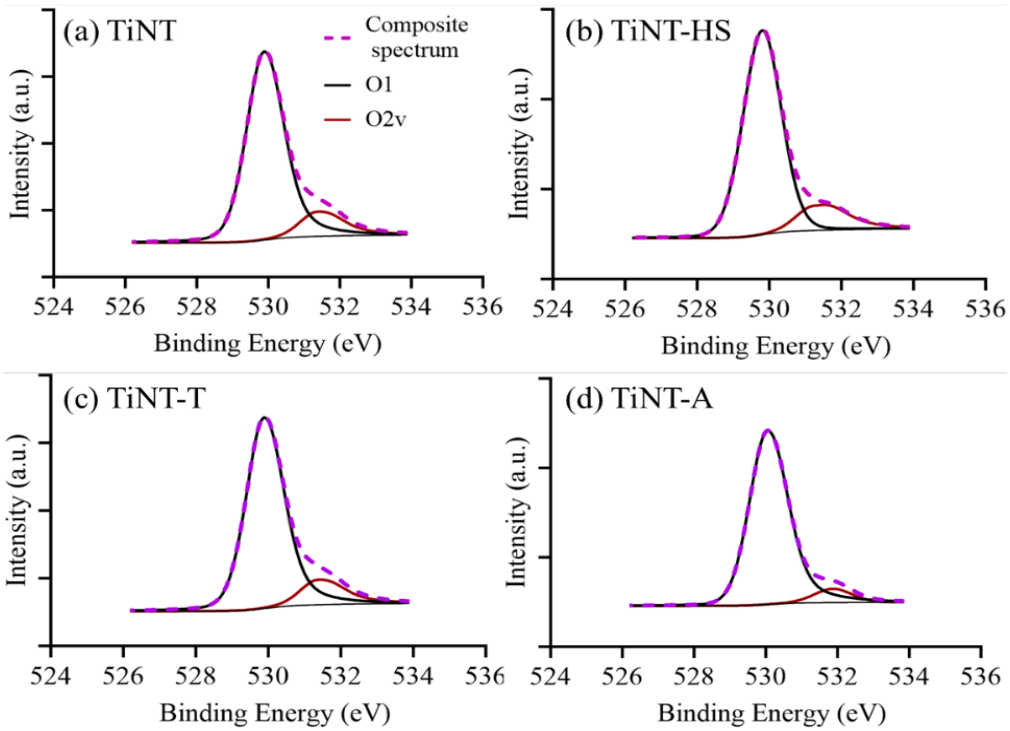

Figure 3.6 *O1s X-ray photoemission spectra of the investigated electrodes*

The near-surface area exhibits a higher concentration of oxygen species, as evidenced by the asymmetric curve and narrow shoulder observed in all of the high-resolution O*1s* core level spectra presented in fig. 3.6 [19]. The O*1s* spectrum of each sample was deconvolved into two peaks, O1 and O2v. The O2v peak at 531.32±0.2 eV was identified as the oxygen coupled to Ti^{3+} species inside Ti_2O_3, which is connected with superficial oxygen species neighboring to oxygen vacancies. The more intense O1 peak, observed at 529.81±0.2 eV, was assigned to the oxygen contained in the TiO_2 crystal lattice [20]. The XPS analysis revealed two distinct oxygen peaks. The presence of Ti^{3+} species is further confirmed by the high agreement between the XPS and CV results.

Table 3.2 reports the binding energy and the percentage of Ti^{3+} and O2v species calculated using Multipack software. The percentage of Ti^{3+} changes slightly in all samples, but a linear correlation with the amount of O2v oxygen vacancies is observed, as discussed later.

Table 3.2 *Binding energies (eV) of Ti 2p and O 1s peaks present in the XPS spectra of TiNT samples and the corresponding percentage of oxygen vacancies (O2v) and Ti^{3+}. The average OX conversion is also reported.*

	Ti^{4+}(eV)		*Ti^{3+}(eV)*		*O (eV)*		*Composition (%)*		*OX Con avg (%)*
Sample	$Ti2p_{3/2}$	$Ti2p_{1/2}$	$Ti2p_{3/2}$	$Ti2p_{1/2}$	O_1	O2v	O2v	Ti^{3+}	-
TiNT	458.67	464.21	456.95	462.49	530.05	531.87	7.00	5.14	6.81
TiNT-A	458.45	463.99	456.88	462.42	529.64	531.70	6.80	5.11	6.62
TiNT-HS	458.50	464.04	456.91	462.45	529.81	531.32	14.70	5.54	26.0
TiNT-T	458.60	464.14	456.95	462.49	529.90	531.31	19.00	5.71	32.0

3.3.5 Crystalline phases

Grazing angle X-ray diffraction (GAXRD) was used to identify the crystalline titania phases present in NTs electrodes. The results showed that only the TiO_2 anatase phase was present in samples annealed at 450°C. These findings were confirmed by Raman spectroscopy (see figure A8a), observing five different peaks corresponding to Raman active modes in the anatase phase: peaks $E_g(1)$ (145.3 cm^{-1}), $B_{1g}(1)$ (395.9 cm^{-1}), and $E_g(3)$ (639.0 cm^{-1}) are more intense, instead $E_g(2)$ (197.9 cm^{-1}) is less intense while the peak located at 515.7 cm^{-1} is due to the overlapping between $B_{1g}(2)$ and A_{1g} movements. However, at annealing temperatures of 500°C or higher, reflections from the TiO_2 rutile phase appear in addition to those from the TiO_2 anatase phase (see Fig. S8c in appendix). The sample annealed at 450°C was characterized using high-resolution transmission electron microscopy (HRTEM) [21]. According to the results, the TiO_2 rutile phase is present at the bottom of the NTs, at the interface with the metallic Ti layer. The top structure, on the other hand,

is still characterized by a crystalline TiO_2 anatase structure (refer to figure A7 in appendix A). Additionally, the surface debris or titania patches of the TiO_2 NTs ordered array provide an amorphous outcome. Crystalline TiO_2 anatase lines are clearly defined in TiNT-HS (sample synthesized hydrothermally) after being calcined at 450°C (see figure A8b).

3.3.6 Electrocatalytic tests

Figure 3.7 displays the Faradic efficiencies (FE) for GO (glyoxylic acid, FE_{GO}) and GC (glycolic acid, $FE_{GC)}$ as well as the OX conversion after two hours of electrocatalytic experiments at three applied potentials (-0.8, -0.9, and -1.0 V vs RHE). The OX concentration used in all sample tests was 0.03M. Scheme 3.1 displays the experimental setup.

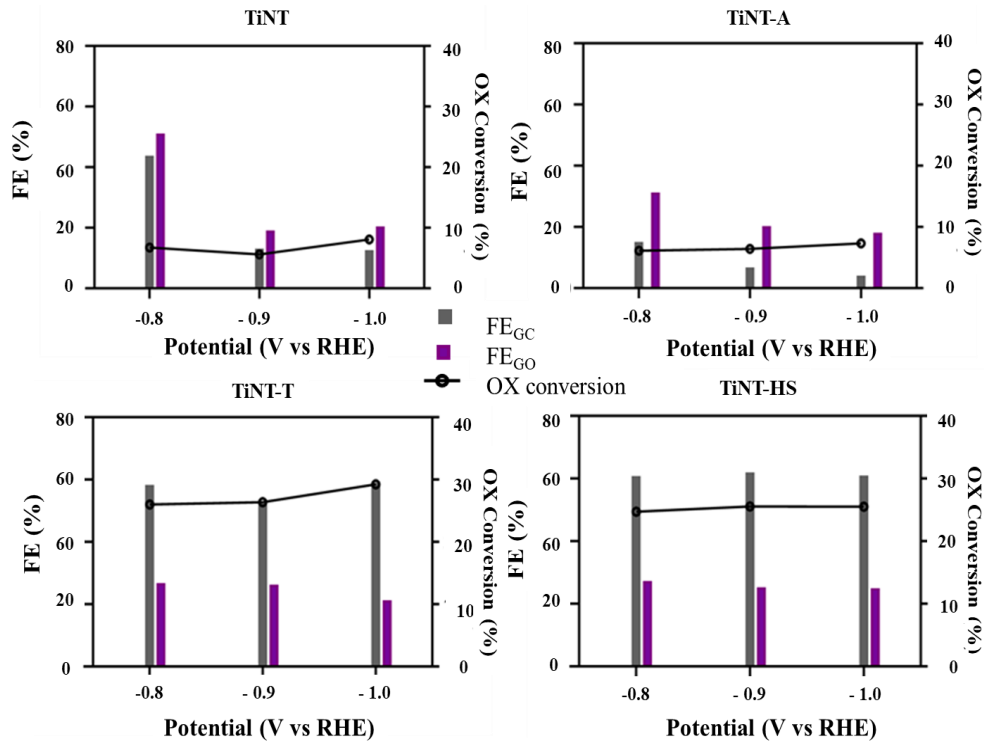

Figure 3.7 *Performances (Faradaic efficiency (FE) and OX conversion) at three potentials examined for the prepared electrodes*

The electrocatalytic performances can be categorized into two types:

(i) Although TiNT and TiNT-A show low OX conversion (<10%) and predominant GO creation in relation to GC, TiNT-A has lower total FEs (FE_{GO} + FE_{GC}) compared to TiNT. The difference lies in the formation of H_2 on the side.

(ii) The TiNT-T and TiNT-HS samples showed approximately three times better OX conversion and larger FE_{GC} compared to the initial set of electrodes. Additionally, they exhibited higher global efficiency (FE_{GC} + FE_{GO}).

The applied potential had no effect on performance, although it did cause a slight increase in OX conversion. At the ideal applied potential of -0.8 V, TiNT-T and TiNT-HS had FE_{GC} values of 58.3% and 60.8%, respectively. Every sample at each potential under investigation had a similar OX conversion. Table 3.2 shows the average value. It is noted that the conversion increases from approximately 7% (for TiNT and TiNT-A) to 26% and 32% with TiNT-HS and TiNT-T, respectively.

The full set of electrocatalytic results, including faradaic efficiency, conversion and average current density, can be found in the Appendix A (Table A1). A comparison with the Ti foil after an oxidative pretreatment (Ti-T) at 450°C for 30 minutes (the same pretreatment for the TiNT-T electrode) is also provided. Table A1 does not show the behavior of the Ti foil substrate, which is completely inert in GO or GC synthesis. Although there is some activity after the pre-oxidation treatment (Ti-T), it is often less than in electrodes made by anodic oxidation. These findings confirm the role of TiO_2 as the electroactive element.

Although ultrasonic treatment has been reported in the literature as a method to remove surface TiO_2 amorphous patches or debris and clean the electrode surface [22,23], it has been found to have a minor or even negative effect on the electro reduction of OX, confirming that these patches contribute to the process rather than improve performance (Figure A9).

3.4 Relationships between electrode properties and reactivity

Some linear correlations were found between electrocatalytic reactivity and electrode properties as determined by previously mentioned characterization methods. The findings are summarized in Fig. 3.8. Additionally, a linear relationship was observed between the XPS analysis quantified Ti^{3+} species and the intensities of the O2v peaks (Figure 3.8 b). O2v (indicated in this work as oxygen vacancies for conciseness) are correlated to a chemical shift in the O1s peak due to oxygen species neighboring to oxygen vacancies. However, it can be concluded that O2v are linked to the formation of reduced titanium ions (Ti^{3+}) in amorphous titanium dioxide.

There are more debris on the surface of TiNT-T, followed by TiNT-HS, suggesting that little debris are more easily reducible when they interact with the underlying TiO_2 NTs array. Instead, more dense and compact debris and patches are less reducible. The relationship between the anodic peak intensity determined by CV (Figure 3.5) and the O2v concentration determined by XPS (Figure 3.8 c) supports this hypothesis. Furthermore, there is a linear correlation between the average OX conversion and the O2v concentration (Figure 3.8 a). Therefore, to increase the reactivity in these electrodes, it is necessary to enhance the reducibility of the TiO_2.

When analyzing the anodic peak intensity between -0.46V and -0.56 V in CV tests (Ipa) vs. O2v correlation (figure 3.8), it is important to note that the regression line does not pass through zero. Instead, it intersects the X-axis at O2v=7%. This indicates that only a small percentage of oxygen vacancies (O2v) are inactive. This could be because they are mostly inaccessible for electrocatalytic activity, as they are located at the interface between the TiO_2 nanotubes and the Ti substrate and therefore do not contribute to the activity.

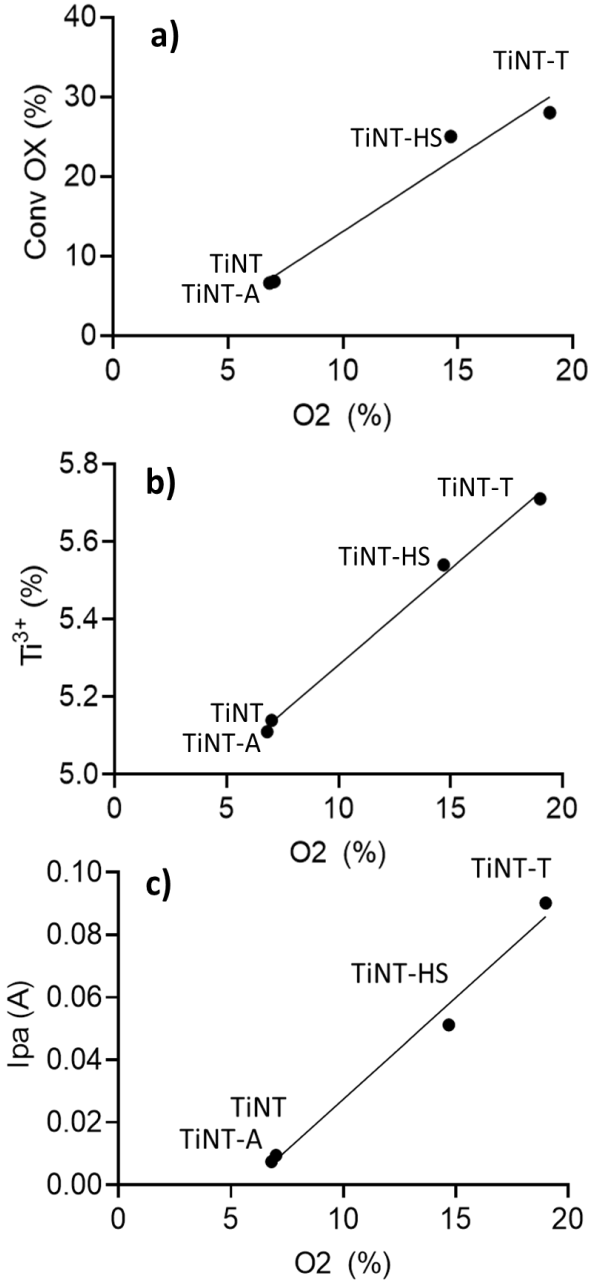

Figure 3.8 *The TiO_2 NTs electrode exhibited linear relationships among the percentage of O2v (oxygen vacancies determined by XPS) percentage and (a) the conversion of OX, (b) the concentration of Ti^{3+} (determined by XPS), and (c) Ipa (peak intensity in CV tests for the anodic peak in the range between −0.8 V and −0.9 V)*

3.5 RBA growth mechanism

The previous section discusses the characteristics and reactivity of electrodes created through anodic oxidation of Ti foils in aged solution. This provides insight into the active species involved in the electrocatalytic reduction of OX to glycolic acid. It was observed that a more aged solution only resulted in a dense nanostructured TiO_2 (TiNT-A) layer without nanotubes, which are essential for the reduction of OX to GC. This is confirmed by the higher performances (FE_{GC} and OX conversion) of the TiNT sample and the TiNT-T, which show the presence of small amorphous patches, debris or nanoparticles of TiO_2 together with the TiO_2 nanotubes, and the TiNT-HS used as an alternative preparation to obtain nanotubes without an ordered packing.

The anodization curves in Figure 3.3 provide indications of the formation mechanism, emphasizing the role of thermal pretreatment (TiNT-T) in producing more defined and uniform nanotubes. Additionally, linear correlations were obtained by correlating XPS and CV data with catalytic behavior (OX conversion), highlighting the key role of oxygen vacancies and identifying Ti^{3+} sites as the active species in the reaction.

The following section will discuss the synthesis of pure titania electrodes using rapid breakdown anodization (RBA) instead of traditional field assisted anodization mechanism (FAD). Regarding the hydrogenation of OX, this process has been researched because a more porous nanostructure should increase both the surface area and the quantity of active species on the surface and exposed to the reaction environment. To reach RBA condition the applied anodization potential has been increased. An exhaustive description of RBA and its differences with FAD theory was provided in the previous chapter.

3.5.1 Interpretation of RBA anodization curves and morphologic features

The anodization curves (I-t) of the electrodes anodized at 60 V consistently displayed greater anodic currents over time compared to the samples prepared at 50 V (Figure 3.9 a).

Specifically, TiNT60-15 exhibited initial (I_0) and minimum (I_{min}) currents of 0.087 and 0.046 A, respectively, with an anodization time of 900 s (15 min). After 65

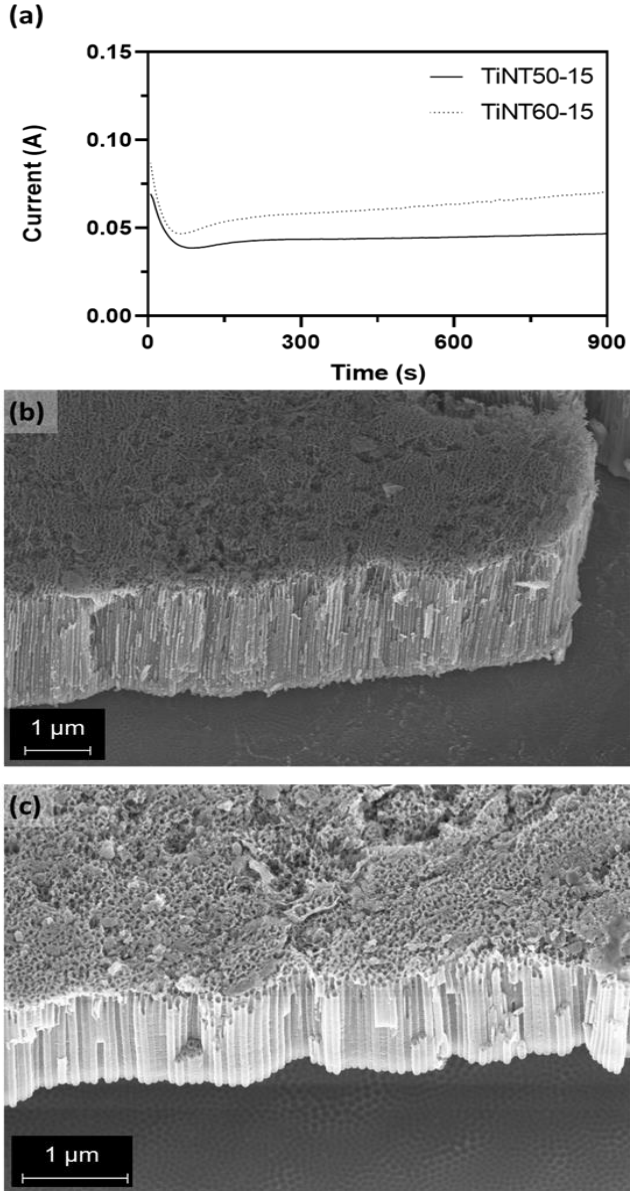

Figure 3.9 *Anodization curves (current vs time) (a) and FESEM micrographs of TiNT60-15 (b) and TiNT50-15 (c) samples.*

seconds (t_{min}), I_{min} was measured and compared to TiNT50-15. The study found that I_0 was 0.069 A, I_{min} was 0.038 A, and t_{min} was 90 s. The AO current steadily increased after reaching I_{min} until the end of the AO procedure at 900 s, without reaching a plateau. The increase in AO current was most significant at 60 V, where notable current fluctuations were observed.

The anodic current (called ionic current in this stage) first decreases up to I_{min} because of the migration of Ti^{4+} and O^{2-} ions to form a compact TiO_2 layer. This process continues until the oxide layer reaches the critical thickness (I_{min}, t_{min}), and it is accelerated by increasing the field strength and, consequently, the ionic current. The critical thickness of TiO_2 may be determined by the difference between I_0 and I_{min} (ΔI_{min}). This is in accordance with previous studies [24,25].

The anodic current (named electronic current in this phase) gradually increases after t_{min}, until it reaches a plateau. However, under fast breakdown circumstances and prominent oxygen release phenomena, the current rises with fluctuations after t_{min} [15,24,26]. Therefore, TiNT60-15 greater ΔI_{min} suggests the formation of a thicker, more compact, and non-conductive oxide layer at 60 V compared to 50 V [24,25]. Additionally, the significant increase in the AO current and the detected oscillations after t_{min} [27–29] suggest the presence of prevailing breakdown conditions and oxygen bubble release.

FESEM micrographs of TiNT60-15 and TiNT50-15 show an orderly array of vertically aligned nanotubes randomly coated by TiO_2 debris (see figure 3.9 b–c). The lack of a uniform oxide coating on the nanotubes' surface indicates that the development process stopped after 900 seconds [7]. The TiNT50-15 sample has TiO_2 NTs long 0.9 μm. They are smooth and compact, with an average outer diameter of 82 nm and wall thickness of 20 nm (see Figure A10).

The TiNT60-15 sample has larger dimensions than the other sample, with an average diameter of 85 nm and an average wall thickness of 23 nm. It has partly split NTs

[28] and a rougher surface (see Figure A11). The TiO_2 NT length is longer (2.1 μm), and it resembles porous anodic alumina (PAA) structure [30,31].

The shape of the second sample is associated to the formation of oxygen bubbles under RBA conditions. Conversely, according to the analysis of the AO curves (Figure 3.9 a) presented above, longer NTs are linked to the AO potential [32,33]. Therefore, TiO_2 was continuously produced at the base of the pores during AO at 60 V, while the critical oxide thickness remained constant. Due to the plasticity of TiO_2, the newly produced oxide migrates upward but flows around the bubbles under continuous oxygen evolution [34,35]. The FAD theory [7,36] supports anodization at 50 V as it allows for smooth walls to be achieved and reduces the likelihood of breakdown. Meanwhile, the crucial breakdown potential is achieved at 60 V in these experiments, and the nanotubes develop with rough walls in accordance with oxygen bubble theory (OBT) [37].

For the TiNT50 and TiNT60 samples anodized at 50 V and 60 V, respectively, the anodization time was increased to 1 hour to prolong the NTs development process. Increasing the anodization duration from 900 s to 3600 s (Figure 3.10 a) resulted in the TiNT50 sample reaching a distinct I_{max} of 0.0300 A after 1200 s, followed by a plateau. Furthermore, according to the FAD theory [8], the slight reduction in current observed after 2600 s suggests the formation of irregular oxide particles (debris) on the upper surface of the NTs. In contrast, the current density of the TiNT60 sample increases steadily up to 0.1231 A at 3600 s without plateauing and with noticeable current fluctuations, similar to the behavior observed in the TiNT60-15 sample.

The FESEM image of the TiNT60 sample in Figure 3.10 (b) shows a surface that is partially coated with a porous oxide layer. It is characterized by debris, nanograss [38,39], and a nanolances-like nanostructure [38,40,41] (figure A12). These morphologies were attributed to the overetching of the upper section of the nanotubes by the fluorine electrolyte solution [8,33,38,42], which also caused the partial

collapse of the tubes [43]. No drop in current was detected in the anodization curve.

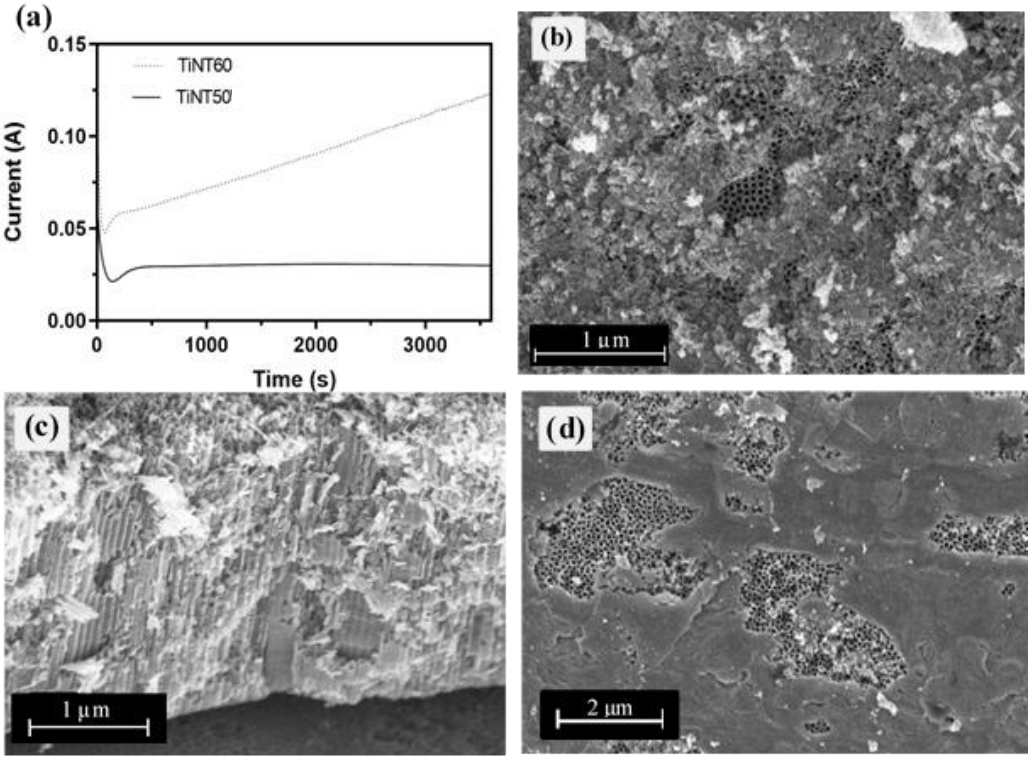

Figure 3.10 *Anodization curves (a) and FESEM micrographs of TiNT60 (b,c) and TiNT50 (d).*

The lack of similar morphologies on the TiNT60-15 surface supports this theory, indicating that the etching of the outermost surface occurred over prolonged contact with an electrolyte containing fluoride. Beneath the porous inhomogeneous oxide layer (figure 3.10 c), there are aligned TiO_2 NTs with a wall thickness of 21 nm, an average tube diameter of 83 nm, and a length of 3 µm. As previously observed for TiNT60-15, the NT walls exhibit porosity similar to that of PAA. A FESEM image of TiNT50 (figure 3.10 d) shows a NTs array beneath a porous oxide layer, that was produced by debris formation during the last part of the anodization process, as explained above.

Figure A13 compares the anodization curves for TiNT and TiNT50 samples, both obtained at 50V for 1h but with a 60-min aged and fresh solution, respectively. The

current of TiNT50 is consistently higher than that of TiNT, despite its lower I_0. This difference can be attributed to the varying fluoride ion concentrations in the electrolyte solutions. I_{min} is reached after 120 seconds for both samples because the oxide thickness is independent from F^- concentration but it depends mostly on the applied voltage [44]. Although the ΔI between I_{min} and I_{max} appears to be lower for TiNT50, the current increases less markedly until 1200 seconds, unlike TiNT, which reaches I_{max} after 480 seconds. This indicates that the nanotube growth process takes longer for TiNT50, explaining why the nanotubes in this sample are more defined and longer than those in the TiNT sample.

3.5.2 The effects of pretreatments

The passivation of the Ti foil and the formation of a TiO_2 layer resulted from the thermal and electrochemical pretreatments applied to the Ti foil surface. Specifically, the thermal pretreatment produced a compact and stable anatase oxide film layer [45], while the electrochemical pretreatment resulted in a compact and amorphous oxide coating [46,47] (Figure A14 b). In the latter sample, the current gradually diminished over time as a result of the formation of a compact oxide layer (Figure A14a-c) [7].

Figure 3.11 (a) compares the anodization curves of TiNT60-T (thermal pretreatment) and TiNT60-E (electrochemical pretreatment) samples with TiNT60.

The current values of the pretreatment samples were consistently lower than those of TiNT60:

(i) Specifically, for TiNT60-T and TiNT60-E, I_0 was 33% and 50% lower than that of TiNT60. Additionally, in both samples, the current dropped significantly slower, reaching an I_{min} of 0.026 A for TiNT60-E and 0.039 A for TiNT60-T after 450 and 700 seconds, respectively. This characteristic is due to the reduced conductivity of the prepared oxide layer following thermal or electrochemical preparation. Compared to TiNT60-T, TiNT60-E exhibited the lowest I_0 and a less significant reduction in current. This finding suggests that the electrochemical

pretreatment delays the formation of NTs by creating a thicker preformed oxide layer.

(ii) Due to the RBA effect, the current in TiNT60-E increased with fluctuations in the current density after reaching a minimum. In contrast, sample TiNT60-T has a smaller current slope than the preceding sample, and the last portion of the curve nearly reaches a plateau, signifying that the growth process is complete. This finding suggests that, even when anodized at 60 V, the RBA condition is not prominent in this sample and that the growth process is consistent with the FAD theory. However, TiNT60-T exhibited a greater increase in current with minimal fluctuations when compared to TiNT sample, the pre-treatment thermal sample produced at 50 V in an aged solution (Figure A15), as previously described in this work. RBA conditions are also present here but with a less marked effect observable in the anodization curve. Even in the latter part of the anodization curve, where a near-plateau was observed, the current gradually increased.

Figures 3.11 (b) and 3.11 (c) display FESEM micrographs that support these observations. In both samples, a TiO_2 array is visible behind the oxide layer, but the morphologies differ significantly. TiNT60-E (Figure 3.11 c) exhibits an apparent curvature in its NTs due to certain concave and convex patches in the underlying layer [8] generated during the electrochemical pretreatment. The samples under investigation had a wall thickness of 15 nm, which was the thinnest among all samples. Additionally, the average tube diameter was larger than that of the previous samples, measuring approximately 95 nm. The magnification in figure 3.11 (c) shows rough NTs walls that support the RBA condition and the growth of oxygen bubbles throughout the anodization process. The upper portion of the nanotubes is specifically broken vertically, but the tube form is still discernible, and there are no nanolance or nanograss-like morphologies. This suggests that the amorphous oxide

layer created during the electrochemical pretreatment is likely what limits the etching of the NTs. The larger length of the NTs (about 4.7 µm) supports this result.

Furthermore, Figure A16 shows a rough surface with many protrusions and holes in the overlying oxide layer. Zhang et al. [47] synthesized an NTs array under a prefabricated compact film. After 180 seconds of anodization at 60 V, the compact film swelled due to the expanding oxide's volume, resulting in ridges or fissures on the upper surface. Oxygen bubbles collected beneath the prepared oxide layer and protrusion can be observed onto the top of compact layer in TiNT60-E.

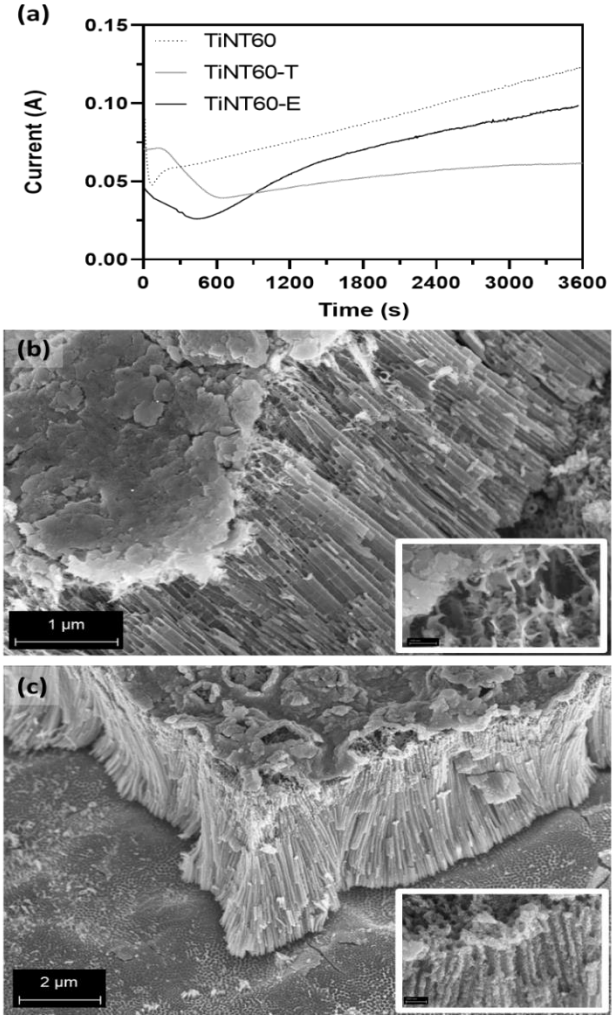

Figure 3.11 *Anodization curves (a) and FESEM micrographs of TiNT60-T (b) and TiNT60-E (c)*

The oxide layer breaks down and pores start to develop when the oxygen pressure reaches a certain point. As a result, the electrolyte may enter the pores. The shape of the holes and protrusions that are developed from outside to inside supports this suggestion.

Otherwise, the overlying oxide layer in TiNT60-T (Figure 3.11 b) is more compact and no holes and protrusions are observed. Additionally, a few irregular fractures randomly appear on the surface (Figure A17), likely due to pretreatment-induced stress [48]. The underlying TiO_2 NT array exhibits high order and vertical alignment with the surface. The NTs have uniform dimensions, smooth walls that are fractured, and with some surface holes. The low roughness and absence of holes and protrusions in the walls of the NTs suggest that oxygen evolution is not the primary process. However, even if the bubble mold effect is not observed, RBA conditions are created due to the presence of holes in the NT walls [8].

Additionally, upon magnification of Figure 3.11 (b), it is evident that the upper section of the NTs had significantly dissolved. This outcome suggests that the anatase TiO_2 layer that covers the NT array is not effectively protecting it from etching by fluorine ions that seep through surface fissures [49]. Supporting this suggestion is the fact that the NTs in TiNT60-T are shorter (1.5 μm) than those in TiNT60-E. These findings demonstrate that the development of NTs is influenced by pretreatment:

- Thermal pretreatment resulted in a layer of compacted oxide with uneven fractures. The smooth walls of the NTs suggest that oxygen bubble development is not significant, despite the presence of RBA conditions. This finding is consistent with Huang et al.'s research [28]. Moreover, the length of the NTs was affected by the etching of the electrolyte solution.
- The electrochemical pretreatment inhibited the dissolution on the top portion of the NTs by fluorine electrolyte solution and encouraged the development of oxygen bubbles. This result is consistent with Song et al. work [50], who

reported an undamaged tube top on the Ti substrate prior to anodization without nanolance or nanograss-like morphologies.

The variation in morphology could be attributed to the type of pretreatment used. During the electrochemical process carried out in an acidic solution, some anion impurities are introduced into the TiO_2 film, which increases oxygen bubble release and favors RBA conditions. In TiNT60-T, the incorporation of anions during anodization is limited by the thermally generated TiO_2 layer, leading to a lower diffusion rate. As a result, the anodization curve showed a less noticeable impact. Additionally, the fissures on the thermally produced oxide surface prevented oxygen from building up.

3.5.3 TiO_2 NTs surface roughness

Using tapping mode AFM analysis, the surface nanostructure of the working electrodes was assessed. Appendix A provides information on the 2D and 3D pictures acquired using AFM (Figure A18), which show regions coated with TiO_2 debris and other regions where NTs are visible.

Table 2.3 presents the root mean square roughness (RMS) values. The application of voltage resulted in an increase in both diameter and surface roughness. The effects of the pretreatments on roughness varied. TiNT60 (RMS=64 nm) experienced a decrease in RMS to 37.61 nm after thermal treatment, while TiNT60-E showed an increase to the highest value of 70.73 nm. FESEM revealed the presence of grains covering the TiNT with a diameter of up to 1 μm.

The morphology of pretreatments caused the varied effects on the surface roughness. Following thermal treatment, the Ti foil's RMS remained almost unchanged at 33.63 nm (Ti-T). For Ti-E, the RMS increased to 53.67 nm. The roughness of the initial surface was followed by the growing layer, which, along with the RBA conditions found during the AO, contributed to the increase in RMS of TiNT60-E. On TiNT60-T, where the FAD mechanism governs the growth process and the RBA condition is

not dominant, this effect is less pronounced. This confirms that the increased roughness is caused by the RBA conditions.

Table 3.3 Main morphological features and ECSA results for tested cathodes

Short Name	*[a]Rms [nm]*	*[b]Tube diameter [nm]*	*[b]Wall thickness [nm]*	*[b]Tube length [nm] x10^3*	*ECSA [cm^2][c]*
Ti foil	*33.63*	-	-	-	-
Ti-E	*53.67*	-	-	-	-
Ti-T	*34.12*	-	-	-	-
TiNT50-15	*30.74*	*82*	*20*	*0.9*	*3.7*
TiNT60-T	*37.61*	*100*	*19*	*1.5*	*18.6*
TiNT60-15	*51.69*	*85*	*23*	*2.1*	*19.8*
TiNT50	*61.32*	*65*	*19*	*2.2*	*21.1*
TiNT60	*64.00*	*83*	*21*	*3.0*	*29.1*
TiNT60-E	*70.73*	*95*	*15*	*4.7*	*30.5*

[a] AFM calculated by software Gwyddion on about 10 images

[b] Measured by FESEM images

[c] Calculated by Double Layer Capacitance (CDL) via cyclic voltammetry (CV) in a non-faradaic range

3.5.4 Electrocatalytic behavior

The previous sections outcomes indicate that the literature-based findings can be controlled and rationalized, allowing for the creation of a variety of TiNT electrodes with precise control over their macro, micro, and nanostructure characteristics. This control is achieved by adjusting the preparation settings of the AO method. The electrodes were studied in the -0.8V – -1.0 V vs. RHE potential range for OX selective conversion to GC at different potentials (see figure 3.12).

The electrocatalytic findings are presented in Table A1, which shows that the only products detected were GO and GC (FE_{GO}, FE_{GC}), formed via OX conversion. As samples discussed in the first part of this chapter, the OX conversion was minimally affected by the tested potentials. However, FE_{GO} and FE_{GC} experienced a reduction when potentials ranging from -0.8 to -1.0 V in relation to RHE were applied. The significance of the competitive hydrogen evolution (HER) reaction at -1.0 V was linked to the latter event. The electrode characteristics significantly impacted the activity and selectivity. Increasing the AO potential from 50 to 60 V and the AO time from 900 s to 3600 s at all investigated applied potentials resulted in an increase in the average OX conversion and FE_{GC} on unpretreated Ti foils from 32% (TiNT50-15) to 50.5% (TiNT-60) and from 38.3% (TiNT50-15) to 82.2% (TiNT-60), respectively. These values were averaged for the three evaluated potentials. The average FE_{GO} decreases from 38.4% (TiNT50-15) to 9.9% (TiNT60).

The thermally pretreated catalyst (TiNT60-T) reduces FE_{GC} and OX conversion by 11% and 29%, respectively, compared to the untreated catalyst (TiNT60). As a result, FE_{GO} increases by 10%. However, there are minimal performance differences between TiNT-60 and the electrochemically processed catalyst (TiNT60-E). In contrast, we examined a Ti foil that had undergone electrochemical preparation without first undergoing an AO treatment (Ti-E) showing the lowest activity (Figure A19).

Specifically, the OX conversion decreased along with the FE_{GO} and FE_{GC} with the applied potential, going from 7% (-0.8 V) to 3% (-1.0 V). This observation is consistent with Zhao et al. results [20] on a rough TiO_2 layer. Prevalent HER was associated with low FE_{GC} and FE_{GO}. The reaction pathway, in which GO acts as an intermediary for the production of GC (Scheme 2.2), is consistent with the reported trends for OX conversion, FE_{GO}, and FE_{GC}. These trends also demonstrate the

positive influence of AO potential and AO duration on electrode activity and selectivity.

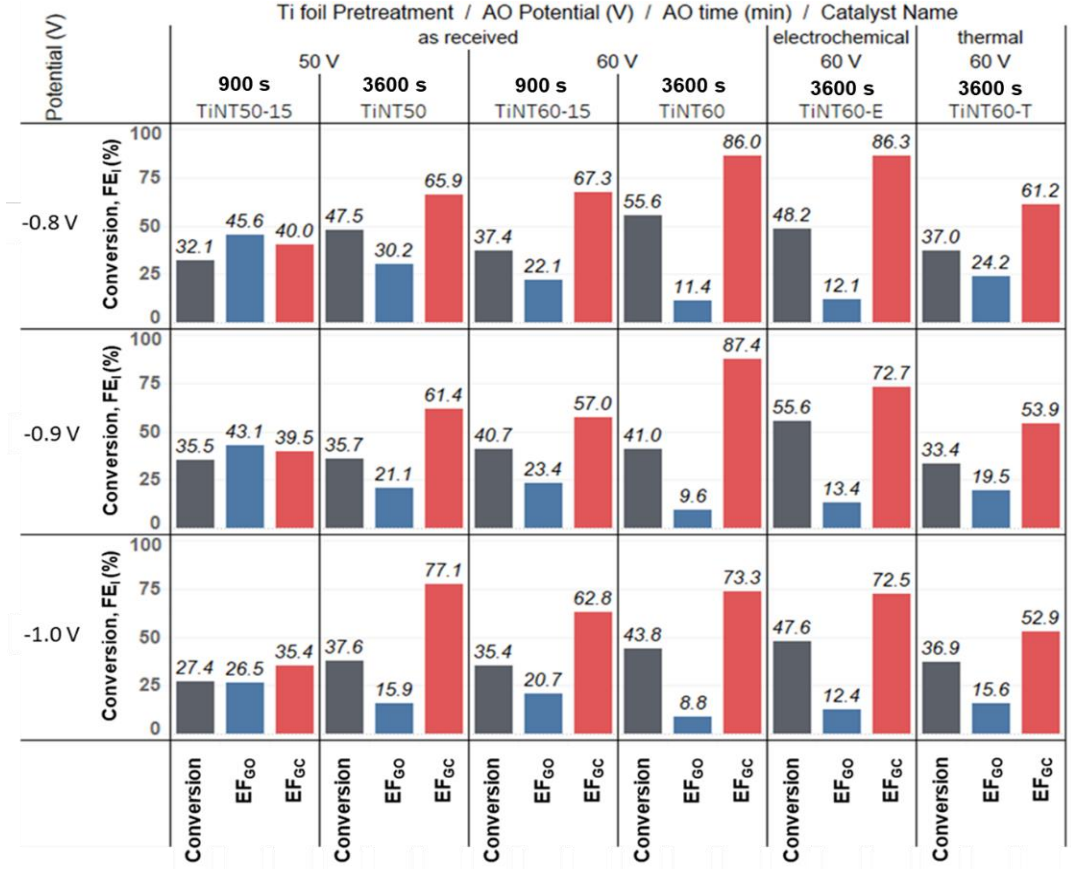

Figure 3.12 *For the synthesized cathodes, faradaic efficiency (FE) and oxalic acid conversion (OX conv) were determined at −0.8, −0.9, and −1.0 V against RHE (amperometric tests conducted at room temperature for two hours, with an initial [OX] of 0.03 M; anodic compartment: 0.2 M Na_2SO_4 and H_2SO_4 to adjust to pH 2)*

Preliminary experiments were conducted on TiNT60-15, TiNT60-T and TiNT-T catalysts to assess their stability. The experiments were carried out for 8 hours at -0.9 V vs. RHE (Figure A20). All samples showed an increase in FEs, but with different patterns. TiNT60-T catalyst showed the highest increase in FE_{GC}, reaching 74%, while FE_{GO} increased by around 17% compared to only 3% FE_{GC} in the TiNT60-15 and TiNT-T catalysts. TiNT60-15 catalyst showed a drop of 10% in OX conversion, while for the thermal pretreated samples remained steady.

Figure A21 compares the performances of the TiNT and TiNT50 samples in terms of FEs and OX conversion. The results show a significant difference in selectivity between the two samples. Specifically, the FE_{GC} of TINT50 is almost four times that of the TiNT sample, while FE_{GO} is about 3 times lower in TiNT50, indicating significantly higher conversion. These results highlight the importance of using a fresh anodization solution to achieve a more catalytically active nanostructure.

3.5.5 Redox proprieties

Figure 3.13 (a–c) shows the blank voltammograms (0.2 M Na_2SO_4 solution, pH 2) for all the investigated samples. Similar behavior to the samples examined in the first part of the chapter can be observed:

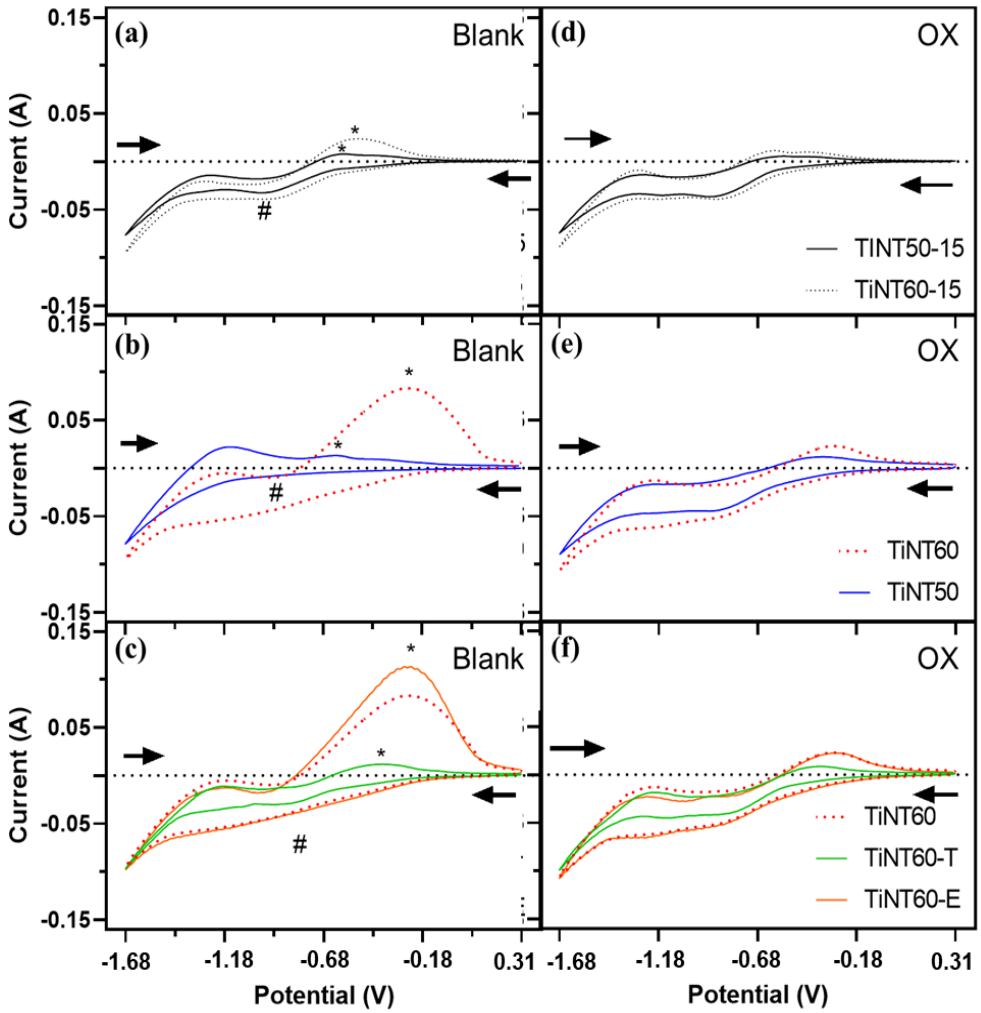

Figure 3.13 *CV in blank (a – c); $[Na_2SO_4]_{cathode} = [Na_2SO_4]_{anode} = 0.2$ M, pH = 2) and in OX solution (d – e); $[OX]_{0,\ cathode} = 0.03$M, $[Na_2SO_4]_{cathode} = [Na_2SO_4]_{anode} = 0.2$ M, pH = 2). Potentials are referred to RHE.*

- At -0.62 V vs RHE there is the reversible peak due to Ti^{4+} reduction into Ti^{3+} (# symbol in Figure 3.13 a–c) according to eq. 10.
- At -0.96 V vs RHE the gaseous hydrogen production occurs (eq. 8).

- At -0.86V vs RHE the proton insertion-coupled electron transfer reaction and its decomposition follows (eq. 12).

The oxidation of Ti^{3+} to Ti^{4+} resulted in an anodic peak in all samples when the potential range was between -0.03 V to -0.26 V vs. RHE (* symbol in Figure 3.13 a–c). The intensity of the peak decreased in the following order:

TiNT60-E > TiNT60 > TiNT50 > TiNT60-T > TiNT60-15 > TiNT50-15

The order suggests that TiNT60-E and TiNT60 had higher concentrations of Ti^{3+} species compared to other samples with longer NTs. The anodic peak becomes less prominent at 0.03 M oxalic acid due to the conversion of oxalic acid to glyoxylic and glycolic acid by Ti^{3+} species (figure 3.13 d-f). The presence of Ti^{3+} sites increase the conductivity of the TiO_2 electrode as they act as electron-donor species located underneath the conduction band of TiO_2[51,52].

3.5.6 Presence of oxygen vacancies and crystalline features

As for previous samples, the survey spectra of catalyst studied in this section by XPS analysis shows mainly Ti and O elements. At the same time, only carbon (C 1 s peak) is present as an impurity (see Figure A22, where the TiNT-50 sample was only reported for conciseness). The high-resolution Ti2p spectra, show the doublet Ti$2p_{3/2}$ at 458.65±0.1 eV and Ti$2p_{1/2}$ at 464.19±0.1 eV, consistent with Ti^{4+} in the TiO_2 lattice. The shoulder peaks at 456.82±0.1 eV and 462.36±0.1 eV are due to Ti$2p_{3/2}$ and Ti$2p_{1/2}$ and correspond to Ti^{3+} species in Ti_2O_3 [15]. The Ti$2p_{1/2}$-Ti$2p_{3/2}$ splitting energy was 5.54 eV. Regarding fitting, see figure A23 as an example; all the other samples showed similar behavior and are not reported for conciseness.

All high-resolution O1s core level spectra of the samples (Figure A24) displayed an asymmetric curve and a small shoulder, indicating a higher concentration of oxygen species in the near-surface area [66]. The O1s spectrum of each sample was deconvoluted into two peaks, O1 and O2v. The most intense component (O1) was identified as the oxygen present in the TiO_2 crystal lattice at 529.81 ± 0.2 eV. The O2v component (531.32 ± 0.2 eV) is associated with the Ti_2O_3 surface state, which

is a combination of oxygen atoms near oxygen vacancy and Ti^{3+}. The number of O2v (indicated as oxygen vacancies) and the OX conversion exhibit a linear relationship confirming what has been previously reported (refer to Figure A25).

Glading Angle X-ray diffraction (GAXRD) was used to examine the TiO_2 NT arrays. The GAXRD pattern in Figure 3.14 confirms the presence of anatase (PDF 04-0477) and titanium metallic (PDF 44-1294) crystal diffraction peaks, originating from the anodic TiNT layer and the titanium substrates, respectively.

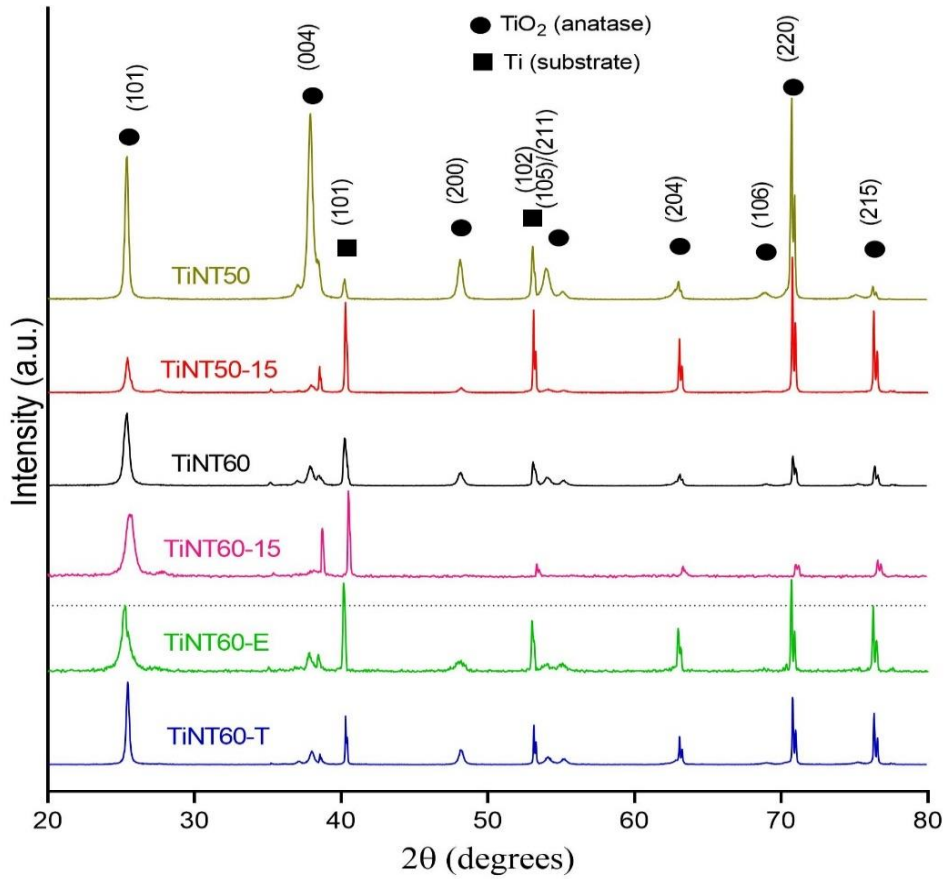

Figure 3.14 *Glading angle X-ray diffraction (GAXRD) pattern of all the synthesised electrodes*

The appearance of the expected peaks confirms that annealing resulted in the crystallization of the amorphous layers. No additional peaks were observed,

indicating the exceptional phase purity of the NTs. Table A3 shows that the high peak intensity of the samples is due to their exceptional crystallinity. The findings are consistent with the TiO_2 NTs crystallization properties described in the literature [53,54]. The diffraction peaks observed at 2θ = 25.35°, 36.96°–38.54°, 48.12°, 53.98°, 55.13°, 62.88°, 68.88°, 70.60°, and 75.18°, respectively, reflected the orientation planes of the anatase phase (101), (004), (200), (105), (211), (204), (116), (120), and (215). The Ti substrate is associated with the peaks at 2θ = 40.33° and 53.15°, which correspond to the (101) and (102) orientation planes, respectively. The high crystallinity of the TiO_2 NT arrays, which reaches about 98.8%, is shown by the sharpness of the peaks (Table A3).

3.6 RBA influence on nanostructure and other aspect on the electrocatalytic behavior of NTs electrode

3.6.1 Nanostructure and electrocatalytic behavior relationships

Even though the RBA conditions accelerate the evolution rate of NTs, it is generally believed that these conditions should be avoided due to the high defectivity, continuity and roughness of the resulting NTs (including the rapid evolution of O_2). These characteristics are unfavorable for photocatalytic activities because they increase electron-hole recombination and decrease charge separation. On the other hand, it was shown here that low homogeneity, roughness, and structural flaws of NTs are crucial for enhancing their activity in the electrocatalytic hydrogenation of oxalic acid. The experimental conditions, such as the composition of the electrolytic solution and the characteristics of the electrochemical cell, influenced the breakdown voltage.

In this work RBA conditions were established at 60 V (TiNT60-15, TiNT60, and TiNT60-E), as evidenced by the fluctuating pattern of the electronic current over time, which deviated from the FAD theory. In comparison to electrodes anodized at 50 V, the FESEM micrographs confirm that the NTs produced at 60V are split and rougher. The surface nanostructure of the untreated sample produced at 60 V

(TiNT60) differs from that of the thermally and electrochemically pretreated samples (TiNT60-T, TiNT60-E). Notably, TiNT60-E NTs array is the longest of all the samples examined, and its walls are much rougher. Probably this could be to incorporation of anions impurities during the anodization pretreatment in H_2SO_4, which can move inside the non-fully crystalline surface oxidic layer. This allows for a faster and easier formation of RBA, resulting in longer expansion of NTs and increased production of oxygen bubbles. Compared to TiNT50, the nanotubes in the thermally pretreated sample (TiNT50-T) were shorter, but their walls were smooth and severely damaged.

The anodization curve shows a trend between traditional growth (FAD) and RBA, as well as the evolution of oxygen bubbles (figure 3.11). As a result, only minor variations were observed and the anodic oxidation current nearly reached a plateau. Since the anatase layer is produced by heat treatment, anions do not contaminate it. Additionally, the crystal structure can prevent the inclusion of contaminants during the anodization process. The RBA and oxygen bubbles resulted in shorter and smoother nanotubes, likely due to their less defined or pronounced evolution. As shown in Table 3.3, the TiO_2 layer in both samples aids in increasing the tube diameter by preventing excessive etching of the nanotubes by F^- ions. The tube size of the pretreatment samples (TiNT60-T and TiNT60-E) is larger than that of untreated the sample (TiNT60), even if the anodization time was 1 hour for all three catalysts. Additionally, the samples synthesized at 50 V (TiNT50 and TiNT50-15) had different sizes compared to those anodized at 60 V (TiNT60 and TiNT60-15), which had similar diameters. The variation in tube diameters is caused by the growing processes and overetching of the top part of NTs. TiNT50 has grown in accordance with the FAD model, and overetching shortened the NTs ultimate length, resulting in smaller diameter NTs due to the decrease in inner diameter with length. In contrast, the tube diameter of the TiNT60 sample produced following the RBA model was similar to that of TiNT60-15. This was because, despite the top being

overetched, the tube development at the bottom was quicker and new oxides were continually developing. Therefore, the etching phenomena had less of an impact on the NT length and diameter at 60 V, although it was still present, as seen by the porous top layer (Figure A12).

The performances of the electrocatalysts vary based on their nanostructural characteristics. The length and roughness of the nanotube walls, in particular, are important factors that affect the catalysts activity. Samples with rough walls and grew under RBA showed increased FE_{GC} and OX conversion. TiNT60-15 showed an average increase of almost 63% in FE_{GC} and 19% in OX conversion compared to TiNT50-15. TiNT50-15 produces almost equal amounts of GO and GC with its smooth TiO_2 array (see Figure 2.13 c). By increasing the anodization time to one hour, the nanotubes became longer. As a result, their selectivity to GC improved, resulting in an average FE_{GC} of 60%, which was greater than that of TiNT50-15. Additionally, while FE_{GO} rises to around 50%, the average FE_{GC} and OX conversions of TiNT60-T are 32% and 24% lower, respectively, then those of TiNT60. Figure 3.15 (a) shows a linear relationship between the NT length and the GC selectivity, indicating the crucial role of NT length in modifying selectivity.

Previous literature suggests that longer TiO_2 NTs promote further reduction of GO to GC, as the creation of GC is a two-step reduction process with GO as an intermediary [55]. TiNT60-15 and TiNT50 operate similarly, while the sample produced after 900 seconds of anodization has shorter NTs. This finding implies that the TiO_2 catalysts activity was influenced by the NTs walls roughness. In general, the samples grown by OBT exhibit higher roughness (see Table 3.3). The root mean square (RMS) of the TiNT60-15 sample is greater than that of TiNT50-15. Additionally, as the anodization time increases to 50 V (TiNT-50) and 60 V (TiNT-60), the roughness also increases. The roughness of the pretreatment samples corresponds with the previously described morphological characteristics.

TiNT60-T exhibits greater roughness than TiNT50-15 but is less rough than samples obtained at 60 V (TiNT60 and TiNT60-15). This suggests that the growth process of TiNT60-T is intermediate between RBA (and oxygen bubble development) and traditional growth (FAD). TiNT60-E has the greatest RMS (70.3 nm) of all the samples due to its ease of setup for RBA conditions. Longer and rougher NTs can improve OX conversion, as supported by the linear relationships seen in Figure 3.15 (b). This may be due to the abundance of accessible sites for electron transfer associated with Ti^{3+} and oxygen vacancies (see below), which is also supported by the linear correlation in Figure A25. Additionally, the validity of this concept was confirmed through CV analysis in a blank solution (0.2 M Na_2SO_4, pH=2). The analysis revealed an increase in the anodic peak intensity due to the oxidation of Ti^{3+} to Ti^{4+}, which occurred in the same order as the length of the NTs. Additionally, a decrease in the potential of the Ti^{3+}/Ti^{4+} oxidation peak was observed. This shift can be attributed to two factors:

i) the length of the nanotubes: longer nanotubes showed a more significant shift, as seen in TiNT60-E compared to TiNT60.

ii) the roughness of the sample: samples produced during oxygen bubbles release (OBT) show a greater shift. For instance, although TiNT50 had longer NTs than TiNT60-15, the shifting is less noticeable.

The estimate of the electrochemical active surface area (ECSA) also indicates a significant increase in accessible Ti^{3+} active sites in longer and rougher NTs. Figure 3.15 (c) shows that larger ECSAs correspond to greater O2v values. This suggests a synergistic relationship between the roughness and length of the NTs, resulting in increased OX conversion and ECSA. Figure 3.15 (d) demonstrates a linear relationship between ECSA and selectivity to GC (S_{GC}) and GO (S_{GO}), indicating that selectivity can be influenced by factors other than length since the ECSA increases with the roughness (Table 3.3), and the correlation in Figure 3.15 (a) is less precise than that in Figure 3.15 (d). Specifically, S_{GO} declines as ECSA rises, while a greater S_{GC} is shown. In the latter case, the regression line crosses the Y-axis at

around 4% instead of passing through zero. This observation is in line with the results of Zhao et al. [15], which proposed that a roughened TiO_2 film could serve as an active catalyst for the hydrogenation of OX to GC.

Additionally, this is supported by the testing results of the electrochemical pretreated sample (TiNT-E), which show GC production after two hours at -0.8 V vs. RHE.

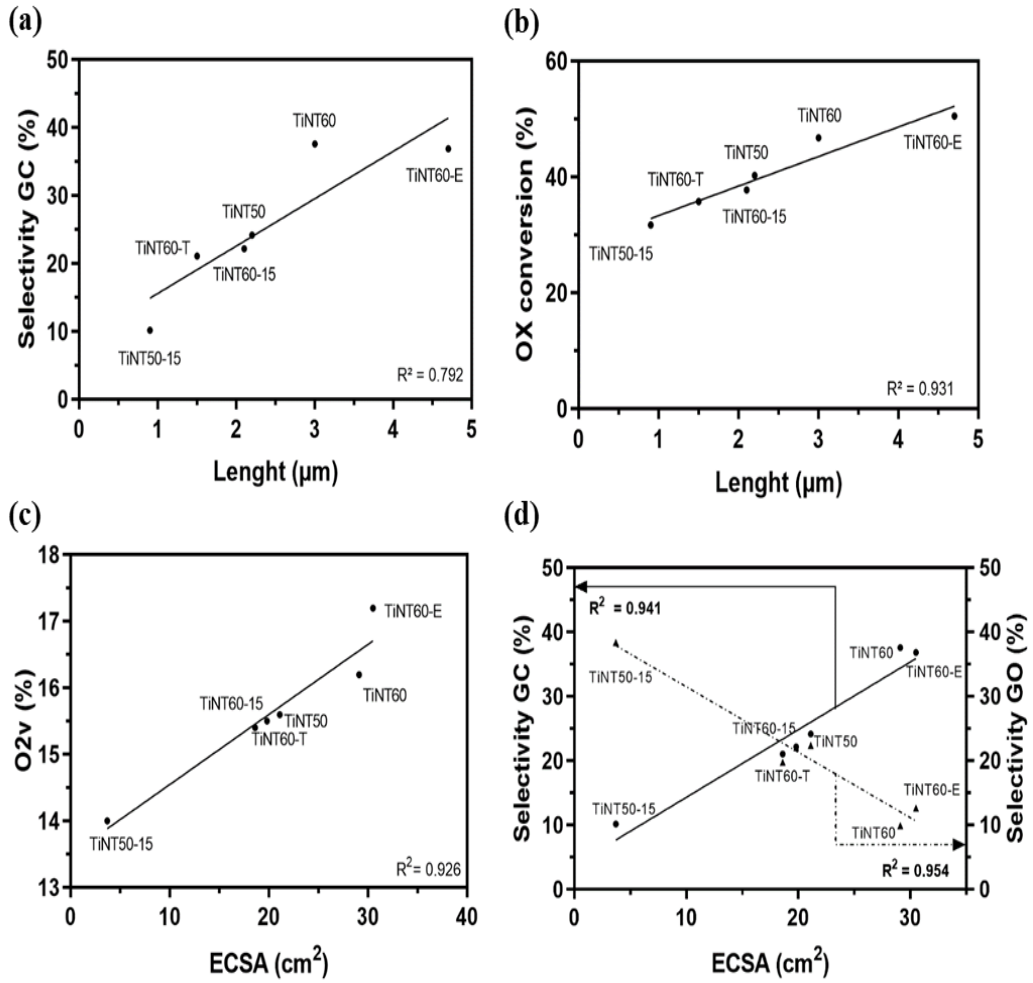

Figure 3.15 *Correlation between length of NTs and average selectivity to GC (a) and OX conversion (b). Correlation between ECSA and O2v (c), and Selectivity to GC (dark line) and GO (dashed line) (d)*

3.6.2 Mechanistic aspects of electrocatalytic hydrogenation of OX

The results are consistent with the literature, indicating that OX undergoes a selective reaction resulting in the formation of GO, which subsequently forms GC through a two-step sequential process of two-electron reduction (Scheme 2.2). For example, FE_{GO} and FE_{GC} exhibit an inverse linear relationship with respect to ECSA (see Figure 3.15d). It is important to note that the mechanistic elements of electrocatalytic processes differ significantly from those observed in solid catalysts [56,57]. In fact, in electrochemistry factors governing electron transport have a greater impact on reaction rate than the characteristics of the active sites. One of the most crucial factors is charge localization. The rate of electron transfer is influenced by local changes in the electrical field and electrolyte rearrangement, which are determined by the nanostructure and electrode properties. Most electrocatalytic research tends to overlook the electrode nanostructure in favor of a uniform potential distribution. On the other hand, the presented data demonstrate how the electrode's nanostructure affects both activity and selectivity. In addition, the results collected by CV and XPS in this second section confirm what has been highlighted in the first part of this chapter, namely that Ti^{3+} species can be identified as the active site of the reaction. In heterogeneous catalysts, electron transfer takes place at Ti^{3+} or O2v sites, which serve as electrocatalytic sites, rather than at hydrogenation sites in the conventional hydrogenation process. Considering the (101) crystalline plane of the anatase phase, which is the most exposed on the surface, an oxygen atom bridges two Ti atoms, one with coordination number six and the other with coordination number five. This provides a tentative explanation for the nature of the reduced titania species formed. After the removal of oxygen, the coordination number of Ti changes to 5 and 4, respectively. This results in the reduction of Ti^{4+} to Ti^{3+} via electron transfer in the third orbital, producing a molecule that resembles Ti_2O_3. Oxygen vacancies in the bulk or surface of TiO_2 generate one or two free electrons, which occupy the space previously occupied by the O^{2-} anion in the lattice. This minimizes the energy cost of vacancy formation in the faulty crystal [54]. By creating a donor level 0.7 eV

below the bottom conduction band, these electrons directly alter the electronic structure of TiO_2 [58].

Another aspect to consider is whether the process occurs through inner- or outer-sphere electron transfer or via the adsorption of reactants or intermediates. It has been reported that the presence of oxygen vacancies can alter the adsorption of certain small molecules, such as CO, N_2O, H_2O, H_2, O_2, and HCOOH, by promoting dissociative adsorption over molecular adsorption [40,59]. The CV tests suggest an outer sphere electron transfer, and the concentration of OX does not significantly affect the electron transfer [60]. However, the negatively charged (cathode) surface of the TiO_2 NTs hinders the chemisorption of OX, which mainly occurs through the coordination of the carbonyl group or the creation of a carboxylate [61–63]. Studies published in the literature on OX chemisorption on titania investigate the process as it may arise in heterogeneous catalysis. However, it is important to note that these studies do not take into account the surface charge present in electrocatalysis. Based on research on the primary electrochemical processes in semiconductors [64], it is propose here that an outer-sphere electron transport mechanism governs the behavior for additional electrocatalytic events, such as oxygen reduction [65]. Further research is necessary. Moreover, this outer-sphere electron transfer process [66] would exclude the existence of coupled electron/proton transfer, for which there is no evidence in our data.

These species control the accumulation of charges and promote electron transfer to the incoming reagent (OX) or intermediates (GO) through inner- or outer-sphere electron transfer or electron transfer to chemisorbed species.

3.6.3 Other factors influencing the performance

The critical involvement of the Ti^{3+}/Ti^{4+} redox pair in the process has been demonstrated and is consistent with findings from other literature sources [15,55]. The performance of the reduction process depends on several parameters, including the existence of readily accessible active sites and the length-dependent diffusion

time inside the nanotubes. It has been proposed, but not validated, that longer times inside the nanotubes encourage sequential responses and thereby affect selectivity [55,67]. The effective residence time of the reagents and intermediates within the electrocatalyst layer may be determined by mass diffusion features associated with the nanotube parameters, such as length and diameter. Although research on this topic is still in its early stages [68,69] and does not address selective hydrogenation reactions, it is important to note that diffusion within a charged layer (electrode) differs from that of gas or liquid catalytic processes.

It is important to note that heterogeneous catalytic processes, such as selective hydrogenation, can be carried out at high space velocities or with extremely small particle sizes without being limited by mass or heat diffusional restrictions. These tests can be used to determine the actual kinetics of the reaction. Due to the features of electrocatalytic reactors and electrodes, there are limited opportunities for comparable research in electrocatalytic experiments, especially with the nanoporous electrodes examined here, to avoid mass transfer constraints. It is essential to consider these factors in mechanistic and design considerations, even though they are often overlooked in electrocatalytic research.

The porosity of the active electrocatalyst is a crucial element that controls the ECSA and, consequently, the reaction rate. The electrochemical surface area (ECSA) is related to the catalytic behavior and is inversely correlated with the density of Ti^{3+} or O2v sites. The number of these sites and the electrocatalytic efficiency are determined by the nanostructure. Specifically, the accessibility (a critical factor in porous electrodes) and stability of these defect sites are controlled by the nanostructure. It is important to note that these TiO_2 NT materials contain nanoporosity associated their growth process and the superficial patches of titania. However, leaching during the catalytic process may improve the performance and porosity. Diffusion within this nanopore is more challenging than within the NTs due

to its mesoporous nature, with a size of around 100 nm compared to a few nm in microporosity. The electrocatalysts' properties and performance show an intricate correlation, as seen below. It is crucial that the roughness and length of TiO_2 NTs work together. Figure 3.15c shows that higher accessible surface Ti^{3+} sites lead to improved ECSA. As a result, when the NTs roughness increases, the ECSA also rises (Figure A27). Furthermore, Figures 3.15 (a) and 3.15 (b) demonstrate that the NTs length significantly affects the availability of active sites. This discovery is supported by the linear association observed in Figure A25.

Amperometric measurements (figure A28) with higher concentrations of OX were used to demonstrate the significance of the quantity of accessible active sites for the reaction. When the OX concentration was increased to 0.1 M, both OX conversion and FEs decreased. This outcome may be due to the saturation of the surface-active site by the reactant molecules. However, based on the prior discussion, it appears that this impact is more likely related to changes in the interfacial dielectric constant. This affects the rate of outer-sphere electron transport as well as the reorganization energy [70].

The length and roughness of NTs determine the residence period of reactants/intermediates, which in turn affects selectivity. Supporting this indication, Figures 3.15 show a higher rate of GO formation as the active area increases. However, it is unclear whether GO develops at the surface (at the NTs pore mouth or on titania surface patches) or in the nanopores found in the depth of the NTs, which would determine whether it is further converted to GC. In the later scenario [67], the GO intermediate will be further reduced to GC. However, if GO is primarily generated on the exterior surface, its subsequent conversion is hindered by inadequate diffusion within the nanopores (or NTs). Thus, there may be a complex relationship between selectivity, NTs length, and ECSA. The linear relationships indicate that diffusion within the NTs is sufficiently rapid to contribute to OX conversion for most of the ECSA, including the component associated with the

active region located deep within the NTs. As the residency period of the GO intermediate within the NTs increases, its subsequent conversion is enhanced, resulting in an increase in selectivity to GC as NTs length increases. However, it is possible that diffusional constraints may affect both the relative selectivity to GO and GC and the OX conversion, thus influencing the performances. It is important to note that this statement is not a subjective evaluation, but rather a possibility that should be considered.

Figure 3.16 presents the results of experiments conducted in the flow electrochemical cell with varying electrolyte flow rates. The electrode size was adjusted to provide similar electrolyte residence periods in the anodic portion of the cell. The microturbulence at the titania electrode's surface increases with increased flow rate, which increases the diffusional rate of the reactant (OX) and the back diffusion rate of the products (GO and GC). Figure 3.16 shows a slight decrease in the relative FEs, along with a small increase in the rate of OX conversion.

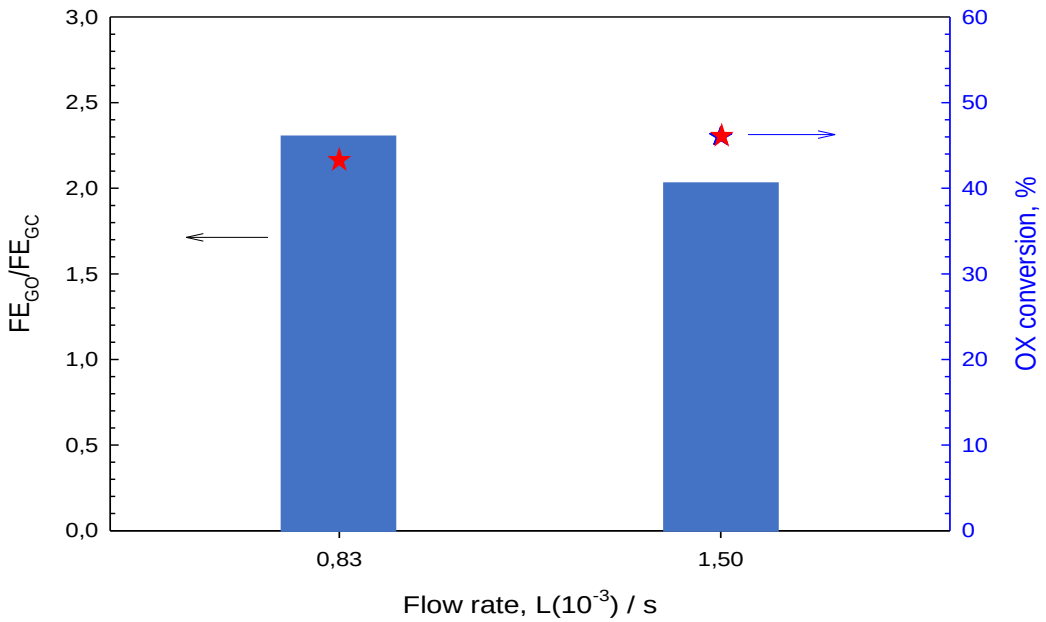

Figure 3.16 *Effect of the flow rate (at equal contact time) on TiNT50-15 performance after 5h tests: FE_{GO}/FE_{GC} ratio(left) and OX conversion (right)*

Therefore, increasing OX diffusion rates has no impact on reactant conversions, and the production of GO is only marginally improved compared to GC. This finding suggests that small diffusional constraints affect the diffusion behavior inside the NTs. However, it is worth discussing other factors related to these diffusional and mechanistic characteristics. The electron transport barrier increases as the distance from the base Ti foil increases. The base Ti foil is the growth site of the nanotubes and serves as a conductive substrate for the collection and movement of electrons. This is because titania has a relatively low electron conductivity. Thus, the length of the NTs is directly proportional to both the ECSA and resistance to electron transport. This phenomenon may cause a potential gradient along the axial profile of the NTs. Diffusional restrictions are negligible, while electron transport limitations are substantial near the pore mouth (in the NTs film formed over the Ti foil). Therefore, the linear relationship between performance and electrode nanostructure may be explained by an inverted relationship between these two factors. These factors are dependent on the nanotube length in distinct ways.

Mass transfer varies linearly with potential, but current density depends on the square of the distance. Therefore, the findings here reported suggest a limited effect of diffusional characteristics on performance, as previously suggested. Observe that these features demonstrate the substantial distinctions in mechanistic factors between heterogeneous catalysis and selective hydrogenation in electrocatalysis, excluding the fact that the latter involves gaseous H_2, whereas the active hydrogenation elements in electrocatalysis are H^+/e^-.

3.6.4 TiO_2 NTs electrode stability and robustness

After 2h or 8h of continuous testing, figure A20 shows the stability of the catalysts for TiNT60-15, TiNT60-T and TINT-T at -0.9 V vs. RHE. A general increase in FEs, particularly in GC, and a very moderate decrease in OX conversions, can be observed for all three samples, even though there are some slight behavioral differences. In

longer-term studies, no further behavioral changes were observed between 8 and 20 hours.

Figure A26 shows the FESEM pictures after an 8-hour test at each potential investigated. The array of vertically oriented TiO_2 NTs is still visible in all samples. However, in TiNT60-15, some NTs are damaged, with randomly fractured NTs shrinking to 1.4 μm in length. The anatase covering oxide layer is present both in TiNT60-T and TiNT-T. Upon magnification, the underlying NT layer appears more homogeneous, maintaining a consistent length, and exhibiting increased porosity (as indicated by the white circles in Figure A26). No additional alterations were observed in longer-term studies lasting up to 20 hours.

To examine these findings, we need to discuss the mechanism behind the creation of the titania nanostructured layer during anodic oxidation from Ti foil. The anodic process produces small titania nanoparticles with many surface hydroxyl groups on the surface of Ti foil [7,43,71]. These nanoparticles are solubilized by F^-ions, and the strong local electrical field causes them to be reconstituted as NTs. It is possible for debris from titania to fall on top of them. Figure 3.14 shows that the reaction between surface hydroxyl groups is caused by thermal annealing, resulting in the formation of highly crystalline titania nanotubes. Due to its strong interaction with the underlying titania NTs, the surface titania debris cannot be mechanically removed by ultrasonic therapy. However, a small percentage of these titania nanoparticles did not fully combine with others to produce a crystalline porous oxide that was nanostructured. As results, only a small portion (less than a few percent) of the titania can be extracted initially, most likely from the surface titania debris. Stable behavior was observed after their removal.

Micrographs show that additional porous titania debris remains after the removal of these non-interacting titania nanoparticles, which are only a few nm in size. As a result, the performances were somewhat improved. However, the TiO_2-only electrodes remained stable and can be considered robust during this initial transition. This finding is consistent with literature data [86], which indicates that TiO_2

dissolves in an acidic environment and reaches a plateau after a few hours. The stability of the electrode and the reaction parameters, such as pH, OX concentration, and temperature, determine when this plateau is reached. The decrease in OX conversion after 8 hours and the rise in FE_{GO} can be attributed to the lower NTs thickness in TiNT60-15 (Figure A20). The decrease in FE_{GC} is in line with the correlation presented in Figure 3.15 (a), and the conversion value aligns with the linear correlation depicted in Figure 3.15 (d). After 8 hours of testing, Figure A20 shows an increase in FE_{GC} and equivalent OX conversion in TiNT60-T. The OX conversion remains the same due to the constant length of the NTs, but the greater porosity of the overlying oxide layer makes the active sites more accessible. This impact raises FE_{GC}.

3.7 Literature comparison

Titania electrodes for electrocatalytic reduction are essential in industry because they allow the creation of durable, low-cost electrodes free of metal nanoparticles and critical raw materials (CRMs). Avoidance of CRMs is becoming relatively mandatory in emerging sustainable electrocatalytic processes, at least in some geographical locations, such as the EU, where strict CRM restrictions are being discussed [72]. There are other selective electrocatalysts for OX reduction that have been reported based on expensive materials and CRM, including gallium [46] or IrO_2 [67], that exhibit great selectivity to GC (>90%). Additionally, the electrode based on Ga loses approximately one-third of its activity in less than ten hours of operation and has to operate at higher temperatures (80 °C). However, the current study focused on titania-only electrodes due to their cheap preparation costs and lack of CRM. Moreover, the results discussed in this chapter are obtained in the lowest energy consumption condition, i.e. atmospheric pressure and room temperature at -0.8 – -1V vs RHE. Conversely literature data shows higher temperature (>50°C) or higher applied potential or light-assisted reaction. For instance, Yamamuchi et al. [73] doped TiO_2 with different concentrations of zirconium to improve the

electrocatalytic efficiency of the TiO_2 as electrodes for GC production via OX electrocatalytic reduction. The study did not employ a complete electrocatalytic cell but rather evaluated the system using CV and chronoamperometry at 50 °C. The authors concluded that amorphous oxide is necessary for improved electrocatalytic performance compared to crystalline oxide. Atomic disordering may stabilize the production of oxygen vacancies and the oxide's reducibility, although characterization information on these points was not provided. Furthermore, they found that while GC was maximized in the most active samples, GO production was increased in the less active ones. A direct comparison of the data is not possible due to variations in the experimental program.

Under UV-visible irradiation ($\lambda > 300$ nm) at 50°C for two hours, the same research group [74] investigated light-assisted electrochemical OX reduction (in the presence of external bias) using a TiO_2 cathode and a WO_3 photoanode. They obtained 80% FEs ($FE_{GC} + FE_{GO}$). The authors created the cathode by coating a Ti foil with TiO_2 nanoparticles. However, they noted that the electrodes lack robustness, and the reaction rates were modest, only a few μmol h^{-1}, which is two to three orders of magnitude lower than what was observed.

Song et al. [75] synthesized a Ti/Pr-PVP-nano TiO_2 film using the sol-gel method. Praseodymium was added to TiO_2 to modify its crystal structure, while polyvinylpyrrolidone was used to prevent the aggregation of TiO_2 nanoparticles. The results of the analysis were compared with those of Ti/PVP-nanoTiO_2 and Ti/nano TiO_2. The SEM and XRD analyses revealed that the crystal size in Ti/Pr-PVP-nano TiO_2 was smaller and more uniform than in Ti/PVP-nanoTiO_2 and Ti/nano TiO_2. Additionally, the XPS analysis showed that praseodymium was uniformly distributed in the TiO_2 phase. The cyclovoltammetry results indicated that the Ti/Pr-PVP-nano TiO_2 catalyst with a Pr/Ti molar ratio of 0.006 had the highest FE_{GO} of around 81%.

Sadakiyo et al. [76] constructed a PEAEC (polymer electrolyte alcohol electrosynthesis cell) with a cathode made of porous TiO_2 produced by hydrothermal synthesis on a Ti felt to achieve almost full OX conversion and 31.9% FE_{GC} at 3.0 V

applied voltage at 60 °C. However, the highest energy conversion efficiency was still below 50%, and H_2 was the predominant product with a FE of around 60% under these circumstances. The specific current density for GC is approximately 20 mA cm^{-2}, which is consistent with our findings of approximately 10 mA cm^{-2} at ambient temperature and with a lower applied voltage.

Yang et al. [77] achieved GC selectivity of 38.7% and OX conversion of 51.2% by utilizing multi-walled carbon nanotubes (MWNT) encased in an anatase TiO_2 layer. These results are similar to those described in this chapter, but they applied a potential of −2.2V vs. RHE and high temperature (60 °C). However, they did not report the creation of GO, despite the large generation of H_2 as a side product.

In reference to the earlier study conducted by Zhao et al. [15], it was observed that using a roughened TiO_2 film electrode resulted in GC being the primary product rather than GO. Furthermore, it was demonstrated several correlations between NTs features and selectivity to GC (see figure 3.15). Moreover, the study reported in this chapter used lower applied voltages than 2.9-3.4 V adopted by Zhao probably for the low conductivity of their electrode which explain also the longer reaction times used. Although GO has almost twice the added value of GC, electrode activity is equally important to the industrial development of this approach. Thus, it is possible to adjust the GC to GO ratio based on market demands by simply modifying the electrode.

Furthermore, the improved electrocatalysts described in this chapter outperformed the state-of-the-art as selective hydrogenation catalysts, although their performance depends on the specifics of the preparation process. Table 3.4 compares the findings obtained for TiNT60 and TiNT60-E with the data from the literature under similar reaction conditions and room temperature OX reduction, providing evidence for this claim. Literature results based on electrodes containing CRM or results obtained under different experimental conditions are not included. This table only compares literature results obtained under the same reaction conditions for Ti-only electrodes.

Table 3.4 *Comparison of the results obtained for TiNT60 and TiNT60-E with the literature results under comparable reaction conditions (room temperature and Ag/AgCl reference electrode).*

Sample	*Note*	*FE (GO), %*	*FE (GC), %*	*Current densities (mA/cm²)*	*Ref.*
TiNT60-E	this work	12.1	86.3	16	-
TiNT60	this work	11.4	86.0	3	-
TiO_2 nanotubes	TNT	25.8	42.7	30	[78]
TiO_2 flame-like	TNF	16.7	33.0	30	[78]
TiO_2 nanoparticles	TNP	21.1	22.6	30	[78]
TiO_2 commercial	TiO_2-R500	68.6	23.3	20	[79]
TiO_2 spheres		58.3	38.7	17	[79]
M−TiO_2 spheres	mesoporous	35.8	60.1	22	[79]
TiO_2/Ti-Mesh		6.0	46.7	5	[80]
TiO_2 columnar	①	6.6	23.1	-	[80]
TiO_2 bipyramidal (101)	②	4.1	64.4	-	[80]
TiO_2 bipyramidal (001)	③	9	53.6	-	[80]
TiO_2 condensed sheet (001)	④	3	39.2	-	[80]
TiO_2 stacked sheet (001)	⑤	12.5	40.5	-	[80]

TiO_2 bipyramidal (201)	⑥	11.9	48.3	-	[80]
TNT-45	2700 s anodization	10	59.9	-	[55]

① columnar truncated bipyramidal decahedron with exposed (101) facets (101-column)

② truncated bipyramidal decahedron with exposed (101) facets (101-deca)

③ truncated bipyramidal decahedron with exposed (001) facets (001-deca)

④ sphere condensed sheet with exposed (001) facets (001-sheet-C)

⑤ sphere stacked sheet with exposed (001) facets (001-sheet-S)

⑥ truncated asymmetric bipyramidal decahedron with exposed (201) facets (201-deca)

3.8 Conclusion

The electrocatalytic hydrogenation of OX is a sustainable synthesis method that produces high-value C2 compounds from CO_2 and renewable energy sources without the need for additional reagents like H_2. This method is unique and has the potential to contribute to a more sustainable future. The electrocatalytic approach eliminates the need for a separate stage of H_2 synthesis, which reduces associated expenses and environmental impact. Additionally, it avoids the energy costs of high-pressure/temperature operations that are required for OX hydrogenation by heterogeneous catalysis under ambient conditions. Thus, the electrocatalytic approach is an example of how to overcome environmental catalysis problems and advance fossil fuel substitution and electrification of chemical production.

TiO_2 NT arrays are used to reduce OX to GO and GC by applying a potential that is equivalent to or greater than -0.8 V vs. RHE. These cathodes are a unique type of strong, inexpensive, non-CRM-based selective hydrogenation electrode that can be used in the growing field of electrification of chemical processes to produce chemicals that are not derived from fossil fuels.

The pathway that converts CO_2 to GO and GC through the OX intermediate is a clear example of this. The activity and selectivity of the process are determined by the defective nature and nanostructure. However, the literature does not provide clear evidence of the relationship between these factors and the outcomes of the electrocatalytic OX reduction to GO and GC. This study shows that it is possible to control the nanostructure and the presence of defects in TiO_2 NTs electrodes produced by anodic oxidation. The relationship between these characteristics and the NT growth mechanism, as well as their impact on preparation parameters, is also discussed.

The examined electrodes exhibit various features. Without TiO_2 NTs, TiNT-A show the presence of a densely nanostructured TiO_2 layer. Instead, together with the TiO_2 nanotubes, TiNT, TiNT-T, and TiNT-HS (the latter used as alternative synthesis to obtain NTs without an orderly packing) demonstrate the presence of tiny amorphous patches, debris, or TiO_2 nanoparticles. A fresh electrolyte solution is beneficial to obtain NTs longer and more defined (TINT50-15 and TINT50). However, the selective hydrogenation of OX can be achieved more effectively when compared to state-of-the-art titania-only electrodes under rapid breakdown anodization conditions, that were achieved at 60 V in this work (TiNT60-15, TiNT60, and TiNT60-E).

The relationship between the nanostructure of the produced samples and their performance in the electrocatalytic reduction of OX can be established by comparing their features and performances, as shown in Figure 3.8 and 3.15. Evidence of these relationships can be found in the concentration of oxygen vacancies (O2v) found in XPS, length of TiO_2 NTs array, ECSA as well as the catalytic behavior (OX conversion).

Moreover, the study examined the impact of two pretreatments, thermal or electrochemical, prior to anodizing the Ti foil. By comparing the results of testing with the morphological characteristics shown in FESEM and AFM micrographs, it can be concluded that:

the release of oxygen bubbles during RBA is a side reaction that leads to longer nanotubes with rough walls. When using rougher nanotubes instead of smooth NTs, the average OX conversion increased by approximately 7% when the same anodization time was used. Additionally, an average increase in FE_{GC} was observed when compared to FE_{GO}. Over etching of NTs resulted in less reducible material and the presence of compact patches of debris could increase the production of GO. This is especially noticeable for TINT-A, where the nanostructured oxide layer addresses the reaction to GO.

The pretreatments had different impacts on the performance of the samples. The thermal pretreatment had contrasting results: on one hand, it had a positive effect when a 60-minute-aged electrolyte solution was used, resulting in an increase in OX conversion and a change in selectivity through GC. On the other hand, it had a negative effect, lowering the performance when a fresh electrolyte solution and RBA conditions were adopted. In the latter case, the NTs remained smooth even though the samples were developed under RBA conditions, suggesting that oxygen release-induced porosity was essential for the electrocatalytic reduction of OX. The TiNT60-E sample had an average OX conversion rate that was around 5% and 10% higher than that of TiNT60 and TiNT50, respectively, due to the rougher NTs in TiNT60-E. Linear correlations suggest a synergistic relationship between roughness and TiO_2 NT length that affects the ECSA. This allows for a higher OX conversion and more active sites in the form of oxygen vacancies (O2v). Additionally, a larger ECSA improves selectivity to GC, highlighting the crucial role of NT morphology in adjusting selectivity to GO or GC.

Besides, the study examined the relationships between the factors from a mechanistic standpoint. It was found that the function of the Ti^{3+}/O2v active sites needs to be considered from an electrochemical perspective. These sites promote electron accumulation, which causes the activity correlation through an outer-sphere electron transfer mechanism. The selectivity is associated with the surface titania debris and

porous NTs' nanostructure properties, which impact the likelihood of GO and GC being reduced consecutively.

The discussion concluded with an examination of the function of diffusional limits and their relationship to nanostructure. The TiO_2-only electrodes are robust and stable, despite a small initial loss of titania nanoparticles produced during the anodization process. These nanoparticles do not react with each other when the anodization method is followed by thermal annealing. Although the extent of improvement in FEs depends on sample preparation, this initial transformation enhances FEs while having a negligible impact on OX conversion.

Bibliography

1. Watanabe, R.; Yamauchi, M.; Sadakiyo, M.; Abe, R.; Takeguchi, T. CO2-Free Electric Power Circulation via Direct Charge and Discharge Using the Glycolic Acid/Oxalic Acid Redox Couple. *Energy Environ. Sci.* **2015**, *8*, 1456–1462, doi:10.1039/c5ee00192g.

2. Connor, P.; Schuch, J.; Kaiser, B.; Jaegermann, W. The Determination of Electrochemical Active Surface Area and Specific Capacity Revisited for the System MnOx as an Oxygen Evolution Catalyst. *Zeitschrift fur Phys. Chemie* **2020**, *234*, 979–994, doi:10.1515/zpch-2019-1514.

3. Li, X.; Pustulka, S.; Pedu, S.; Close, T.; Xue, Y.; Richter, C.; Taboada-Serrano, P. Titanium Dioxide Nanotubes as Model Systems for Electrosorption Studies. *Nanomaterials* **2018**, *8*, doi:10.3390/nano8060404.

4. Qiao, J.; Jiang, P.; Liu, J.; Zhang, J. Formation of Cu Nanostructured Electrode Surfaces by an Annealing-Electroreduction Procedure to Achieve High-Efficiency CO2 Electroreduction. *Electrochem. commun.* **2014**, *38*, 8–11, doi:10.1016/j.elecom.2013.10.023.

5. Centi, G.; Passalacqua, R.; Perathoner, S.; Su, D.S.; Weinberg, G.; Schlögl, R. Oxide Thin Films Based on Ordered Arrays of 1D Nanostructure. A Possible Approach toward Bridging Material Gap in Catalysis. *Phys. Chem. Chem. Phys.* **2007**, *9*, 4930–4938, doi:10.1039/b703326p.

6. Apolinário, A.; Quitério, P.; Sousa, C.T.; Ventura, J.; Sousa, J.B.; Andrade, L.; Mendes, A.M.; Araújo, J.P. Modeling the Growth Kinetics of Anodic TiO2 Nanotubes. *J. Phys. Chem. Lett.* **2015**, *6*, 845–851, doi:10.1021/jz502380b.

7. Roy, P.; Berger, S.; Schmuki, P. TiO2 Nanotubes: Synthesis and Applications. *Angew. Chemie - Int. Ed.* **2011**, *50*, 2904–2939, doi:10.1002/anie.201001374.

8. Albu, S.P.; Roy, P.; Virtanen, S.; Schmuki, P. Self-Organized TiO2 Nanotube Arrays: Critical Effects on Morphology and Growth. *Isr. J. Chem.* **2010**, *50*, 453–467, doi:10.1002/ijch.201000059.

9. Macak, J.M.; Albu, S.P.; Schmuki, P. Towards Ideal Hexagonal Self-Ordering of TiO2 Nanotubes. *Phys. Status Solidi - Rapid Res. Lett.* **2007**, *1*, 181–183, doi:10.1002/pssr.200701148.

10. Moazeni, M.; Hajipour, H.; Askari, M.; Nusheh, M. Hydrothermal Synthesis and Characterization of Titanium Dioxide Nanotubes as Novel Lithium Adsorbents.

Mater. Res. Bull. **2015**, *61*, 70–75, doi:10.1016/j.materresbull.2014.09.069.

11. Sugiawati, V.A.; Vacandio, F.; Galeyeva, A.; Kurbatov, A.P.; Djenizian, T. Enhanced Electrochemical Performance of Electropolymerized Self-Organized TiO2 Nanotubes Fabricated by Anodization of Ti Grid. *Front. Phys.* **2019**, *7*, 1–8, doi:10.3389/fphy.2019.00179.

12. Fabregat-Santiago, F.; Mora-Seró, I.; Garcia-Belmonte, G.; Bisquert, J. Cyclic Voltammetry Studies of Nanoporous Semiconductors. Capacitive and Reactive Properties of Nanocrystalline TiO2 Electrodes in Aqueous Electrolyte. *J. Phys. Chem. B* **2003**, *107*, 758–768, doi:10.1021/jp0265182.

13. Yu, H.; Ma, J.; Zhang, Y.; Zhang, X.; Shi, W. Cyclic Voltammetry Studies of TiO2 Nanotube Arrays Electrode: Conductivity and Reactivity in the Presence of H+ and Aqueous Redox Systems. *Electrochim. Acta* **2011**, *56*, 6498–6502, doi:10.1016/j.electacta.2011.05.004.

14. Makivić, N.; Cho, J.Y.; Harris, K.D.; Tarascon, J.M.; Limoges, B.; Balland, V. Evidence of Bulk Proton Insertion in Nanostructured Anatase and Amorphous TiO2Electrodes. *Chem. Mater.* **2021**, *33*, 3436–3448, doi:10.1021/acs.chemmater.1c00840.

15. Zhao, F.; Yan, F.; Qian, Y.; Xu, Y.; Ma, C. Roughened TiO2 Film Electrodes for Electrocatalytic Reduction of Oxalic Acid to Glyoxylic Acid. *J. Electroanal. Chem.* **2013**, *698*, 31–38, doi:10.1016/j.jelechem.2013.03.014.

16. Bellamkonda, S.; Thangavel, N.; Hafeez, H.Y.; Neppolian, B.; Ranga Rao, G. Highly Active and Stable Multi-Walled Carbon Nanotubes-Graphene-TiO2 Nanohybrid: An Efficient Non-Noble Metal Photocatalyst for Water Splitting. *Catal. Today* **2019**, *321–322*, 120–127, doi:10.1016/j.cattod.2017.10.023.

17. Gakhar, T.; Hazra, A. Oxygen Vacancy Modulation of Titania Nanotubes by Cathodic Polarization and Chemical Reduction Routes for Efficient Detection of Volatile Organic Compounds. *Nanoscale* **2020**, *12*, 9082–9093, doi:10.1039/c9nr10795a.

18. Li, Z.; Bian, H.; Xiao, X.; Shen, J.; Zhao, C.; Lu, J.; Li, Y.Y. Defective Black TiO2 Nanotube Arrays for Enhanced Photocatalytic and Photoelectrochemical Applications. *ACS Appl. Nano Mater.* **2019**, *2*, 7372–7378, doi:10.1021/acsanm.9b01878.

19. Bharti, B.; Kumar, S.; Lee, H.N.; Kumar, R. Formation of Oxygen Vacancies and Ti3+ State in TiO2 Thin Film and Enhanced Optical Properties by Air Plasma Treatment. *Sci. Rep.* **2016**, *6*, 1–12, doi:10.1038/srep32355.

20. Zhang, X.; Tian, H.; Wang, X.; Xue, G.; Tian, Z.; Zhang, J.; Yuan, S.; Yu, T.; Zou, Z. The Role of Oxygen Vacancy-Ti3+ States on TiO2 Nanotubes' Surface in Dye-Sensitized Solar Cells. *Mater. Lett.* **2013**, *100*, 51–53, doi:10.1016/j.matlet.2013.02.116.

21. Passalacqua, R.; Perathoner, S.; Centi, G. Use of Modified Anodization Procedures to Prepare Advanced TiO2 Nanostructured Catalytic Electrodes and Thin Film Materials. *Catal. Today* **2015**, *251*, 121–131, doi:10.1016/j.cattod.2014.11.003.

22. Abbas, W.A.; Abdullah, I.H.; Ali, B.A.; Ahmed, N.; Mohamed, A.M.; Rezk, M.Y.; Ismail, N.; Mohamed, M.A.; Allam, N.K. Recent Advances in the Use of TiO2 Nanotube Powder in Biological, Environmental, and Energy Applications. *Nanoscale Adv.* **2019**, *1*, 2801–2816, doi:10.1039/c9na00339h.

23. Xu, H.; Zhang, Q.; Zheng, C.; Yan, W.; Chu, W. Application of Ultrasonic Wave to Clean the Surface of the TiO 2 Nanotubes Prepared by the Electrochemical Anodization. *Appl. Surf. Sci.* **2011**, *257*, 8478–8480, doi:10.1016/j.apsusc.2011.04.135.

24. Zhao, S.; Xing, J.; Fan, H.; Zhang, S.; Li, D.; Zhu, X. Derivation of a Mathematical Model for the Growth of Anodic TiO2 Nanotubes under Constant Current Conditions. *J. Electrochem. Soc.* **2017**, *164*, E187–E193, doi:10.1149/2.0421709jes.

25. Madey, T.E. The Interaction CF Water with Solid Surfaces: Fundamental Aspects. *Vacuum* **1990**, *40*, 224, doi:10.1016/0042-207x(90)90169-y.

26. Tao, J.; Zhao, J.; Tang, C.; Kang, Y.; Li, Y. Mechanism Study of Self-Organized TiO2 Nanotube Arrays by Anodization. *New J. Chem.* **2008**, *32*, 2164–2168, doi:10.1039/b808719a.

27. Fukushima, T.; Kitano, S.; Hata, S.; Yamauchi, M. Carbon-Neutral Energy Cycles Using Alcohols. *Sci. Technol. Adv. Mater.* **2018**, *19*, 142–152, doi:10.1080/14686996.2018.1426340.

28. Huang, W.; Xu, H.; Ying, Z.; Dan, Y.; Zhou, Q.; Zhang, J.; Zhu, X. Split TiO2 Nanotubes − Evidence of Oxygen Evolution during Ti Anodization. *Electrochem. commun.* **2019**, *106*, 106532, doi:10.1016/j.elecom.2019.106532.

29. Aladjem, A. Anodic Oxidation of Titanium and Its Alloys. *J. Mater. Sci.* **1973**, *8*, 688–704, doi:10.1007/BF00561225.

30. Sousa, C.T.; Leitao, D.C.; Proenca, M.P.; Ventura, J.; Pereira, A.M.; Araujo, J.P. Nanoporous Alumina as Templates for Multifunctional Applications. *Appl.*

Phys. Rev. **2014**, *1*, doi:10.1063/1.4893546.

31. Ruiz-Clavijo, A.; Caballero-Calero, O.; Martín-González, M. Revisiting Anodic Alumina Templates: From Fabrication to Applications. *Nanoscale* **2021**, *13*, 2227–2265, doi:10.1039/d0nr07582e.

32. Ghicov, A.; Schmuki, P. Self-Ordering Electrochemistry: A Review on Growth and Functionality of TiO2 Nanotubes and Other Self-Aligned MOx Structures. *Chem. Commun.* **2009**, 2791–2808, doi:10.1039/b822726h.

33. Kim, D.; Ghicov, A.; Schmuki, P. TiO2 Nanotube Arrays: Elimination of Disordered Top Layers ("nanograss") for Improved Photoconversion Efficiency in Dye-Sensitized Solar Cells. *Electrochem. commun.* **2008**, *10*, 1835–1838, doi:10.1016/j.elecom.2008.09.029.

34. Yu, M.; Chen, Y.; Li, C.; Yan, S.; Cui, H.; Zhu, X.; Kong, J. Studies of Oxide Growth Location on Anodization of Al and Ti Provide Evidence against the Field-Assisted Dissolution and Field-Assisted Ejection Theories. *Electrochem. commun.* **2018**, *87*, 76–80, doi:10.1016/j.elecom.2018.01.003.

35. Yu, M.; Huang, W.; Li, P.; Huang, H.; Zhang, K.; Zhu, X. Morphology Evolution of TiO2 Nanotubes with Additional Reducing Agent: Evidence of Oxygen Release. *Electrochem. commun.* **2019**, *98*, 28–32, doi:10.1016/j.elecom.2018.11.010.

36. Watcharenwong, A.; Chanmanee, W.; de Tacconi, N.R.; Chenthamarakshan, C.R.; Kajitvichyanukuk, P.; Rajeshwar, K. Self-Organized TiO2 Nanotube Arrays by Anodization of Ti Substrate: Effect of Anodization Time, Voltage and Medium Composition on Oxide Morphology and Photoelectrochemical Response. *J. Mater. Res.* **2007**, *22*, 3186–3195, doi:10.1557/jmr.2007.0391.

37. Garcia-Vergara, S.J.; Skeldon, P.; Thompson, G.E.; Habazaki, H. A Flow Model of Porous Anodic Film Growth on Aluminium. *Electrochim. Acta* **2006**, *52*, 681–687, doi:10.1016/j.electacta.2006.05.054.

38. Zhao, S.; Chen, Y.; Zhao, Z.; Jiang, L.; Zhang, C.; Kong, J.; Zhu, X. Enhanced Capacitance of TiO2 Nanotubes Topped with Nanograss by H3PO4 Soaking and Hydrogenation Doping. *Electrochim. Acta* **2018**, *266*, 233–241, doi:10.1016/j.electacta.2018.02.037.

39. Broens, M.I.; Ramos Cervantes, W.; Oyarzún Jerez, D.; López Teijelo, M.; Linarez Pérez, O.E. The Keys to Avoid Undesired Structural Defects in Nanotubular TiO2 Films Prepared by Electrochemical Anodization. *Ceram. Int.* **2020**, *46*, 13599–13606, doi:10.1016/j.ceramint.2020.02.145.

40. Quitério, P.; Apolinário, A.; Sousa, C.T.; Costa, J.D.; Ventura, J.; Araújo, J.P. The Morphological Characterization of Anodic TiO2 Nanotube Arrays. *Microsc. Microanal.* **2015**, *21*, 39–40, doi:10.1017/S1431927615014002.

41. Lim, J.H.; Choi, J. Titanium Oxide Nanowires Originating from Anodically Grown Nanotubes: The Bamboo-Splitting Model. *Small* **2007**, *3*, 1504–1507, doi:10.1002/smll.200700114.

42. Rajapakse, H.D.; Rathnayaka, S.G.; Sitinamaluwa, H.S.; Jayasundara, D.R.T. Synthesis and Morphological Characterization of TiO 2 Nanotube Arrays. **2020**, 210–214, doi:10.1109/mercon50084.2020.9185366.

43. Regonini, D.; Bowen, C.R.; Jaroenworaluck, A.; Stevens, R. A Review of Growth Mechanism, Structure and Crystallinity of Anodized TiO2 Nanotubes. *Mater. Sci. Eng. R Reports* **2013**, *74*, 377–406, doi:10.1016/j.mser.2013.10.001.

44. Chong, B.; Yu, D.; Jin, R.; Wang, Y.; Li, D.; Song, Y.; Gao, M.; Zhu, X. Theoretical Derivation of Anodizing Current and Comparison between Fitted Curves and Measured Curves under Different Conditions. *Nanotechnology* **2015**, *26*, 145603, doi:10.1088/0957-4484/26/14/145603.

45. Lausmaa, J. Mechanical, Thermal, Chemical and Electrochemical Surface Treatment of Titanium. **2001**, 231–266, doi:10.1007/978-3-642-56486-4_8.

46. Cheng, Y.; Xu, W.; Hou, J.; Kang, P. Temperature-Dependent Electrosynthesis of C2 Oxygenates from Oxalic Acid Using Gallium Tin Oxides. *ACS Catal.* **2023**, 3676–3683, doi:10.1021/acscatal.2c06120.

47. Zhang, S.; Yu, D.; Li, D.; Song, Y.; Che, J.; You, S.; Zhu, X. Forming Process of Anodic TiO 2 Nanotubes under a Preformed Compact Surface Layer. *J. Electrochem. Soc.* **2014**, *161*, E135–E141, doi:10.1149/2.0661410jes.

48. So, S.; Hwang, I.; Riboni, F.; Yoo, J.E.; Schmuki, P. Robust Free Standing Flow-through TiO2 Nanotube Membranes of Pure Anatase. *Electrochem. commun.* **2016**, *71*, 73–78, doi:10.1016/j.elecom.2016.08.010.

49. Ohno, T.; Sarukawa, K.; Matsumura, M. Photocatalytic Activities of Pure Rutile Particles Isolated from TiO2 Owder by Dissolving the Anatase Component in HF Solution. *J. Phys. Chem. B* **2001**, *105*, 2417–2420, doi:10.1021/jp003211z.

50. Song, Y.Y.; Lynch, R.; Kim, D.; Roy, P.; Schmuki, P. TiO2 Nanotubes: Efficient Suppression of Top Etching during Anodic Growth: Key to Improved High Aspect Ratio Geometries. *Electrochem. Solid-State Lett.* **2009**, *12*, 17–20, doi:10.1149/1.3126500.

51. Pan, X.; Yang, M.Q.; Fu, X.; Zhang, N.; Xu, Y.J. Defective TiO2 with Oxygen Vacancies: Synthesis, Properties and Photocatalytic Applications. *Nanoscale* **2013**, *5*, 3601–3614, doi:10.1039/c3nr00476g.

52. Nah, Y.C.; Paramasivam, I.; Schmuki, P. Doped TiO2 and TiO2 Nanotubes: Synthesis and Applications. *ChemPhysChem* **2010**, *11*, 2698–2713, doi:10.1002/cphc.201000276.

53. Pishkar, N.; Ghoranneviss, M.; Ghorannevis, Z.; Akbari, H. Anodic Growth and Characterization of Highly Nitrogen Doped Titanium Dioxide Nanotubes with Ordered Structure on Hot Argon DC Plasma Treated Titanium Substrates. *J. Inorg. Organomet. Polym. Mater.* **2018**, *28*, 2154–2159, doi:10.1007/s10904-018-0883-y.

54. Robotti, M.; Dosta, S.; Cano, I.G.; Concustell, A.; Cinca, N.; Guilemany, J.M. Attrition and Cryogenic Milling Powder Production for Low Pressure Cold Gas Spray and Composite Coatings Characterization. *Adv. Powder Technol.* **2016**, *27*, 1257–1264, doi:10.1016/j.apt.2016.04.014.

55. Im, S.; Saad, S.; Park, Y. Facilitated Series Electrochemical Hydrogenation of Oxalic Acid to Glycolic Acid Using TiO2 Nanotubes. *Electrochem. commun.* **2022**, *135*, 107204, doi:10.1016/j.elecom.2022.107204.

56. Heard, D.M.; Lennox, A.J.J. Electrode Materials in Modern Organic Electrochemistry. *Angew. Chemie - Int. Ed.* **2020**, *59*, 18866–18884, doi:10.1002/anie.202005745.

57. Kang, H.; Ma, J.; Perathoner, S.; Chu, W.; Centi, G.; Liu, Y. Understanding the Complexity in Bridging Thermal and Electrocatalytic Methanation of CO2. *Chem. Soc. Rev.* **2023**, *52*, 3627–3662, doi:10.1039/d2cs00214k.

58. Valentin, C. Di; Pacchioni, G.; Selloni, A. Reduced and N-Type Doped TiO2: Nature of Ti3+ Species. *J. Phys. Chem. C* **2009**, *113*, 20543–20552.

59. Kulkarni, M.; Mazare, A.; Schmuki, P.; Iglic, A. Influence of Anodization Parameters on Morphology of TiO2 Nanostructured Surfaces. *Adv. Mater. Lett.* **2016**, *7*, 23–28, doi:10.5185/amlett.2016.6156.

60. Cassidy, J.F.; de Carvalho, R.C.; Betts, A.J. Use of Inner/Outer Sphere Terminology in Electrochemistry—A Hexacyanoferrate II/III Case Study. *Electrochem* **2023**, *4*, 313–349, doi:10.3390/electrochem4030022.

61. Sun, T.; Wang, Y.; Zhang, H.; Liu, P.; Zhao, H. Adsorption and Oxidation of Oxalic Acid on Anatase TiO2 (001) Surface: A Density Functional Theory Study. *J. Colloid Interface Sci.* **2015**, *454*, 180–186, doi:10.1016/j.jcis.2015.05.016.

62. Mendive, C.B.; Bredow, T.; Blesa, M.A.; Bahnemann, D.W. ATR-FTIR Measurements and Quantum Chemical Calculations Concerning the Adsorption and Photoreaction of Oxalic Acid on TiO2. *Phys. Chem. Chem. Phys.* **2006**, *8*, 3232–3247, doi:10.1039/b518007b.

63. Robert, D.; Parra, S.; Pulgarin, C.; Krzton, A.; Weber, J.V. Chemisorption of Phenols and Acids on TiO2 Surface. *Appl. Surf. Sci.* **2000**, *167*, 51–58, doi:10.1016/S0169-4332(00)00496-7.

64. Santos, E.; Nazmutdinov, R.; Schmickler, W. Electron Transfer at Different Electrode Materials: Metals, Semiconductors, and Graphene. *Curr. Opin. Electrochem.* **2020**, *19*, 106–112, doi:10.1016/j.coelec.2019.11.003.

65. Ramaswamy, N.; Mukerjee, S. Influence of Inner- and Outer-Sphere Electron Transfer Mechanisms during Electrocatalysis of Oxygen Reduction in Alkaline Media. *J. Phys. Chem. C* **2011**, *115*, 18015–18026, doi:10.1021/jp204680p.

66. Janda, D.C.; Barma, K.; Kurapati, N.; Klymenko, O. V.; Oleinick, A.; Svir, I.; Amatore, C.; Amemiya, S. Systematic Assessment of Adsorption-Coupled Electron Transfer toward Voltammetric Discrimination between Concerted and Non-Concerted Mechanisms. *Electrochim. Acta* **2022**, *428*, 140912, doi:10.1016/j.electacta.2022.140912.

67. Fukushima, T.; Higashi, M.; Kitano, S.; Sugiyama, T.; Yamauchi, M. Multiscale Design for High-Performance Glycolic Acid Electro-Synthesis Cell: Preparation of Nanoscale-IrO2-Applied Ti Anode and Optimization of Cell Assembling. *Catal. Today* **2020**, *351*, 12–20, doi:10.1016/j.cattod.2019.03.071.

68. Le, T.D.; Lasseux, D.; Nguyen, X.P.; Vignoles, G.; Mano, N.; Kuhn, A. Multi-Scale Modeling of Diffusion and Electrochemical Reactions in Porous Micro-Electrodes. *Chem. Eng. Sci.* **2017**, *173*, 153–167, doi:10.1016/j.ces.2017.07.039.

69. Kas, R.; Yang, K.; Yewale, G.P.; Crow, A.; Burdyny, T.; Smith, W.A. Modeling the Local Environment within Porous Electrode during Electrochemical Reduction of Bicarbonate. *Ind. Eng. Chem. Res.* **2022**, *61*, 10461–10473, doi:10.1021/acs.iecr.2c00352.

70. Huang, B.; Rao, R.R.; You, S.; Hpone Myint, K.; Song, Y.; Wang, Y.; Ding, W.; Giordano, L.; Zhang, Y.; Wang, T.; et al. Cation- and PH-Dependent Hydrogen Evolution and Oxidation Reaction Kinetics. *JACS Au* **2021**, *1*, 1674–1687, doi:10.1021/jacsau.1c00281.

71. Su, Z.; Zhou, W. Formation, Morphology Control and Applications of Anodic TiO2 Nanotube Arrays. *J. Mater. Chem.* **2011**, *21*, 8955–8970,

doi:10.1039/c0jm04587j.

72. Centi, G.; Perathoner, S. Status and Gaps toward Fossil-Free Sustainable Chemical Production. *Green Chem.* **2022**, *24*, 7305–7331, doi:10.1039/d2gc01572b.

73. Yamauchi, M.; Hata, S.; Eguchi, H.; Kitano, S.; Fukushima, T.; Higashi, M.; Sadakiyo, M.; Kato, K. Catalytic Enhancement on Ti-Zr Complex Oxide Particles for Electrochemical Hydrogenation of Oxalic Acid to Produce an Alcoholic Compound by Controlling Electronic States and Oxide Structures. *Catal. Sci. Technol.* **2019**, doi:10.1039/c9cy01541h.

74. Kitano, S.; Yamauchi, M.; Hata, S.; Watanabe, R.; Sadakiyo, M. Hydrogenation of Oxalic Acid Using Light-Assisted Water Electrolysis for the Production of an Alcoholic Compound. *Green Chem.* **2016**, *18*, 3700–3706, doi:10.1039/c6gc01135g.

75. Song, W.; Zhang, Y.; Jin, H.; Kim, M.; Kim, S.; Kim, I. Fabrication of Pr-PVP-Co-Doped NanoTiO 2 Film on Titanium Matrix with Outstanding Electrocatalytic Reduction Activity for Oxalic Acid. **2017**, *164*, 260–264, doi:10.1149/2.1231709jes.

76. Sadakiyo, M.; Hata, S.; Cui, X.; Yamauchi, M. Electrochemical Production of Glycolic Acid from Oxalic Acid Using a Polymer Electrolyte Alcohol Electrosynthesis Cell Containing a Porous TiO2 Catalyst. *Sci. Rep.* **2017**, *7*, 1–9, doi:10.1038/s41598-017-17036-3.

77. Yang, J.; Cheng, J.; Tao, J.; Higashi, M.; Yamauchi, M.; Nakashima, N. Wrapping Multiwalled Carbon Nanotubes with Anatase Titanium Oxide for the Electrosynthesis of Glycolic Acid. *ACS Appl. Nano Mater.* **2019**, *2*, 6360–6367, doi:10.1021/acsanm.9b01357.

78. Farkhondehfal, M.A.; Savino, U.; Chiodoni, A.; Pirri, C.F.; Sacco, A. Electrocatalytic Reduction of Oxalic Acid Using Different Nanostructures of Titanium Oxide. *Electrocatalysis* **2023**, *14*, 195–201, doi:10.1007/s12678-022-00786-8.

79. Xu, W.; Cheng, Y.; Hou, J.; Kang, P. Selective Electroreduction of Oxalic Acid to Glycolic Acid by Mesoporous TiO2 Spheres. *ChemCatChem* **2023**, *15*, 1–7, doi:10.1002/cctc.202201687.

80. Eguchi, H.; Kato, K.; Juhasz, G.; Yamauchi, M. Selectivity Enhancement in the Electrochemical Reduction of Oxalic Acid over Titanium Dioxide Nanoparticles Achieved by Shape and Energy-State Control. *Catal. Sci. Technol.* **2021**, *11*, 7592–7597, doi:10.1039/d1cy01239h.

4

PLASMA ASSISTED CO_2 SPLITTING

4.1 Plasma chemistry

Irving Langmuir was the first person who introduced the term ‘plasma’ in 1928. Generally, when a solid adsorbs energy (heating, irradiation…) it is heated up and then it turns in liquid before and gas after. If other energy is absorbed by the gas, plasma is generated. According to this, it is possible to define plasma as the ‘fourth state of matter’ or the state of an ionized gas, i.e., when at least one gas molecule is split into one free electron and one positive ions. This suggests that plasma can also be obtained with a low degree of ionization (i.e., the ratio of the density of the main charged species to that of the neutral gas), usually down to 10^{-6} [1]. However, plasma is electrically neutral as the number of free electrons is balanced by an equal number of cations, but the significant number of the electrically charged particles influence its electrical properties and behavior. In fact, the interesting aspect on plasma lies in:

(i) Higher energy density then conventional chemical technologies.

(ii) It is far from thermodynamic equilibrium, making plasma a highly reactive environment because of the high amount of energetic and chemically active species that can react with each other[2].

(iii) Plasma is a highly reactive and complex chemical cocktail as it consists not only by ions but there are also many neutral species, e.g., different types of atoms, molecules, radicals and excited species.

Although plasma is less known then other than the other states of matter, the universe is made for about 99% of plasma, in the form of stars, solar corona, solar wind, nebula. Besides, natural plasma can be found also on the Earth in weather phenomena emitting light such as Saint Elmo’s fire, lightning, red sprites, auroras, and lightning [2]. Instead, man-made plasma can be classified into main groups:

(i) Fusion plasma in which the gas is almost completely ionized. It is a type of plasma used in thermonuclear plasma systems: tokomaks, stellarators, plasma pinches, focuses, and so on [3,4].

(ii) Weekly ionized plasma or so-called gas discharges, which is the focus of plasma chemistry.

In laboratory scale, plasma is created using an electric field that transmit its energy to the gas electrons as they are the most mobile charged species [5]. During their mean free path, the electrons collide with heavy particles transmitting to them a portion of the accumulated energy. These collisions can be divided in:

(1) Elastic collision in which the internal energy of the neutral species is conserved but slightly rise their kinetic (joule heating).

(2) Inelastic collision in which the energy transferred is enough to ionize the neutral species. It's the type of collision that creates plasma.

Since electrons are much lighter than heavy particles, their temperature in the plasma is initially higher than that of heavy particles. In fact, the plasma temperature is the average energies of the plasma particles (neutral and charged) and their relevant degrees of freedom (translational, rotational, vibrational, and those related to electronic excitation). Therefore, initially there is a temperature difference between the electrons (T_e) and the heavy particles (T_{hp}) which can be maintained over time, or a thermal equilibrium can be reached among all species. For this reason, another difference can be done between thermal and non-thermal plasma.

4.1.2 Thermal plasma or LTE plasma

Thermal plasma is characterized by local thermal equilibrium (LTE) because T_e is equal to T_{hp}. This can be achieved using high gas temperatures, typically ranging from 4000 K (for easy-to-ionize elements, such as cesium) to >20000 K (for hard-to-ionize elements, like helium)[6] or using high pressure. Depending on the equilibrium temperature, the thermal plasma may also be divided into (i) high

temperature thermal plasma is in equilibrium at a temperature between 10^6 and 10^8 K while (ii) low temperature thermal plasma is in quasi-equilibrium at < 2 10^4. An example of thermal plasma is the solar plasma. As described above, electrons lose some of their energy through elastic collisions with heavy particles, which then heat up (joule heating). Since the temperature difference is proportional to the square of the ratio of the electric field (E) to the pressure (p), i.e., $(E/p)^2$, thermal equilibrium is reached when E/p is small [2].

$$\Delta T = \left(\frac{E}{p}\right)^2 \quad (1)$$

Therefore, for high pressure values there are more elastic collisions and thus more efficient energy exchange between electrons and heavy particles, leading to equilibrium. Furthermore, LTE requires both that all collision processes are reversible, in the sense that they must be balanced by its inverse (excitation/de-excitation; ionization/recombination), and that all plasma properties (temperature, energy density, thermal conductivity) are the same [5].

In LTE plasma, ionization and chemical processes are due to temperature and only indirectly by the electric fields through Joule heating [1], also providing the plasma with high energy density. These features make thermal plasma ideal for some high temperature applications such as for coating technology, fine powder synthesis, (extractive) metallurgy (e.g., welding, cutting) and the treatment of hazardous waste materials [2,7].

4.1.3 Non-thermal plasma or non-LTE

In the non-thermal plasma, the local thermal equilibrium is not reached, and T_e is extremely higher (~ 1 eV or 10000 K) than gas temperature that is close to the room temperature. In general, however, the various plasma components have different temperatures: T_e is the highest, followed by the vibrationally excited molecules (Tv), while the neutral species (T_0) and the ions (Ti) have a similar temperature, close to the gas temperature; hence: $T_e >> T_v > T_i \approx T_0$ [1].

As described above (eq. 1), the temperature difference is proportional to $(E/p)^2$, so non-thermal plasma can be easily obtained in low gas pressure conditions. In this situation, as the electromagnetic field is applied, the energy is quickly transmitted to the electrons because they are lighter than other plasma components (ions, ionized molecules) and they are accelerated more easily. These primary energetic electrons give rise to inelastic collisions with the heavy particles, but the electrons lose less energy during collisions, so they can easily keep their high energy gained from the electric field. This result in the production of excited species, free radicals, and ions as well as additional electrons through electron-impact dissociation, excitation, and ionization of background gas molecules that sustain the plasma.

The described mechanism can allow to underline some advantages of non-thermal plasma that make this technology extremely suitable for carbon-free future [2]:

1) Since the non-thermal plasma is a reactive chemical mixture, it can activate gas at room temperature, even thermal stable gases such as CO_2.
2) There is no need to heat the gas or reactor because the plasma is initiated and sustained by the high-energy electrons, applying the electromagnetic field. This makes plasma a very flexible technology because it can be easily and instantaneously switched on and off, as the plasma stabilization time is less than 30 minutes.
3) Power consumption can easily be modulated. This results in suitable technology for the irregular supply of renewable electricity (e.g., from wind turbines or solar panels), because by storing electricity in a desirable chemical form, it can make up for the fluctuating imbalance between energy supply and market demand.
4) Plasma reactor can be easily scaled up due to their low cost because they do not use rare earth elements.
5) Plasma technology can use electricity from different energy sources. On one hand, this could be a limitation for the energy efficiency, but on other hand it makes plasma

technology more flexible, as it can be operated 24/7, even when other renewable sources are not available (e.g., when the sun is not shining, or it is not a windy day).

Non-thermal plasma has been used for various types of applications in different fields. For example, in the medical field it is used for sterilization [8], but it can also be a valuable method for the treatment of materials and surfaces [9]. In addition, it is currently the method by which ozone is produced at the industrial level [10], while several studies consider it a valid strategy for the abatement of gaseous pollutants, first among them volatile organic compounds VOC [10,11].

4.2 CO_2 plasma

As stated in Chapter 1, greenhouse gas emissions, particularly CO_2, will cause significant and adverse environmental consequences. These consequences lead to severe and damaging events. Despite industrial-scale development and implementation of various CCS and CCUS processes, these technologies alone are insufficient in meeting the goals specified in global initiatives to limit global warming. Therefore, the role of electrification in achieving a circular carbon economy is critical for the industrial sector since it can greatly reduce emissions.

The adoption of this technology can take place in several stages, starting with the

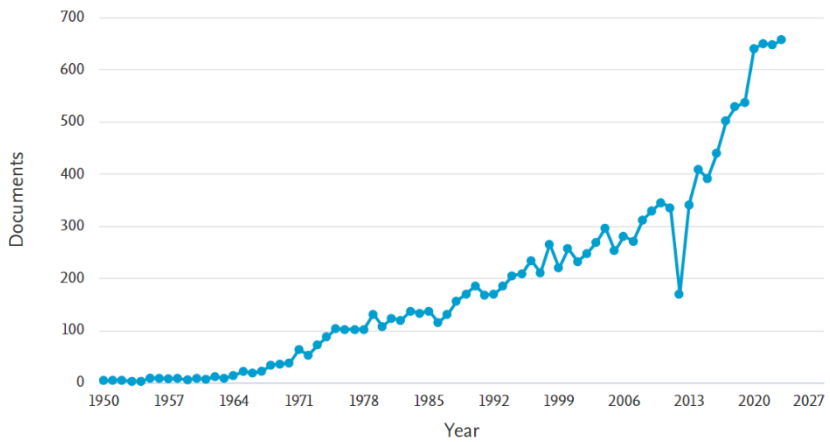

Figure 4.1 *Number of publications about CO_2 plasma. From Scopus database*

immediate electrification of current chemical reactors, and then advancing to the

wider implementation of electrochemical solutions in the medium term. In the long term, recycling CO_2 is the sole viable way of achieving a fossil-fuel-free economy. CO_2 valorization can yield various fuels (methanol, ethanol, formic acid, etc.) and chemicals (olefins, raw aromatics, etc.). Although this topic has received significant research attention, breaking the chemical bond of C=O in the CO_2 molecule poses a significant challenge due to its high stability. It requires a 5.5 eV/molecule energy input (equivalent to +283 kJ/mol using standard enthalpy) [1]. There are numerous innovative methods to convert CO_2, as discussed in chapter 1. Plasma technology presents several advantages that warrant its increasing popularity in the scientific community (figure 4.1).

4.2.1 Channels for CO_2 splitting in non-thermal plasma

Snoeckx and Bogaerts [2] have examined the positive aspects and criticisms of conventional and novel CO_2 conversion methods, highlighting the future potential of plasma in a long-term context (Table 4.1). Many of the significant challenges associated with the aforementioned technologies can be resolved with nonthermal plasma. Notably, plasma does not require high temperatures since the gas is activated at room temperature by highly energetic electrons. The second major advantage of non-thermal plasma technology for CO_2 conversion is its high level of flexibility. It relies on various types of renewable energy and can be rapidly switched on and off, with stabilization times typically under 30 minutes. This provides an enormous advantage in terms of locational flexibility. Furthermore, plasma technology can effectively utilize any excess intermittent renewable energy by storing it in a chemical form. Furthermore, plasma reactors are simple and inexpensive, making them easily scalable from small to large applications. The most direct method of reusing CO_2 is through CO_2 splitting, which can yield high concentrations of CO for the synthesis of oxygenated compounds and hydrocarbons.

Due to their mild working conditions and improved energy efficiency, atmospheric pressure, non-thermal plasma applications have undergone significant research. In

conventional heterogeneous catalysis, thermal energy transfers occur, but most chemical transformations take place on the catalyst surface.

Table 4.1 *Summary of classical thermal catalysis and developing methods, highlighting advantages and disadvantages. The color coding adds a visual sense to the importance of the feature, as further detailed in the text: negative (red), neutral (orange) and positive (green). Revised from ref [2]*

	thermal conversion	electrical conversion	solar conversion	Cold Plasma
Need of Heat	Yes (700 K – 3000K	No, room Temperature	Yes (< 1500K)	No, room temperature
Renewable use	No use	Indirectly	Directly[c]	Indirectly
Commercialization [a]	Possible	Possible	Possible	Easy
Type of products	limited	Wide range	Wide range	Wide range
Cost [b]	High	Moderate	Moderate	Low
Performance	High	Moderate	Moderate	Moderate

a Commercialization includes overall flexibility of the process and if it is a turnkey process
b Cost includes Investment cost, operating cost and use of rare earth metals
c Solar conversion can use only solar irradiation as renewable energy

Conversely, in non-thermal plasma, various energy channels activate the gas phase and ionize gas molecules. Electrons acquire their energy from the applied electric field and collide with heavy particles during their mean free path, transferring a portion of the accumulated energy to them. This energy is divided between elastic energy losses and various channels of excitation, ionization, and dissociation. Upon discharge application, the gas molecule undergoes rotational motion followed by vibration, leading to electronic excitation and resulting in bond dissociation. Table

4.2 presents an overview of the primary plasma channels for electron-molecule reactions.

Table 4.2 *Overview of the main electron/molecular interaction in plasma chemical processes. A and B represent atoms. From ref.* [1]

Excitation Vibrational Rotational Electronic	 $e^- + AB \rightarrow AB^* + e^-$ $e^- + AB(V1) \leftrightarrow AB^-(Vi) \rightarrow AB(V2) + e^-$ $e^- + AB(R1) \leftrightarrow AB^-(Ri) \rightarrow AB(R2) + e^-$
Dissociation	$e^- + AB \rightarrow A + B + e^-$ $e^- + AB \rightarrow A + B^* + e^-$
Polar dissociation	$e^- + AB \rightarrow A^- + B^+ + e^-$
Attachment	$e^- + AB \rightarrow AB^-$ $e^- + A + B \rightarrow A^- + B$
Dissociative electron attachment	$e^- + AB \rightarrow (AB^-)^* \rightarrow A^- + B$
Non-dissociative ionization	$e^- + AB \rightarrow AB^+ + e^- + e^-$
Dissociative ionization	$e^- + AB \rightarrow A^+ + B + e^- + e^-$
Step-wise ionization	$e^- + A \rightarrow A^* + e^- \rightarrow A^+ + e^- + e^-$
Electron-ion recombination	$e^- + AB^+ \rightarrow AB$ $e^- + e^- + A^+ \rightarrow A^* + e^-$
Dissociative electron-ion recombination	$e^- + AB^+ \rightarrow (AB)^* \rightarrow A + B^*$

Radiative electron-ion recombination	$e^- + A^+ \rightarrow A^* \rightarrow A + h\nu$
Electron impact detachment	$e^- + AB^- \rightarrow AB + e^- + e^-$

As energy is primarily transferred to gas molecule by the applied electric field, the amount of it transferred in different channels can be correlated to the reduced electric field of the plasma, E/n_0, as indicative of the average energy transferred to gas molecule (figure 4.2).

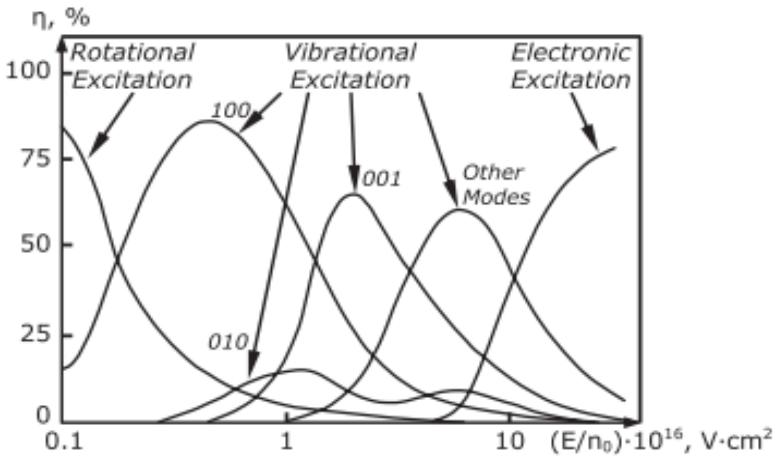

Figure 4.2 *Fractions of non-thermal CO_2 discharge energy transferred from plasma electrons to different channels of excitation of the molecule [1].*

It is defined as a ratio of the applied electrical field (E) divided by the number of gas (n_0), expressed as relative pressure, density or concentration of neutral species [2,12,13]. His ratio is referred to as Townsend (Td), where 1 Td is equivalent to 10-21 V*m^2 and 100 Td is equivalent to an electron temperature of 2 eV.

CO_2 is a linear triatomic molecule that possesses four vibrational modes. However, due to its symmetry, it possesses only three vibrational modes with one of them being doubly degenerate. These three modes are typically denoted by (a,b,c), and are associated with the symmetric stretch mode (1,0,0), the doubly degenerate symmetric bending mode (0,1,0), and the asymmetric stretch mode (0,0,1). The

energies for these modes are respectively 0.172 eV, 0.083 eV, and 0.291 eV. Furthermore, molecular interaction involves various channels, including electron-translational (e-T), electron-vibrational (e-V), vibrational-vibrational (V-V), vibrational-translational (V-T), rotational-translational (R-T), and translational-translational (T-T). The dissipation of electron energy can be attributed to electron transfers, i.e. e-T and e-V. The V-T mode transfers energy to the translational degrees of freedom via collisions, resulting in the conversion of vibrational energy into heat. The e-V transfer rapidly excites the discharge molecules' lowest vibrational states and is accompanied by V-V exchange within each vibrational mode, as well as V-V" exchange between different vibrational modes [14]. At electron temperatures that are typical for non-thermal discharges (Te ~ 1 eV), most of the discharge energy is transferred from plasma electrons to CO_2 vibration. Vibrational energy losses happen through vibrational-vibrational (VV and VV") relaxation. This occurs at sufficiently high plasma ionization levels to attain a significant deviation from the equilibrium population of the CO_2 ground electronic state ($^1\Sigma^+$).

The direct dissociation of a vibrationally excited CO_2 molecule (figure 4.3) leads to an electronically exited O atom and a CO molecule with same spin.

$$CO_2^*(^1\Sigma^+) \rightarrow CO(^1\Sigma^+) + O(^1D) \qquad Ea = 7 \text{ eV}$$

The reaction necessitates an energy exceeding 7 eV/molecule, which is higher than the theoretical value required for breaking the C=O bond (i.e., 5.5 eV/molecule). However, vibrational-vibrational (VV) collisions progressively populate the higher vibrational levels, ultimately causing the CO_2 molecule to dissociate. The gradual vibrational excitation leads to a spin change of ($^3B^2$), resulting in the formation of CO and an oxygen atom in the ground electronic state. This reaction is faster than direct dissociation because its activation energy is lower, which is the same as that of a C=O bond [2,13,15].

$$CO_2^*(^1\Sigma^+) \rightarrow CO_2^*(^3B^2) \rightarrow CO(^1\Sigma^+) + O(^3P) \qquad Ea = 5.5 \text{ eV}$$

The formed atomic oxygen is able to react with another CO_2 molecule, according to reaction:

$$CO_2^*(^3B^2) + O(^3P) \rightarrow CO(^1\Sigma^+) + O_2(^1\Sigma^+) \qquad Ea = 0.3 \text{ eV}$$

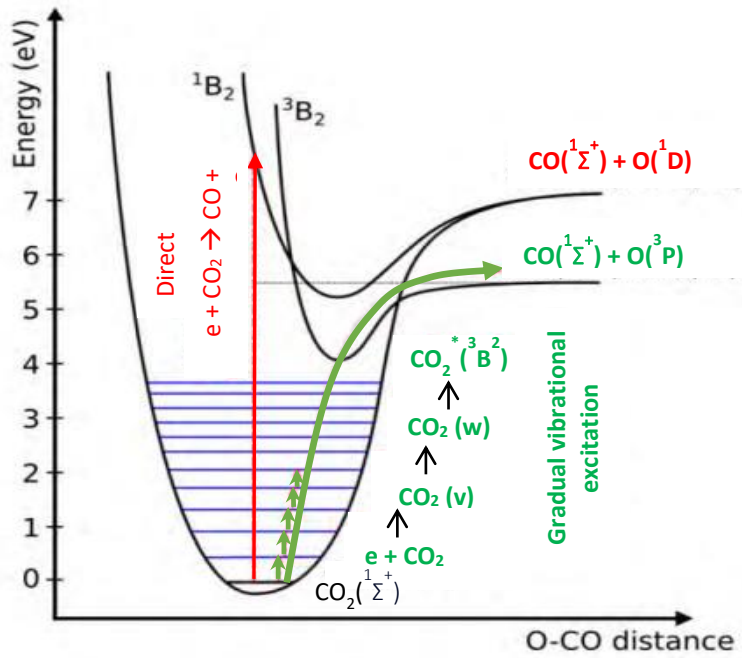

Figure 4.3 *Schematic illustration of direct dissociations (in red) and stepwise vibration excitation way (in green). The latter proceeds with a lower energy activation. Adapted from ref. [21]*

4.2.2 Different type of reactor for CO_2 splitting and Performance parameters

Dielectric barrier discharges, microwave plasmas, gliding arc plasmas, atmospheric pressure glow discharges, nanosecond-pulsed discharges, and corona and spark discharges are all under investigation for their potential to convert CO_2. These plasmas are distinct in their application of electricity and the specific values of electric field, reactor configuration, pressure, power, among other factors. In figure 4.4, the fractions of non-thermal CO_2 discharge energy transferred from plasma electrons to various channels of molecule excitation are demonstrated by the primary type of reactor design for CO_2 splitting.

At low reduced electric fields, energy is converted into the rotational and vibrational motion of molecules, resulting in electronic excitations. For example, at 50 Td,

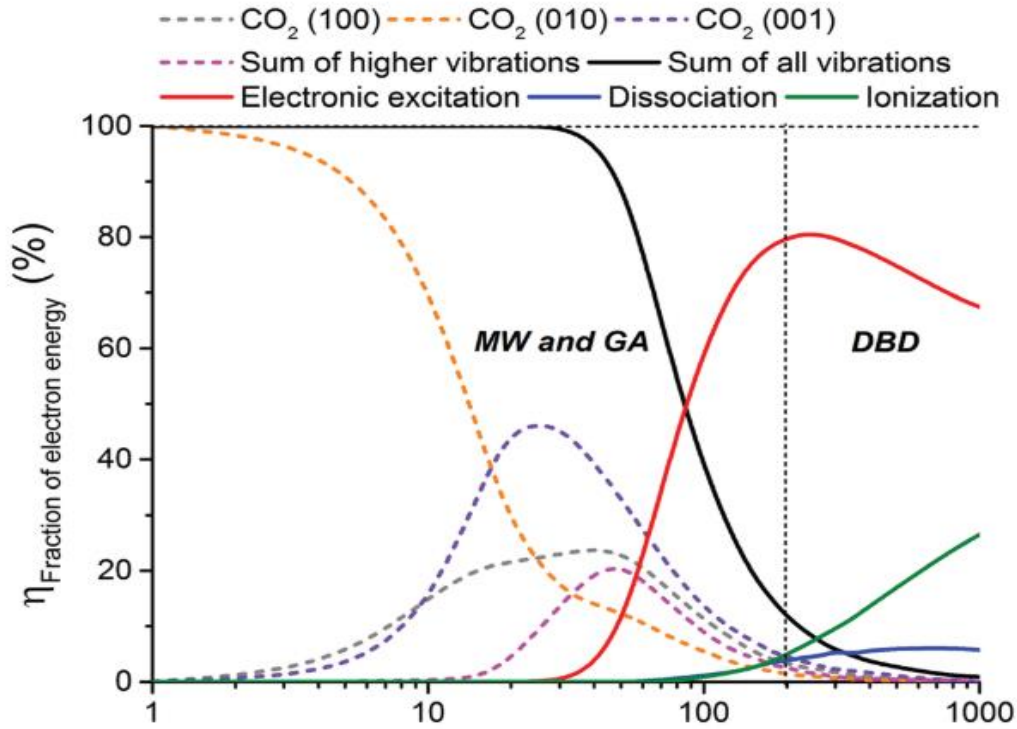

Figure 4.4 *The fraction of electron energy transferred to different excitation pathways, as well as to CO_2 ionization and dissociation, is calculated based on the corresponding cross-sections of electron-impact reactions. It is calculated as a function of the reduced electric field (E/n), and the E/n regions specific to MW and GA plasmas, as well as DBD plasma, are displayed. From ref [2]*

where MW and GA operate, almost all the energy (90%) is directed towards vibrational modes, thus increasing the speed of stepwise vibration excitation. Conversely, at reduced electric fields of >100 Td, high levels of electronic excitations lead to ionization and molecular dissociation.

DBD plasma operate in this region. For instance, at approximately 200 Td, the average electron energy of 2-3 eV is excessively high for efficient population of CO_2 vibrational levels. As a result, it is primarily transferred to electronic excitation, while only a small fraction is utilized for ionization and vibrational excitation

[2,15,16]. Consequently, vibrational excitation plays a minor role in the DBD region. However, the nature of the gas (CH_4, H_2O, H_2, Ar, He, and N_2) significantly influences this trend as the composition modifies the distribution of energy channels. Therefore, it is crucial to understand the magnitude of electric field reduction needed for a particular gas mixture to generate the relevant amounts of electronic activation, disassociation, and ionization.

4.2.2.1 DBD plasma

In 1857, Siemens carried out pioneering experiments with DBDs to produce ozone [17]. He designed a brand-new device which situated the electrodes beyond the plasma chamber, keeping them apart from the plasma. To sustain a discharge in a small circular gap between the two coaxial glass tubes, an alternating voltage with an appropriate amplitude was utilized.

The DBD discharge type is commonly known for preventing electric current from entering by the dielectric barrier of the glass walls. DBD remains the most effective industrial technology for producing ozone from air or oxygen, and is also utilized in CO_2 lasers[18], as a UV source in excimer lamps, and to treat polymer surfaces[19]. Its effectiveness persists even after a century. In addition, the utilization of dielectric barrier discharge (DBD) plasma has become prevalent due to its ease of construction, ability to operate under regular conditions, and scalability. Industrial-scale expansion can be achieved effortlessly by operating multiple DBD systems simultaneously [13].

This is also why DBD still remains in a leading position among plasma-chemical reactors. The use of a dielectric barrier makes DBD incapable of operating with direct current. Instead, it generally deploys frequencies between 0.05 and 500 kHz and high voltage, and an amplitude of 1–100 kV, is crucial to initiate gas discharges in the gap. Various materials with high breakdown strength and low dielectric loss, including glass, quartz, ceramics, or other functional materials, can be used as the dielectric barrier. After the barrier is formed, a metal electrode coating can be added.

The geometry may be planar or tubular depending on the application (figure 4.5). A gas flow is then applied between the discharge gap at about atmospheric pressure, which usually ranges from 0.1 to 10 atm but is typically set at 1 atm. The discharge gap can vary from 0.1 mm (as seen in plasma displays) to over 1 mm (for ozone generators) and up to several cm (in CO_2 lasers).

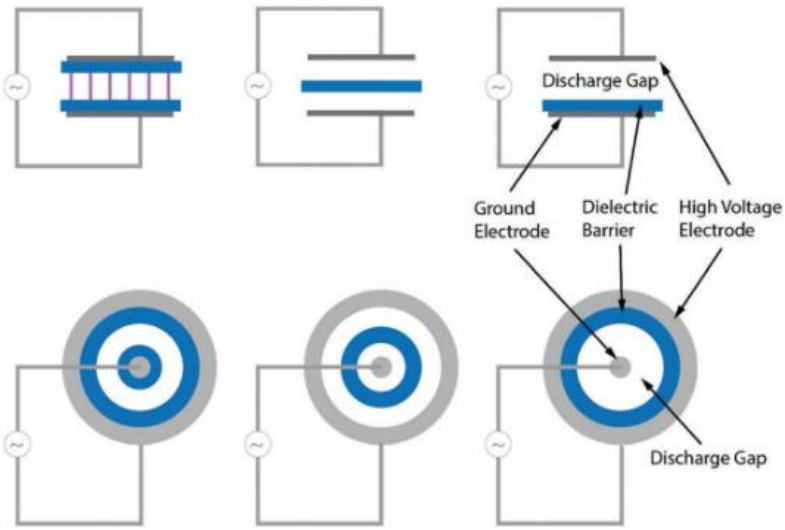

Figure 4.5. *Planar (a) or tubular dielectric barrier discharge configurations. From ref [2]*

Alternatively, the metal electrodes can be coated with dielectrics by inverting the arrangement. These dielectric barrier discharges are also known as silent discharges because they are non-uniform and consist of multiple microdischarges spread across the discharge gap, preventing spark discharge and the resulting localized overheating, shock waves, and noise. This phenomenon is called the filamentary mode since plasma generation is confined to these micro-discharges. The plasma mode type is determined by the gas nature, either filamentary or homogeneous.

CO_2, alongside most gases, generates a filamentary mode with a plasma volume ranging from 1% to 10% of the gas volume [2,20], This mode is recognized by CO_2 being dissociated into CO and O due to electron impact, followed by two O atoms recombining into O_2 [20,21]. The non-ionized residual gas serves as an energy-

absorbing reservoir during micro-discharges and also collects and transfers long-lasting species produced during these discharges [1,19,22]. Furthermore, DBD plasma has been most widely used because it is simple to build, easy to operate with more normal operating conditions, and easy to scale up or down. The scale up at an industrial scale can be easily done by using a number of DBD in parallel.

4.2.2.2 MW e GA reactor

When excited molecules collide with molecules in a ground state, they may lose energy through vibrational-translational (VT) relaxation. This process decreases vibrational levels and hampers the energy-efficient conversion of CO_2 in the pathway of ascending vibrational ladder. Furthermore, the process raises the temperature of gas molecules. As the gas temperature increases, the rate coefficients for VT relaxation also accelerate, which expedites the vibrational depopulation process. In fact, VT relaxation plays a crucial role in both Microwave (MW) and Gliding arc (GA) plasmas, resulting in gas temperatures of 3000K or higher. This variant of plasma is commonly referred to as "warm plasma" due to its intermediate temperature range between non-thermal plasmas like DBD, which operate at or slightly above room temperature, and thermal plasmas, which exceed 10000K in gas temperature (equivalent to electron temperature). Microwave and gliding arc plasmas have higher electron temperatures than gas temperatures, categorizing them as non-thermal plasmas. The vibrational and gas temperatures typically become equal, allowing them to also be categorized as quasi-thermal plasmas. Accordingly, thermal processes are responsible for the majority of CO_2 conversion in MW and GA plasmas during operation [23–25].

Microwave induced plasmas (figure 4.6 a) is an electrode-less system in which plasma is ignited and maintained by microwaves (frequency from 300 MHz to 10 GHz) [5]. Gas electrons adsorb energy by microwaves, giving rise to elastic collisions with heavy particles. After several elastic collisions, some inelastic and ionizing collisions are produced and the plasma is created [26]. Generally, a plasma

discharge system consists in: a microwave power source; microwave equipment (wave guides, tuning system); an ignition system and a gas injections [2,19,27].

Gliding arc (figure 4.6) is composed of two diverging flat electrodes between which gas flows. By applying a potential difference between the two electrodes, a thermal arc plasma is formed in the narrower gap, which is then entrained by the gas flow to an increasing interelectrode distance up to a critical value beyond which the plasma becomes non-thermal. The plasma then traverses the space between the electrodes until it completely dissipates. If a 2D electrode geometry is used (figure 4.6 c), gas conversion is non-uniform because a significant portion of the gas does not pass through the active plasma region. Additionally, the arc requires a high gas flow rate for propulsion, which leads to limited gas residence time and further constrains conversion.

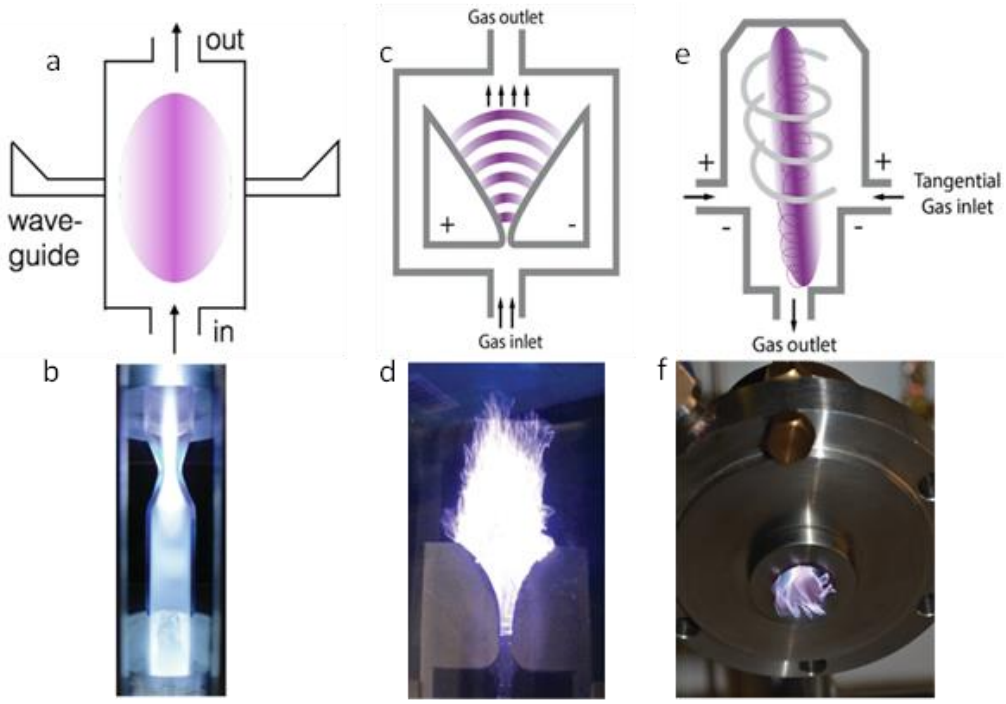

Figure 4.6 *Non-thermal plasma reactor configuration: Microwave induced plasma reactor (a,b) traditional gliding arc reactor (c,d) and gliding arc plasmatron (d,e). DBD is not reported. From ref [2]*

A more efficient 3D cylindrical plasma reactor utilizing vortex flow stabilization through a tangential inlet is presented in figure e, called gliding arc plasmatron (GAP). A vortex gas flow is created depending on the diameter of the anode tube. When the anode diameter matches the cathode diameter, gas exits the reactor through the anode outlet, generating a forward vortex flow. If the diameter of the anode is smaller than that of the cathode, gas cannot escape the reactor at a rapid pace. Instead, the gas moves upward in a forward vortex along the walls of the reactor. As the gas reaches the top section of the reactor, friction and inertia cause it to lose velocity. Then, the gas moves downward in a smaller inner vortex known as a reverse vortex, where it combines with the plasma arc. This type of conversion results in greater energy efficiency [2,23].

4.3 PLASMA CATALYSIS

One of the key advantages of non-thermal plasma is its ability to induce a non-equilibrium state through the activation of stable molecules. However, low selectivity for the intended formation of targets remains a significant concern. The reactive species produced by the electrons follow chemical kinetics principles, and consequently, they can recombine to form several different products based on the reaction conditions. Further, newly formed products can be destroyed by electron collisions. This is not a concern for the simple dissociation of CO_2 because the only potential outputs are CO and O_2, with minimal quantities of O_3. However, the incorporation of a catalyst can improves the conversion efficiency. Plasma catalysis is a developing field in plasma processing, and it theoretically provides the benefits of both worlds.

Plasma has the ability to activate inert molecules at room temperature, and these activated species can then undergo selective recombination on the surface of the catalyst, resulting in the desired products. Plasma-catalysis has been the subject of research for more than sixty years in reactive systems. A study conducted in 1954 [28], on the formation of hydrazine in a low-pressure DC discharge of ammonia

found that coating the discharge tube walls with platinum increased the hydrazine yield due to its catalytic properties in hydrogen atom removal. Mizuno and colleagues [29] were the first to apply atmospheric pressure plasma with a catalyst to the synthesis of methanol from CH_4 and CO_2. The researchers analyzed the process in a dielectric barrier discharge utilizing a $ZnO–CrO_3–H_2O$ catalyst. They concluded that this catalyst significantly improved the efficacy of the synthesis.

The catalysts can be incorporated in the plasma setup by two main configurations (figure 4.7):

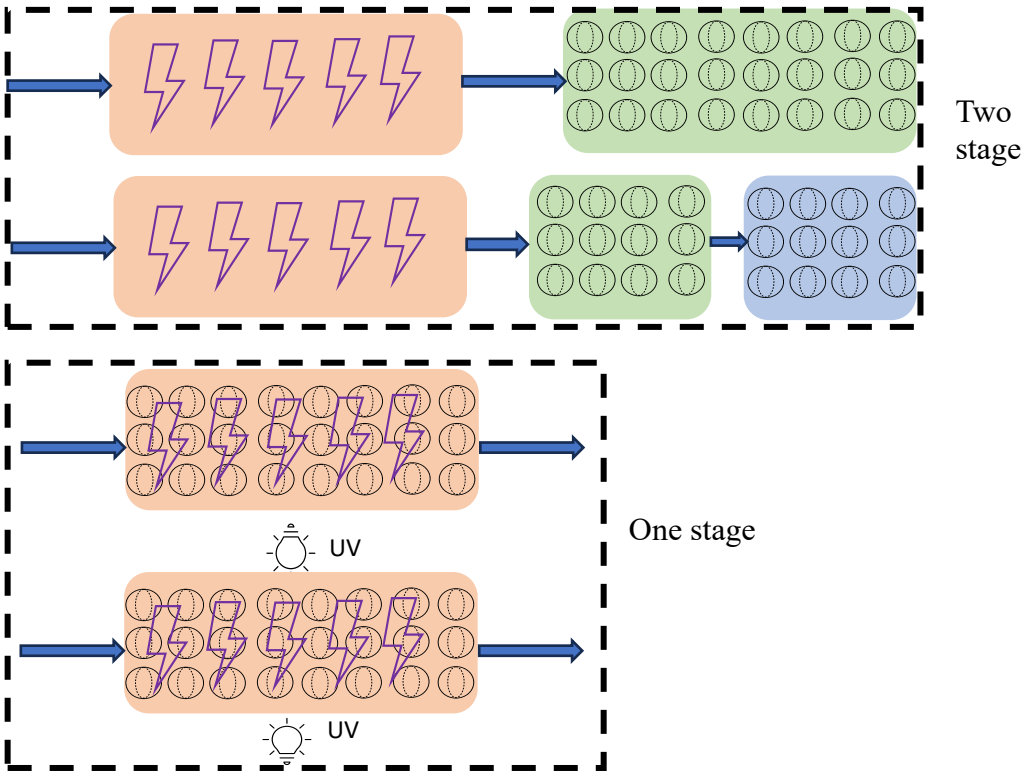

Figure 4.7 *Differt type of plasma-catalyst configuration*

(i) A two-stage configuration, where the catalyst is spatially separated from the plasma zone, either upstream or downstream; accordingly, only end products and long-lived intermediates undergo reactions with it. Furthermore, a multistage plasma-catalysis process may be implemented to include more than one catalyst in sequence. Each catalyst in the

sequence has a unique functionality and can treat different components of the gas stream. Additionally, it is commonly utilized to remove unwanted by-products after plasma processing.

(ii) Regarding the one-stage configuration, the catalyst is located within the discharge zone, allowing it to interact with all short-lived species, including excited species, radicals, photons, and electrons. This provides a substantial benefit as certain products that were previously unobtainable with the previous configuration can now be produced. Additionally, this method can be coupled with UV irradiation to generate plasma photocatalysis.

Catalysts can be deposited onto electrodes or packed into the discharge zone. Catalyst options include pellets, fine powders, foams, honeycomb monoliths, various electrode materials, electrode coatings, and coated quartz wool. The ease of incorporating a catalyst into the discharge zone can vary depending on the plasma reactor used. Implementing a catalyst in a DBD reactor is typically straightforward because of the reactor's basic design and close-to-room temperature functionality. However, due to a high gas temperature in the discharge zone (1000-2000 K compared to 300-400 K for DBD), catalysts are usually placed downstream because of their limited thermal stability, despite MWs having a simple shape. Additionally, catalyst injection downstream is typical in GA discharges due to their complex geometries and high temperatures [2,30].

4.3.1 Synergistic effect

The one stage configuration, the most commonly utilized option, exhibits a synergistic relationship between plasma and catalyst. The combination of both creates a more profound impact than the mere sum of their individual contributions with respect to conversion, selectivity, and energy efficiency. For instance, a "synergy factor" was defined by Vandenbroucke et al. [31] in their investigation of plasma-catalytic removal of trichloroethylene (TCE), as the ratio of the degree of

TCE degradation by plasma-catalysis with the sum of the degrees of TCE degradation by plasma alone and the degrees of TCE degradation by catalyst alone. In a synergistic system, the synergy factor will be greater than one. This effect can be broadly explained as either the plasma altering the performance of the catalyst or the catalyst changing the discharge proprieties. The two types of effects are physical and chemical. Although physical effects are primarily responsible for improved energy efficiency, chemical effects can boost selectivity for specific commodities. Since the majority of CO and O_2 is produced during CO_2 splitting, the primary advantage of using the catalyst is to enhance energy efficiency[2].

The effects of adding a catalyst into a discharge gap are mainly physical:

1. The electric field can be altered by geometric distortion and surface roughness of the catalyst [32]. For instance, contact points in a packed bed reactor, can change reaction rate and selectivity.
2. Inside pore the electric field could be more intense, creating more powerful microdischarges, resulting in a different plasma behavior compared to the bulk [33].
3. The interactions could lead to a change of discharge type, especially if insulating surfaces are used [34].
4. The adsorption and desorption of species on the catalyst surface, affecting their concentration and conversion through prolonged residence time and altering the distribution of active species [35].

However, plasma effects on catalysts are reported to be both physical and chemical. However, the latter are less understood because they are associated with physical effects:

1. Changes in its physicochemical properties, such as increased probability of adsorption on the catalyst surface, change in catalyst surface area by sintering and particle agglomeration, change in the oxidation state of the catalyst or reduction of metal oxide catalysts to metallic form, reduced coke formation on the surface, and change in the work function of the catalyst.

2. Formation of local high temperature spots on the surface by high energetic microdischarges that influence local reaction rates and product selectivity, as well as coke deposition rate.
3. Activation of the catalyst by photon irradiation emission.
4. New reaction pathways for the presence of a wide variety of reactive species and strong microdischarges.
5. Lower activation energies thanks to activation of gas molecule by plasma (vibrational excitement).

In addition, the presence of inert gases such as N_2, Ar, and He in the plasma can alter the plasma-catalyst interactions increasing CO_2 conversion, with Ar performing better than He [36].

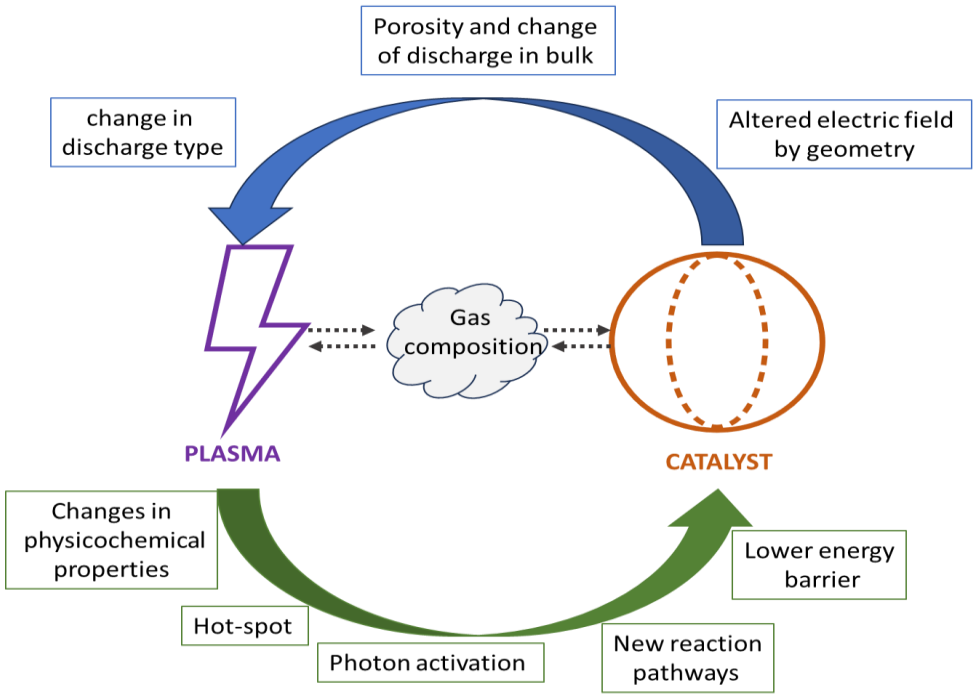

Figure 4.8 *Summary of Plasma effects on catalysts and vice versa*

Because of these synergistic effects, there is a constant interaction between the active and neutral species of the gas phase, the properties of the plasma and the various physical, chemical, thermal and electrical properties of the catalyst, and *vice-versa*

(figure 4 .8). For this reason, although a generalization has been made, it cannot include all possible interactions, which should be studied on a case-by-case basis.

4.4 Performance parameters and reactor design influence on CO_2 splitting

Several critical metrics are used to evaluate the performance of a plasma reactor. Two essential metrics, conversion (χ) and energy efficiency (η), are conventionally utilized to define process efficiency. Additionally, from these two, specific energy input (SEI) and selectivity to the target compounds are important variables to consider. However, as only one valuable product is produced during CO_2 dissociation, the selectivity parameter is unnecessary.

The specific energy input is calculated by the ration of plasma power with gas flow rate, and it can be expressed in J cm^{-3} or kJ/L or electron volts (eV) per molecule (24.5 L/mol is valid for 298 K and 1 atm):

$$\text{SEI (J cm}^{-3}\text{ or kJ L}^{-1}\text{)} = \frac{\text{Power (kW)}}{Flow\ rate\ (L\ /sec)}$$

$$\text{SEI (eV/molecule)} = \text{SEI}\ (KJ/L) * \left(\frac{6{,}24*10^{21}\ (eV\ KJ^{-1})*24.5\ (L\ mol^{-1})}{6{,}022*10^{23}(molecule\ mol^{-1})}\right)$$

The calculation of conversion can consider the yield of byproducts. However, this approach ignores any undesired byproducts or coke formation. Therefore, it is advisable to calculate the conversion based on the amount of unreacted gas.

$$\text{X (\%)} = \left(\frac{\dot{n}\ \text{in} - \dot{n}\ \text{out}}{\dot{n}\ \text{out}}\right) * 100$$

Where ṅ indicates the molar flow rates (mol/s) entering and exiting the system.

The energy efficiency and cost are contingent upon the specific process being analyzed. The energy efficiency measures how effectively the process operates in comparison to the standard reaction enthalpy, taking into account the specific energy input (SEI):

$$\eta(\%) = \frac{\Delta H°(\text{KJ mol}^{-1}) * \text{X(\%)}}{SEI(KJ\ mol^{-1})}$$

Where ΔH° indicates the enthalpy variation associated with the reaction at 298,15K. For instance, in the case of pure CO_2 splitting $\Delta H°_{298K}$ is 283 kJ mol^{-1} or 2.93 eV/molecule is SEI is calculated in this manner.

The energy cost (EC) refers to the quantity of energy utilized during the processing:

$$EC = \frac{SEI\ (KJ\ mol^{-1}) * 24.5\ (L\ mol^{-1})}{X}$$

Except for conversion, all the parameters are proportional (directly or indirectly) to SEI and therefore to plasma power. Moreover, this parameter enables the comparison of discharges across different configurations, such as shape, dimensions, working gas mixtures, and driving voltage waveforms. Generally electrical power is provided by a generator but not all the power is used by plasma. In fact, part of the energy is dissipated by the set-up resistance or is transferred as gas heating [37]. The actual plasma power is calculated by detecting the transported charge with a current transformer and measuring the voltage drop across the electrode gap with a high voltage and low voltage probe. These measurements are obtained through a digital oscilloscope. The applied voltage and the dissipated charge result in a Q-U graph, also known as a Lissajous figure, which can be used to determine the plasma power by measuring the area of the resulting graph [36,38,39].

After explaining the most frequently employed CO_2 splitting reactor types and how the energy is transferred from the plasma to the molecules' different excitation levels within them, an outline of the diverse aspects that impact the process is presented. Explanatory in this context is figure 4.9, reported by Snoeckx et Bogaerts [2]. The image compares literature data for different reactor types while considering limitations resulting from thermodynamics and the target efficiency to achieve.

The thermal equilibrium limit is due to the high energy required to break a C=O bond, while the target efficiency is derived Spencer et al.'s work [40] predicting that plasma-based CO_2 processes need to achieve an energy efficiency of at least 52-60% to eliminate all CO_2 emissions from a natural gas power plant while maintaining

energetic net positivity and a zero carbon footprint. The image demonstrates that all types of reactors have limitations when it comes to both energy efficiency and conversion. They often exhibit high conversion rates at the expense of low efficiency and vice versa. Gliding arc reactors display strong energy efficiency potential and can achieve the desired target, but the conversion rate is usually less than 20%. On the flip side, the efficiency of DBD reactors is lacking, typically around 10%, due to energy being transferred mainly through high levels of electronic excitations that lead to ionization and molecular dissociation. This also clarifies the reason why conversion rates increase to 40%. A vast range of conversion rates and energy efficiencies can be attained through microwave discharges in transforming pure CO_2.

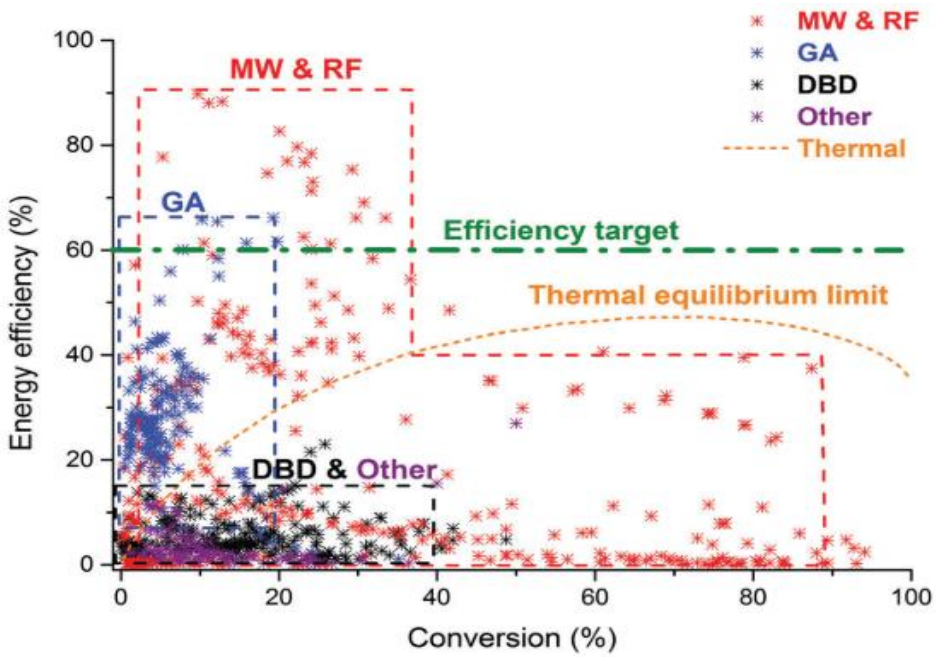

Figure 4.9 *Comparison of literature data for CO_2 splitting in different plasma types, illustrating the energy efficiency in relation to conversion. The study also displays the thermal equilibrium limit and the targeted efficiency.*

The efficiency target is attained with a conversion of around 40%. However, despite most research obtaining extremely high conversion rates (over 60%), the energy efficiency hovers around 5%.

An ideal reactor should be located at the top right of the graph, indicating high efficiency and conversion rates. However, currently, there is no reactor or configuration that meets these criteria. According to the brief analysis, MW plasma appears to be the most promising technology. However, the commercial and industrial feasibility of the process depends on various factors beyond the MW discharges and values illustrated in the graph. For instance, it is important to consider that many applications occur under reduced pressure, which can reduce the overall efficiency of the process. In contrast, the GA and DBD reactors operate at atmospheric pressure. Additionally, the DBD reactor features a straightforward design that can be easily scaled up for industrial use, with established applications such as ozone production [41] or VOC abatement [42].

Regarding the DBD reactor, multiple strategies have been evaluated for achieving higher CO_2 conversion and energy efficiency values. Since the process involves the interaction among plasma, gas, and the reactor, one can modify each of them in a specific way: it is possible to vary the parameters that generate the plasma (power and frequency), or those that affect the gas (flow rate and type of gas), or even change the reactor. In the latter case, we can change either the geometry, specifically the discharge length or the gap in the discharge zone, or the used materials, including the electrodes and the dielectric.

4.4.1 Plasma parameters

The applied voltage and frequency are the most adjusted parameters to investigate plasma behavior. Usually at the increase of the voltage, the CO_2 conversion increases because more power is applied, only a slightly reduction of energy efficiency is observed [43–45]. Increasing the applied power means increasing the electric field and thus the electron density and average energy (i.e., temperature). However, the positive effect could be valid as long as the energy remains low. In fact, for higher powers (>50W) some factors intervene that reduce the effect of electron density. An

increase is observed in the possibility of recombination between CO and O, which leads to a decrease in net CO_2 conversion, as well as an increase in power dissipation[45,46]. A significant portion of the applied power is inevitably wasted as gas heating, but its effects on CO_2 thermodynamics are negligible since it is still close to room temperature. In addition, abnormal discharge (corona) inside the trapped air between the wrapped outer electrode and the dielectric could be observed, drastically reducing the conversion [46–48]. This is consistent with the results of Niu and colleagues [49] who observed a significant increase in the conversion of CO_2 up to 13 kV (peak to peak voltage). However, for higher voltages, there was a substantial decrease in energy efficiency, with a small increase in conversion.

Increased frequency can impact the memory effect by accumulating charges and polarization on the dielectric surface due to the higher speed of voltage switching between electrodes [1]. As a result, the higher filamentary regime leads to lowered breakdown voltage[20]. Thus, a reduction in the electric field within the plasma discharge results in a decrease in the average energy of electrons, leading to a lower number of electrons participating in the CO_2 dissociation process[44,50,51]. This, in turn, leads to decreased conversion and energy efficiency[43,44,52].

4.4.2 Effect of the gas flow rate and chemical composition

The gas flow rate determines the residence time of gas in the reactor gap volume, which in turn affects the gas conversion rate. When using a low gas flow rate, gas molecules remain in the plasma regions for a longer period, increasing the likelihood of interaction and obtaining higher conversion rates. Conversely, high flow rates result in a shorter residence time of gas in the reactor volume and lead to lower conversion rates [2,49,53]. Achieving high flow rates is crucial for scaling up in the industry [43]. Furthermore, flow rate impacts other parameters. Specifically, increasing the gas flow rate leads to a decrease in SEI and energy cost, while boosting energy efficiency [43,46,49]. Anyway the effect of flow rates seems less dominant then applied power [54]. However, greatly increasing the residence time (or decreasing the gas flow rate) is not the ideal choice for increasing performance, both

because larger flows are preferable on an industrial scale, and because the conversion reaches equilibrium and does not increase after a given residence time [21,39].

The use of an inert gas such as helium, argon, or occasionally nitrogen is a common tactic to enhance conversion and energy efficiency in plasma-based processes. In fact these gas reduced the breakdown voltage if compared with pure CO_2 because the inert gas increase the first Townsend ionization coefficient α and consequently number of secondary electrons created per unit length along the electric field [1,6,55]. This also explains why better results are obtained with Ar than with He. Additionally, the higher energy for ionization and excitation of Ar and He then CO_2 results in a decreased likelihood of inelastic collisions between electrons and Ar or He, as well as recombination with Ar^+ or He^+ ions in the Ar or He plasma. As a result, there is a longer mean free path in the Ar or He plasma, giving electrons more time to accelerate in the applied electric field, allowing for electrical breakdown to occur with lower voltages. However, it must be kept in mind that the absolute conversion is typically lower then pure CO_2 because the gas is diluted. As a consequence, the energy efficiency also decreases.

For instance, Remakers et al.[36] reached a conversion of 41% and 25% at an applied power of 80 W, a frequency of 23.5 kHz and gap of 1.83 mm but in a mixture of CO_2/Ar(95%) or CO_2/He(95%) respectively, observing a CO_2 conversion drop from about 5.5% (in pure CO_2) to 2% upon addition of 95% Ar, and even to 1.2% in the case of adding 95% He. N_2 improves the absolute CO_2 conversion by dissociating CO_2 during collision with N_2 metastable molecules, which is sufficient to counter the mixture's lowered CO_2 level. The addition of N_2 produces varying results. Nevertheless, the introduction of N_2 in the mixture generates undesired by-products, such as N_2O and several NO_x compounds at levels that pose a significant air pollution hazard [56,57].

4.4.3 Influence of reactor

The performance of a DBD reactor can be influenced by both the gas composition and flow rate, as well as by the reactor's features such as geometry, dielectric and

electrode shape. The length of the discharge zone and other factors can affect the plasma behavior within the reactor.

Concerning the electrodes material, Li et al. [58] comparing aluminum rod, copper and stainless steel inner electrode highlights the importance of a both electrical and thermal conductivity in CO_2 conversion. Improved electrical conductivity can release high-energy electrons, leading to more reactive species and greater CO_2 conversion rates. On the other hand, higher thermal conductivity raises the inner electrode's temperature, requiring additional energy for heat and reducing the positive effect of higher electrical conductivity on CO_2 breakdown. In agreement, research by Wang et al.[59], shows that Cu and Au electrodes increase the conversion rate by 1.5 times compared to Fe electrodes and by three times the energy efficiency compared to a Rh electrode under identical conditions. Similar conclusion were obtained by Dat et Kamble comparing Cu and Pyrex electrode [52]. Nonetheless, these electrodes and coatings can be pricey and vulnerable to chemical (oxidation) and plasma erosion (as Au sputtering), despite their effectiveness. In the case of an external electrode the thermal conductivity has less importance as fully exposed to air. This allowed for the accumulated heat within the reactor to be released more quickly from the outer electrode than from the inner electrode [58].

The electrode length affects the discharge zone length and the residence time within the plasma zone, which enhances CO_2 conversion [54]. This is due to the increased probability of CO_2 molecules colliding with highly energetic electrons and reactive species [48,49]. However, for the same power input, the electron flux density decreased since the plasma field strength decreased due to an increase in plasma volume. Additionally, increasing the surface area of the dielectric material results in increased energy loss through heat dissipation [60,61].

Another controversial parameter in the DBD reactor is the choice of dielectric material. It is responsible for maintaining a cool and uniform plasma by preventing arcing and must be able to withstand the reactive conditions present. The dielectric's nature and thickness are directly related to physical parameters such as the secondary

electron emission coefficient and dielectric constant [62]. The dielectric constant affects the flow of current during the discharge, thereby altering the electron density. Belov et al.[63] observed that the conductive properties of the dielectric material may play a crucial role in CO_2 discharge. They found that the conversion rate was higher when a conductive layer was deposited on the inner side of the outer dielectric wall, compared to uncoated surfaces. Li et al. [64] achieved higher conversion rates through the use of a $Ca_{0.7}Sr_{0.3}TiO_3$ ceramic with 0.5 wt.% $Li_2Si_2O_5$ additive as a dielectric barrier. This is due to the ceramic's higher relative permittivity compared to alumina or silica glass, which allows for greater discharge currents.

Wang et al. [65] also utilized the same ceramic, but added varying percentages (0.5-5 wt%) of CaO-B_2O_3-SiO_2 glass. They found that this resulted in an increase in conversion and energy. At the same an higher dielectric permittivity can increase the amount of energy dissipated as heat[37]. The dielectric material also affects the coefficient of secondary emission (γ) since it is related to the self-sustainment of the plasma and the emitted secondary electron [1,19]. For example, Ohtsu et al. [66] reported a decreased breakdown voltage for plasma ignition using MgO metal-oxide dielectric as a result of increased secondary electron emission. However, alumina and quartz remain the most commonly used materials due to their good dielectric properties [43] and affordability, despite these results.

Alumina appears to be less brittle and more stable [20], but quartz allows for Optical Emission Spectroscopy to investigate active plasma species as a spectroscopic method. The thickness of the dielectric affects plasma behavior by increasing the number of microdischarges. However, it also decreases transferred change [62] and thus conversion and energy efficiency. This is due to the higher probability of interaction with a CO_2 molecule [43]. Additionally, power dissipation as heat is more significant with thicker dielectric [37].

The gap size has a great influence both on the reactor volume and on the electric field straight. If a greater gap increases the residence time which can have positive effect on the CO_2 conversion, at the same time it decreased the reduced electric field inside

the discharge gap at same applied potential. Consequently lower electron temperature results from a less strongly reduced electric field, ensuing in lower probability for electron impact excitation and ionization processes, which are the most important reactions for CO_2 dissociation in a DBD reactor [2,19]. These leads to a minor density of electrons and ions, resulting in an overall less reactive plasma and thus higher conversion. In addition, for a larger gap less microdischarges per period are formed because the streamers cannot fully bridge the discharge volume and a microdischarge is not established [1,5,60]. All these effect leads to reduction of overall conversion and efficiency [20,21,39,60]. For example, Uytdenhouwen et al. [21] observed a extreme drops in CO_2 conversion, from 53.6% for a gap size of 455 μm to only 23% at 4705 μm. In addition, using different flow rates for diverse gaps, they noticed that the overall efficiency of each reactor is similar for low SEI value, while it becomes crucial at grater SEI.

4.4.4 Effect of temperature and pressure

One of the most critical factors controlling reaction rates in thermochemical reactions is gas temperature. In a DBD reactor, heat comes from dielectric heating and gas warming: Dielectric heating is caused by dielectric hysteresis phenomena, which results in the consumption of significant energy, while gas eating is due to energy transferred from electrons to neutral particles in the form of rotational and vibrational excitation. However, the effect of temperature on plasma-based conversion in a DBD is less obvious. For instance, Paulussen et al. [67] observed a small and linear rise in conversion from 26% to 28.5% when the inlet gas was heated from 303 K to 443 K. Conversely Khunda et al. [68] measured a decrease in conversion from 273 to 293 K. Since CO_2 splitting is an endothermic reaction, increasing the temperature could have a positive effect. Besides, more energy is transferred to the vibrational levels of CO_2, facilitating the vibrational ladder climbing process rather than electronic excitation. However, an increase in temperature can also lead to a higher power dissipation, reducing the overall energy efficiency of the reactor [45]. In addition, as the reactor temperature rises, the

dielectric medium heats up, which has a negative effect on the dielectric coefficient. As a result, the discharge characteristics may be adversely affected, resulting in reduced electric field strength [46]. Moreover, as the gas heats up, it expands, reducing the residence time in the reactor. To avoid excessive heating of the gas, the reactor wall material should have a high thermal conductivity and low dielectric permittivity while the dielectric thickness should be modulated to reduce gas overheating [37]. This may partly explain why alumina performs well as a dielectric barrier material [43]. Alternatively pulsing the power or cooling down DBD may be useful to reduce the gas heating [43,69].

Most experiments on CO_2 splitting by DBD have been conducted at ambient pressure. However, the industry often requires high working pressures. An increase in pressure has a negative impact on the thermodynamic equilibrium of the reaction. This is due to Le Chatelier's principle, which states that the reaction shifts toward the reactants, subsequently reducing the conversion. Additionally, Paschen's law dictates that an increase in pressure has an adverse effect on the breakdown potential and the consequent maintenance of the discharge [1,70]. In fact, Uytdenhouwen et al.[21] observed a decline in conversion when increasing the pressure from 1 to 3 bar. However, they expected a greater decrease, suggesting that an increase in pressure can enhance the reaction rate. This was further supported by Hosseini Rad et al. [71], who found that using a CeO_2-coated packed bed at 2 bar resulted in a fourfold increase in energy yield for CO production compared to an empty reactor at 1 bar. Moreover, Belov et al.[72] reported an increase in CO_2 conversion until 1.5 bar, explain that an increased pressure leads to greater discharge currents but simultaneously decreasing the number of filaments. In conclusion, the influence of temperature and pressure on CO_2 splitting by DBD plasma is not fully understood and further studies are needed. However, it seems that an increase in temperature, which is also synonymous with more power dissipated by the reactor, is unfavorable, while an increase in pressure seems to have a dual and opposite effect on performance.

4.4.5 Effect of packing

As mentioned earlier (plasma catalysts, section 4.4), incorporating a packing material within the discharge gap could enhance the efficiency of the DBD reactor. However, it has no impact on the selectivity during CO_2 splitting. The addition of the packing material has been attributed to the interaction between the individual beads inside the plasma reactor and between the beads and dielectric barrier through modeling [15,73]. A packed bed effect could cause the discharge behavior to change from filamentary to a mixture of surface and filamentary discharge. Filamentary discharges are limited to the narrow gap between the pellet-pellet and pellet-dielectric wall, while surface discharges can occur on the surface of the pellets at their contact points. Based on the characteristics of the packing materials, including contact angle, shape, and dielectric constant, the local electric field in the gas region around these contact points could be up to 10-10^4 times larger. This increases the electron temperature and decreases the breakdown voltage [73–75].

Several types of packing materials where used including SiO_2[39,76], Al_2O_3[39,76,77], ZrO_2[39,73,76,78], $BaTiO_3$[74,76,79], CaO[75] and TiO_2[79,80] which influence the dielectric constant and electric strength, ultimately reducing the breakdown voltage [74–76]. A larger dielectric constant result in stronger polarization of the dielectric material, leading to a larger difference between closely spaced opposing charges in the vicinity of the contact points of the dielectric objects. It is important to note that the use of specific packing materials can have a significant impact on the performance of the dielectric materials. Anyway, once the dielectric constant reaches a certain level, the enhancement plateaus [10,81]. Furthermore as the electric field strength increases, the electrons can move faster with the enhanced electric field and this could increase the electron loss rate at the walls, resulting in a lower overall electron density [81]. On the other hand, the size of the packing material significantly affects the reactor's performance. Introducing a packed bead inside the gap decreases the discharge volume, thereby reducing the residence time of the gas inside the reactor. This effect is particularly relevant when using smaller

particles. For instance, Michielsen et al. [76] found that CO_2 conversion and energy efficiency were lower when using Al_2O_3, ZrO_2 and SiO_2 dielectric packing for particles smaller than 1.6-1.8 mm at the same flow rate compared to an empty reactor. However, when $BaTiO_3$ was used, improved results were observed for all investigated particle sizes due to its higher dielectric constant. In larger packing dimensions, more voids are present among dielectric particles, resulting in a lower probability of electron losses on particle surfaces, leading to increased electron density and performance[81].

Another significant factor could be the gas composition. Butterworth and colleagues [82] observed that increasing CO_2 concentration in a CO_2-Ar mix using small Al_2O_3 particles (180-300 μm) resulted in a drop of conversion, and no conversion occurred with particle sizes under 850 μm for 100% CO_2.

In conclusion the effect of a packing material is controversial. The parameters influencing the rector performances are:

1) The particles materials: Higher dielectric constants lead to increased material polarization, which in turn results in a higher local electric field. The ultimate effect of this phenomenon is increased conversion due to a lower breakdown voltage and higher electron temperature.
2) The particle size: A smaller packing dimension increases the contact points between particles, resulting in an increase in the local electric field and a decrease in the breakdown voltage. However, it also leads to a reduction in electron density due to the higher probability of electron losses through collisions with the surface of the particles. Smaller grains reduce the voids, causing the discharge behavior to shift from filamentary to a mixture of surface and filamentary discharge. Additionally, plasma-catalyst interactions are heightened. However, these benefits may be outweighed by the shorter residence time of the gas in the reactor.
3) The gas composition could influence the packing effect, but further investigation should be done.

Bibliography

1. Fridman, A. *Plasma Chemistry*; 2008; ISBN 9780521847353.

2. Snoeckx, R.; Bogaerts, A. Plasma Technology – a Novel Solution for CO2. *Chem. Soc. Rev.* **2017**, *46*, doi:10.1039/c6cs00066e.

3. Dimits, A.M.; Bateman, G.; Beer, M.A.; Cohen, B.I.; Dorland, W.; Hammett, G.W.; Kim, C.; Kinsey, J.E.; Kotschenreuther, M.; Kritz, A.H.; et al. Comparisons and Physics Basis of Tokamak Transport Models and Turbulence Simulations. *Phys. Plasmas* **2000**, *7*, 969–983, doi:10.1063/1.873896.

4. Craxton, R.S.; Anderson, K.S.; Boehly, T.R.; Goncharov, V.N.; Harding, D.R.; Knauer, J.P.; McCrory, R.L.; McKenty, P.W.; Meyerhofer, D.D.; Myatt, J.F.; et al. Direct-Drive Inertial Confinement Fusion: A Review. *Phys. Plasmas* **2015**, *22*, doi:10.1063/1.4934714.

5. Tendero, C.; Tixier, C.; Tristant, P.; Desmaison, J.; Leprince, P. Atmospheric Pressure Plasmas: A Review. *Spectrochim. Acta - Part B At. Spectrosc.* **2006**, *61*, 2–30, doi:10.1016/j.sab.2005.10.003.

6. MICHAEL A. LIEBERMAN ALLAN J. LICHTENBERG; A *PRINCIPLES OF PLASMA DISCHARGES AND MATERIALS PROCESSING*; 1994; Vol. 4; ISBN 9786468600.

7. Gomez, E.; Rani, D.A.; Cheeseman, C.R.; Deegan, D.; Wise, M.; Boccaccini, A.R. Thermal Plasma Technology for the Treatment of Wastes: A Critical Review. *J. Hazard. Mater.* **2009**, *161*, 614–626, doi:10.1016/j.jhazmat.2008.04.017.

8. Klämpfl, T.G.; Morfill, G.E. Cold Atmospheric Plasma Decontamination against Nosocomial Bacteria. **2014**.

9. Henningsen, A.; Smeets, R.; Heuberger, R.; Jung, O.T.; Hanken, H.; Heiland, M.; Cacaci, C.; Precht, C. Changes in Surface Characteristics of Titanium and Zirconia after Surface Treatment with Ultraviolet Light or Non-Thermal Plasma. *Eur. J. Oral Sci.* **2018**, *126*, 126–134, doi:10.1111/eos.12400.

10. Chen, H.L.; Lee, H.M.; Chen, S.H.; Chang, M.B. Review of Packed-Bed Plasma Reactor for Ozone Generation and Air Pollution Control. *Ind. Eng. Chem. Res.* **2008**, *47*, 2122–2130, doi:10.1021/ie071411s.

11. Van Durme, J.; Dewulf, J.; Leys, C.; Van Langenhove, H. Combining Non-Thermal Plasma with Heterogeneous Catalysis in Waste Gas Treatment: A Review. *Appl. Catal. B Environ.* **2008**, *78*, 324–333, doi:10.1016/j.apcatb.2007.09.035.

12. Guoxing Chen, Ling Wang, T.G. and R.S. *Progress in Plasma-Assisted Catalysis for Carbon Dioxide Reduction*; 2016; Vol. 11; ISBN 0000957720.

13. Shah, Y.T.; Verma, J.; Katti, S.S. Plasma Activated Catalysis for Carbon Dioxide Dissociation: A Review. *J. Indian Chem. Soc.* **2021**, *98*, 100152, doi:10.1016/j.jics.2021.100152.

14. Chen, G.; Snyders, R.; Britun, N. CO2conversion Using Catalyst-Free and Catalyst-Assisted Plasma-Processes: Recent Progress and Understanding. *J. CO2 Util.* **2021**, *49*, 101557, doi:10.1016/j.jcou.2021.101557.

15. Annemie, B.; Tomáš, K.; Koen, V.L.; Ramses, S.; Bogaerts, A.; Kozak, T.; Laer, K. Van Plasma-Based Conversion of CO2 : Current Status and Future Challenges. *Faraday Discuss.* **2015**, *183*, 217–232, doi:10.1039/c5d00053.

16. Aerts, R.; Martens, T.; Bogaerts, A. Influence of Vibrational States on CO2 Splitting by Dielectric Barrier Discharges. *J. Phys. Chem. C* **2012**, *116*, 23257–23273, doi:10.1021/jp307525t.

17. Siemens, W. Ueber Die Elektrostatische Induction Und Die Verzögerung Des Stroms in Flaschendrähten. *Ann. der Phys. und Chemie* **1857**, *178*, 66–122.

18. Bogaerts, A.; Neyts, E.; Gijbels, R.; Van der Mullen, J. Gas Discharge Plasmas and Their Applications. *Spectrochim. Acta - Part B At. Spectrosc.* **2002**, *57*, 609–658, doi:10.1016/S0584-8547(01)00406-2.

19. Fridman, A.; Chirokov, A.; Gutsol, A. Non-Thermal Atmospheric Pressure Discharges. *J. Phys. D Appl. Phys. Top.* **2005**, *38*, doi:10.1088/0022-3727/38/2/R01.

20. Aerts, R.; Somers, W.; Bogaerts, A. Carbon Dioxide Splitting in a Dielectric Barrier Discharge Plasma: A Combined Experimental and Computational Study. *ChemSusChem* **2015**, *8*, 702–716, doi:10.1002/cssc.201402818.

21. Uytdenhouwen, Y.; Bal, K.M.; Michielsen, I.; Neyts, E.C.; Meynen, V.; Cool, P.; Bogaerts, A. How Process Parameters and Packing Materials Tune Chemical Equilibrium and Kinetics in Plasma-Based CO2 Conversion. *Chem. Eng. J.* **2019**, *372*, 1253–1264, doi:10.1016/j.cej.2019.05.008.

22. Chirokov, A.; Gutsol, A.; Fridman, A. Atmospheric Pressure Plasma of Dielectric Barrier Discharges. *Pure Appl. Chem.* **2005**, *77*, 487–495, doi:10.1351/pac200577020487.

23. Bogaerts, A.; Centi, G. Plasma Technology for CO2 Conversion: A Personal Perspective on Prospects and Gaps. *Front. Energy Res.* **2020**, *8*, 1–23,

doi:10.3389/fenrg.2020.00111.

24. Wolf, A.J.; Righart, T.W.H.; Peeters, F.J.J.; Bongers, W.A.; Van De Sanden, M.C.M. Implications of Thermo-Chemical Instability on the Contracted Modes in CO2 Microwave Plasmas. *Plasma Sources Sci. Technol.* **2020**, *29*, doi:10.1088/1361-6595/ab5eca.

25. Kotov, V.; Koelman, P.M.J. Plug Flow Reactor Model of the Plasma Chemical Conversion of CO2. *Plasma Sources Sci. Technol.* **2019**, *28*, doi:10.1088/1361-6595/ab3774.

26. Kabouzi, Y.; Calzada, M.D.; Moisan, M.; Tran, K.C.; Trassy, C. Radial Contraction of Microwave-Sustained Plasma Columns at Atmospheric Pressure. *J. Appl. Phys.* **2002**, *91*, 1008–1019, doi:10.1063/1.1425078.

27. Kosanke, R.M. *Libro CO2 Plasma*; 2019; ISBN 9781119130536.

28. Devins, J.C.; Burton, M. Formation of Hydrazine in Electric Discharge Decomposition of Ammonia. *J. Am. Chem. Soc.* **1954**, *76*, 2618–2626, doi:10.1021/ja01639a006.

29. Mizuno, A.; Chakrabarti, A.; Okazaki, K. Application of Corona Technology in the Reduction of Greenhouse Gases and Other Gaseous Pollutants. *Non-Thermal Plasma Tech. Pollut. Control* **1993**, 165–185, doi:10.1007/978-3-642-78476-7_14.

30. Whitehead, J.C. Plasma-Catalysis: The Known Knowns, the Known Unknowns and the Unknown Unknowns. *J. Phys. D. Appl. Phys.* **2016**, *49*, doi:10.1088/0022-3727/49/24/243001.

31. Vandenbroucke, A.M.; Mora, M.; Jiménez-Sanchidrián, C.; Romero-Salguero, F.J.; De Geyter, N.; Leys, C.; Morent, R. TCE Abatement with a Plasma-Catalytic Combined System Using MnO2 as Catalyst. *Appl. Catal. B Environ.* **2014**, *156–157*, 94–100, doi:10.1016/j.apcatb.2014.03.007.

32. Yu-ru, Z.; Erik, N. Enhancement of Plasma Generation in Catalyst Pores with Different Shapes. *Plasma Sources Sci. Technol.* **2018**, *5*.

33. Zhang, Y.R.; Van Laer, K.; Neyts, E.C.; Bogaerts, A. Can Plasma Be Formed in Catalyst Pores? A Modeling Investigation. *Appl. Catal. B Environ.* **2016**, *185*, 56–67, doi:10.1016/j.apcatb.2015.12.009.

34. Rajasekaran, P.; Mertmann, P.; Bibinov, N.; Wandke, D.; Viöl, W.; Awakowicz, P. Filamentary and Homogeneous Modes of Dielectric Barrier Discharge (DBD) in Air: Investigation through Plasma Characterization and

Simulation of Surface Irradiation. *Plasma Process. Polym.* **2010**, *7*, 665–675, doi:10.1002/ppap.200900175.

35. Kim, H.H.; Ogata, A.; Futamura, S. Oxygen Partial Pressure-Dependent Behavior of Various Catalysts for the Total Oxidation of VOCs Using Cycled System of Adsorption and Oxygen Plasma. *Appl. Catal. B Environ.* **2008**, *79*, 356–367, doi:10.1016/j.apcatb.2007.10.038.

36. Ramakers, M.; Michielsen, I.; Aerts, R.; Meynen, V.; Bogaerts, A. Effect of Argon or Helium on the CO2 Conversion in a Dielectric Barrier Discharge. *Plasma Process. Polym.* **2015**, *12*, 755–763, doi:10.1002/ppap.201400213.

37. Rodrigues, F.; Pascoa, J.; Trancossi, M. Heat Generation Mechanisms of DBD Plasma Actuators. *Exp. Therm. Fluid Sci.* **2018**, *90*, 55–65, doi:10.1016/j.expthermflusci.2017.09.005.

38. Manley, T.C. The Electric Characteristics of the Ozonator Discharge. *Trans. Electrochem. Soc.* **1943**, *84*, 83, doi:10.1149/1.3071556.

39. Uytdenhouwen, Y.; Van Alphen, S.; Michielsen, I.; Meynen, V.; Cool, P.; Bogaerts, A. A Packed-Bed DBD Micro Plasma Reactor for CO2 Dissociation: Does Size Matter? *Chem. Eng. J.* **2018**, *348*, 557–568, doi:10.1016/j.cej.2018.04.210.

40. Spencer, L.F.; Gallimore, A.D. Efficiency of CO 2 Dissociation in a Radio-Frequency Discharge. *Plasma Chem. Plasma Process.* **2011**, *31*, 79–89, doi:10.1007/s11090-010-9273-0.

41. Mouele, E.S.M.; Tijani, J.O.; Badmus, K.O.; Pereao, O.; Babajide, O.; Fatoba, O.O.; Zhang, C.; Shao, T.; Sosnin, E.; Tarasenko, V.; et al. A Critical Review on Ozone and Co-Species, Generation and Reaction Mechanisms in Plasma Induced by Dielectric Barrier Discharge Technologies for Wastewater Remediation. *J. Environ. Chem. Eng.* **2021**, *9*, 105758, doi:10.1016/j.jece.2021.105758.

42. Li, S.; Dang, X.; Yu, X.; Abbas, G.; Zhang, Q.; Cao, L. The Application of Dielectric Barrier Discharge Non-Thermal Plasma in VOCs Abatement: A Review. *Chem. Eng. J.* **2020**, *388*, 124275, doi:10.1016/j.cej.2020.124275.

43. Ozkan, A.; Bogaerts, A.; Reniers, F. Routes to Increase the Conversion and the Energy Efficiency in the Splitting of CO2 by a Dielectric Barrier Discharge. *J. Phys. D. Appl. Phys.* **2017**, *50*, doi:10.1088/1361-6463/aa562c.

44. Ozkan, A.; Dufour, T.; Silva, T.; Britun, N.; Snyders, R.; Bogaerts, A.; Reniers, F. The Influence of Power and Frequency on the Filamentary Behavior of a Flowing DBD - Application to the Splitting of CO2. *Plasma Sources Sci. Technol.*

2016, *25*, doi:10.1088/0963-0252/25/2/025013.

45. Yu, Q.; Kong, M.; Liu, T.; Fei, J.; Zheng, X. Characteristics of the Decomposition of CO 2 in a Dielectric Packed-Bed Plasma Reactor. *Plasma Chem. Plasma Process.* **2012**, *32*, 153–163, doi:10.1007/s11090-011-9335-y.

46. Jahanbakhsh, M.R.; Taghvaei, H.; Khalifeh, O.; Ghanbari, M.; Rahimpour, M.R. Low-Temperature CO2Splitting in a Noncatalytic Dielectric-Barrier Discharge Plasma: Effect of Operational Parameters with a New Strategy of Experimentation. *Energy and Fuels* **2020**, *34*, 14321–14332, doi:10.1021/acs.energyfuels.0c02116.

47. Khalifeh, O.; Mosallanejad, A.; Taghvaei, H.; Rahimpour, M.R.; Shariati, A. Decomposition of Methane to Hydrogen Using Nanosecond Pulsed Plasma Reactor with Different Active Volumes, Voltages and Frequencies. *Appl. Energy* **2016**, *169*, 585–596, doi:10.1016/j.apenergy.2016.02.017.

48. Taghvaei, H.; Kheirollahivash, M.; Ghasemi, M.; Rostami, P.; Gates, B.C.; Rahimpour, M.R. Upgrading of Anisole in a Dielectric Barrier Discharge Plasma Reactor. *Energy and Fuels* **2014**, *28*, 4545–4553, doi:10.1021/ef500529r.

49. Niu, G.; Qin, Y.; Li, W.; Duan, Y. Investigation of CO2 Splitting Process Under Atmospheric Pressure Using Multi-Electrode Cylindrical DBD Plasma Reactor. *Plasma Chem. Plasma Process.* **2019**, *39*, 809–824, doi:10.1007/s11090-019-09955-y.

50. Valdivia-Barrientos, R.; Pacheco-Sotelo, J.; Pacheco-Pacheco, M.; Benítez-Read, J.S.; López-Callejas, R. Analysis and Electrical Modelling of a Cylindrical DBD Configuration at Different Operating Frequencies. *Plasma Sources Sci. Technol.* **2006**, *15*, 237–245, doi:10.1088/0963-0252/15/2/008.

51. Godyak, V.A. Nonequilibrium EEDF in Gas Discharge Plasmas. *IEEE Trans. Plasma Sci.* **2006**, *34*, 755–766, doi:10.1109/TPS.2006.875847.

52. Dey, G.R.; Kamble, S. Effects of Electrode Material and Frequency on Carbon Monoxide Formation in Carbon Dioxide Dielectric Barrier Discharge. *J. CO2 Util.* **2020**, *40*, 101207, doi:10.1016/j.jcou.2020.101207.

53. Liu, C.Y.; Wang, H.X.; Wang, C.; Meng, X.; Huang, H.J.; Cao, J.W.; Sun, S.R.; Yan, C. Experimental Study of the Effect of Dielectric Materials on the Decomposition of Carbon Dioxide in a Dielectric Barrier Discharge. *Plasma Sources Sci. Technol.* **2023**, *32*, doi:10.1088/1361-6595/acb816.

54. Yannick, U.; Jonas, H.; Tom, B.; Pegie, C. How Gas Flow Design Can Influence the Performance of a DBD Plasma Reactor for Dry Reforming of Methane.

2021, *405*.

55. Pinhão, N.R.; Janeco, A.; Branco, J.B. Influence of Helium on the Conversion of Methane and Carbon Dioxide in a Dielectric Barrier Discharge. *Plasma Chem. Plasma Process.* **2011**, *31*, 427–439, doi:10.1007/s11090-011-9294-3.

56. Xu, S.; Whitehead, J.C.; Martin, P.A. CO2 Conversion in a Non-Thermal, Barium Titanate Packed Bed Plasma Reactor: The Effect of Dilution by Ar and N2. *Chem. Eng. J.* **2017**, *327*, 764–773, doi:10.1016/j.cej.2017.06.090.

57. Snoeckx, R.; Heijkers, S.; Van Wesenbeeck, K.; Lenaerts, S.; Bogaerts, A. CO2 Conversion in a Dielectric Barrier Discharge Plasma: N2 in the Mix as a Helping Hand or Problematic Impurity? *Energy Environ. Sci.* **2016**, *9*, 999–1011, doi:10.1039/c5ee03304g.

58. Wu, P.; Li, X.; Ullah, N.; Li, Z. Synergistic Effect of Catalyst and Plasma on CO2 Decomposition in a Dielectric Barrier Discharge Plasma Reactor. *Mol. Catal.* **2021**, *499*, 111304, doi:10.1016/j.mcat.2020.111304.

59. Wang, J.Y.; Xia, G.G.; Huang, A.; Suib, S.L.; Hayashi, Y.; Matsumoto, H. CO2 Decomposition Using Glow Discharge Plasmas. *J. Catal.* **1999**, *185*, 152–159, doi:10.1006/jcat.1999.2499.

60. Mei, D.; Tu, X. Conversion of CO2 in a Cylindrical Dielectric Barrier Discharge Reactor: Effects of Plasma Processing Parameters and Reactor Design. *J. CO2 Util.* **2017**, *19*, 68–78, doi:10.1016/j.jcou.2017.02.015.

61. Wang, B.; Yan, W.; Ge, W.; Duan, X. Methane Conversion into Higher Hydrocarbons with Dielectric Barrier Discharge Micro-Plasma Reactor. *J. Energy Chem.* **2013**, *22*, 876–882, doi:10.1016/S2095-4956(14)60267-9.

62. Meiners, A.; Leck, M.; Abel, B. Efficiency Enhancement of a Dielectric Barrier Plasma Discharge by Dielectric Barrier Optimization. *Rev. Sci. Instrum.* **2010**, *81*, 1–9, doi:10.1063/1.3501963.

63. Belov, I.; Paulussen, S.; Bogaerts, A. Appearance of a Conductive Carbonaceous Coating in a CO2 Dielectric Barrier Discharge and Its Influence on the Electrical Properties and the Conversion Efficiency. *Plasma Sources Sci. Technol.* **2016**, *25*, doi:10.1088/0963-0252/25/1/015023.

64. Li, R.; Tang, Q.; Yin, S.; Sato, T. Plasma Catalysis for CO2 Decomposition by Using Different Dielectric Materials. *Fuel Process. Technol.* **2006**, *87*, 617–622, doi:10.1016/j.fuproc.2006.01.007.

65. Wang, S.; Zhang, Y.; Liu, X.; Wang, X. Enhancement of CO2 Conversion Rate and Conversion Efficiency by Homogeneous Discharges. *Plasma Chem. Plasma Process.* **2012**, *32*, 979–989, doi:10.1007/s11090-012-9386-8.

66. Ohtsu, Y.; Shimazoe, T.; Misawa, T.; Fujita, H. Influences of Oxide Material on High Density Plasma Production Using Capacitively Coupled Discharge. *Thin Solid Films* **2006**, *506–507*, 545–549, doi:10.1016/j.tsf.2005.08.071.

67. Paulussen, S.; Verheyde, B.; Tu, X.; De Bie, C.; Martens, T.; Petrovic, D.; Bogaerts, A.; Sels, B. Conversion of Carbon Dioxide to Value-Added Chemicals in Atmospheric Pressure Dielectric Barrier Discharges. *Plasma Sources Sci. Technol.* **2010**, *19*, doi:10.1088/0963-0252/19/3/034015.

68. Khunda, D.; Li, S.; Cherkasov, N.; Rishard, M.Z.M.; Chaffee, A.L.; Rebrov, E. V. Effect of Temperature on the CO2 Splitting Rate in a DBD Microreactor. *React. Chem. Eng.* **2023**, *8*, 2223–2233, doi:10.1039/d3re00113j.

69. Yuan, D.; Zhang, G.; Ling, Z.; Wu, A.; He, Y.; Wang, Z. Characteristics of Temperature Distribution in Atmospheric Pulsed Surface Dielectric Barrier Discharge for Ozone Production. *Vacuum* **2020**, *176*, 109351, doi:10.1016/j.vacuum.2020.109351.

70. Tomai, T.; Ito, T.; Terashima, K. Generation of Dielectric Barrier Discharge in High-Pressure N2 and CO2 Environments up to Supercritical Conditions. *Thin Solid Films* **2006**, *506–507*, 409–413, doi:10.1016/j.tsf.2005.08.101.

71. Hosseini Rad, R.; Brüser, V.; Schiorlin, M.; Schäfer, J.; Brandenburg, R. Enhancement of CO2 Splitting in a Coaxial Dielectric Barrier Discharge by Pressure Increase, Packed Bed and Catalyst Addition. *Chem. Eng. J.* **2023**, *456*, doi:10.1016/j.cej.2022.141072.

72. Belov, I.; Paulussen, S.; Bogaerts, A. Pressure as an Additional Control Handle for Non-Thermal Atmospheric Plasma Processes. *Plasma Process. Polym.* **2017**, *14*, 1–9, doi:10.1002/ppap.201700046.

73. Van Laer, K.; Bogaerts, A. Improving the Conversion and Energy Efficiency of Carbon Dioxide Splitting in a Zirconia-Packed Dielectric Barrier Discharge Reactor. *Energy Technol.* **2015**, *3*, 1038–1044, doi:10.1002/ente.201500127.

74. Mei, D.; Zhu, X.; He, Y.L.; Yan, J.D.; Tu, X. Plasma-Assisted Conversion of CO2 in a Dielectric Barrier Discharge Reactor: Understanding the Effect of Packing Materials. *Plasma Sources Sci. Technol.* **2015**, *24*, 15011, doi:10.1088/0963-0252/24/1/015011.

75. Qiao, Z.; Wang, Z.; Zhang, C.; Yuan, S.; Zhu, Y.; Wang, J. Effect of Dielectric Packing Materials on the Decomposition of Carbon Dioxide Using DBD Microplasma Reactor. *AIChE J.* **2012**, *59*, 215–228, doi:10.1002/aic.

76. Michielsen, I.; Uytdenhouwen, Y.; Pype, J.; Michielsen, B.; Mertens, J.; Reniers, F.; Meynen, V.; Bogaerts, A. CO2 Dissociation in a Packed Bed DBD Reactor: First Steps towards a Better Understanding of Plasma Catalysis. *Chem. Eng. J.* **2017**, *326*, 477–488, doi:10.1016/j.cej.2017.05.177.

77. Li, J.; Zhai, X.; Ma, C.; Zhu, S.; Yu, F.; Dai, B.; Ge, G.; Yang, D. DBD Plasma Combined with Different Foam Metal Electrodes for CO2 Decomposition: Experimental Results and DFT Validations. *Nanomaterials* **2019**, *9*, doi:10.3390/nano9111595.

78. Zhou, A.; Chen, D.; Ma, C.; Yu, F.; Dai, B. DBD Plasma-ZrO2 Catalytic Decomposition of CO2 at Low Temperatures. *Catalysts* **2018**, *8*, 1–11, doi:10.3390/catal8070256.

79. Mei, D.; Zhu, X.; Wu, C.; Ashford, B.; Williams, P.T.; Tu, X. Plasma-Photocatalytic Conversion of CO2 at Low Temperatures: Understanding the Synergistic Effect of Plasma-Catalysis. *Appl. Catal. B Environ.* **2016**, *182*, 525–532, doi:10.1016/j.apcatb.2015.09.052.

80. Kaliyappan, P.; Paulus, A.; D'Haen, J.; Samyn, P.; Uytdenhouwen, Y.; Hafezkhiabani, N.; Bogaerts, A.; Meynen, V.; Elen, K.; Hardy, A.; et al. Probing the Impact of Material Properties of Core-Shell SiO2@TiO2spheres on the Plasma-Catalytic CO2 Dissociation Using a Packed Bed DBD Plasma Reactor. *J. CO2 Util.* **2021**, *46*, doi:10.1016/j.jcou.2021.101468.

81. Van Laer, K.; Bogaerts, A. How Bead Size and Dielectric Constant Affect the Plasma Behaviour in a Packed Bed Plasma Reactor: A Modelling Study. *Plasma Sources Sci. Technol.* **2017**, *26*, doi:10.1088/1361-6595/aa7c59.

82. Butterworth, T.; Allen, R.W.K. Plasma-Catalyst Interaction Studied in a Single Pellet DBD Reactor: Dielectric Constant Effect on Plasma Dynamics. *Plasma Sources Sci. Technol.* **2017**, *26*, 65008, doi:10.1088/1361-6595/aa6c35.

5

CO_2 splitting using porous electrodes and boehmite layer

5.1 Introduction and aim of the chapter

This section discusses the influence of a tubular and coaxial DBD reactor with a porous tube as the internal electrode on CO_2 splitting into CO and O_2. The previous chapter provided an overview of the current state of the art and a comprehensive description of the various parameters that affect the plasma-based reaction. Several reviews on the subject are also referenced.

The main focus of this chapter is on the reactor design and the impact of the inner electrode porosity on CO_2 splitting. The study compares the results of two different porosities (0.2 μm and 0.5 μm) with a smooth inner electrode. Furthermore, the research examines whether altering the gas path within the reactor can enhance conversion. The gas can flow in either a shell in – shell out configuration, solely through the gap between the inner electrode and dielectric, or in a shell – in tube out configuration, passing through the porous inner electrode (figure 5.1).

This study aims to compare the performance of a thin film of boehmite (γ-Al_2O_3) deposited on the internal electrode with that of a reactor packed with γ-Al_2O_3 spheres. The objective of this study is to determine whether the thin film reactor can achieve comparable or superior performance to the packed reactor, potentially opening up new possibilities in the field of plasma-catalysis. Alumina is commonly used as a catalyst or support for other metals that catalyze plasma reactions. However, the performance of the latter often decreases due to a reduction in residence time. A thin alumina film could provide catalytic support without the side effects of packing.

5.2 Experimental

5.2.1 Reactor design

The set-up used in this work is schematically illustrated in scheme 5.1, while a more detailed image of DBD reactor is presented in figure 5.1.

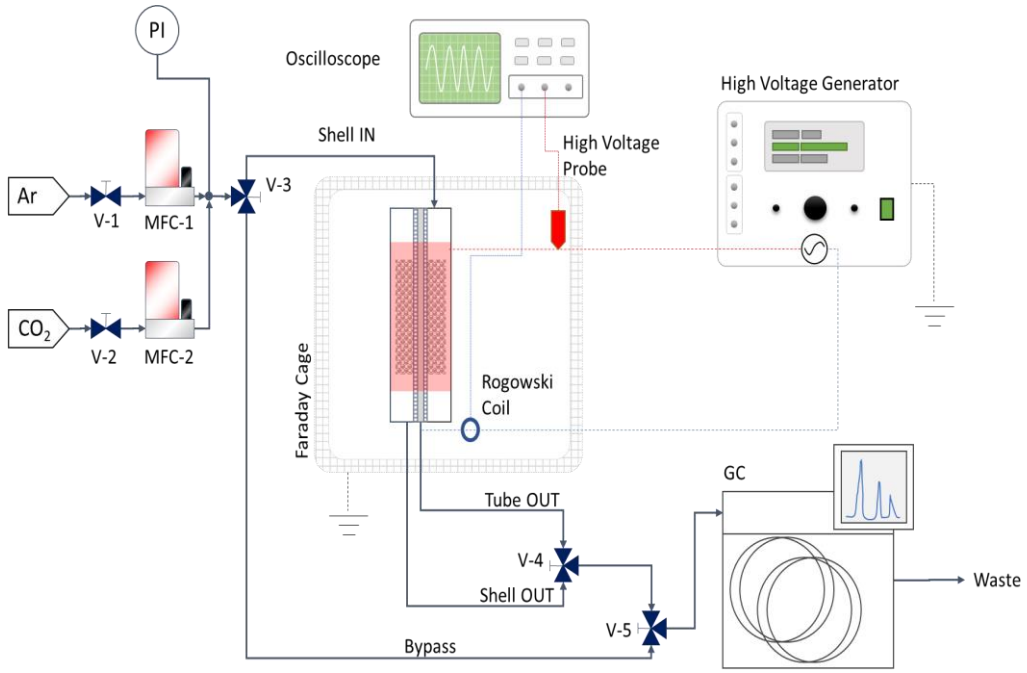

Scheme 5.1 *Schematical refiguration of the experimental set up*

The device consists of a tubular DBD reactor composed of a cylindrical alumina dielectric tube (thickness 4 mm) with an external aluminum foil electrode. The internal electrode is a stainless-steel cylindrical membrane (Mott Corporation; length 10 cm, diameter 3.8 cm) with two different porosities (0.2 μm, 0.5 μm). The distance between the internal electrode and the dielectric was 2.7 mm. The deposited boehmite layer did not significantly affect the gap dimension, as it was less than 1 μm thick. The experiments were conducted with the reactor in an empty state, as well as with 1 mm diameter γ-alumina spheres (Sigma-Aldrich) as packing materials.

5.2.2 Gas circuit

The reactor was injected with pure CO_2 or diluted gas (20% Ar/80% CO_2) at three different flow rates (20, 30, and 50 ml min^{-1}). The gas flow residence time inside the

reactor was estimated for both the empty and packed configurations, as shown in table 5.1

Table 5.1 Residence time for different gas flow and packaging

Flow rate ($ml*min^{-1}$)	Residence Time-Empty (s)	Residence Time-Packed (s)
20	25.4	16.8
30	17	11.2
50	10.2	6.7

Although small flow rates may not be practical in an industrial setting [1], this study examines the individual impacts of the porosity of the internal electrode and the boehmite layer. Furthermore, as reported in the previous chapter, several studies have demonstrated the impact of increasing the flow rate in a reactor. However using larger reaction volumes or setting up multiple reactors in parallel may be a complementary solution [2].

In addition, the gas flow was flushed inside the reactor into two ways as shown figure 5.1:

- shell in-shell out: The gas enters and exits the gap between the internal tube and the dielectric.
- shell in-tube out: The gas enters the electrode through a gap and exits from its internal part after passing through the porous electrode. However, gas diffusion is not possible inside the smooth tube, making this configuration untestable.

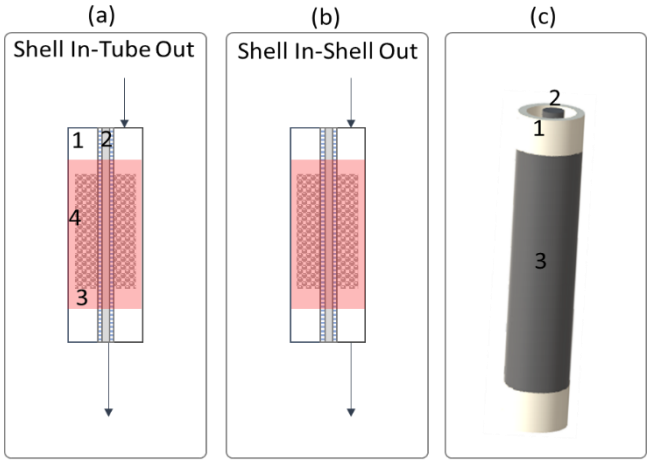

Figure 5.1 *Illustration of reactor flow configurations shell in-tube out (a), shell in-shell out (b) and pictural representation (c)*

Considering the different configurations, gas flow rates and gas feed a total of 84 experiments are performed and summarized in table 5.2. The results are reported in table B1 in appendix B.

Table 5.2 schematical representation of performed tests.

Porosity	Gas composition	Gas flow configuration	Flow rate ($ml*min^{-1}$)
0 [(a)]	CO_2	Shell in - shell out	20
			30
			50
	20% Ar – 80% CO_2	Shell in - shell out	20
			30
			50
0.2[(b)]	CO_2	Shell in - shell out	20
			30
			50
		Shell in - tube out	20
			30
			50
	20% Ar – 80% CO_2	Shell in - shell out	20
			30

			50
		Shell in - tube out	20
			30
			50
0.5[b]	CO_2	Shell in - shell out	20
			30
			50
		Shell in - tube out	20
			30
			50
	20% Ar – 80% CO_2	Shell in - shell out	20
			30
			50
		Shell in - tube out	20
			30
			50

(a) The smooth electrode was tested empty or packed with γ-Al_2O_3 spheres

(b) 0.2 and 0.5 were tested empty, packed and with boehmite layer

5.2.3 Performance evaluations

The gas stream exiting the reactor was analyzed using a gas chromatograph (GC Thermoscientific, trace 1310) equipped with two thermal conductivity detector (TCD) channels and a flame ionization detector (FID). Only the TCD channels were used since the only other products of this reaction, besides unreacted CO_2, were CO and O_2.

The performances of different tested configurations were evaluated considering conversion (X), specific energy input (SEI) and energy efficiency (η). The converted CO_2 moles are also reported.

The formula used to estimate CO_2 conversion is as follows:

$$X\ (\%) = \left(\frac{\dot{n}\ \text{in} - \dot{n}\ \text{out}}{\dot{n}\ \text{out}}\right) * 100 \qquad (1)$$

Where ṅ indicates the CO_2 molar flow rates (mol*min^{-1}) entering and exiting the system.

The specific energy input is calculated in kJ*L^{-1} as follows:

$$\text{SEI (kJ L}^{-1}) = \frac{\text{Power (kW)}}{\text{Flow rate (L /sec)}} \quad (2)$$

The energy efficiency is contingent upon the specific process being analyzed. The energy efficiency measures how effectively the process operates in comparison to the standard reaction enthalpy, taking into account the specific energy input:

$$\eta(\%) = \frac{\Delta H°(\text{KJ mol}^{-1}) * X(\%)}{\text{SEI(KJ mol}^{-1})} \quad (3)$$

Where ΔH° indicates the enthalpy variation associated with CO_2 splitting at 298,15K equal to 283 kJ mol^{-1}. The conversion rate ($mmol_{CO2}$ h^{-1}) refers to the number of millimoles converted in 1 hour:

$$\text{Conversion rate} = X * \dot{n}\,\text{in} * 1000 * 60 \quad (4)$$

5.2.4 Electrical characterization

The outer electrode was connected to a high-voltage generator (AFS G05S-150k) while the internal electrode was connected to the ground via three external capacitors connected in series, each with a capacitance of 100 nF. The input signal was monitored by a high voltage prove (Tektronix) at an imposed frequency of 35 KHz and adjustable amplitude, depending on reactor configuration and gas composition, in order to have a constant applied power of 70 W. The input signal was amplified by a factor 1000. The behavior of the plasma was monitored, and all signals were recorded using a digital oscilloscope (Picotech Picoscope 6402D). The real plasma power was calculated using the area of the Q-U graph, also known as a Lissajous figure, which was created using the applied voltage and the dissipated charge using a MATLAB script [3]:

$$P = \frac{1}{T} \oint U(Q)\, dQ \quad (5)$$

5.2.5 Boehmite coating

Deposition of a thin layer of boehmite on the porous stainless-steel electrode involved a pre-calcination step of the stainless-steel tube at 550°C for 1 hour. This

was followed by three consecutive stages, following the procedure reported in literature [4]: (i) preparation of a aqueous solution of boehmite and additives; (ii) deposition with controlled parameters (dip-coating); (iii) controlled drying and annealing.

(i) Alumisol 10 A (Boehmite conc. 10.1 wt%), a commercial boehmite solution, was purchased from Kawaken fine Chemicals, Japan. Three electrode solutions were created by diluting Alumisol 10 A in distilled water with boehmite loadings of 0.9 wt%, 1.2 wt%, and 1.8 wt%. Each of these solutions were then combined with a water-based solution of organic additives, specifically 3.5 wt% polyvinyl alcohol (PVA) (MW 130000) and 1 wt% polyethylene glycol (PEG) (MW 400).

(ii) The boehmite dispersion is applied to the electrode supports using a specially designed automated system. The setup includes a pneumatic slider that accommodates a membrane holder, and it was remotely programmed in immersion speed (5 mms^{-1}), waiting time inside solution (5s), withdrawal speed (5 mms^{-1}), and number of dips (2 or 4).

(iii) In a climate-controlled room set at 40°C and 60% relative humidity, the deposited layer is dried for one hour while rotating. Subsequently, the layer is sintered in a static air furnace for one hour at 550°C.

The thickness and the loading of the different layer for different boehmite concentration is reported in Table B2.

5.2.6 Boehmite characterization

A field emission scanning electron microscope (FESEM, ZEISS Auriga) operating at an accelerating voltage of 5KV was used to examine the morphology of the boehmite. Images were collected on both boehmite coating as powder and boehmite-covered electrode.

X-ray diffraction (XRD) measurements were conducted on boehmite powder using a Bruker D8-Advance diffractometer with a Cu-Kα (λ= 1.54186 Å)

monochromatized radiation source. The scans were collected at a continuous rate of one degree per minute over an angular range of 0° to 90° at 25 °C. The step size was 0.02° with a dwell period of 1.2 s for each increment, by applying an accelerating voltage and current of 40 kV and 30 mA, respectively.

The chemical surface composition of the boehmite powder was examined using ultrahigh vacuum X-ray photoelectron spectroscopy (Thermo Scientific K-Alpha). The instrument was equipped with an Al anode (Al Kα=1486.68 eV) monochromatized X-ray source. Wide-range survey spectra were recorded using a 200 eV pass energy, while high-resolution core level spectra were captured using a 50 eV pass energy. The background pressure within the analytical chamber was maintained at or below $8e^{-8}$ mbar. To account for surface charge, all spectra were taken using the flood cannon (low energy Ar^{+} ions).

The surface area of boehmite powder was determined by the physical adsorption of N_2 onto the surface of the sample at liquid nitrogen temperatures by using a Trifex sorption analyzer (Micromeritics) system.

5.3 Results

5.3.1 Boehmite coating deposition

Figure 5.2 shows the SEM images for boehmite layers deposited on 0.5 μm, as illustrative example, according to different number of immersion and concentration of boehmite in dip solution using same amount of polymers (table B2).

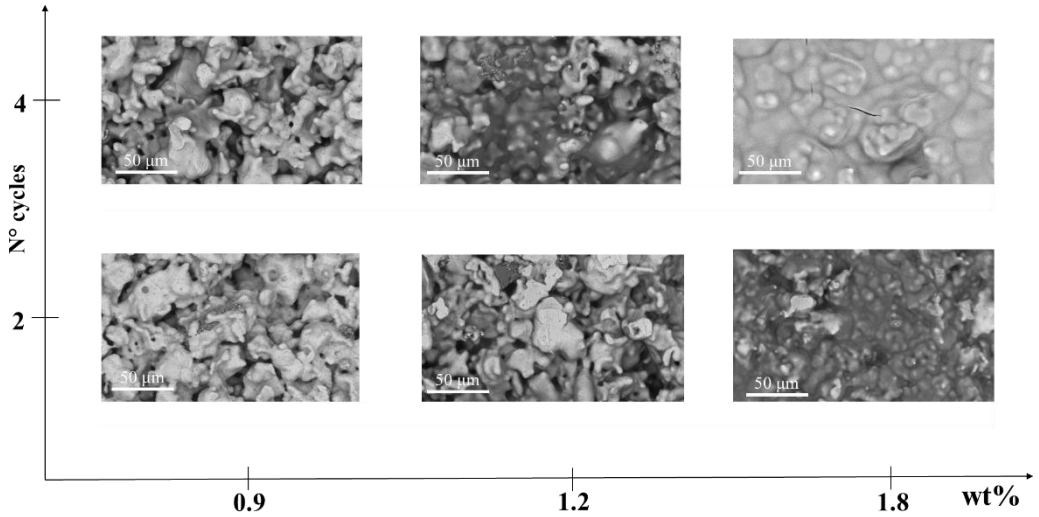

Figure 5.2 *SEM images of different boehmite layers for 0.5 μm*

The SEM images indicate that increasing the number of immersions and the concentration of boehmite in the dip solution gradually fills the tube pores. This effect is especially noticeable in the images obtained with 1.8 wt% and 4 immersions, where the boehmite layer completely covers the pores and some irregular cracks can be observed due to thermal stress during annealing at 550°C. Table B2 reports the thickness and loading of boehmite for each electrode. If the loading and thickness increase with a greater number of immersions, the viscosity of the dip solution increases with a higher amount of boehmite (wt%) [4,5] and a greater loading is obtained. In fact, boehmite solutions have pseudoplastic (shear-thinning) behavior at all pH values because of weak Van der Waals interactions between the particles [5]. The optimal condition for obtaining a coating without significantly reducing electrode porosity was the boehmite layer thickness obtained through 2 immersions and 0.9 wt%. Figure B1 displays the electrode covered in boehmite.

The BET isotherm method was used to investigate the superficial area and porosity of the boehmite. As shown in figure 5.3 (a), the boehmite (analyzed as powder after annealing) exhibited an IV type isotherm with an H3 type hysteresis [6]. This indicates the presence of mesoporous holes with dimensions of 4.1 nm, while the surface area is 320 m^2g^{-1}.

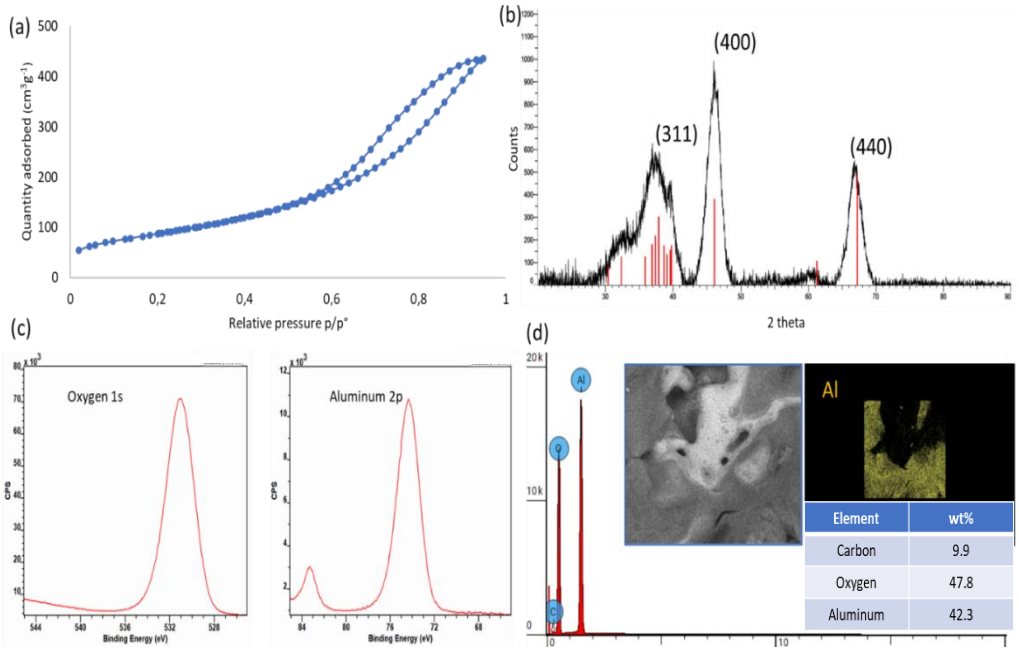

Figure 5.3 *Characterization of the boehmite layer: BET (a), XRD (b), XPS (c) and EDX (d)*

Figure 5.3 (b) shows the XRD analysis, which indicates the presence of typical peaks at 38.05° (311), 46° (400), and 66.8° (440) associated with γ-Al_2O_3 [7–9]. According to literature [4,10], boehmite transforms into this crystalline phase during annealing at 550°C.

The XPS (figure 5.3 c) and EDX (Figure 5.3 d) images confirm the presence of Al, O, and C (carbon derives from the polymers added to the dipping solution). The EDX mapping analysis on the covered electrode shows a uniform layer deposition.

5.3.2 Plasma performances of the porous electrode

Figure 5.4 shows how plasma parameters (CO_2 conversion, SEI, and η) change with internal electrode porosity for both empty and packed reactors with 1mm Al_2O_3 spheres. The shell in – shell out configuration is the only one reported here, as it is the only one possible for the smooth electrode.

The conversion rate decreases with higher flow rates and in packed reactors due to the shorter residence time of CO_2 within the plasma region. For instance, in the case of a smooth and empty electrode, the decrease is from 21.8% at 20 ml min^{-1} to 15.6% at 50 ml min^{-1}, while the CO_2 conversion is halved (10.5%) for the packed configuration at 20ml min^{-1}.

However, the permeable electrodes always exhibit an increase, with a more significant increment for the highest porosity. For the electrode with a porosity of 0.5 μm, the conversion rates are 25.1% and 21.9% in the empty and packed reactors, respectively. Figure 5.4 (c, d) shows that the latter value was similar to that of the empty smooth reactor.

The SEI increases as porosity and flow rate decrease. The highest values of 96.7KJ L^{-1} and 89.1KJ L^{-1} in the packed and empty configuration were observed for the smooth reactor at 20ml min^{-1}. Generally, the packed reactor shows SEI values higher than the empty reactor, with the exception of the 0.2 μm packed electrode, which shows similar SEI values (figure 5.4 d) to the smooth one. In Figure 5.4 f, it can be observed that the smooth packed electrode at 50ml min^{-1} has a lower energy efficiency (2.5%) compared to the 0.2 μm packed electrode (2.5%).

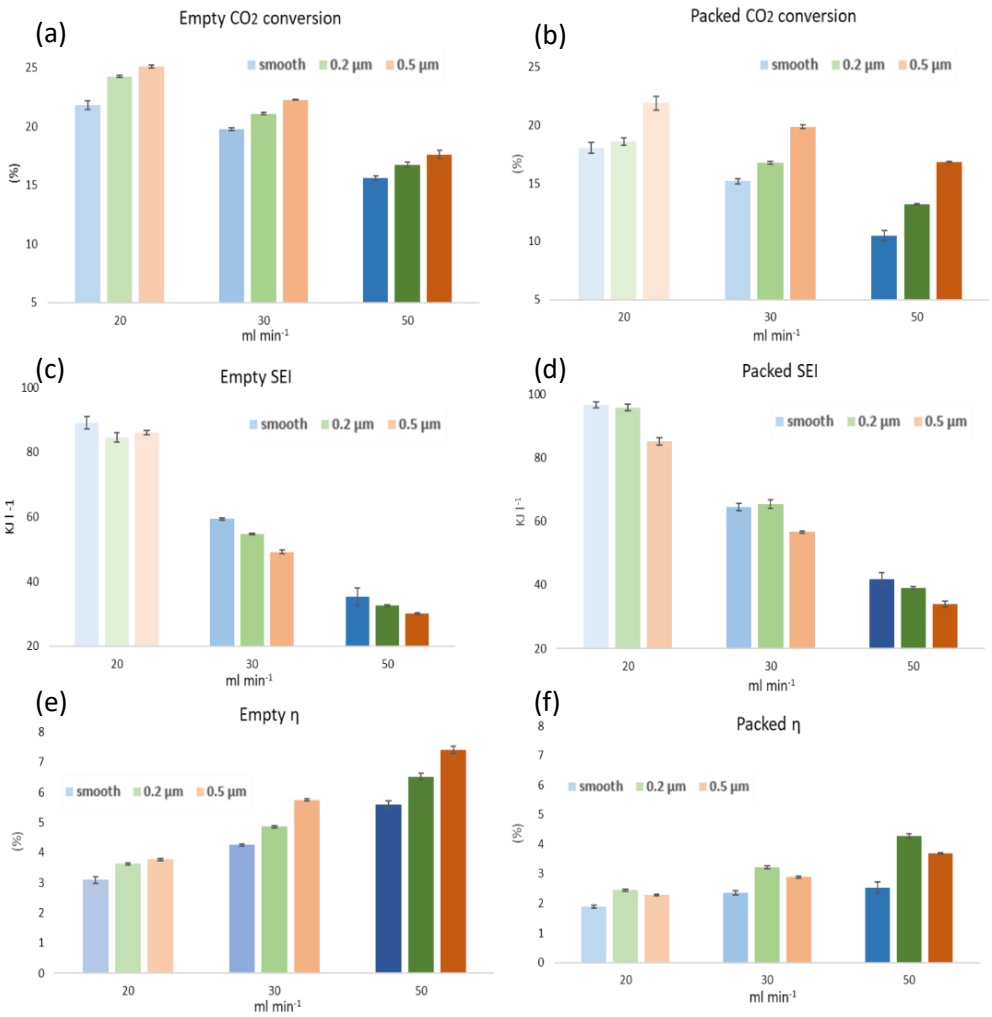

Figure 5.4 *CO_2 conversion for empty (a) and packed (b) reactors. SEI for empty (c) and packed (d) reactor and energy efficiency for empty (e) and packed (f) reactor. All values are referred to shell out- shell out configurations.*

Porous electrodes consistently show an increase in η, with the empty configuration having the highest values at greater flows (Figure 5.4 e, f). The 0.5 µm configuration has the highest values, measuring a maximum percentage of 7.4% at 50ml min^{-1}.

5.3.3 Effect of the boehmite layer

The boehmite is deposited as a thin coating of γ-Al_2O_3 on the porous electrode surface, forming the boehmite layer. This layer typically exhibits reaction parameters (CO_2 conversion, SEI, and η) that are intermediate between those of the empty and packed reactors, for the same porosity, in both the 0.2 µm and 0.5 µm electrodes (figure 5.5).

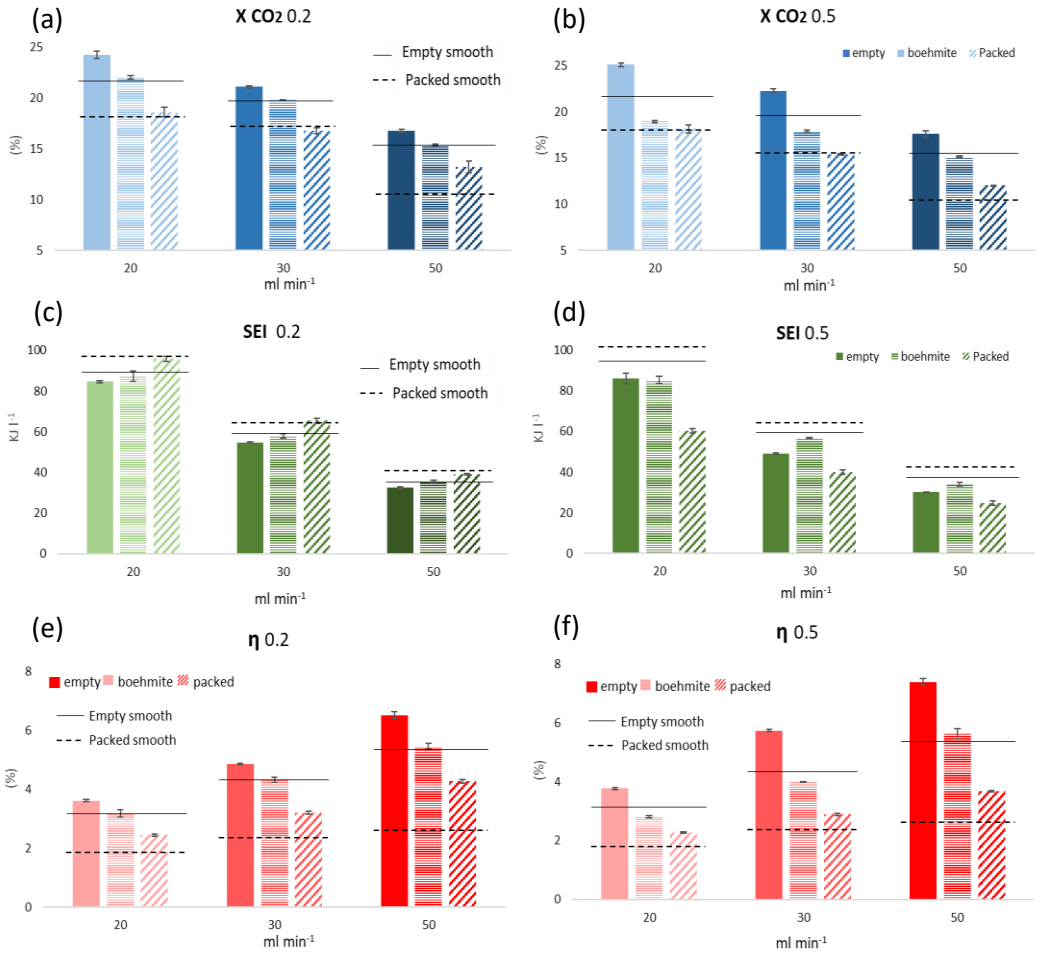

Figure 5.5 *Reactions parameters for shell in-shell out configuration for 0.2µm and 0.5µm porous electrode.*
CO_2 conversion (blue), SEI (green) and energy efficiency (red) for the empty (left) boehmite (middle) and packed (right) reactor.
The black and dash lines indicate the same value for the empty or packed smooth reactor.

However, some differences can also be observed.

- The performance of the boehmite coated electrode are comparable or slightly higher than that of the smooth reactor for 0.2 µm, while they are similar or lower for the 0.5 µm boehmite coated electrode.
- The SEI values are higher for the 0.2 µm packed reactor. Conversely, they are the lowest for 0.5 µm packed electrode, instead showing the highest results with boehmite coating.
- The CO_2 conversion and η of the boehmite coated electrodes are always higher than those of the packed configuration for all porosities.

Furthermore, the packed porous electrodes demonstrate comparable or superior results to the packed smooth reactor, particularly at higher flow rates. The only exception is the SEI at 0.5 µm (figure 5.5 d).

Regarding the boehmite-covered electrode, the one with a porosity of 0.2 µm exhibits higher conversion (22% at 20ml min^{-1}) and efficiencies (5.6% at 50ml min^{-1}) than the electrode with greater porosity (15.4% CO_2 conversion and 2.8% η at respective flow rates), while the SEI remains similar. This trend is opposite to that of empty configurations. However, lower differences can be observed at higher flow rates.

5.3.4 Effect of gas flow configuration

The gas feed can flow into reactor parallel to the gap in the shell out- shell out configuration or through the permeable electrode in the shell out-tube in configuration.

As shown in Figure 5.6 (a, b) the conversion concerning

- The empty set-up: is similar in both configurations at 0.2 µm, with a slight increase observed in shell in- shell out configuration in electrode with porosity 0.5 µm.
- In the shell-tube out configuration, the covered set-up always has a higher value, reaching 23.4% and 20.4% for 0.2 µm and 0.5 µm, respectively, at 20ml min^{-1}.

- In the packed set-up, the shell out-shell out configuration has a higher value for 0.2 µm, and shell out-shell in for 0.5 µm, reaching 19.4% at 20ml min^{-1}.

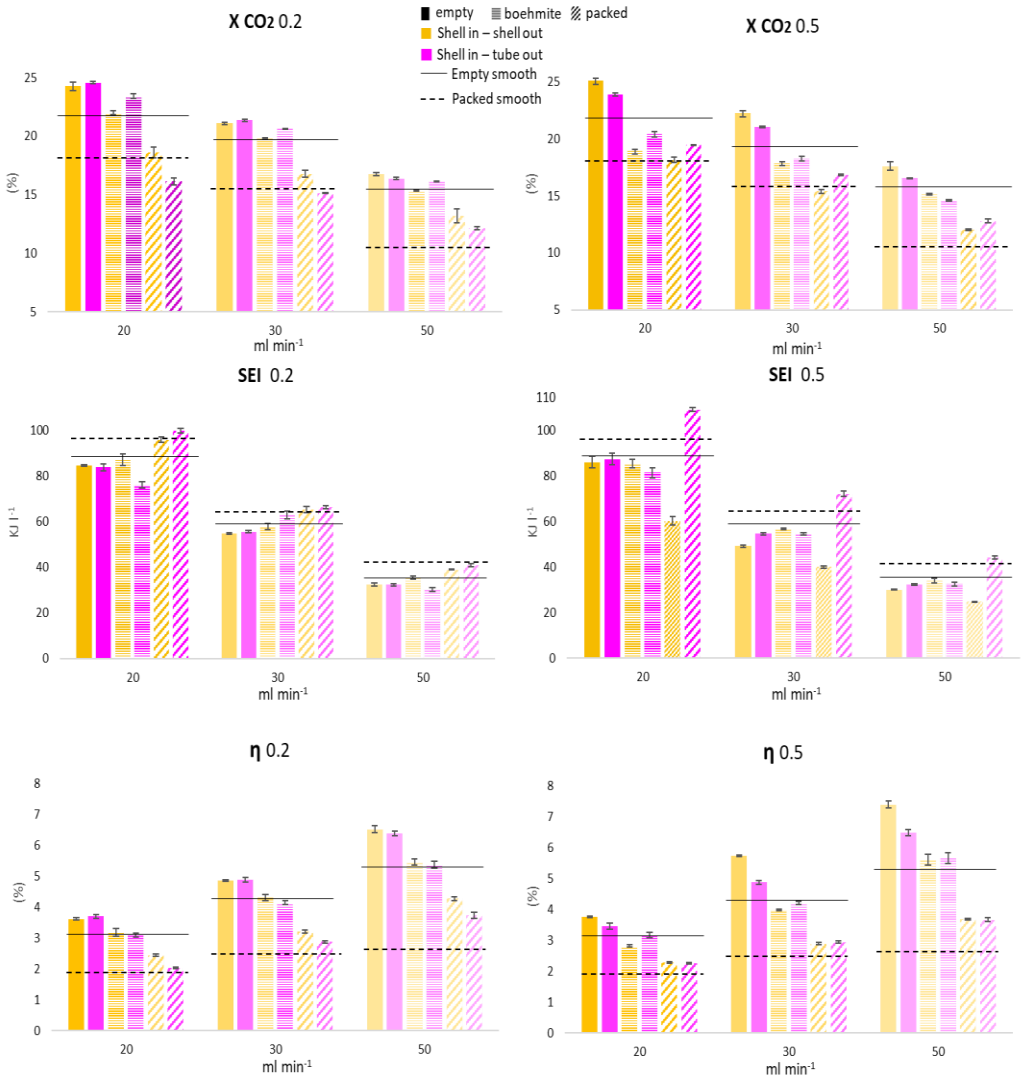

Figure 5.6 *Reactor performances (CO_2 conversion, SEI and energy efficiency) for shell in-shell out (yellow) or shell in-tube out (purple) gas flow configurations. Values refer to empty, boehmite covered and packed electrodes. The black and dash lines indicate the performances for the empty or packed smooth reactor.*

Figure 5.6 (c, d) show differences in SEI when the gas flows through the reactor. No significant differences in SEI were observed for the empty reactors at both flow

configurations and porosity. Regarding the boehmite layer, the shell-out to shell-out configuration generally favored SEI in both electrodes, although an opposite trend was observed at 30ml min^{-1} with pores of 0.2μm.

The configuration of shell in-tube out consistently yields higher SEI for packed configurations, with more pronounced differences in the 0.5 μm electrode. The maximum value of 109 KJ L^{-1} is reached at 20ml min^{-1}, surpassing the values of the smooth reactor. This effect is more pronounced at lower flows.

Regarding energy efficiency, similar values were measured for both flow configurations in both electrodes. However, higher efficiencies were observed in the shell in-shell out configuration for the empty setup in the electrode with a porosity of 0.5 μm.

5.3.5 Effect of gas dilution

Tests were conducted using either a pure CO_2 stream or a diluted mixture of 20% Ar in CO_2. As reported in the literature, the addition of Ar in the gas mixture always increases conversion.

However, it is important to note that an increase in conversion does not necessarily indicate an actual increase in the converted moles due to gas dilution. To account for this, a comparison based on the actual number of moles converted in the form of conversion rate ($mmolCO_2\ h^{-1}$) is shown in Figure 5.7.

In the smooth reactor, the addition of 20% argon to the gas mixture has a positive effect only for the packed configuration (figure 5.7).

However, higher flow rates result in more moles being converted in both pure and diluted gas feeds, indicating an opposite trend with respect to conversion. The porous electrodes exhibit a similar trend.

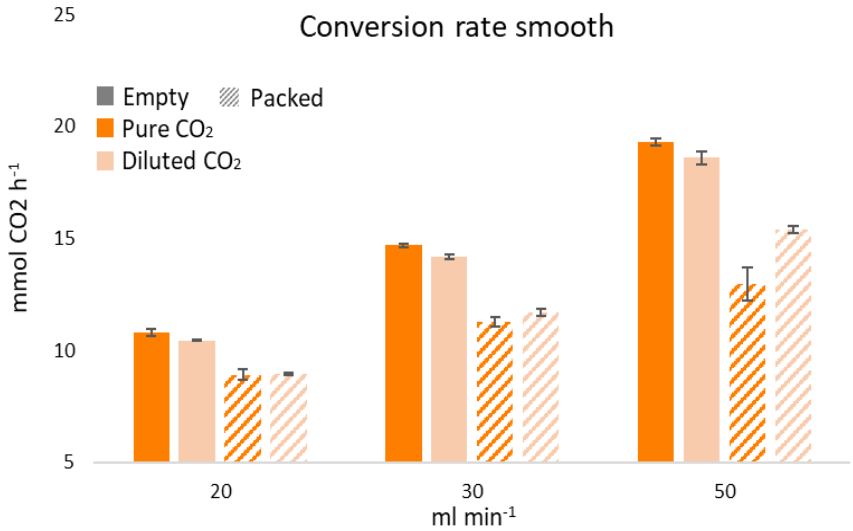

Figure 5.7 *Effect of CO_2 pure (dark orange) or argon dilution (light orange) on conversion rate for the smooth reactor*

The conversion rate is higher in the porous electrodes than in the empty configuration, followed by the boehmite-covered electrode, and lowest in the packed configuration. However, the results are always higher than those observed in the smooth reactor. Higher values are consistently observed in pure CO_2 than in diluted flow with empty and covered electrodes. At a flow rate of 50 ml min^{-1} in an empty shell in – shell out configuration, the 0.5 µm electrode exhibited the highest CO_2 conversion rate among all electrodes and configurations, reaching a maximum of 22 mmol h^{-1} (figure B2). However, a higher conversion rate was observed in the packed configuration when using a diluted gas flow for all porosity levels.

Additionally, the introduction of argon in the gas mixture decreases the SEI in the porous electrodes for all configurations. In contrast, similar values to pure CO_2 are observed in the smooth reactor configurations.

The use of a diluted gas flow leads to higher energy efficiency compared to pure CO_2, regardless of porosity and configuration (figure 5.8)

However, both empty and packed porous electrodes consistently exhibit higher values than smooth electrodes (6.5% for empty and 4.7% for packed).

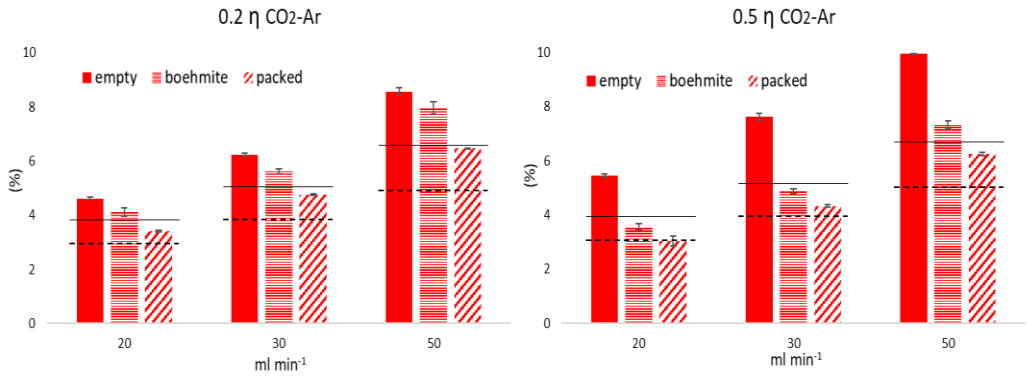

Figure 5.8 *Energy efficiencies in diluted CO_2 for porous electrodes. The black and dash lines indicate the performances for the empty or packed smooth reactor.*

The electrode with a porosity of 0.2 µm exhibited greater energy efficiency with the boehmite-covered electrode than with the empty smooth reactor in both gas direction configurations. Conversely, an opposite trend was observed for the reactor with a porosity of 0.5 µm, but only in the shell in-shell out configuration at low flow rates (see Figure 5.8). However, highest values are generally observed in the shell in-shell out configurations, resulting in the best value of 10% and 8.6% for the empty electrode with 0.5 µm and 0.2 µm porosity, respectively.

5.4 Discussion

A- Effect of the porosity

The previous section's results suggest that the plasma behavior is affected by the textural properties of the internal electrode. A higher conversion and conversion rate are consistently observed in the empty configuration with both porosities, which is also linked to greater energy efficiency compared to the smooth electrode. The presence of pores and sharp zones in the electrode could positively influence plasma performance [11–13].

Several studies have shown that microdischarges can develop inside catalyst pores, which significantly alter the plasma's characteristics. The high electric field within

the pores causes distinct electron energy distributions, which in turn affect electron impact reaction rates and modify the plasma's chemistry and performance [14–21].

Holzer et al. [14,16] provide evidence for the presence of short-lived species inside catalyst pores that are 10 nm in size. This is due to a stronger electric field inside the pores compared to the bulk plasma, as well as the stabilization of these reactive species through adsorption on the surface during their diffusion from the plasma into the pores. Hensel et al. [17,20] observed plasma formation on the surface of porous ceramic dielectric material when the pore size is less than 1 μm. For pore sizes of 15 μm, a transition to microdischarges inside the pores occurs when the applied voltage exceeds the breakdown value (8.6 kV). It should be noted that the researchers were able to generate a pulsed discharge inside pores by utilizing back corona discharge phenomena, despite using direct current, due to the high resistivity of the dielectric material. Similar results were obtained using alternate current [18,19]. The researchers also observed that the size of the pores influenced the onset voltage of the microdischarges and the diameter of the discharge channels. Reducing the pulsed current amplitude and microdischarge channel dimensions leads to greater breakdown voltage due to smaller pores.

However, the literature suggests that pores should have dimensions similar to the Debye length of the reactor. For example, Bhoj and Kushner [22] investigated the possibility of ions accessing the superficial pores of a rough polymer surface during a corona discharge in humid air. They concluded that electrons and ions can only penetrate pores with dimensions greater than 1 μm, which is comparable to the Debye length. Bogaerts er al. [23] indicate in their simulation that microdischarges can only penetrate pores of 600 nm and above due to a calculated Debye length of 415 nm (dry air, atmospheric pressure, and an applied voltage of -8kV).

In the reactor used in this research, it was not possible to determine the Debye length because the alumina dielectric does not allow for optical characterization, which is essential for measuring electron temperature and calculating the Debye length. However, the value of this parameter typically varies within the nm to μm range, so

it is uncertain whether the 0.2 and 0.5 μm pores of the inner electrode play a role. Additionally, streamers may still be able to penetrate pores smaller than the Debye length [24,25].

In a computational study by Zhang et al. [11] the impact of various pore sizes and applied voltages was investigated in terms of plasma density, electron temperature, electric field, electron impact ionization rate, and electric potential. The study confirmed a higher electric field within pores larger than 10 μm (Debye length around 40 μm), resulting in an increase in electron temperature. This increase favors electron impact ionization and excitation, leading to a higher number of ions and electrons and ultimately an increased plasma density within the pores. However, the model predicts the formation of streamers inside pores smaller than the Debye length, even if the ionization rate is higher in larger pores due to their larger effective volume [25].

The same research group [21] examined the impact of pore shape (cylindrical and conical) on the electric field within the pores. They found that the electric field was stronger at the opening and bottom corners of the pores, particularly for conical pores, due to the tip-like structure in that region.

The sharp ends of the pores play a fundamental role in accumulating electrical charges on the tip, which has been widely demonstrated and utilized in various applications, including gas discharges [26–28]. Sharp edges or tips can focus the electric field [27,28], increasing the likelihood of vibrational excitation or ionization of the surrounding gas molecules, which produces a high surface charge density [12,26]. In contrast, the electric field in a smooth electrode is uniform, and the charge density is inversely proportional to the surface's curvature [27]. Conversely, the porous electrodes are rich of edges and rounded tips where the electric field is stronger. Therefore the velocity of ions, that regulate the number of secondary electrons is also higher [29]. As a result, the process of secondary emission may be more intense around sharp points where the electric field has accumulated [12,26]. Additionally, the higher electric field promotes collisions between dense energetic

electrons and neutral molecules, resulting in better energy transmission to CO_2 molecules and increasing the population of vibrationally excited molecules. The splitting of CO_2 molecules is facilitated by this process, resulting in a higher conversion rate compared to a smooth electrode. Furthermore, the sharp tips or edges on electrodes can promote the formation of streamers or filaments in the plasma, which enhances the overall energy efficiency of the reactor[12].

Meanwhile, the SEI decreases with respect to the smooth reactor due to the edges and conical tips that could aid in the dissipation of the applied power as gas heating. This could also explain why the SEI values in the packed configuration are similar among porous electrodes and the smooth reactor. It is likely that in the packed configuration, the edge effect is limited due to the packing material that levels the roughness of the electrode, resulting in comparable conversion. This is also confirmed by the Lissajous figure (figure B3) which shows fewer peaks and greater uniformity in the packed reactor[30]. However, the formation of micro-discharges is probably improved, as suggested by the higher energy efficiencies obtained by using the porous electrode respect to those obtained with the packed smooth electrode.

B-Effect of boehmite layer.

Porous electrodes covered by boehmite layer shows always intermediate performances between the empty reactor and the packed one, with same porosity.

This confirms the role of the porosity of the internal electrode. In fact, the boehmite layer covers the surface of the electrode, blocking partially the pores of the reactor. This is clearly shown in figure 3.11, where a greater number of immersions in the dipping solution results in a gradual filling of the pores. Furthermore dip coating in a boehmite solution is a common method adopted to reduce the roughness and porosity of metallic support in membrane fabrication for gas separation [4,10]. Therefore, the boehmite-covered electrode has lower porosity than the empty configuration, which explains the lower performance. However, there is still some

residual porosity, as shown in the figure, which leads to similar or slightly higher performance than the smooth electrode. However, there are some differences between the two covered electrodes. These differences may be due to the deposition of boehmite, which could vary depending on the porosity of the stainless-steel electrode.

When comparing the covered electrode with the packed configuration at the same porosity, better performance is observed.

At same porosity, but also for the smooth reactor, the packed configuration exhibits lower conversion (and conversion rate) because the residence time is lower as shown in table 5.1. Literature reports contrasting results, evidencing higher or lower conversions respect the non-packed reactors, based principally on the reactor geometry and packaging material and dimension of the spheres [24,30–33]. Typically, the use of a catalyst as packaging material leads to improved results. The lack of catalytic effect of γ-alumina on plasma-assisted CO_2 splitting in my experiments is not unexpected.

However, the higher energy efficiencies observed in the packed configuration suggest facilitated plasma formation. The discharge behavior of the packed bed may shift from filamentary to a combination of surface and filamentary discharge. Surface discharges occur on the surface of the pellets at their contact sites, while filamentary discharges are limited to the small space between the pellet-pellet and pellet-dielectric wall. The electric field in the gas surrounding the contact sites may increase up to 10-10^4 times, depending on the dielectric constant, shape, and contact angle of the packing materials. This leads to a decrease in the breakdown voltage and an increase in the electron temperature [30–32,34]. The lower applied voltage required for the packed reactors, which is around 70 W (from approximately 30 kV to 25 kV), confirms this.

Additionally, the higher SEI in the packed configuration supports this finding. Furthermore, at the same applied power, the peak-to-peak voltage (Vptp) of the plasma increases in the packed configuration [30]. For example, in a electrode with

a porosity of 0.2 μm, Vptp increases from 9.5 kV without packing to 10.9 kV with a packed configuration. An exception to the observed trend is the electrode with a porosity of 0.5 μm, which shows higher SEI values with the covered electrode. This could be attributed to differences in boehmite deposition, although further studies are needed to confirm this hypothesis.

C- Effect of gas flow configuration

The porous electrodes were tested both in shell in - shell out flow configuration, which is only possible configuration for the smooth reactor, or shell in - tube out flow configuration where the gas flow through the porous electrode. Energy efficiencies are similar for both flow configurations, suggesting not important differences in the plasma behavior as supported by the Lissajous figures (figure B4). Conversion is influenced by the flow configurations, but systematic differences cannot be observed. This could be ascribed by the chaotic gas flow direction inside the reactor. Gas fractions may enter into reactor without undergoing molecular conversion both into axial and radial diffusion because of the possibility of gas fractions taking shortcuts through the reactor [35].

However, the shell in-tube out configuration shows higher SEI reaching or abundantly exciting, the value of the packed and empty smooth reactor. At the same time conversion is higher for shell in-shell out configuration with the covered electrodes especially for lower flow rate. This differences can be explained because the interactions between gas phase radicals and the electrode surface occur only when the radicals develop in a thin boundary layer of approximately 50 μm near the electrode surface [36,37]. It is for this reason, also, that the tube in-shell out flow configuration was not tested. In fact, in this case the gas would not have interacted with the surface and pores of the electrode because it would have passed as non-ionized gas.

In packed bed reactor formation of active species very near to the electrode surface is facilitated because the plasma evolves to a combination of filamentary mode (microdischarges) and superficial plasma. Moreover, as described above, porous

electrode can facilitate plasma formation inside its pores. As a result, when the gas passes through the reactor surface, it interacts with the thin boundary layer, leading to the formation of a more powerful plasma. However, studies on different gas flow configuration, especially in a tubular coaxial DBD reactor are still limited [38]. The marked differences in SEI for the packed reactor at 0.5 may be explained also by a difference on the slope of the Lissajous figures(see figure B) , indicating a different effective capacitance and probably a lower breakdown voltage in the shell in – tube out flow configuration[23,39].

D- Effect of gas flow rate and dilution

The effect of gas flow rate and dilution on conversion and energy efficiency was measured by adding Ar to the gas mixture. The effect of gas flow rate and dilution on conversion and energy efficiency was measured by adding Ar to the gas mixture. This is due to easier plasma formation, as the breakdown voltage is smaller compared to pure CO_2. The inert gas increases the first Townsend ionization coefficient α, resulting in a higher number of secondary electrons created per unit length along the electric field [29,40,41].

Furthermore, due to the higher energy required for ionization and excitation of Ar, the probability of inelastic collisions between electrons and Ar, as well as recombination with Ar^+ ions, is low. This results in a longer mean free path in diluted gas, allowing electrons more time to accelerate in the applied electric field and leading to electrical breakdown occurring at lower voltages. As a result, energy efficiency also increases [1,42]. However, the conversion of CO_2 decreases when it is diluted. Therefore, the conversion rate is always higher in pure CO_2, except in packed configurations. This can be attributed to a combination of the argon effect on plasma and the more powerful plasma described in the previous paragraph.

Increasing the gas flow rate reduces the conversion due to the lower residence time, but at the same time, an increase in the conversion rate is observed. Increasing the number of input molecules with the gas flow rate not only balances but also overcomes the inevitable reduction of conversion with residence time.

5.5 Conclusion

This section was focused on plasma assisted CO_2 splitting by a coaxial DBD reactor. The role of the internal electrode porosity was discussed, observing higher performances in the electrode with 0.5 µm pores size. The porosity beneficial effect was attributed to two main factors: (i) the possibility of plasma or streamers formation inside the pores and (ii) the presence of edges and curved tips that could enhance locally the electric field and consequently the plasma density.

The effect of a boehmite layer deposited on porous electrode by dip coating was also discussed. It should be highlighted that the boehmite layer configuration seems to be more advantageous than the packed configurations. In fact, conversion and efficiency are always higher in covered electrode compared to the packed reactor at same porosity. This is highlighted in figure 5.9, where is reported the ratio of CO_2 conversion and energy efficiency between covered and packed electrode, at same porosity.

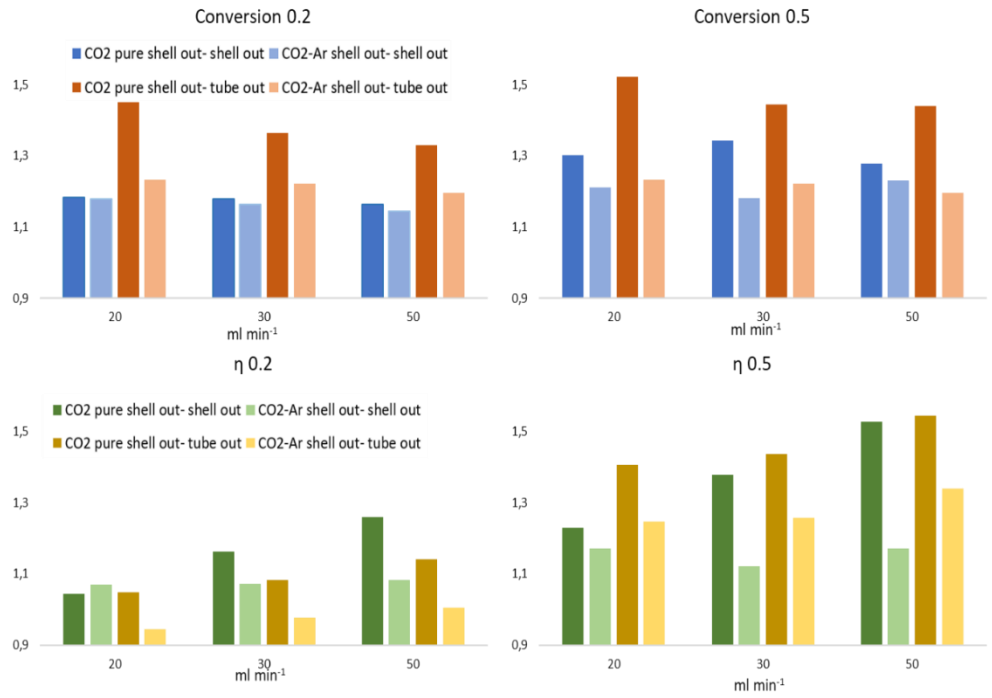

Figure 5.9 *Ratio of the performances (CO_2 conversion and energy efficiency) between boehmite and packed electrodes for pure CO_2, diluted CO_2 and both gas flow configurations*

The ratio is always greater than one, confirming the superior performance of the reactor with boehmite, particularly with a porosity of 0.5 μm.
Additionally, it is observed that the shell in – tube out configuration in pure CO_2 appears to benefit more than the boehmite layer in terms of conversion and efficiency.

Furthermore, the SEI values are similar or even higher than the packed reactor. In addition, the boehmite covered porous electrodes have always better plasma performance than the packed smooth reactor and similar to the smooth empty one. Furthermore, the boehmite-coated porous electrodes always has better plasma performance than the smooth packed reactor and similar to the smooth vacuum one. This is of particular relevance if a metal is deposited on the boehmite which catalyzes the reaction. In fact, a catalyst could be used without having to pack the reactor and thus avoid perforation losses due to the shorter residence time. Furthermore, there would be a cost benefit. In fact, considering that the boehmite layer is extremely thin (in the order of a micron), the quantity of material to be used is significantly lower. The costs would be even lower if a catalyst is deposited on the alumina because expensive materials and critical raw materials often have to be used.

Additionally, the role of gas flow rate and composition was also evaluated. Adding Ar in the gas mixture helps to rise conversion but the conversion rates are usually lower because the gas is diluted. Conversely the conversion rate rises with the gas flow, overcoming the inevitable conversion decrease with the residence time.
Finally, it is worth noting that the performance obtained in CO_2 splitting are comparable to literature data, as reported in figure 5.10. The reactor has good performance within DBD reactors, with high conversion and energy efficiency, as shown in the Bogaerts image below [43]. However, it should be noted that the gap between the dielectric and electrode is almost 3 mm, which is relatively large

compared to the literature. Therefore, decreasing the gap could significantly improve performance by creating a more intense electric field and denser plasma. For example, Uytdenhouwen et al. [35] observed a extreme drops in CO_2 conversion, from 53.6% for a gap size of 455 µm to only 23% at 4705 µm. Similarly, Aerts et al. [44] reported a conversion of approximately 15% and energy efficiency slightly higher than 2% for a SEI of 100 J cm^{-3} using a gap size of 3.3 mm. However, when using a smaller gap (1.8 mm), the conversion and efficiency increased to 30% and 4%, respectively.

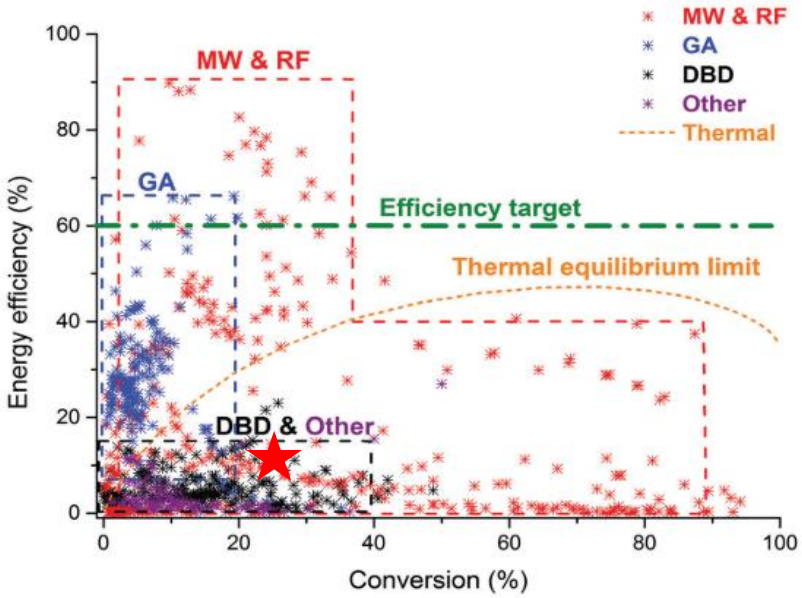

Figure 5.10 *Comparison with literature and performance reported in this work (red star). Revisited from ref. [43]*

Bibliography

1. Ozkan, A.; Bogaerts, A.; Reniers, F. Routes to Increase the Conversion and the Energy Efficiency in the Splitting of CO2 by a Dielectric Barrier Discharge. *J. Phys. D. Appl. Phys.* **2017**, *50*, doi:10.1088/1361-6463/aa562c.

2. Levenspiel, O. Chemical Reaction Engineering. *nd. Eng. Chem. Res.* **1999**, *38*, 4140–4143.

3. Manley, T.C. The Electric Characteristics of the Ozonator Discharge. *Trans. Electrochem. Soc.* **1943**, *84*, 83, doi:10.1149/1.3071556.

4. Agnolin, S.; Melendez, J.; Di Felice, L.; Gallucci, F. Surface Roughness Improvement of Hastelloy X Tubular Filters for H2 Selective Supported Pd–Ag Alloy Membranes Preparation. *Int. J. Hydrogen Energy* **2022**, *47*, 28505–28517, doi:10.1016/j.ijhydene.2022.06.164.

5. Islam, M.A.; Ming, C.C.; Ravindra, P.; Chen, E.S. Rheology and Gelling Behaveor of Boehmite Sols. *J. Appl. Sci.* 2011, *11*, 2327–2333.

6. Thommes, M.; Kaneko, K.; Neimark, A. V.; Olivier, J.P.; Rodriguez-Reinoso, F.; Rouquerol, J.; Sing, K.S.W. Physisorption of Gases, with Special Reference to the Evaluation of Surface Area and Pore Size Distribution (IUPAC Technical Report). *Pure Appl. Chem.* **2015**, *87*, 1051–1069, doi:10.1515/pac-2014-1117.

7. Rozita, Y.; Brydson, R.; Scott, A.J. An Investigation of Commercial Gamma-Al 2 O 3 Nanoparticles. *J. Phys. Conf. Ser.* **2010**, *241*, 012096, doi:10.1088/1742-6596/241/1/012096.

8. Wang, Z.; Wu, W.; Bian, X.; Wu, Y. Synthesis and Characterization of Amorphous Al2O3 and γ-Al2O3 by Spray Pyrolysis. *Green Process. Synth.* **2016**, *5*, 305–310, doi:10.1515/gps-2015-0128.

9. Stuart, N.M.; Sohlberg, K. The Microstructure of γ-Alumina. *Energies* **2021**, *14*, 1–16, doi:10.3390/en14206472.

10. Poto, S.; Endepoel, J.G.H.; Llosa-Tanco, M.A.; Pacheco-Tanaka, D.A.; Gallucci, F.; Neira d'Angelo, M.F. Vapor/Gas Separation through Carbon Molecular Sieve Membranes: Experimental and Theoretical Investigation. *Int. J. Hydrogen*

Energy **2022**, *47*, 11385–11401, doi:10.1016/j.ijhydene.2021.10.155.

11. Zhang, Y.R.; Van Laer, K.; Neyts, E.C.; Bogaerts, A. Can Plasma Be Formed in Catalyst Pores? A Modeling Investigation. *Appl. Catal. B Environ.* **2016**, *185*, 56–67, doi:10.1016/j.apcatb.2015.12.009.

12. Lamichhane, P.; Pourali, N.; Rebrov, E. V.; Hessel, V. Energy Intensified Nitrogen Fixation Through Fast Modulated Gas Discharge from Pyramid-Shaped Micro-Electrode. *Plasma Chem. Plasma Process.* **2023**, doi:10.1007/s11090-023-10376-1.

13. Yu-ru, Z.; Erik, N. Enhancement of Plasma Generation in Catalyst Pores with Different Shapes. *Plasma Sources Sci. Technol.* **2018**, *5*.

14. Roland, U.; Holzer, F.; Kopinke, F.D. Combination of Non-Thermal Plasma and Heterogeneous Catalysis for Oxidation of Volatile Organic Compounds: Part 2. Ozone Decomposition and Deactivation of γ-Al2O3. *Appl. Catal. B Environ.* **2005**, *58*, 217–226, doi:10.1016/j.apcatb.2004.11.024.

15. Zhang, Y.R.; Van Laer, K.; Neyts, E.C.; Bogaerts, A. Can Plasma Be Formed in Catalyst Pores? A Modeling Investigation. *Appl. Catal. B Environ.* **2016**, *185*, 56–67, doi:10.1016/j.apcatb.2015.12.009.

16. Holzer, F.; Roland, U.; Kopinke, F.D. Combination of Non-Thermal Plasma and Heterogeneous Catalysis for Oxidation of Volatile Organic Compounds. Part 1. Accessibility of the Intra-Particle Volume. *Appl. Catal. B Environ.* **2002**, *38*, 163–181, doi:10.1016/S0926-3373(02)00040-1.

17. Hensel, K.; Katsura, S.; Mizuno, A. DC Microdischarges inside Porous Ceramics. *IEEE Trans. Plasma Sci.* **2005**, *33*, 574–575, doi:10.1109/TPS.2005.845389.

18. Hensel, K.; Martišovitš, V.; Machala, Z.; Janda, M.; Leštinský, M.; Tardiveau, P.; Mizuno, A. Electrical and Optical Properties of AC Microdischarges in Porous Ceramics. *Plasma Process. Polym.* **2007**, *4*, 682–693, doi:10.1002/ppap.200700022.

19. Hensel, K. Microdischarges in Ceramic Foams and Honeycombs. *Eur. Phys. J. D* **2009**, *54*, 141–148, doi:10.1140/epjd/e2009-00073-1.

20. Hensel, K.; Matsui, Y.; Katsura, S.; Mizuno, A. Generation of Microdischarges in Porous Materials. *Czechoslov. J. Phys.* **2004**, *54*, 683–689, doi:10.1007/BF03166471.

21. Zhang, Y.R.; Neyts, E.C.; Bogaerts, A. Enhancement of Plasma Generation in Catalyst Pores with Different Shapes. *Plasma Sources Sci. Technol.* **2018**, *27*, doi:10.1088/1361-6595/aac0e4.

22. Bhoj, A.N.; Kushner, M.J. Repetitively Pulsed Atmospheric Pressure Discharge Treatment of Rough Polymer Surfaces: I. Humid Air Discharges. *Plasma Sources Sci. Technol.* **2008**, *17*, doi:10.1088/0963-0252/17/3/035024.

23. Bogaerts, A.; Neyts, E.C.; Guaitella, O.; Murphy, A.B. Foundations of Plasma Catalysis for Environmental Applications. *Plasma Sources Sci. Technol.* **2022**, *31*, doi:10.1088/1361-6595/ac5f8e.

24. Michielsen, I.; Uytdenhouwen, Y.; Pype, J.; Michielsen, B.; Mertens, J.; Reniers, F.; Meynen, V.; Bogaerts, A. CO2 Dissociation in a Packed Bed DBD Reactor: First Steps towards a Better Understanding of Plasma Catalysis. *Chem. Eng. J.* **2017**, *326*, 477–488, doi:10.1016/j.cej.2017.05.177.

25. Zhang, Y.; Wang, H.Y.; Zhang, Y.R.; Bogaerts, A. Formation of Microdischarges inside a Mesoporous Catalyst in Dielectric Barrier Discharge Plasmas. *Plasma Sources Sci. Technol.* **2017**, *26*, doi:10.1088/1361-6595/aa66be.

26. Pourali, N.; Hessel, V.; Rebrov, E. V. The Effects of Pulse Shape on the Selectivity and Production Rate in Non-Oxidative Coupling of Methane by a Micro-DBD Reactor. *Plasma Chem. Plasma Process.* **2022**, *42*, 619–640, doi:10.1007/s11090-022-10242-6.

27. Matehkolaee, M.J.; Asrami, A.N. The Review on the Charge Distribution on the Conductor Surface. *Eur. J. Phys. Educ.* **2013**, *4*, 1–6.

28. Liu, P.; Chen, B.; Liang, C.; Yao, W.; Cui, Y.; Hu, S.; Zou, P.; Zhang, H.; Fan, H.J.; Yang, C. Tip-Enhanced Electric Field: A New Mechanism Promoting Mass Transfer in Oxygen Evolution Reactions. *Adv. Mater.* **2021**, *33*, 1–9, doi:10.1002/adma.202007377.

29. Fridman, A. *Plasma Chemistry*; 2008; ISBN 9780521847353.

30. Mei, D.; Zhu, X.; He, Y.L.; Yan, J.D.; Tu, X. Plasma-Assisted Conversion of CO2 in a Dielectric Barrier Discharge Reactor: Understanding the Effect of Packing Materials. *Plasma Sources Sci. Technol.* **2015**, *24*, 15011, doi:10.1088/0963-0252/24/1/015011.

31. Annemie, B.; Tomáš, K.; Koen, V.L.; Ramses, S.; Bogaerts, A.; Kozak, T.; Laer, K. Van Plasma-Based Conversion of CO2 : Current Status and Future Challenges. *Faraday Discuss.* **2015**, *183*, 217–232, doi:10.1039/c5d00053.

32. Van Laer, K.; Bogaerts, A. Improving the Conversion and Energy Efficiency of Carbon Dioxide Splitting in a Zirconia-Packed Dielectric Barrier Discharge Reactor. *Energy Technol.* **2015**, *3*, 1038–1044, doi:10.1002/ente.201500127.

33. Bogaerts, A.; Neyts, E.C. Plasma Technology: An Emerging Technology for Energy Storage. *ACS Energy Lett.* **2018**, *3*, 1013–1027, doi:10.1021/acsenergylett.8b00184.

34. Qiao, Z.; Wang, Z.; Zhang, C.; Yuan, S.; Zhu, Y.; Wang, J. Effect of Dielectric Packing Materials on the Decomposition of Carbon Dioxide Using DBD Microplasma Reactor. *AIChE J.* **2012**, *59*, 215–228, doi:10.1002/aic.

35. Uytdenhouwen, Y.; Bal, K.M.; Michielsen, I.; Neyts, E.C.; Meynen, V.; Cool, P.; Bogaerts, A. How Process Parameters and Packing Materials Tune Chemical Equilibrium and Kinetics in Plasma-Based CO2 Conversion. *Chem. Eng. J.* **2019**, *372*, 1253–1264, doi:10.1016/j.cej.2019.05.008.

36. Shah, Y.T.; Verma, J.; Katti, S.S. Plasma Activated Catalysis for Carbon Dioxide Dissociation: A Review. *J. Indian Chem. Soc.* **2021**, *98*, 100152, doi:10.1016/j.jics.2021.100152.

37. Whitehead, J.C. Plasma-Catalysis: The Known Knowns, the Known Unknowns and the Unknown Unknowns. *J. Phys. D. Appl. Phys.* **2016**, *49*, doi:10.1088/0022-3727/49/24/243001.

38. Uytdenhouwen, Y.; Hereijgers, J.; Breugelmans, T.; Cool, P.; Bogaerts, A. How Gas Flow Design Can Influence the Performance of a DBD Plasma Reactor for Dry Reforming of Methane. *Chem. Eng. J.* **2021**, *405*, 126618, doi:10.1016/j.cej.2020.126618.

39. Uytdenhouwen, Y.; Van Alphen, S.; Michielsen, I.; Meynen, V.; Cool, P.; Bogaerts, A. A Packed-Bed DBD Micro Plasma Reactor for CO2 Dissociation: Does Size Matter? *Chem. Eng. J.* **2018**, *348*, 557–568, doi:10.1016/j.cej.2018.04.210.

40. MICHAEL A. LIEBERMAN ALLAN J. LICHTENBERG; A *PRINCIPLES OF PLASMA DISCHARGES AND MATERIALS PROCESSING*; 1994; Vol. 4; ISBN 9786468600.

41. Pinhão, N.R.; Janeco, A.; Branco, J.B. Influence of Helium on the Conversion of Methane and Carbon Dioxide in a Dielectric Barrier Discharge. *Plasma Chem. Plasma Process.* **2011**, *31*, 427–439, doi:10.1007/s11090-011-9294-3.

42. Ray, D.; Saha, R.; Subrahmanyam, C. DBD Plasma Assisted CO2 Decomposition: Influence of Diluent Gases. *Catalysts* **2017**, *7*, 1–11, doi:10.3390/catal7090244.

43. Snoeckx, R.; Bogaerts, A. Plasma Technology – a Novel Solution for CO2. *Chem. Soc. Rev.* **2017**, *46*, doi:10.1039/c6cs00066e.

44. Aerts, R.; Somers, W.; Bogaerts, A. Carbon Dioxide Splitting in a Dielectric Barrier Discharge Plasma: A Combined Experimental and Computational Study. *ChemSusChem* **2015**, *8*, 702–716, doi:10.1002/cssc.201402818.

6

Conclusion

Chapter 1 discusses the impact of the continuous rise of CO_2 in the atmosphere and resulting global warming. It explains how the 1.5°C increase in the average global temperature will affect every aspect of the environment and humanity. Nations worldwide are beginning to take action to address this issue, despite the slow start and the fact that we are already experiencing some of the catastrophic effects. For example, Europe has set a goal to eliminate CO_2 emissions by 2050 through net-zero emissions. In this scenario, CCUS technologies are considered crucial to tackle future challenges. The chemical sector is also making efforts, primarily focusing on electrification and the use of renewable sources. The first chapter provides an overview of the changes that must be implemented in the chemical industry to achieve the ambitious goal of zero emissions set by Europe. In the short term, it may be possible to intervene in the electrification of reactors without altering the ongoing chemical processes. However, in the medium and long term, power-to-lumps technologies emerge as the best alternatives. The role of electrochemistry, photocatalysis, and plasma technologies will be fundamental.

Chapters 2 and 3 showcase the potential of electrochemistry through the hydrogenation of oxalic acid catalyzed by a titania nanotube (NTs) based electrocatalyst.

In Chapter 2, the reaction is discussed as part of the Ocean Project (Oxalic acid from CO_2 using electrochemistry at demonstration scale, grant agreement ID: 767798), which aims to produce high-value chemicals from CO_2 using electrocatalytic processes. This chapter provides an overview of the current state of catalytic and electrocatalytic hydrogenation. It then focuses on the synthesis of titanium nanotubes, describing the traditional mechanism known as field-assisted dissolution (FAD) and the main variables that can alter the nanostructure of NTs. Additionally,

the text describes how an increase in anodization potential can trigger another mechanism known as rapid breakdown anodization (RBA). This mechanism is particularly interesting because it allows for the production of longer and rougher nanotubes (NTs).

Chapter 3 reports the experimental section on electrocatalytic hydrogenation of oxalic acid, which is divided into two parts:

- The first section compares the results of NTs grown according to the FAD theory with a sample obtained by hydrothermal synthesis (TiNT-HS). The results indicate that the nanostructure of TiO_2 plays a crucial role in catalyzing and directing the reaction towards glycolic acid (GC). This acid is obtained from oxalic acid through a two-step reaction in which glyoxylic acid (GO) is an intermediate. TiNT-A without TiO_2 NTs shows the presence of a densely nanostructured TiO_2 layer, and GO is the main product. Together with the TiO_2 nanotubes, TiNT, TiNT-T (obtained by thermal pretreatment), and TiNT-HS demonstrate that a tubular structure, along with the presence of tiny amorphous TiO_2 nanoparticles, can tune selectivity. Additionally, a fresh electrolyte solution is beneficial for obtaining longer and more defined NTs (TINT50-15 and TINT50), which address the reaction to GC. It has been demonstrated that the defects studied by CV and XPS, interpreted as oxygen vacancies (O2v), are the active sites of the electrocatalysts.
- However, under fast breakdown anodization conditions, as described in the second section of the chapter, the selective hydrogenation of OX can be performed more effectively compared to state-of-the-art titania-only electrodes. These conditions were achieved at 60 V in our study using TiNT60-15, TiNT60, and TiNT60-E. Additionally, the study investigated the effects of two pretreatments, thermal and electrochemical, before anodizing the Ti foil during RBA. The results showed that the electrochemical pretreatment had a more positive impact. The testing results were then

correlated with the morphological characteristics displayed in FESEM and AFM micrographs. It is worth noting that longer and rough NTs enhance the activity (in terms of OX conversion) and selectivity to GC. This is particularly highlighted by correlation with ECSA, suggesting a synergistic relationship between roughness and TiO_2 NT length, highlighting the crucial role of NT morphology in adjusting selectivity to GO or GC and increase the amount of accessible active sites.

The following chapters focus on plasma as an innovative technology with high potential for the valorization of CO_2.

Chapter 4 includes an excursus on cold plasma technologies, highlighting their potential and critical issues. After an initial introduction to what cold plasma is, attention is turned towards plasma-assisted CO_2 splitting, the focus of the research conducted. This text describes the factors that influence CO_2 splitting in chemical-physical terms, both through direct and step-wise excitation. It then goes on to discuss commonly used plasma reactors, with a focus on the DBD reactor used in the experiments and the role of catalysis.
Subsequently the state of the art on CO_2 splitting using a DBD reactor also allows us to highlight most of the parameters that influence the reaction, which can be grouped into those related to the geometry of the reactor and those dependent on the characteristics of the plasma, but also the influence of the gas, temperature and pressure and the catalyst are discussed.

Chapter 5 reports the results of the experiments conducted with a new type of DBD reactor that uses porous internal electrodes (0.2 μm and 0.5μm) compared to a reactor with a smooth internal electrode. The performance of porous reactors covered with a thin layer of boehmite, obtained by dip coating and which consists of γ-Al_2O_3 as highlighted by the characterization, were compared to packed reactors, with and without porosity.

The data shows that porous reactors perform better in terms of energy conversion and efficiency, with a more marked effect for the reactor with porosity 0.5 μm. These results are interpreted in two ways: on the one hand, inside the pores of the electrode the plasma could be more intense, although the Debye length cannot be determined; on the other hand, the tip effect due to the particular morphology of the electrode could increase the local electric field, increasing the density of the plasma.

Although the boehmite layer reduces porosity and roughness of the electrodes, the performances are still comparable to the smooth reactor and significantly greater than the packed configuration. This shows that using a layer of boehmite makes it possible to overcome problems due to packing, first of all the reduction of residence time and the inevitable reduction of conversion. This could also be a turning point if a catalyst supported on alumina is used because costs could be reduced, especially if we consider that critical raw material are often used to catalyze the splitting of CO_2.

Appendix A - chapter 2

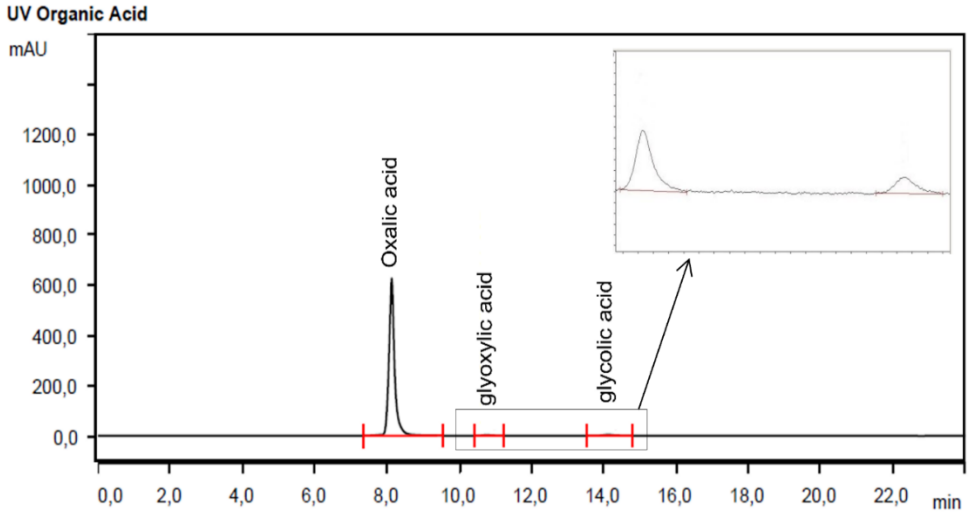

Figure A1 *Ionic Chromatogram for a representative testing sample.*

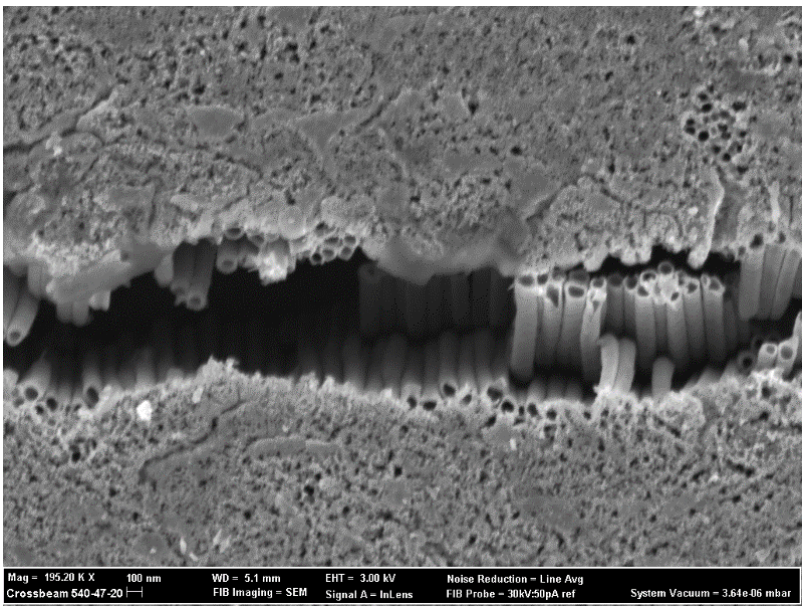

Figure A2 *Close-up of a crack in the oxide layer of TiNT-T*

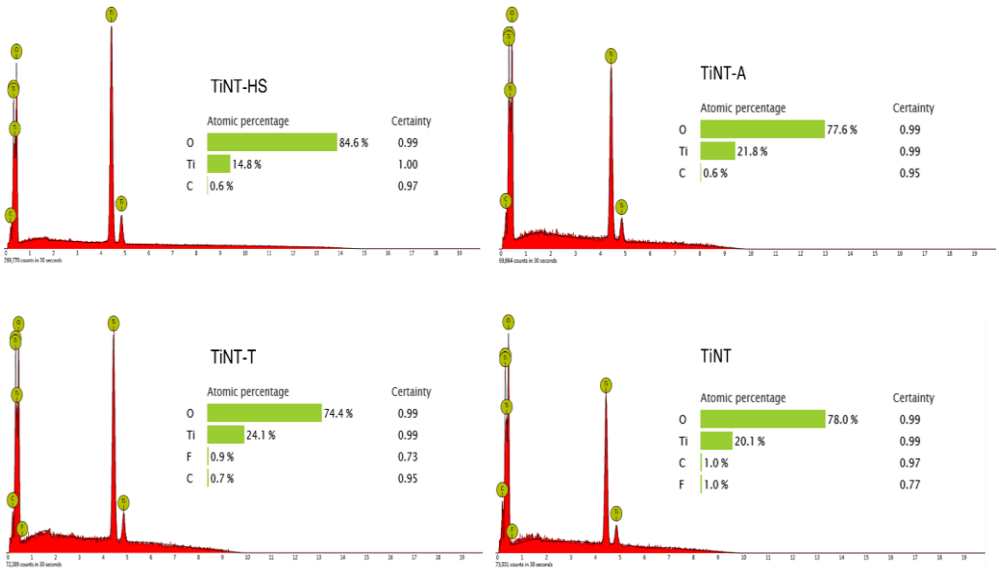

Figure A3 *EDX analysis of the prepared electrodes*

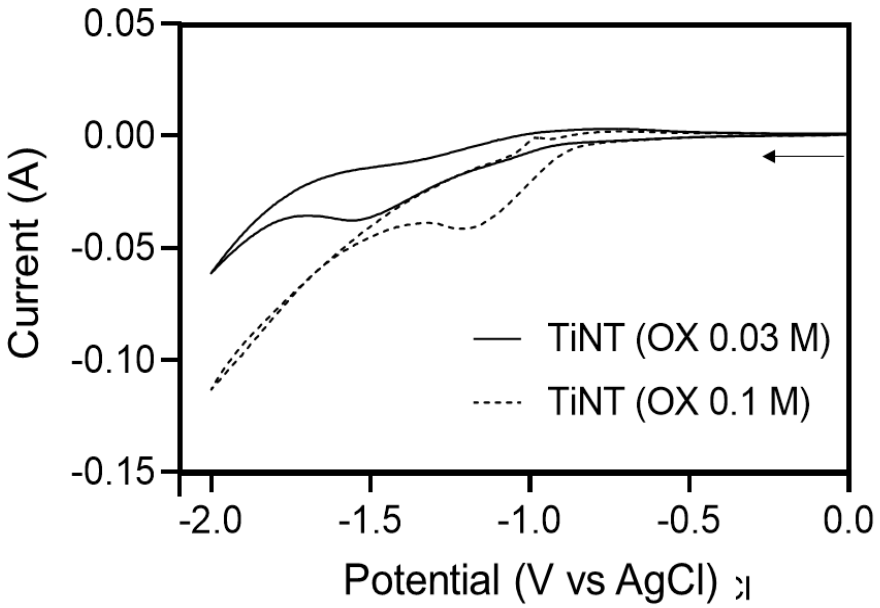

Figure A4 *Cyclic voltammetry in an oxalic acid solution 0.01 M and 0.03 M for the TiNT sample*

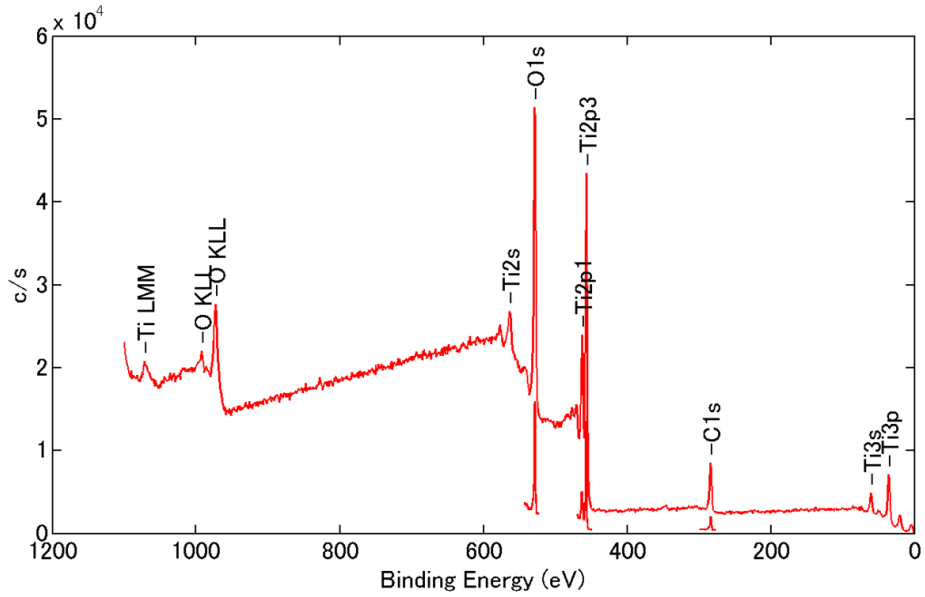

Figure A5 *Survey XPS spectrum for TiNT-T sample*

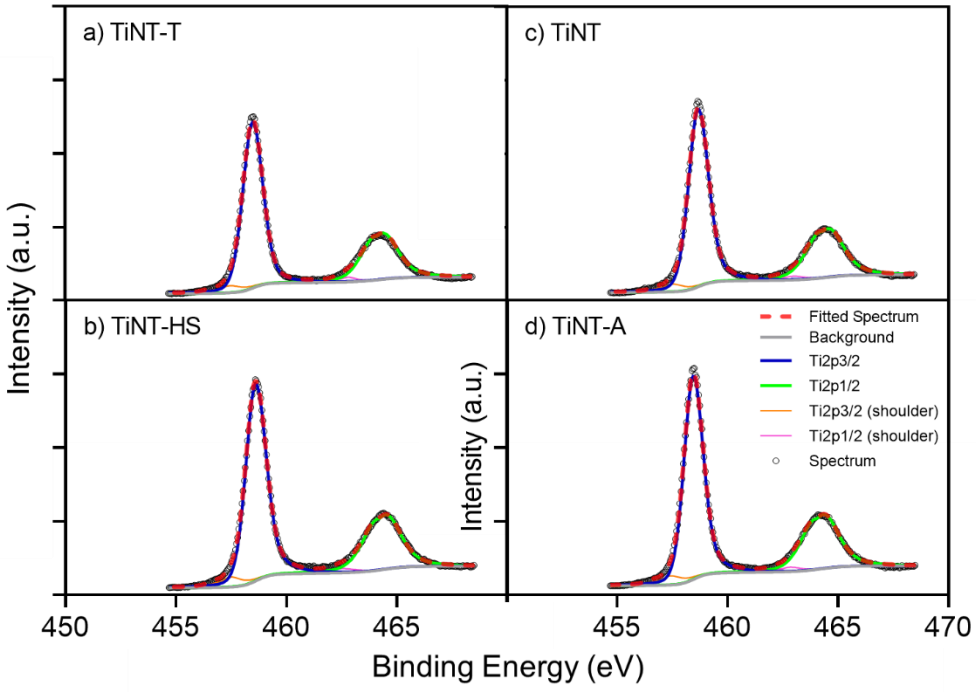

Figure A6 *Ti2p photoemission spectra of the used electrodes.*

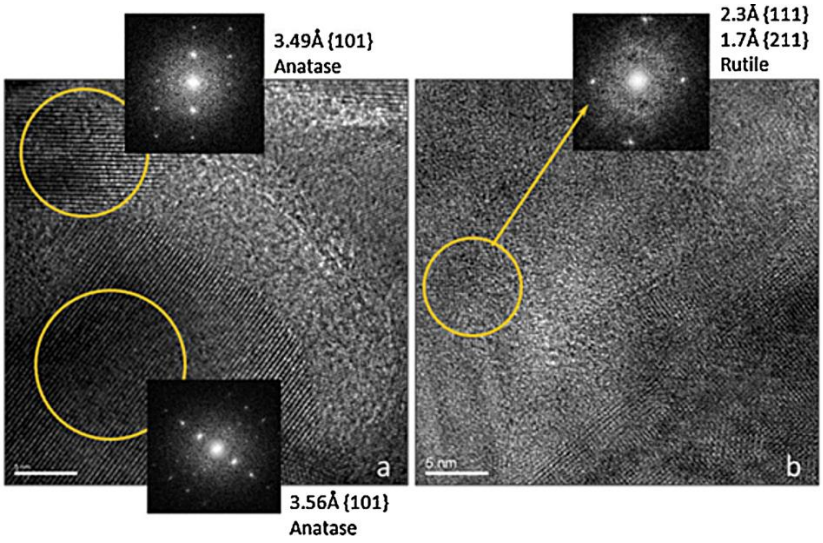

Figure A7. *HRTEM micrographs of supported TiO_2 NTs (on Ti substrate) thermally annealed at 450 °C: (a) anatase phase at the top of the TiNT thin film array and (b) rutile phase of the bottom area at the interface between the oxide thin layer and the metallic substrate [1].*

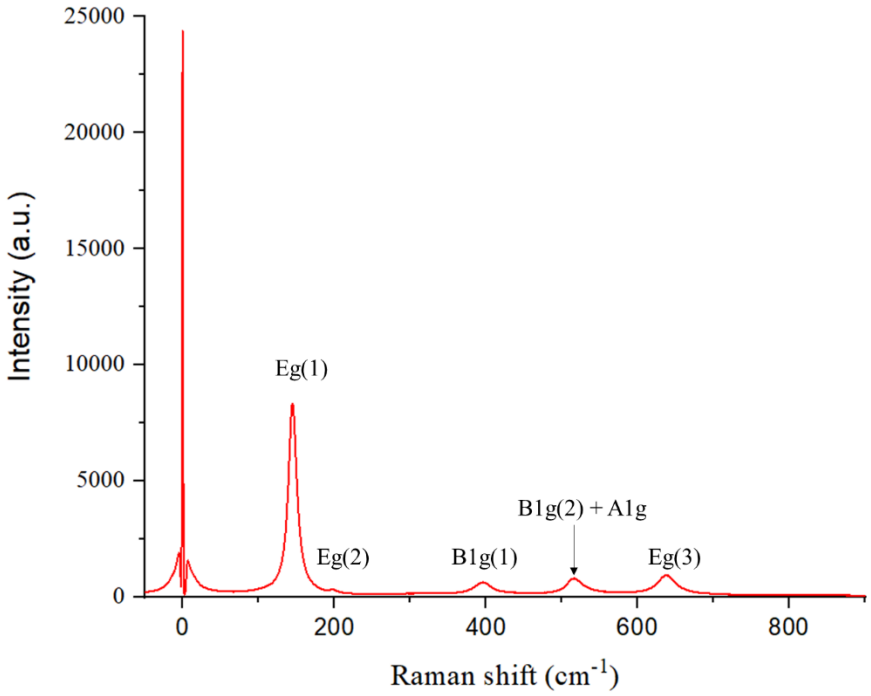

Figure A8a *Raman spectra for TiNT sample*

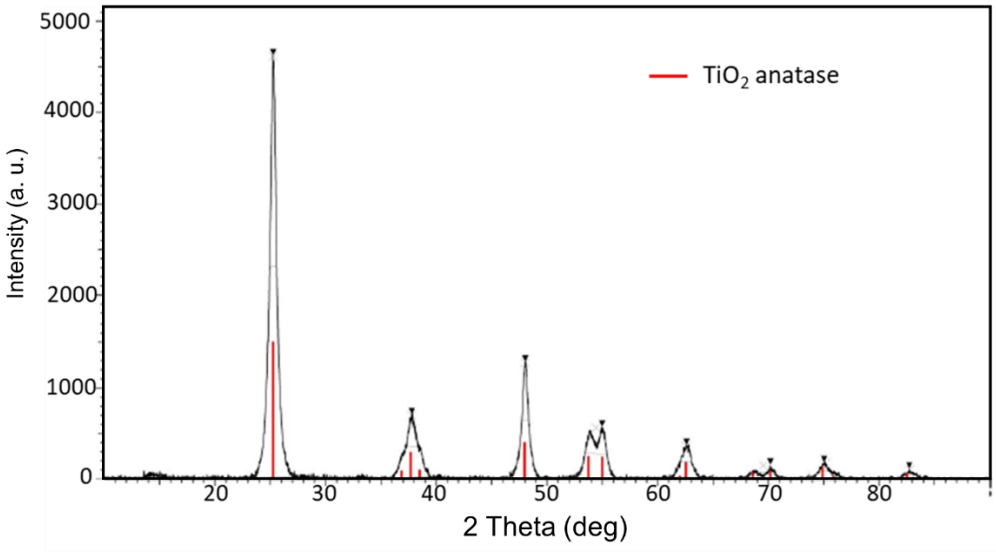

Figure A8b *X-ray diffraction pattern of TiNT-HS*

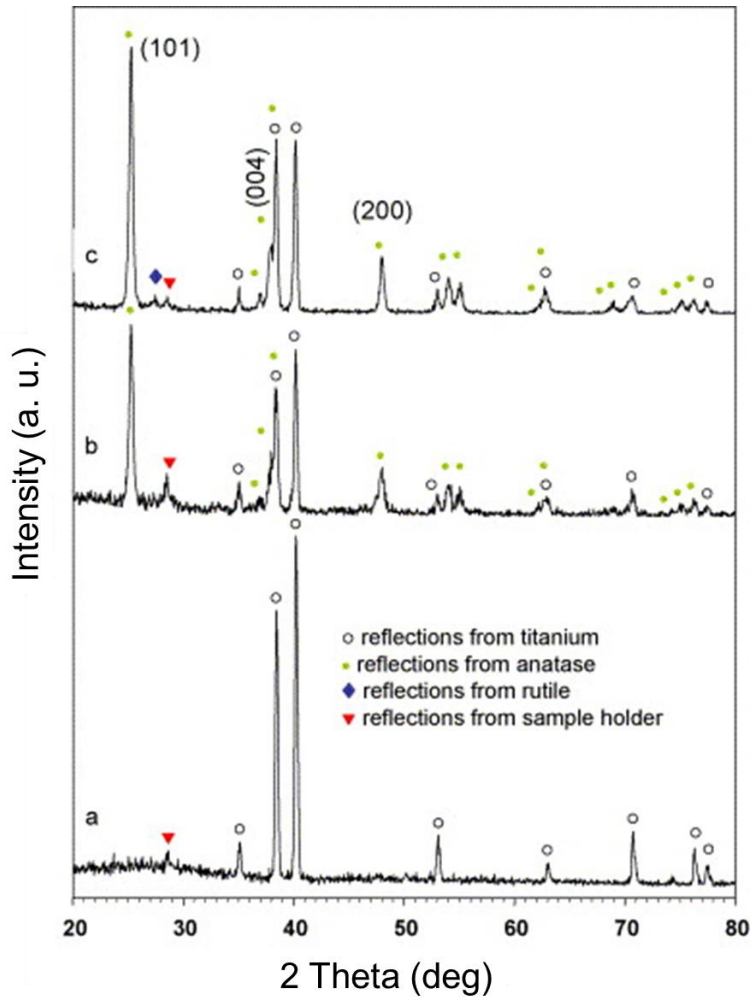

Figure A8c. *GAXRD of TiNT after anodization (a), further annealing in air at 450 °C for 3 h (b) and 500 °C for 3 h (c) [1].*

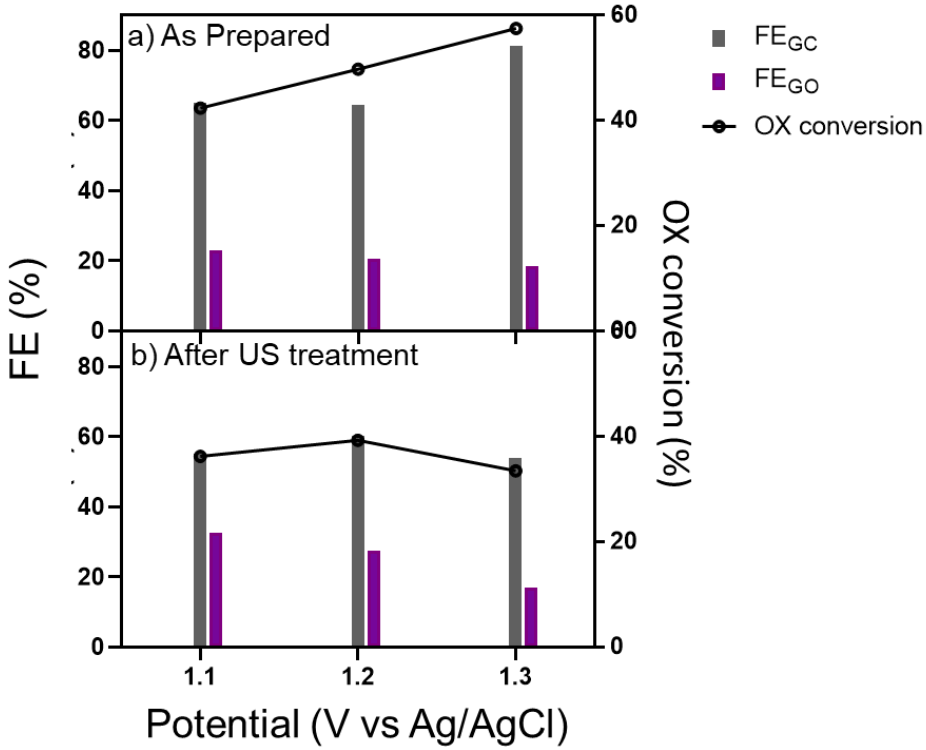

Figure A9 *Electrocatalytic behaviour of an optimized TiNT sample a) before and b) after ultra-sonification treatment.*

Table A1 *Summary of the electrocatalytic results (2h of test at each condition). For definition of FE (Faradaic Efficiency), OX conversion and Y (yield) see text.* $I_{average}$ *is the average current density in 2h continuous tests.*

Potential (V) -0.8 Vs RHE				
Electrode	FE_{GO} *(%)*	FE_{GC} *(%)*	*OX conv. (%)*	$I_{average}$ *(mA/cm²)*
TiNT	*51.1*	*43.8*	*6.8*	*-1.4*
TiNT-A	*31.2*	*15.1*	*6.1*	*-2.5*
TiNT-T	*26.5*	*55.7*	*25.2*	*-2.1*
TiNT-HS	*27.3*	*60.8*	*24.7*	*-2.3*
Ti-T	*10.8*	*5.6*	*4.1*	*-1.1*

Potential (V) -0.9 Vs RHE				
Electrode	FE_{GO} *(%)*	FE_{GC} *(%)*	*OX conv. (%)*	$I_{average}$ *(mA/cm²)*
TiNT	*19.1*	*13.1*	*5.6*	*-3.4*
TiNT-A	*20.3*	*6.7*	*6.4*	*-3.9*
TiNT-T	*24.7*	*52.2*	*25.6*	*-2.3*
TiNT-HS	*25.2*	*61.9*	*25.6*	*-2.5*
Ti-T	*5.3*	*1.4*	*2.9*	*-1.7*

Potential (V) -0.9 Vs RHE				
Electrode	FE_{GO} *(%)*	*FEGC (%)*	*OX conv. (%)*	$I_{average}$ *(mA/cm²)*
TiNT	*20.4*	*12.7*	*8.1*	*-4.7*
TiNT-A	*18.0*	*4.0*	*7.3*	*-6.5*
TiNT-T	*21.3*	*58.9*	*29.3*	*-2.7*
TiNT-HS	*25.0*	*61.0*	*25.5*	*-2.6*
Ti-T	*8.3*	*0.0*	*3.9*	*-1.8*

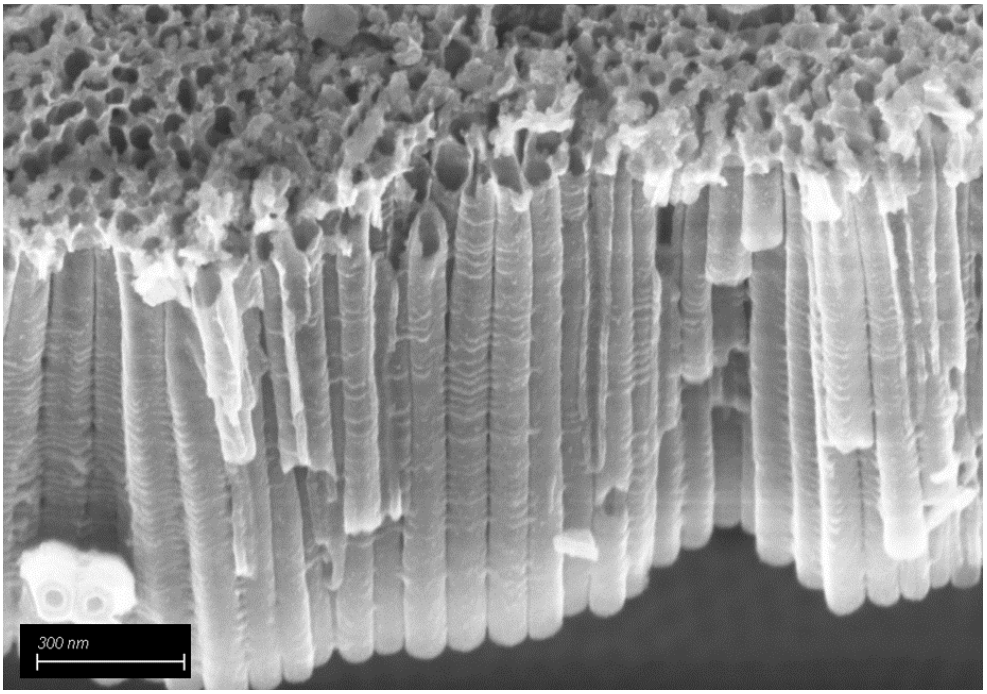

Figure A10 *Magnification of TiNT50-15*

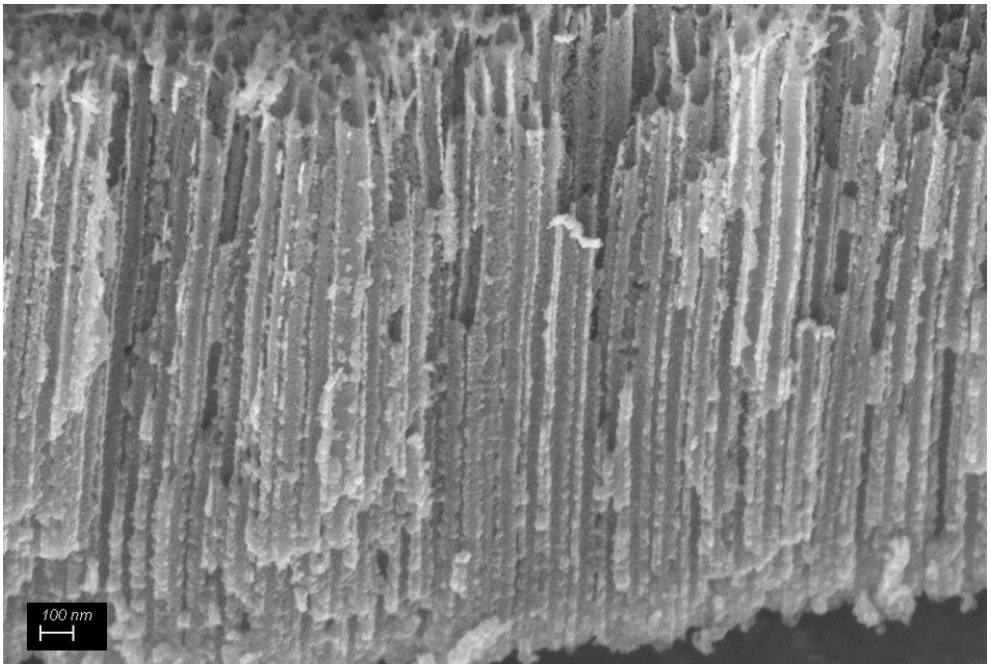

Figure A11 *Magnification of TiNT60-15*

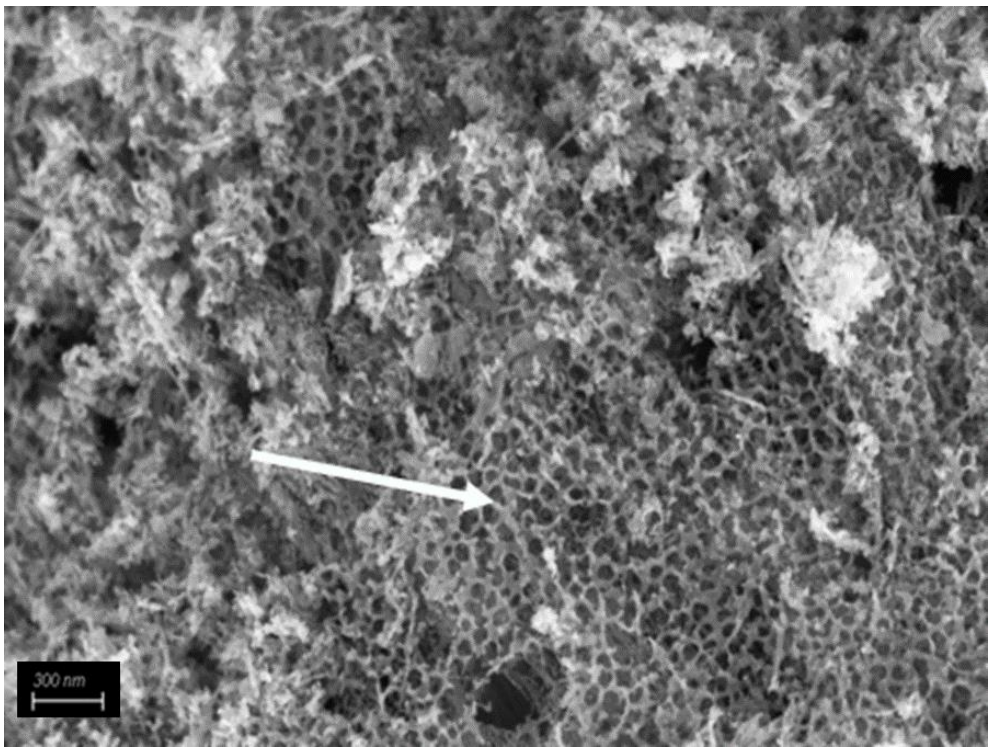

Figure A12 *Magnification of TiNT60 surface. The white arrow indicates the nanolance-like morphology.*

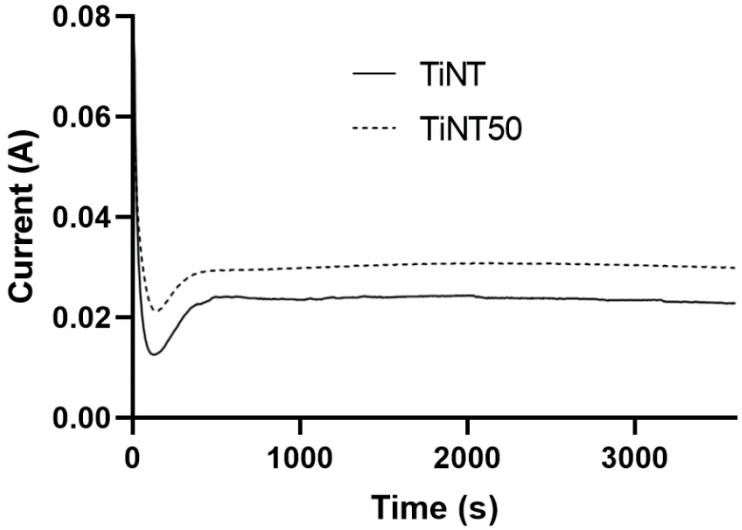

Figure A13 *Anodization curves for samples obtained at 50V in fresh (TINT50) or 60 min-aged (TINT) electrolyte solution.*

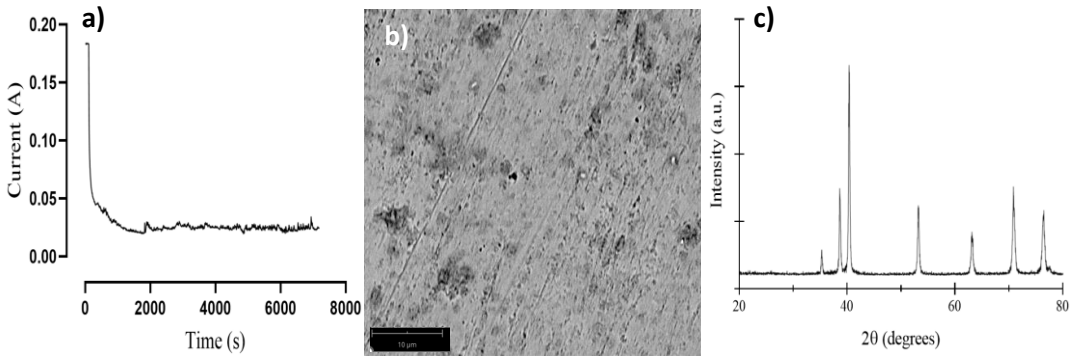

Figure A14 *a) I-t curve of the electrochemical pretreatment. b) FESEM micrograph of Ti-E c) Glading angle X-ray diffraction (GAXRD) pattern of Ti-E.*

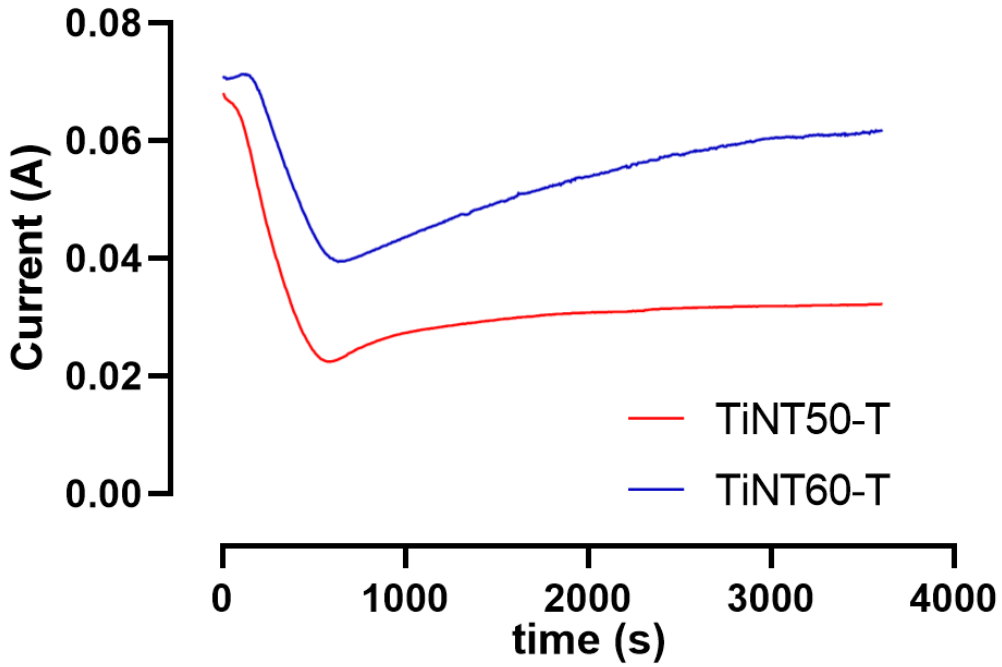

Figure A15 *Comparison of the current-time curves between the thermal pre-treated samples obtained at 50 V in an aged solution (red line) or 60 V in a fresh solution (blue line).*

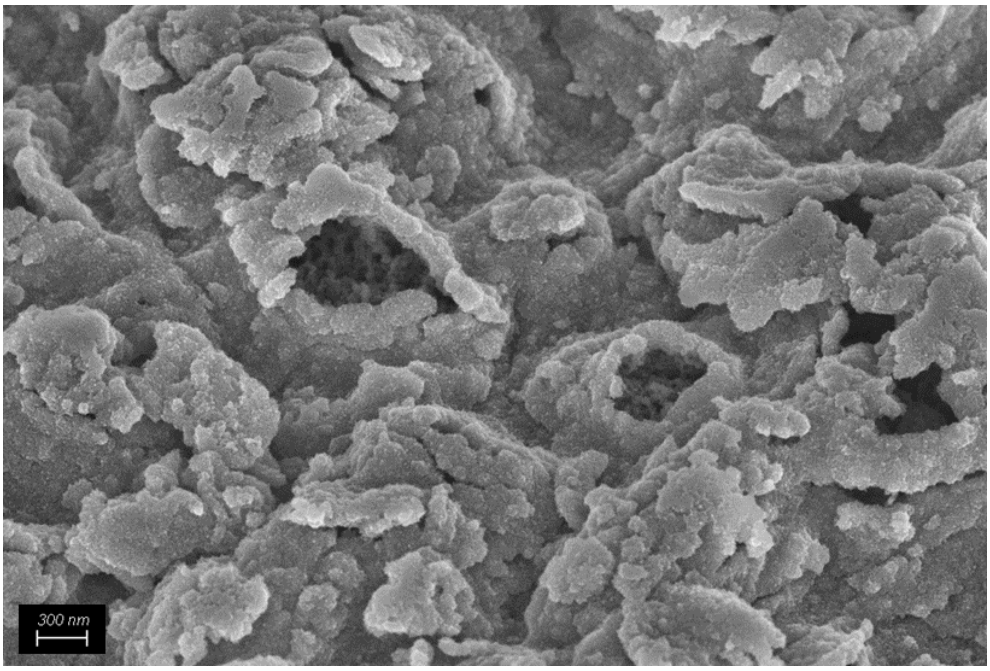

Figure A16 *Magnification of TiNT60-E surface.*

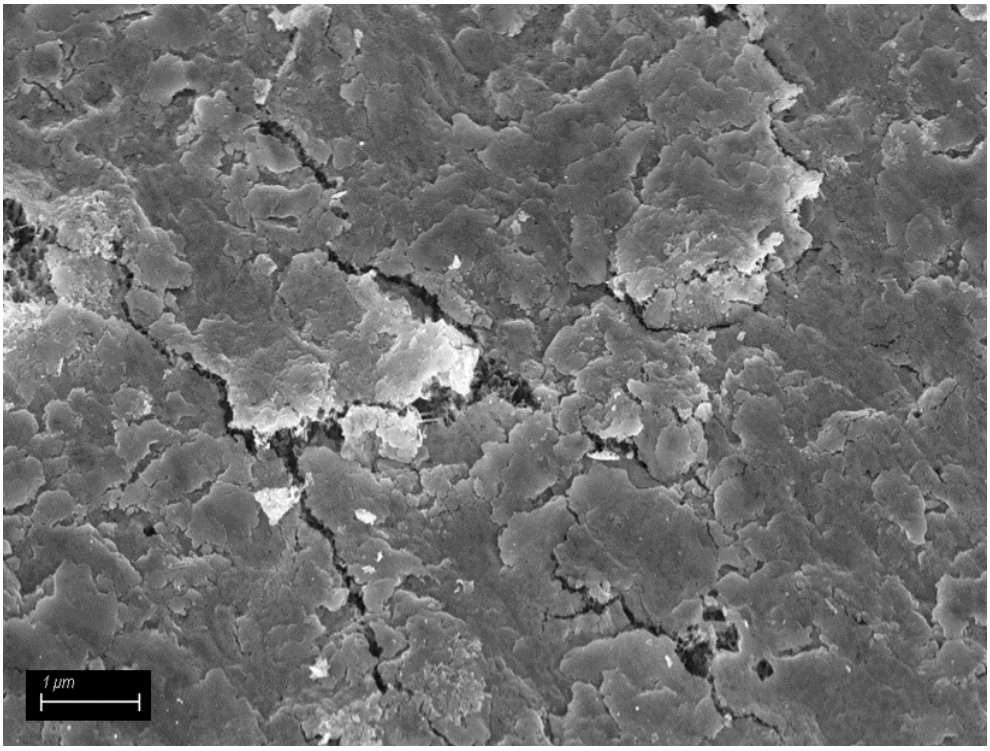

Figure A17 *Magnification of TiNT60-T surface.*

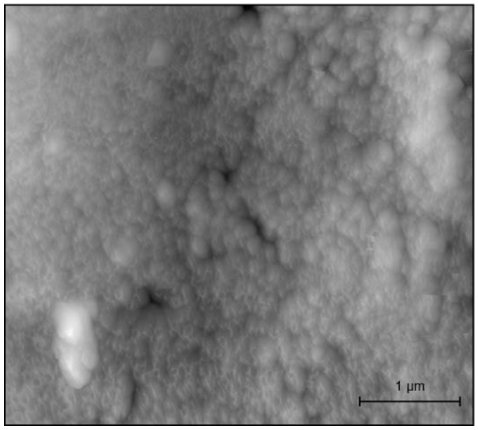

TiNT60-15

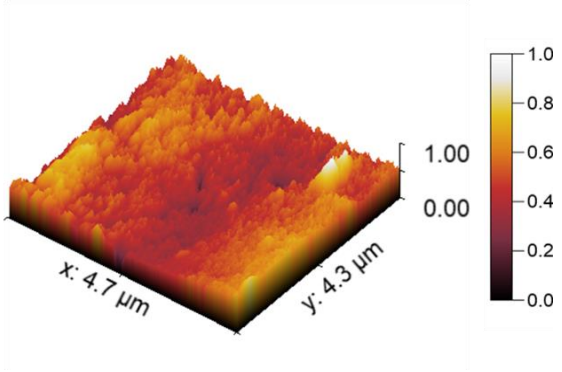

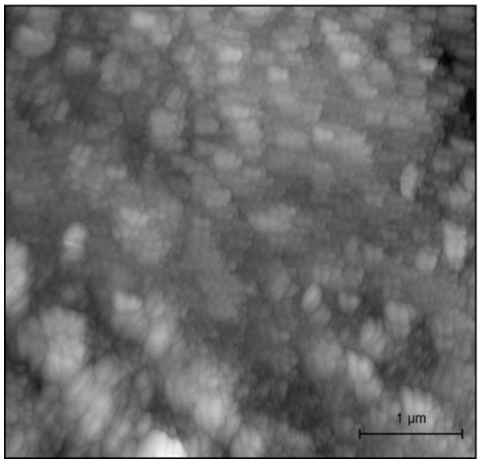

TiNT50-15

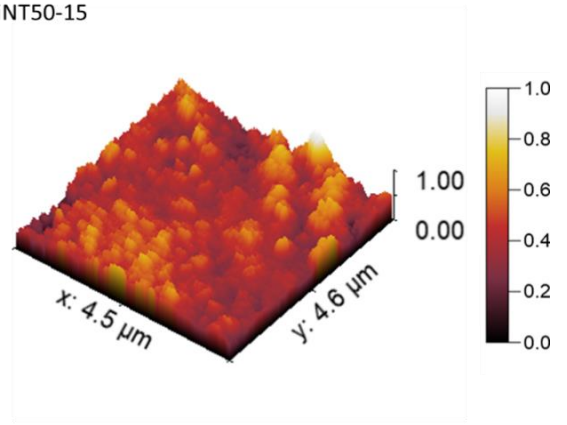

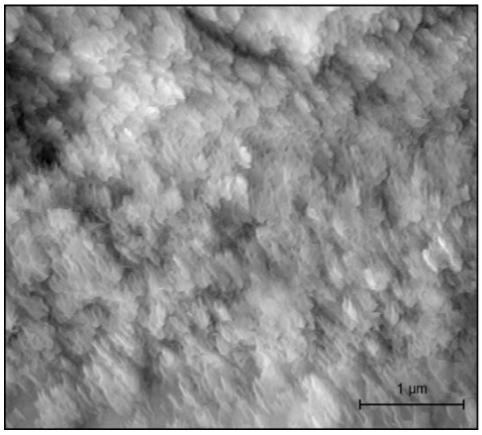

TiNT60

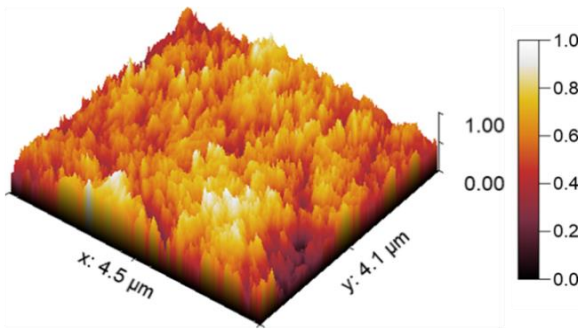

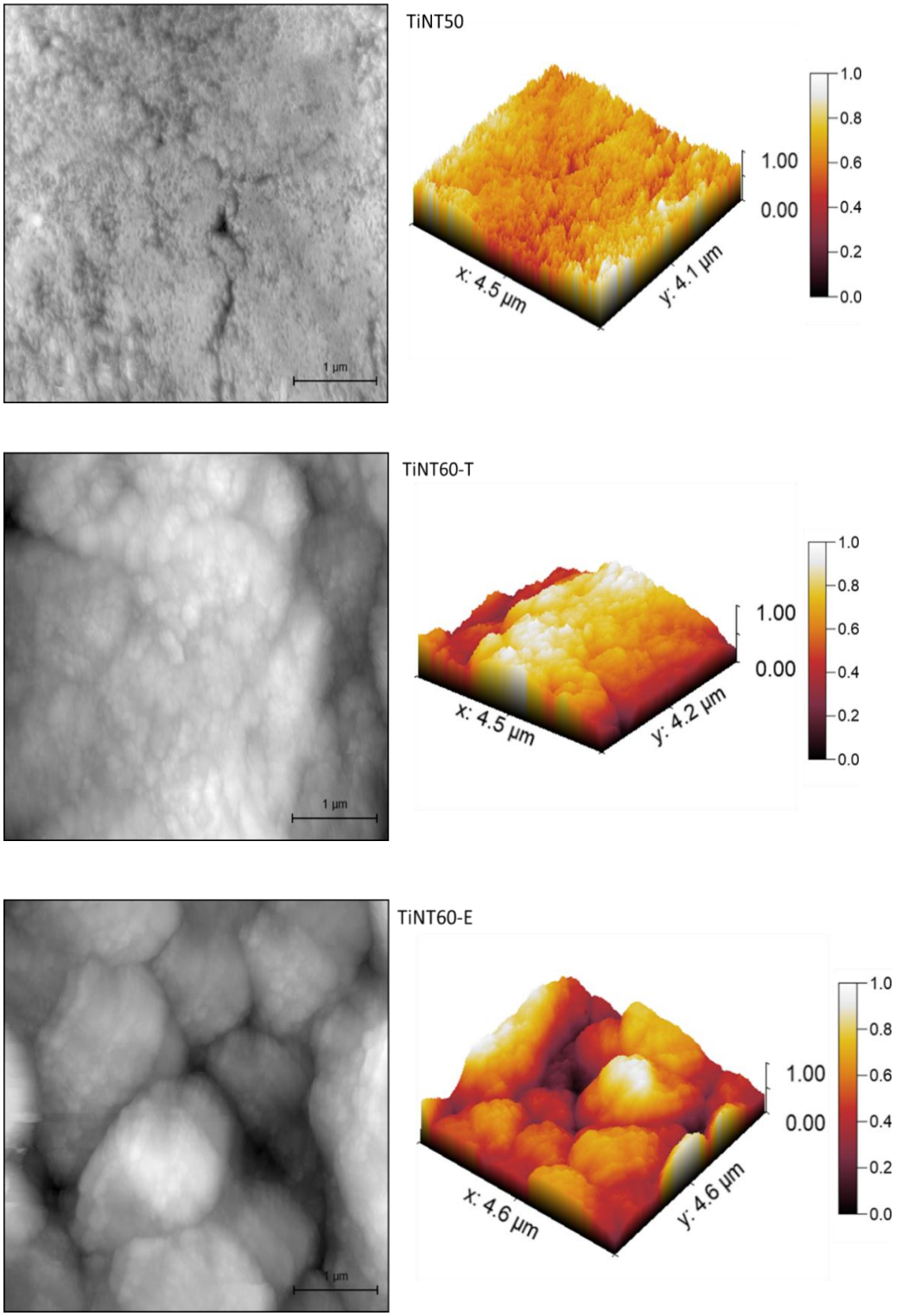

Figure A18 *2D and 3D images obtained by AFM.*

Table A2. *FEs, conversion, selectivity, and average current density of the investigated electrocatalysts (cathodic compartment: $[OX]_0$ = 0.03 M, $[Na_2SO_4]$ = 0.2 M; anodic compartment: $[Na_2SO_4]$ = 0.2 M, pH = 2, adjusted with 0.1 M H_2SO_4; three-electrode configuration; 20 min purging and degassing in Ar; as measured in Ar flow at room temperature after 2 h)*

Electrode	*Potential (V, vs RHE)*	*OX conv. (%)*	*S_{GO} (%)*	*S_{GC} (%)*	*FE_{GO} (%)*	*FE_{GC} (%)*	*$I_{average}$ (mA/cm^2)*
TiNT50-15		*32.1*	*22.3*	*9.8*	*45.6*	*40.0*	*-2.00*
TiNT60-15		*37.4*	*14.8*	*22.6*	*22.1*	*67.3*	*-2.50*
TiNT50		*47.5*	*22.7*	*24.8*	*30.2*	*65.9*	*-2.90*
TiNT60	*-0.8*	*55.6*	*11.6*	*43.9*	*11.4*	*86.0*	*-3.20*
TiNT60-T		*37.0*	*16.3*	*20.6*	*24.2*	*61.2*	*-2.80*
TiNT60-E		*48.3*	*10.6*	*37.6*	*12.1*	*86.3*	*-3.40*
Ti-E		*6.0*	*4.3*	*1.7*	*32.3*	*25.5*	*-0.50*
TiNT50-15		*35.5*	*22.3*	*9.8*	*43.1*	*39.5*	*-1.30*
TiNT60-15		*40.7*	*14.8*	*22.6*	*23.4*	*57.0*	*-3.20*
TiNT50		*35.7*	*14.5*	*21.2*	*21.1*	*61.4*	*-2.70*
TiNT60	*-0.9*	*41.0*	*7.4*	*33.6*	*9.6*	*87.4*	*-3.00*
TiNT60-T		*33.4*	*14.0*	*19.4*	*19.5*	*53.9*	*-2.90*
TiNT60-E		*55.5*	*10.6*	*37.6*	*13.4*	*72.7*	*-4.50*
Ti-E		*2.5*	*2.5*	*0.0*	*10.3*	*0.0*	*-1.00*
TiNT50-15		*27.4*	*16.4*	*11.0*	*26.5*	*35.4*	*-2.60*
TiNT60-15		*35.4*	*14.1*	*21.3*	*20.7*	*62.8*	*-2.70*
TiNT50		*37.6*	*11.0*	*26.6*	*15.9*	*77.1*	*-1.60*
TiNT60	*-1.0*	*43.8*	*8.4*	*35.3*	*8.8*	*73.3*	*-3.80*
TiNT60-T		*36.9*	*13.7*	*23.2*	*15.6*	*52.9*	*-3.60*
TiNT60-E		*47.6*	*12.2*	*35.4*	*12.4*	*72.5*	*-3.90*
Ti-E		*3.2*	*3.2*	*0.0*	*9.9*	*0.0*	*-2.00*

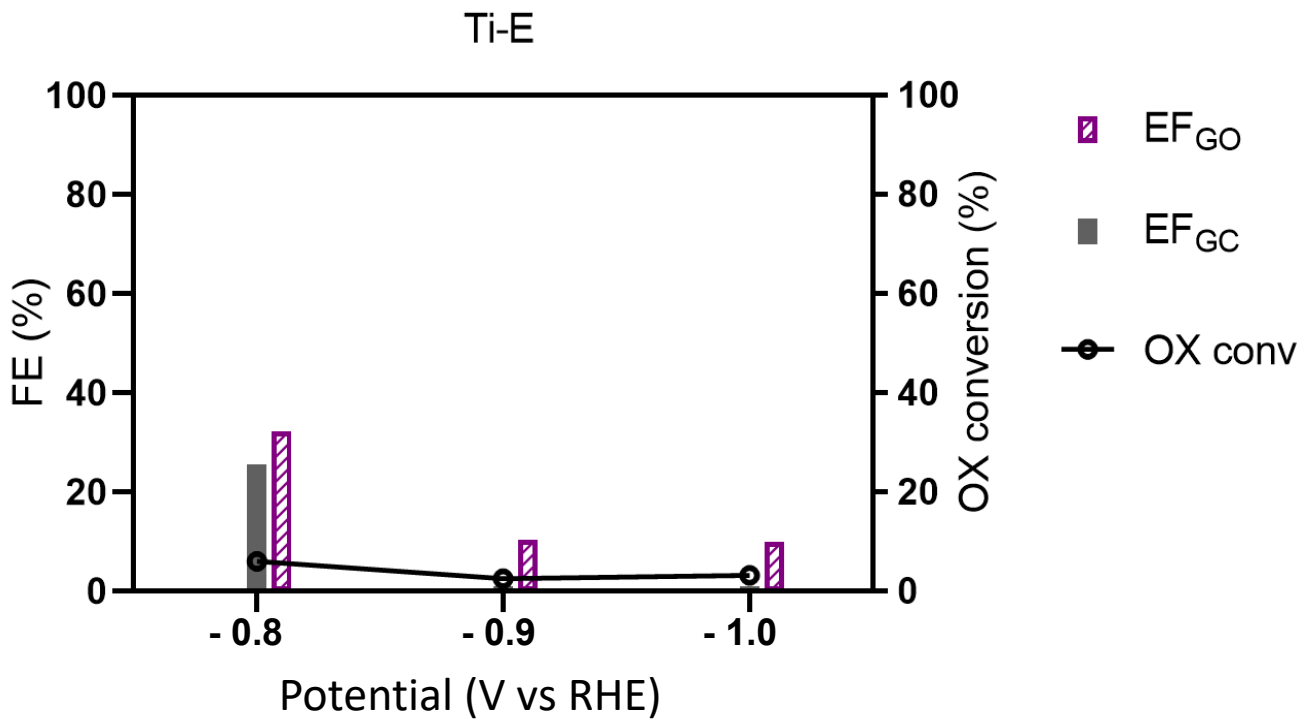

Figure A19 *FEs and OX conversion of Ti-E sample at three investigated potentials.*

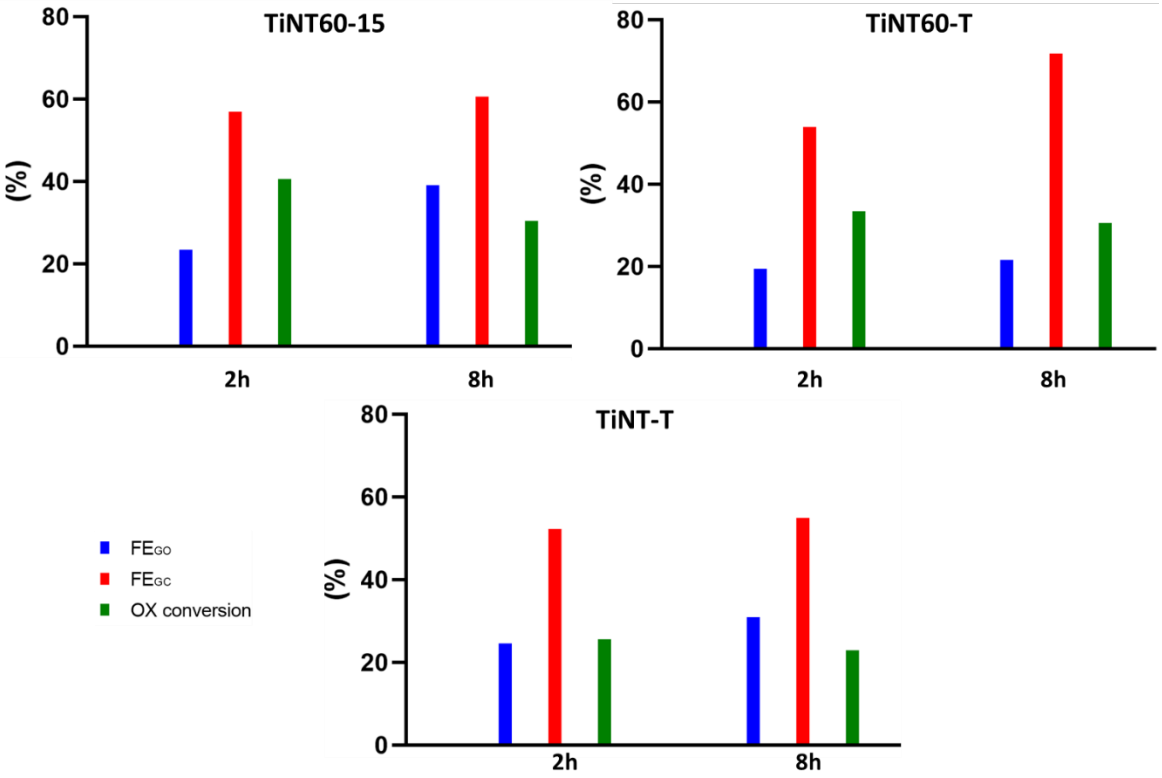

Figure A20 *FEs and OX conversion for TiNT60-15, TiNT60-T and TiNT-T at -0.9V vs. RHE after 2h or 8h.*

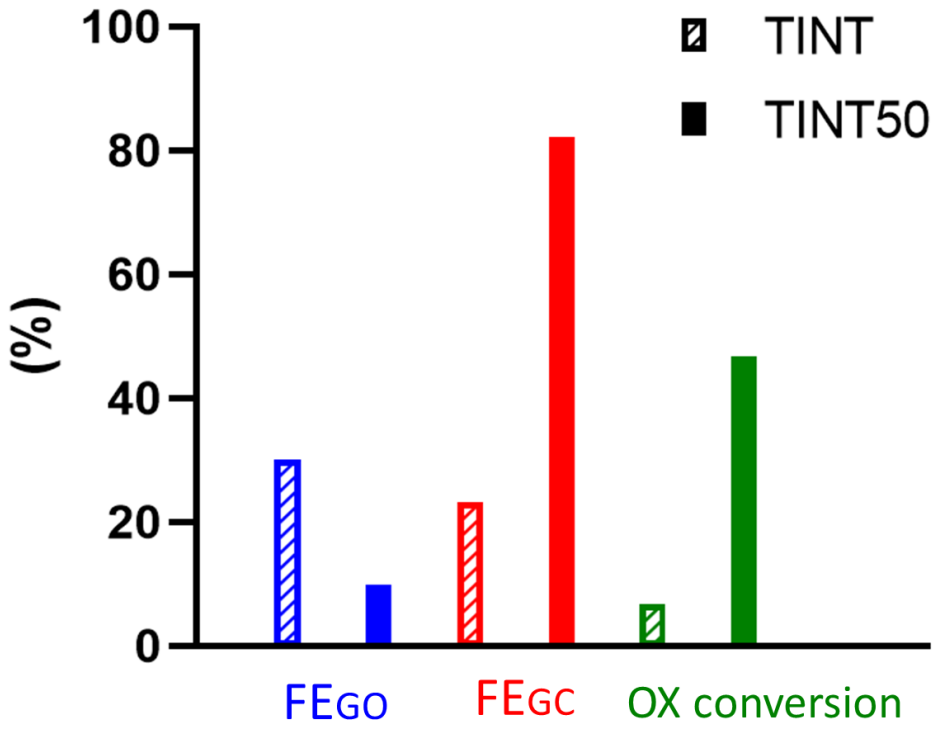

Figure A21 *Performances for TiNT and TiNT50*

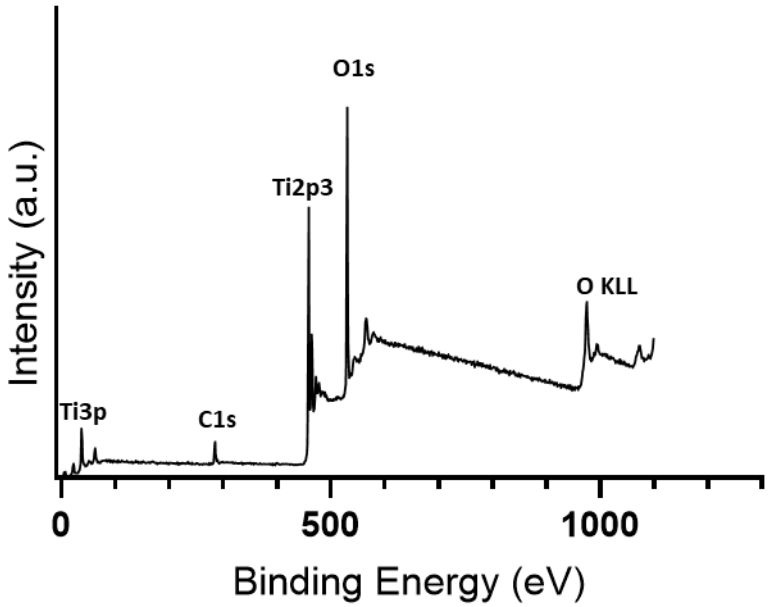

Figure A22 *Survey spectrum of the TiNT50 sample*

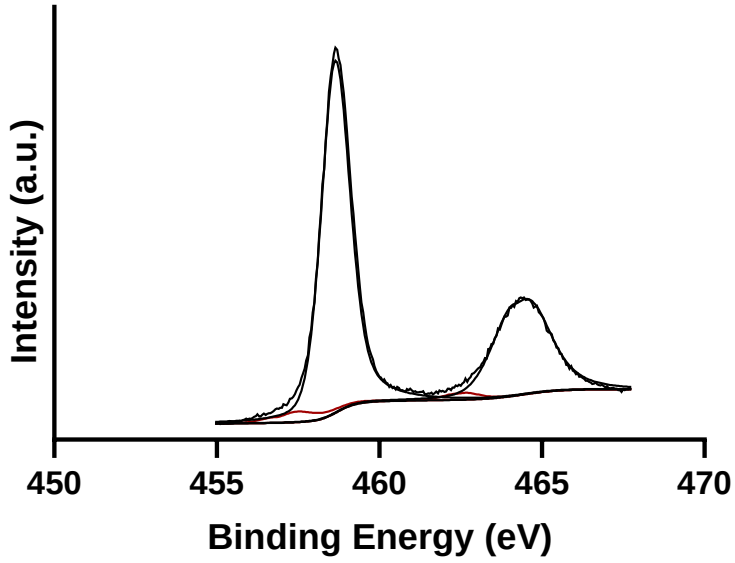

Figure A23 *Ti2p spectrum of the TiNT50 sample*

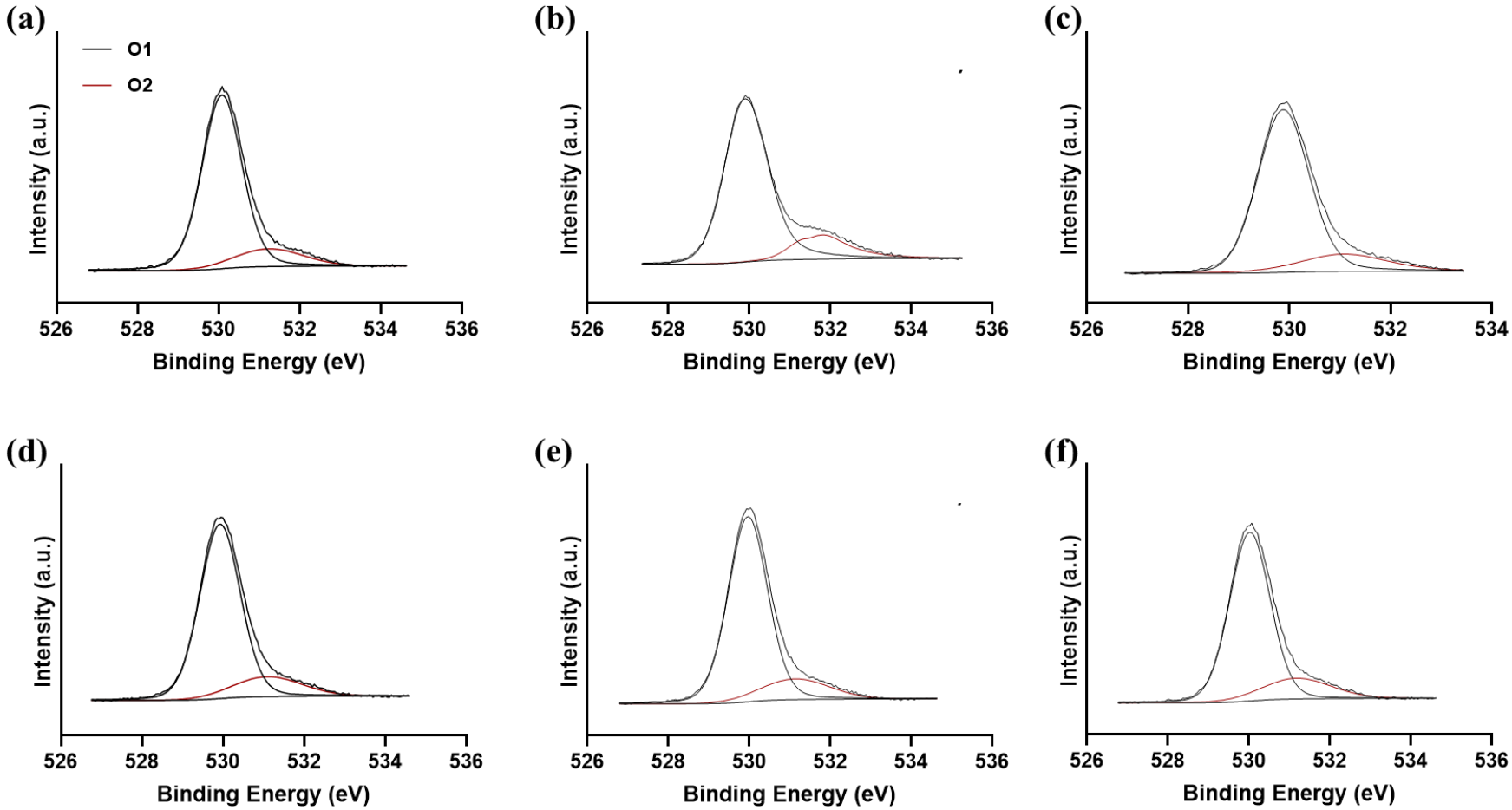

Figure A24 *O1s spectra of a) TiNT50-15, b) TiNT50, c) TiNT60, d) TiNT60-15, e) TiNT60-T, f) TiNT60-E samples*

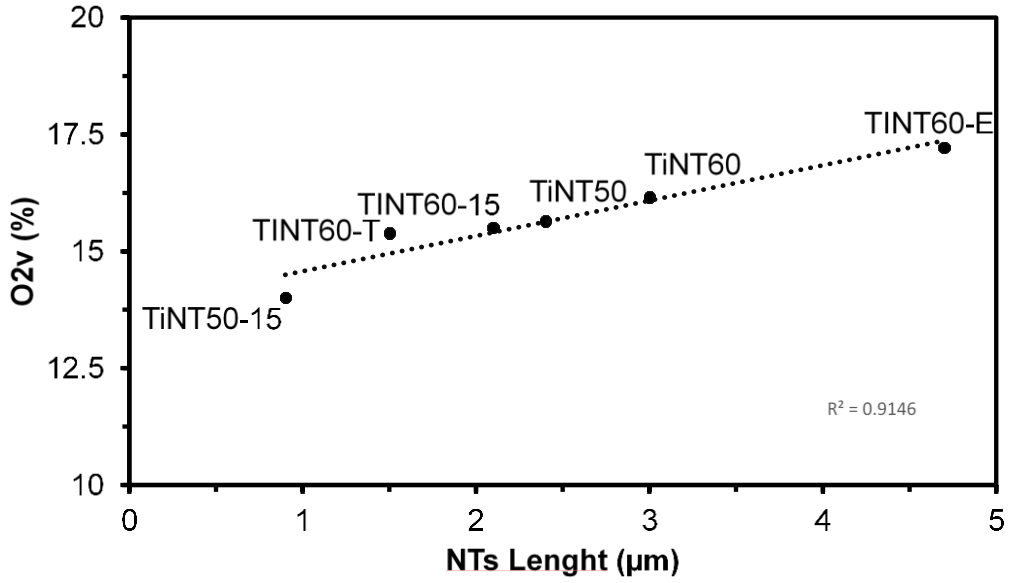

Figure A25 *Correlation between NTs length and O2v (%)*

Table A3 *Crystallinity index and estimate of the TiO_2/Ti content in the samples.*

Sample	*Crystallinity (%)*	*Amorphous (%)*	*Amount TiO_2 (%)*	*Amount Ti (%)*
Ti-E	*75.9*	*24.1*	*-*	*100*
TiNT50	*98.8*	*1.2*	*79.2*	*20.8*
TiNT50-15	*73.8*	*26.2*	*27.7*	*72.3*
TiNT60	*95.3*	*4.7*	*35.6*	*64.4*
TiNT60-15	*51.7*	*48.3*	*32.2*	*67.8*
TiNT60-E	*70.3*	*29.7*	*29.7*	*70.3*
TiNT60-T	*98.8*	*1.2*	*50*	*50*

The following equation was used to evaluate the crystallinity of the investigated samples [2]:

$$CI\ (\%) = 100\ x\ \frac{S_c}{S_t} \qquad (1)$$

Where S_c is the crystalline peak area and S_t represents the total area of the diffractogram, respectively.

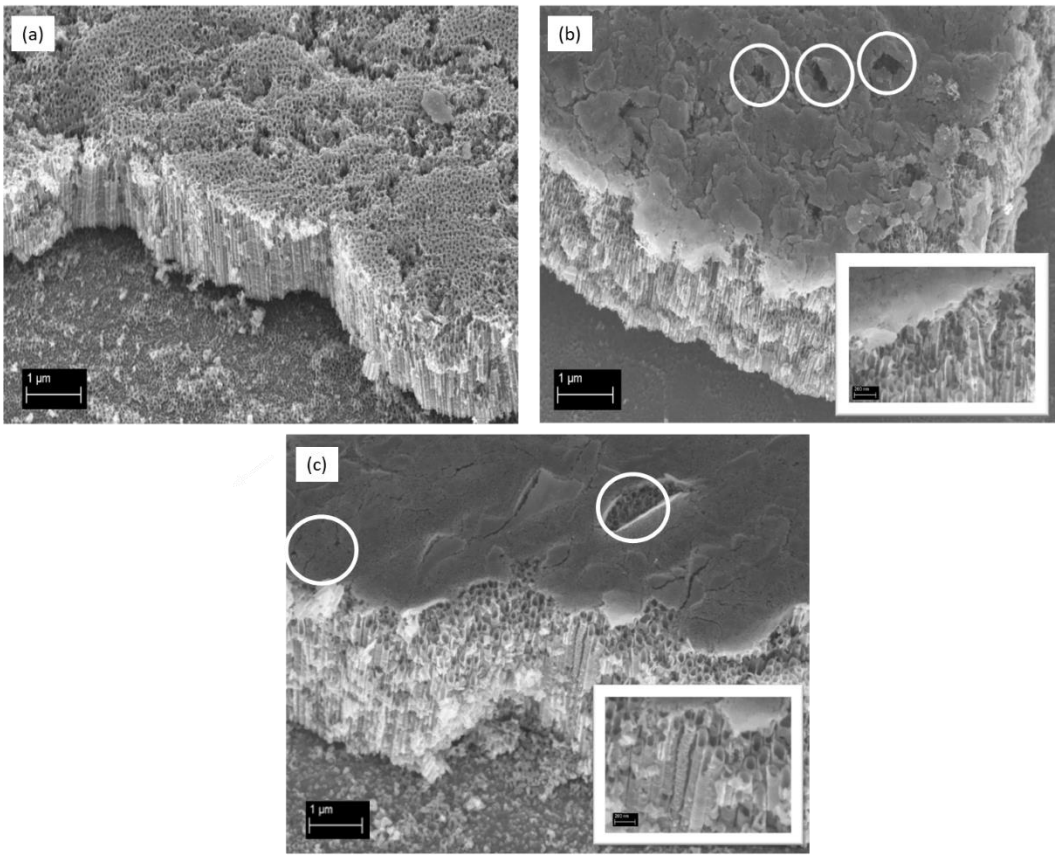

Figure A26 *FESEM images for TiNT60-15 (a) TiNT60-T (b) and TiNT-T (c) after testing at different potential.*

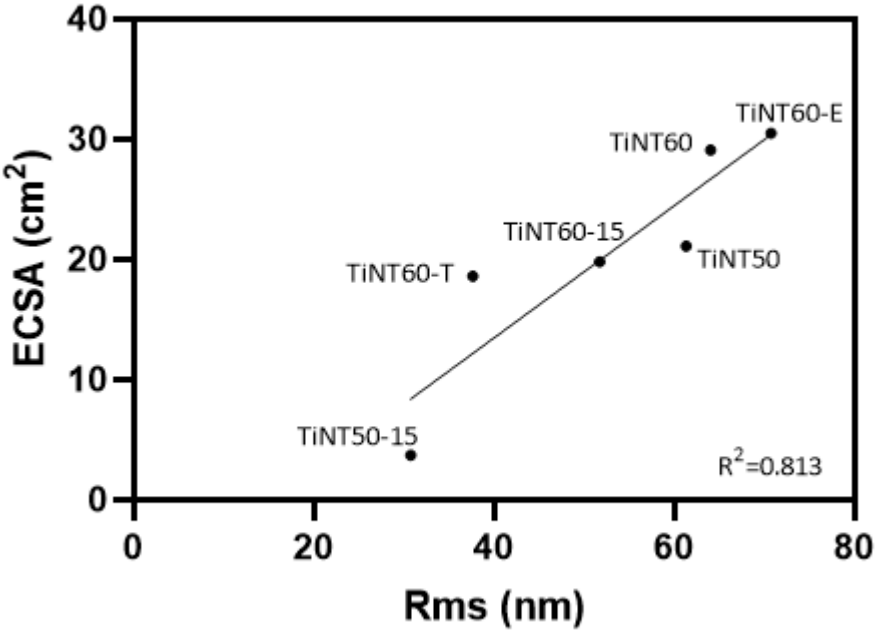

Figure A27 *Correlation between ECSA and Rms*

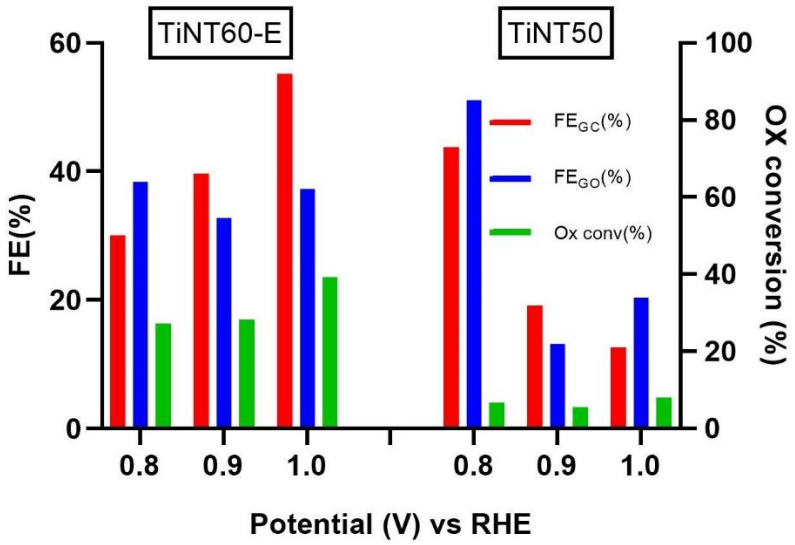

Figure A28 *FEs and OX conversion for TiNT50 and TiNT60-E using [OX]= 0.1M at -0.8, 0.9, 1.0 V vs RHE*

Appendix A References

[1] (a) S. Perathoner, R. Passalacqua, G. Centi, D. S. Su, G. Weinberg, Catal. Today, 122 (2007) 3-13.

(b) R. Passalacqua, S. Perathoner, G. Centi, Catal. Today, 251 (2015) 121-131.

[2] Rotaru, R.; Savin, M.; Tudorachi, N.; Peptu, C.; Samoila, P.; Sacarescu, L.; Harabagiu, V. Ferromagnetic Iron Oxide-Cellulose Nanocomposites Prepared by Ultrasonication. Polym. Chem. 2018, 9, 860–868, doi:10.1039/c7py01587a.

Appendix B - chapter 5

Table B1 Performances of the investigated reactors in different gas flow configurations, gas composition and flow rate. In smooth reactor the shell in -shell out configuration is the only one possible.

		gas flow configuration	gas composition	Flow rate (ml min^{-1})	CO_2 conv (%)	energy effic. (%)	SEI (KJ L^{-1})	Conversion rate (mmol h^{-1})
0.2	empty	shell in - shell out	CO_2	20.0	24.2	3.6	84.6	12.0
0.2	empty	shell in - shell out	CO2	30.0	21.1	4.9	54.8	15.6
0.2	empty	shell in - shell out	CO2	50.0	16.7	6.5	32.5	20.7
0.2	empty	shell in - shell out	CO2 - Ar (20%)	20.0	25.6	4.6	70.1	10.4
0.2	empty	shell in - shell out	CO2 - Ar (20%)	30.0	23.1	6.2	46.9	14.1
0.2	empty	shell in - shell out	CO2 - Ar (20%)	50.0	19.2	8.6	28.4	19.7
0.2	empty	shell in - tube out	CO2	20.0	24.6	3.7	83.8	12.2
0.2	empty	shell in - tube out	CO2	30.0	21.3	4.9	55.5	15.8
0.2	empty	shell in - tube out	CO2	50.0	16.4	6.4	32.4	20.3

0.2	empty	shell in - tube out	CO2 - Ar (20%)	20.0	26.0	4.7	69.9	10.5
0.2	empty	shell in - tube out	CO2 - Ar (20%)	30.0	23.4	6.6	45.0	14.2
0.2	empty	shell in - tube out	CO2 - Ar (20%)	50.0	19.3	8.7	27.9	19.6
0.2	boehmite	shell in - shell out	CO2	20.0	22.0	3.2	87.3	10.9
0.2	boehmite	shell in - shell out	CO2	30.0	19.8	4.3	57.9	14.7
0.2	boehmite	shell in - shell out	CO2	50.0	15.4	5.5	35.5	19.0
0.2	boehmite	shell in - shell out	CO2 - Ar (20%)	20.0	24.8	4.1	76.1	10.0
0.2	boehmite	shell in - shell out	CO2 - Ar (20%)	30.0	22.5	5.6	50.7	13.7
0.2	boehmite	shell in - shell out	CO2 - Ar (20%)	50.0	18.6	8.0	29.6	18.9
0.2	boehmite	shell in - tube out	CO2	20.0	23.4	3.1	76.2	11.6
0.2	boehmite	shell in - tube out	CO2	30.0	20.6	4.1	62.9	15.3
0.2	boehmite	shell in - tube out	CO2	50.0	16.1	5.4	30.3	20.0
0.2	boehmite	shell in - tube out	CO2 - Ar (20%)	20.0	25.0	4.0	78.5	8.0

0.2	boehmite	shell in - tube out	CO2 - Ar (20%)	30.0	22.7	5.4	32.0	11.1
0.2	boehmite	shell in - tube out	CO2 - Ar (20%)	50.0	18.7	7.1	24.9	15.6
0.2	packed	shell in - shell out	CO2	20.0	18.6	2.4	95.9	9.2
0.2	packed	shell in - shell out	CO2	30.0	16.8	3.2	65.4	12.5
0.2	packed	shell in - shell out	CO2	50.0	13.2	4.3	39.0	16.3
0.2	packed	shell in - shell out	CO2 - Ar (20%)	20.0	21.0	3.4	78.1	8.6
0.2	packed	shell in - shell out	CO2 - Ar (20%)	30.0	19.4	4.8	51.9	11.9
0.2	packed	shell in - shell out	CO2 - Ar (20%)	50.0	16.3	6.5	31.8	16.8
0.2	packed	shell in - tube out	CO2	20.0	16.1	2.0	99.8	8.0
0.2	packed	shell in - tube out	CO2	30.0	15.1	2.9	66.4	11.2
0.2	packed	shell in - tube out	CO2	50.0	12.1	3.7	41.0	15.0
0.2	packed	shell in - tube out	CO2 - Ar (20%)	20.0	20.3	3.3	78.5	8.0
0.2	packed	shell in - tube out	CO2 - Ar (20%)	30.0	18.6	4.4	32.0	11.1

0.2	packed	shell in - tube out	CO2 - Ar (20%)	50.0	15.7	6.0	24.9	15.6

		gas flow configuration	gas composition	Flow rate (ml min^{-1})	CO_2 conv (%)	Energy effic. (%)	SEI (KJ L^{-1})	Conversion rate (mmol h^{-1})
0.5	empty	shell in - shell out	CO2	20.0	25.1	3.8	86.0	12.4
0.5	empty	shell in - shell out	CO2	30.0	22.3	5.7	49.1	16.6
0.5	empty	shell in - shell out	CO2	50.0	17.6	7.4	30.1	22.0
0.5	empty	shell in - shell out	CO2 - Ar (20%)	20.0	26.9	5.4	62.1	10.8
0.5	empty	shell in - shell out	CO2 - Ar (20%)	30.0	25.2	7.6	42.1	14.8
0.5	empty	shell in - shell out	CO2 - Ar (20%)	50.0	20.0	9.9	25.4	20.2
0.5	empty	shell in - tube out	CO2	20.0	23.9	3.5	87.4	11.8
0.5	empty	shell in - tube out	CO2	30.0	21.1	4.9	54.5	15.6
0.5	empty	shell in - tube out	CO2	50.0	16.6	6.5	32.3	20.5

0.5	empty	shell in - tube out	CO2 - Ar (20%)	20.0	24.7	4.4	70.9	9.9
0.5	empty	shell in - tube out	CO2 - Ar (20%)	30.0	22.7	6.1	47.0	13.7
0.5	empty	shell in - tube out	CO2 - Ar (20%)	50.0	19.0	8.5	28.3	19.3
0.5	boehmite	shell in - shell out	CO2	20.0	18.9	2.8	85.3	9.3
0.5	boehmite	shell in - shell out	CO2	30.0	17.9	4.0	56.6	13.2
0.5	boehmite	shell in - shell out	CO2	50.0	15.1	5.6	34.1	18.7
0.5	boehmite	shell in - shell out	CO2 - Ar (20%)	20.0	20.7	3.6	59.5	8.1
0.5	boehmite	shell in - shell out	CO2 - Ar (20%)	30.0	19.4	4.9	50.5	11.4
0.5	boehmite	shell in - shell out	CO2 - Ar (20%)	50.0	17.3	7.3	29.9	16.9
0.5	boehmite	shell in - tube out	CO2	20.0	20.4	3.2	81.4	10.1
0.5	boehmite	shell in - tube out	CO2	30.0	18.2	4.2	54.6	13.5
0.5	boehmite	shell in - tube out	CO2	50.0	14.6	5.7	32.5	18.0
0.5	boehmite	shell in - tube out	CO2 - Ar (20%)	20.0	20.7	3.9	67.6	8.3

0.5	boehmite	shell in - tube out	CO2 - Ar (20%)	30.0	19.4	5.3	45.8	11.7
0.5	boehmite	shell in - tube out	CO2 - Ar (20%)	50.0	16.9	7.7	27.6	17.1
0.5	packed	shell in - shell out	CO2	20.0	18.1	2.3	60.2	9.0
0.5	packed	shell in - shell out	CO2	30.0	15.4	2.9	40.0	11.4
0.5	packed	shell in - shell out	CO2	50.0	12.0	3.7	24.7	14.9
0.5	packed	shell in - shell out	CO2 - Ar (20%)	20.0	19.3	3.0	48.1	9.6
0.5	packed	shell in - shell out	CO2 - Ar (20%)	30.0	18.1	4.3	31.6	13.5
0.5	packed	shell in - shell out	CO2 - Ar (20%)	50.0	16.0	6.3	19.4	19.8
0.5	packed	shell in - tube out	CO2	20.0	19.4	2.3	109.0	9.6
0.5	packed	shell in - tube out	CO2	30.0	16.8	2.9	72.2	12.5
0.5	packed	shell in - tube out	CO2	50.0	12.8	3.7	44.1	15.8
0.5	packed	shell in - tube out	CO2 - Ar (20%)	20.0	21.9	3.1	71.0	10.8
0.5	packed	shell in - tube out	CO2 - Ar (20%)	30.0	19.9	4.2	47.2	14.7

0.5	packed	shell in - tube out	CO2 - Ar (20%)	50.0	16.8	5.8	29.4	20.8

		gas composition	Flow rate (ml min^{-1})	CO_2 conv (%)	Energy efficiency (%)	SEI (KJ L^{-1})	Conversion rate (mmol h^{-1})
smooth	empty	CO2	20.0	21.8	3.1	89.1	10.8
smooth	empty	CO2	30.0	19.8	4.3	59.3	14.7
smooth	empty	CO2	50.0	15.6	5.6	35.3	19.3
smooth	empty	CO2 - Ar (20%)	20.0	25.8	3.8	86.9	10.4
smooth	empty	CO2 - Ar (20%)	30.0	23.3	5.0	58.5	14.2
smooth	empty	CO2 - Ar (20%)	50.0	18.2	6.5	35.3	18.6
smooth	packed	CO2	20.0	18.0	1.9	96.7	8.9
smooth	packed	CO2	30.0	15.2	2.4	64.5	11.3
smooth	packed	CO2	50.0	10.5	2.5	41.8	13.0
smooth	packed	CO2 - Ar (20%)	20.0	22.5	2.8	100.0	8.9
smooth	packed	CO2 - Ar (20%)	30.0	19.7	3.7	66.4	11.7
smooth	packed	CO2 - Ar (20%)	50.0	15.4	4.8	41.0	15.4

Table B2 Calculated thickness and weight of different concentration boehmite layer on 0.5 µm stainless-steel membrane.

Boehmite conc. (wt.%)	n° dips	Thickness (µm)	Loading (mg*cm^{-2})
0.9	2	0.72	0.28
0.9	4	0.79	0.33
1.2	2	0.89	0.33
1.2	4	1.06	0.39
1.8	2	1.21	0.44
1.8	4	1.49	0.51

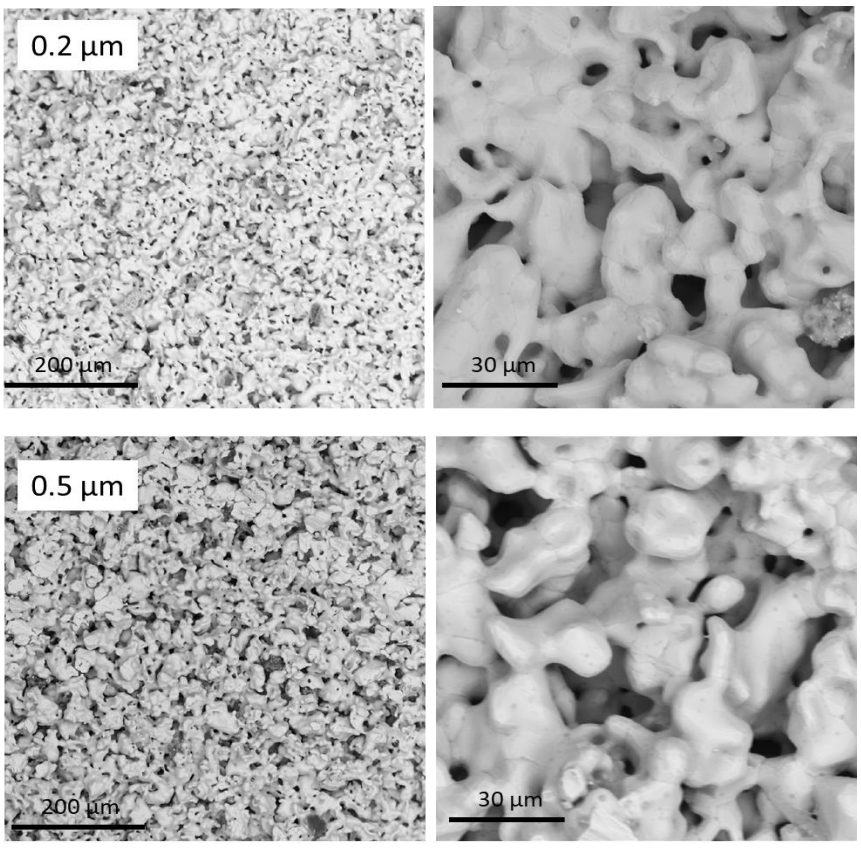

Figure B1 *SEM images of the boehmite covered internal electrodes at two different magnifications.*

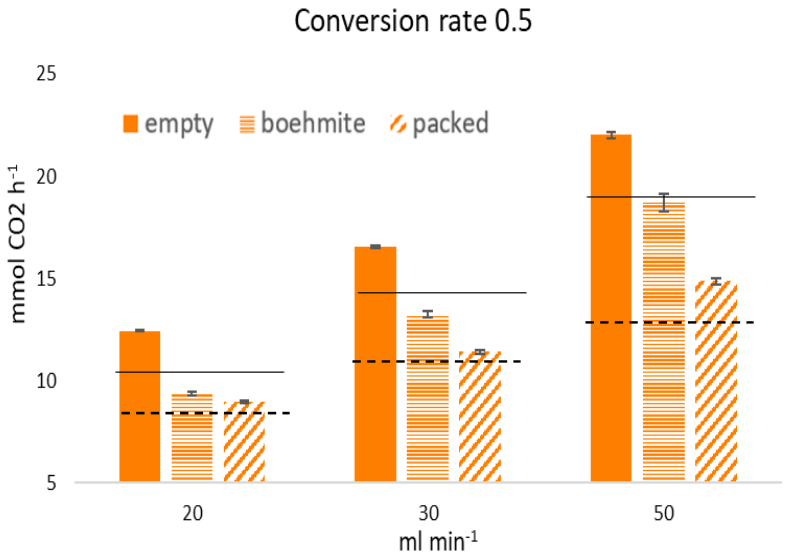

Figure B2 *Effect of 0.5 sample on conversion rate in pure CO_2 with different configuration for 0.5 ractor in shell out -shell out gas direction. The horizontal lines indicate the conversion rate of the smooth reactor empty (solid) or packed (dashed) in pure CO_2*

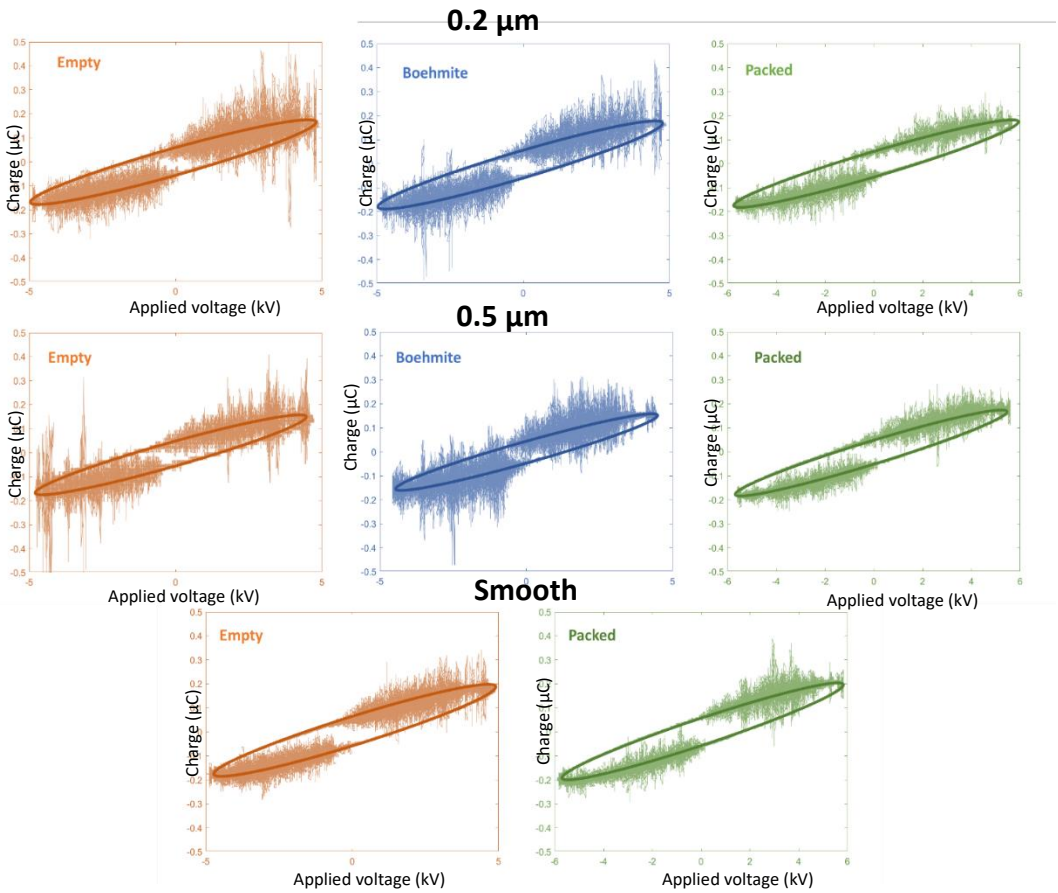

Figure B3 *Lissajous figures in pure CO_2 at 20 ml min^{-1} and shell in - shell out configuration*

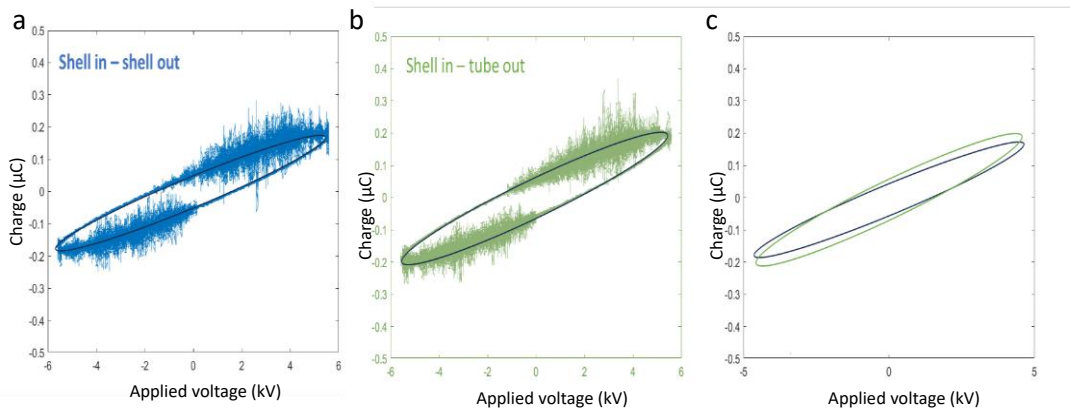

Figure B4 *Lissajous figures for 0.5 µm in packed reactor and pure CO_2 for shell in – shell out (a) and shell in – tube out (b) configuration. A comparison of the Lissajous figures is reported in figure (c)*